Interaction of Nanosecond and Femtosecond Laser Pulses with Carbon: Deposition of Carbon Films having Novel Compositions

by

Anming Hu

A thesis
presented to the University of Waterloo
in fulfillment of the
thesis requirement for the degree of
Doctor of Philosophy
in
Physics

Waterloo, Ontario, Canada, 2008

AUTHOR'S DECLARATION

I hereby declare that I am the sole author of this thesis. This is a true copy of the thesis, including any required final revisions, as accepted by my examiners.

I understand that my thesis may be made electronically available to the public.

Abstract

A comparison of the composition and structure of carbon films deposited by ns and fs laser ablation of graphite is the subject of this thesis. In addition, the effect of irradiation on the surface of graphite has been investigated in detail. Laser-induced phase transitions from graphite to sp-bonded carbon and trans-polyacetylene chains as well as the formation of nano-diamond have been observed after irradiation with fs pulses. An optical orientation mechanism involving both electric and magnetic interactions is proposed to understand the formation of nano-stripes and other structures on irradiated graphite surfaces. These phenomena are not observed after nanosecond laser irradiation.

Tetrahedral carbon (ta-C) films deposited at cryogenic temperatures using ns laser radiation consist of sub-micron graphitized grains embedded in a matrix of sp^3-hybridized bonded carbon. Nano-buckling is evident in ta-C films deposited by fs ablation where the composition is found to consist of mixed *sp*, sp^2, and sp^3 – hybridized carbons species. It is found that the concentration of sp-bonded chains is negligible in ns-C films. Surface enhanced Raman spectroscopy has been used to characterize molecular species in ns and fs carbon films. Time of flight mass spectroscopy has been used to study plume species produced by laser ablation.

It is also found that polyyne molecules can be formed by fs laser dissociation of small molecules in organic solvents. This process is accompanied by the deposition of hexagonal nano-diamond films on substrates placed near the laser focus during irradiation. This opens a new path in the synthesis of 1D conducting molecules and nano-diamond materials for nano-science applications.

Quantum chemical calculations involving density functional theory (Gaussian '03) have been carried out in support of this work and have been used to study Raman and IR vibrational modes of several novel carbon molecules synthesized in ta-C films and in the liquid phase. These studies have been extended to assist in the identification of astronomical spectra.

Acknowledgements

I would like to thank Prof. Walt Duley for giving me the opportunity to tackle a project covered everything from ultrafast laser, nanoscience, physics chemistry to calculating chemistry. I am especially appreciated it very much for him to award me the research freedom in the full-scale. I am indebted to him for his penetrating guidance for the last three years.

I am grateful to the support from Prof. Q. –B. Lu for his permission to use his 120 fs Ti:sapphire laser source. His partial financial supprt is also acknowledged. I would like to thank Prof. J. Sanderson let me to access his 50 fs Ti:sapphire laser system. His cooperation is very impressive. Thanks also go to my committee, Prof. P. Chen, Prof. D. Strickland, and Prof. P. Bernath for taking the time from their busy schedules to answer my questions and guide my research.

Special thanks go to I. Alkhensho for his assistant for prepare the deposition system, to Randy Fagan (earth science), and to Dr. C. Wang for experimental help. International cooperation with Dr. M. Rybachuk, Dr. H. Zhou (Queensland University of Technology, Australia), Mr. Stefan Griesing, Dr. M. Koblischka (Universitaet des Saarlandes, Germany), Dr. Jibao Cai (University of Science and Technology, China), Ms. Y. Xu and Prof. M. Izumi (University of Tokyo Marine Science and Technology, Japan) is also appreciated.

Finally, I would like to thank my parents, my wife, Yi Yang, two kids, Leyang and Jinpeng, for their loving care and support, and for bringing happiness to my life.

Table of Contents

List of Figures

List of Tables

Chapter 1

Laser-Matter Interactions

1.1 Introduction

The study of intense laser-matter interaction is a rapidly expanding field due to the development of ultrafast laser sources and the emergence of novel materials. The nature of this interaction varies with pulse power, wavelength, pulse shape, pulse width and chemical binding (material properties). Table top femtosecond laser systems provide an easy access to laser intensities of 10^{16} W/cm^2 (pulse width $\tau \approx$ 100fs, spatially focused to 1 μm^2). Meanwhile, the typical intensity of a 30 ns excimer laser is 10^8-10^9 W/cm^2. This dramatic difference in laser intensity allows us to conveniently probe different interaction mechanisms. Furthermore, another distinctive feature of ultrafast interactions is that the picosecond energy transfer time from the electrons to ions by coulombic collisions is significantly longer than the laser pulse width (~ 100 fs). Therefore, conventional hydrodynamical motion does not occur on a femtosecond interaction scale.

There are two forces which are responsible for energy transfer from the laser field and the energetic electrons to the ions in the absorption area: one is static Coulomb force due to the charge separation occurring when the absorbed energy by electrons exceeds the Fermi energy (approximately a sum of the binding energy and work function). Excited electrons (single photo or mutilphoto excitation dependent on the laser intensity and wavelength) escape from the target and thereby form a Coulomb force, which pulls the ions out of the target. On the other hand, the ponderomotive force of the laser field in the skin larger pushes electrons deeper into the target. Correspondingly the second force accelerates ions into the target. Gamaly et al. (2002) shows that the first mechanism governs the ablation process by femtosecond pulses at an intensity more than 10^{13} W/cm^2. At a laser intensity more than 10^{15} W/cm^2, the electric field produced by laser pulses is about 8.68 V/Å, which is comparable with the atomic field binding an electron to the proton in hydrogen atom (51.4V/ Å). Electric fields of laser pulses can directly break the chemical binding of molecules and the interaction is thus not treated as a perturbation. Coulomb explosion or photofragment can be the dominant mechanism in ultra intensive interaction instead of conventional ablation with a melting and subsequent vaporization procedure (Stoian et al. 2002, Stuart et al. 1996, Duley 1996). Intense laser

field interaction with atom/molecules can be either through a multiphoton process or through a field ionization.

One important physical effect of laser-matter (solid) interaction is material removal or laser ablation, which can be used for the deposition of thin films, the creation of new materials, and for micromachining or surface-engineering. Fs laser ablation has the important advantage in such applications compared with ablation using ns pulses because there is little or no collateral damage due to shock waves and heat conduction. Thus fs pulses have many potential applications for biomedical proceedures including nanosurgery. These sources are also finding applications in nano-composition analysis and nanoscaled surface processing for microelectronics.

In this chapter, I will first discuss the carbon phase diagram and explain why carbon has been chosen as a target material. I will review the microstructure and chemical binding states of two special carbon materials; carbynes and tetrahedral amorphous carbon, which are materials studied in this work. Subsequently I will review various theoretical models developed to describe fs ablation mechanisms. I will also discuss the dissociation mechanisms of hydrocarbon compounds and small organic molecules. Finally, I describe the research plan for my Ph. D degree study and the structure of this thesis.

1. 2 Carbon science and the phase diagram of carbon

It is long known that carbon is one of the key components of universe and an essential element for life on earth. New carbon materials, such as sp-bonded linear carbon chains (carbynes), nanodiamond, graphene, and carbon nanotubes, are paving the way for next generation microelectronics (Amaratunga 2002; Berger et al. 2006). Of these materials, graphene is an optical 2D conductor (Van Duyne et al. 2004, Andrew and Barnes 2004), carbynes and carbon nanotubes are 1D conductors, and nanodiamond and fullerenes are 0 D materials (Shvartsburg et al. 2002; Kiang and Goddard III 1997; Saito 1997). They present a novel assembly, which can be easily engineered for nanoelectronics and molecular electronics. These introduce carbon as an important material in state-of-the-art science and technology.

The carbon atom can have three different hybridizations; sp^3, sp^2 and sp. In the sp^3 configuration, as in diamond, each of a carbon atoms four valence electrons is bonded via a tetrahedral hybrid σ orbital to an adjacent atom. In the 3-fold sp^2 coordination, as in graphite, three of four valence electrons are assigned to trigonal orbitals which form intra-plane σ bonds. The fourth electron forms a $p\pi$ orbital

which lies normal to this plane. This π bond is weak and also called unsaturated bonding. In the sp configuration, such as in the carbynes, two valence electrons are assigned to linear sp hybrids which form σ orbitals with two neighboring atoms and the other two electrons are placed in each of the $p_{y\pi}$ and $p_{x\pi}$ orbitals.

Crystalline carbon materials may mix two or three of carbon bonds. Shown in Fig. 1.1 is carbon phase diagram.

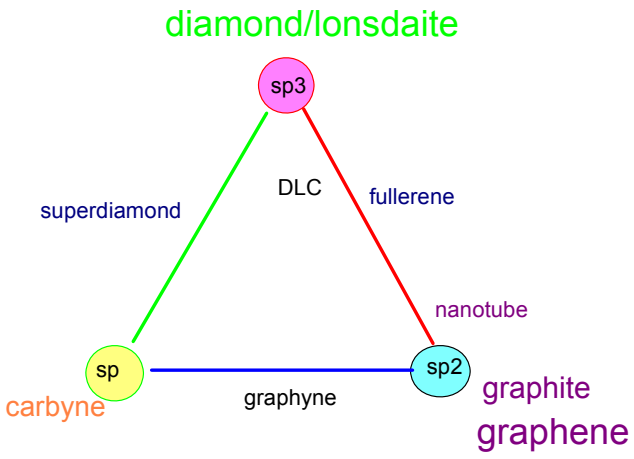

Fig. 1.1 Phase diagram of carbon allotropes

Clearly, fullerenes and carbon nanotubes mix sp^2 and sp^3 bonds, while graphyne combines sp and sp^2 carbon bonds. It is notable that graphene is a 2D layer with hexagonally graphitic binding (sp^2), graphyne is that individual hexagonal carbon rings link by sp-bond carbon chains. Meanwhile, numerous disordered carbons, including soots, chars, carbon fibres, glassy carbon and thermal evaporated amorphous carbon, are basically sp^2 bonded.

Tetrahedral amorphous carbon (*ta-C*) having relative low concentration of sp^2 bonded clusters embedded in a tetrahedral carbon network is a very promising material for various applications because it possess ultrahigh hardness similar to that of diamond and is transparent. The presence of sp^2-bonded clusters modifies its local electron affinity. Such a carbon film can be deposited by nanosecond laser pulsed ablation or other sputtering methods with proper processing parameters (Robertson 2002 & Grill 1999).

Phase transitions between different carbon allotropies generally requires high temperature and high pressure conditions (Bundy et al. 1996; Utsumi and Yagi 1991; Yagi et al. 1992; Scandolo et al. 1995). Fig. 1.2 shows a T-P phase and tranition phase diagram for pure carbon.

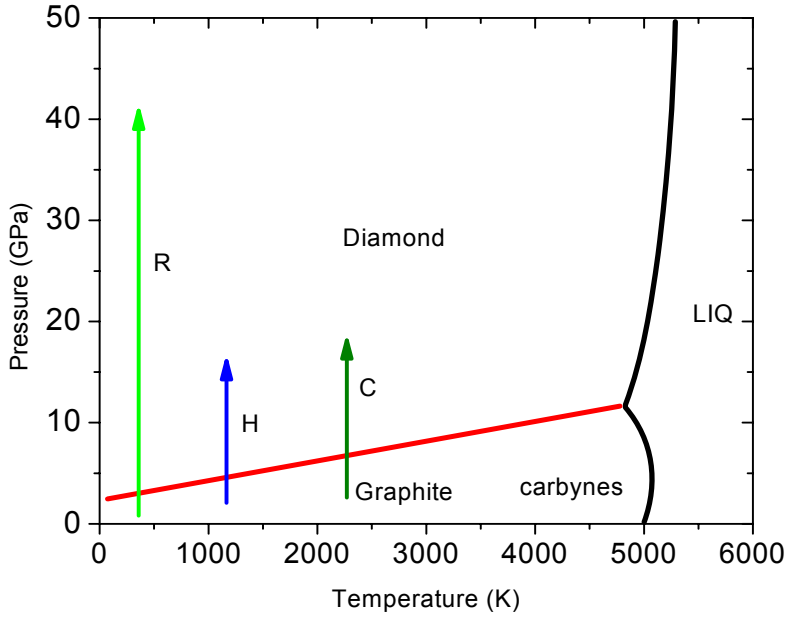

Fig. 1.2 P-T transition phase diagram for carbon

The path R corresponds to a reversible phase transition from hexagonal graphite to hexagonal diamond and then cubic diamond with increasing pressure. An irreversible graphite to cubic diamond transition is marked by path C, and is the basis for a commercial approach to synthesize diamond at high temperatures. Path H represents a phase transition from graphite to the metastable hexagonal diamond phase (Utsumi and Yagi 1991). The transformation of cubic diamond transferring into disordered graphite occurs either under pressure (Gogotsi et al. 1999) or during irradiation with ultrafast laser pulses (Yang and Wang 2000).

Phase transitions from graphite to nanodiamond (Bonelli et al. 1999) and fullerene (Luo et al. 2005) or from cubic diamond to hexagonal diamond (He et al. 2002) can also be obtained with laser irradiation.

1.3 Carbynes

Carbynes are composed of linear carbon chains containing pure sp hybridized bonds, either as alternating triple and single bonds (polyynes) or with conjugated double bonds (polycumulenes) (Kavan and Kastner 1994; Heimann 1994; Szafert et al. 2003). Fig. 1.3 shows these two configurations.

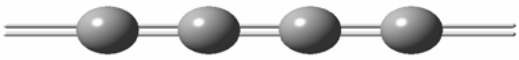

Fig. 1.3 Polyyne and polycumulene bonding configurations in carbynes

Theoretical calculations shows that the first structure is more stable (Kertesz et al. 1978; Springborg and Kavan 1992). Such linear carbon chains are very interesting materials because theoretical studies predict that they may exhibit high temperature superconductivity (Little 1964; Kavan 1988), charge density waves (Springborg and Kavan 1992) and strong nonlinear optical effects (Eisler et al. 2005). Moreover, several laser-induced gas phase studies have suggested that they can be elemental building blocks for three-dimensional fullerenes (Heimann et al. 1983, Shvartsburg et al. 2000) and nanotubes (Kiang and Goddard III 1996). Recently, nanotubes have been successfully synthesized by irradiation of polyynes by electron beams at 800^{o}C (Yasuda et al. 1999) or by polymerization of 1-iodohexa-1,3,5-triyne and hexa-1,3,5-triyne at room temperature (Hlavaty et al. 2000).

sp-bonded carbon chains have been identified in laser ablation products (Heath et al. 1987) and are possibly present in interstellar materials (Duley 2000). Recently, they have been synthesized in grain-assembled amorphous carbon films and embedded in sp^2-bonded matrices (Ravagnan et al. 2002). In organic solvents, sp chains have been grown by arcing graphite electrodes (Cataldo 2003) or laser ablation of suspended nano-graphite, C60 and nano-diamond particles (Tauji et al. 2002 & 2003; Tabata et al. 2006a). However, it is still a challenge topic to fabricate pure carbynes in the laboratory because polyynes are highly reactive with oxygen, water, even N_2, H_2, He (Casari et al. 2000). They can also graphitize via interchain cross-linking of an array of parallel polyyne chains as shown below.

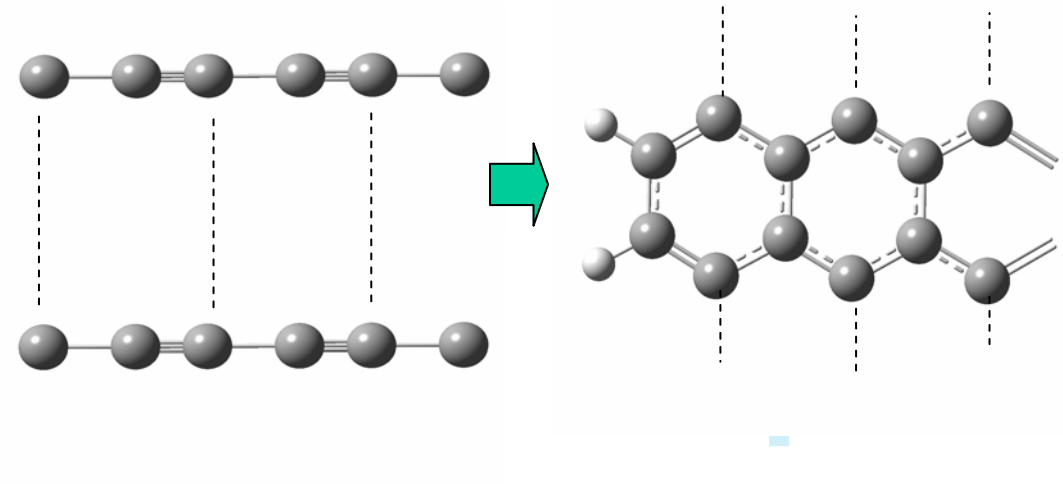

Fig. 1.4 Interchain cross-linking of polyynes leads to graphitization.

Polyynes in solution can only reach a concentration of about 1mM at room temperature. This is limited to lower concentrations (μM) at increased temperature (60^{o}C) (Cataldo 2004, Heymann 2005, Wakabayashi et al. 2007).

Fortunately, recent studies show that cross-linking can be hindered by pinning polyynes on the surface of Ag nanoparticles (Casari et al. 2007) or by intercalating alkali metal nanoclusters (Kavan et al. 1995) or encaging linear chains in a carbon nanotube (Nishide et al. 2006).

1.4 Diamond-like carbon (DLC) films

Diamond-like films are tetrahedral amorphous carbon (ta-C) materials embedded with sp^2 bonded graphite clusters. Theoretical studies show that the density changes from 2.2 g/cm^3 to 4.4 g/cm^3 as the sp^3 content increases from 7.9% to 89%. The concentration of sp–bonded carbon decreases quickly to less than 2% at a density of 3 g/cm^3 (Wang and Ho 1994). Generally the sp-bonded carbon component in ta-C is very small and can be neglected (Ferrari and Robertson 2000) and it has been shown that the mechanical properties and optical gap of ta-C are mainly determined by the concentration of sp^3-bonded species while sp^2 sites govern electrochemical and electrical properties (Robertson 2002; Voevodin et al. 1996). By adjusting the sp^2/sp^3 ratio as well as controlling the microstructure of sp^2 clusters, one can obtain a wide range of mechanical, electronic and optical properties for various applications, such as, high infrared transmission, optical coating, field emission, wear and corrosion protection of magnetic storage media, and biocompatible coatings for biological environments (Grill 1999; Hauert 2003).

ab initio simulation of the structure of ta-C (Wang and Ho 1993, Marks et al. 1996; Schultz et al. 1999) shows that sp^2-bonded sites prefer to cluster in the sp^3 coordinated network. Typical sizes of sp^2 clusters in ta-C are $\approx$ 1-2 nm (Carey and Silva 2004). However, this size increases to 3-5 nm in ta-C after annealing at 600C. 100 nm graphite clusters can also be seen in scanning electron microscopy (Siegal et al. 2000).

The typical Raman vibration band of ta-C under visual excitation does not show individual features at 1600 cm^{-1} for graphite stretching mode (G band) and 1375 cm^{-1} for graphite breathing mode or at 1333 cm^{-1} for diamond crystals. Instead, it shows a broad band centered at 1550 cm^{-1} with an enhanced tail at lower frequencies. Thus, it is widely accepted that the ratio of sp^2/sp^3 contents can be deconvolved with a Breit Wigner Fano (BWF) lineshape (Ferrari and Robertson 2000, Prawer et al. 1996):

$$I(\omega) = \frac{I_0[1 + 2(\omega - \omega_0)/Q\Gamma]^2}{1 + [2(\omega - \omega_0)/\Gamma]^2} \qquad (1.1)$$

Here I_o is the peak intensity, ω_o is the peak position, Γ is the full width at half height (FWHH), and Q^{-1} is the BWF coupling coefficient. A Lorentz lineshape is recovered with $Q^{-1} \rightarrow 0$. It is notable that the sp^3 content can only be detected by UV excitation since the $\sigma \rightarrow \sigma^*$ gap is 5.5 eV, which is well beyond the visual excitation energy (Gilkes et al. 1997; Ferrari and Robertson 2001). Thus a direct observation of sp^3 fractal in tetrahedral amorphous carbon should employ a UV Raman spectroscopy.

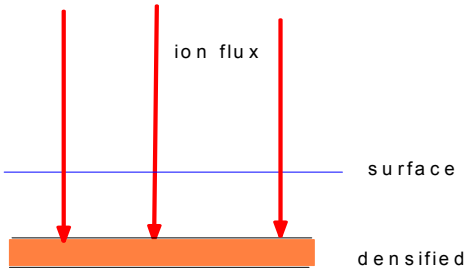

Fig. 1.5 Subplantation model for ta-C deposition

A sub-plantation model is developed to understand the deposition of ta-C (McKenzie et al. 1991, Robertson 1993; Lifshitz et al. 1994). Energetic carbon ions can directly penetrate the film surface and implant at specific depth depending on their energy. This procedure results in the densification of the intra-layer. A compressive stress is thus accumulated due to the plastic deformation of this interlayer. This internal stress is the key to grow sp^3 bonds or to transfer sp^2 to sp^3 bonds. Experiment shows that deposition at high temperatures results in a low sp^3 concentration and that the sp^3 to sp^2 phase transition occurs at 250°C to 300°C (Robertson 2002). Thus carbon ions with higher kinetic energy do not result in higher sp^3 content due to the annealing effect of implanted species. On the other hand, low energy carbon ions cannot generate sp^3 because internal stress is required for this to occur. The optimized energy for carbon ions to promote sp^3 species is found to be 10-100 eV

(Robertson 1993, Prawer et al. 1996). However, internal stress is unnecessary to retain the sp^3 configuration once growth has finished (Ferrari et al. 2002). Experiment shows that the sp^3 bonded network is stable until 1100^{o}C (Ferrari et al. 1999).

1. 5 Positive carbon ions and the growth of carbon clusters

Time-of-flight mass spectrometric studies show that carbon species such as C_n^+ (n=1, 3, 5, 7, 11) are predominant in the ablation of graphite with ns laser pulses (Gaumet et al. 1993; Kokai et al. 2000). This can be explained by the "magic number" of small carbon clusters (n<25) (Bernholc and Phillips 1986), whereby odd-numbered clusters are positively charged while even-numbered clusters are negative. With UV laser ablation (wavelength 355 nm, pulse width of 10 ns), it is found that smaller carbon ions prefer to be generated with increasing laser fluence. This indicates a further interaction between laser pulse and ablation plume (Koo et al. 2002). A fragmentation of large carbon clusters occurs in plume. The yield of C_n^+ as a function of laser intensity is well understood and involves the conversion of multiphoton energy into thermal energy (Gaumet et al. 1993). Theoretical studies also show that clusters having fewer than 10 carbon atoms tend to have a linear structure while larger clusters with 10-29 atoms have a monocyclic ring structure (Yang et al. 1988).

Time of flight (TOF) mass spectra with a delay time after laser ionization (nanosecond pulses), show that cluster sizes increase with delay time (Shibagaki et al. 2000 & 2002; Koo et al. 2002). This shows a clustering of carbon ions through a gas-phase reaction even without ambient gas. Carbon dimerization is also evident under an argon atmosphere (Wakisaka et al. 1993). Bimodal cluster size distribution is also found in carbon vapor by ablation with the second harmonic or 3rd harmonic from a Q-switched Nd:YAG laser (Rohlfing et al. 1984; O'keefe et al. 1984). The experiments show both odd and even C_n^+ clusters for $1 \leq n \leq 30$ and only even numbers of C atoms for larger clusters. This phenomenon is explained by the formation of carbynes induced by laser annealing. Ablation of graphite with 308 nm ns laser radiation produces C_n^+ ions having $n > 300$ (Scott et al. 2001).

Carbon species in the plume accompanying fs laser ablation have kinetic energies extending from 300eV to several keV. This is about one order of magnitude higher than the energies observed in ns ablation (Vanrompay et al. 1998; Qian et al. 1999; Banks et al. 1999, Yao et al. 2000, Duley 1996). Highly charged carbon ions are also present. These do not appear in ns-ablation of graphite (Ehler 1975). These highly charged carbon ions are likely produced by Coulomb explosion in the laser focus (Lenner et al. 2007).

Carbon species in the fs ablation plume have also been studied by emission spectroscopy (Okoshi et al. 2000). Time-resolved images taken by an intensified charged-coupled device (ICCD camera) (Loir et al. 2003; Fuge et al. 2006) indicate that the drift velocity is as high as 10^5 m/s. C^{2+} ions have been identified in these plumes.

1. 6 Light-matter interactions: the general picture

In these experiments, structural modification of solid materials begins with the deposition of a certain amount of laser energy. The total absorbed energy and the spatial and temporal energy distribution, determine the nature of this modification. Fig. 1.6 shows a light transmitting material with absorption coefficient, α. According to the Lambert-Beer law, the transmission T can be expressed as

$$T = I / I_o = e^{-\alpha x} \qquad (1.1)$$

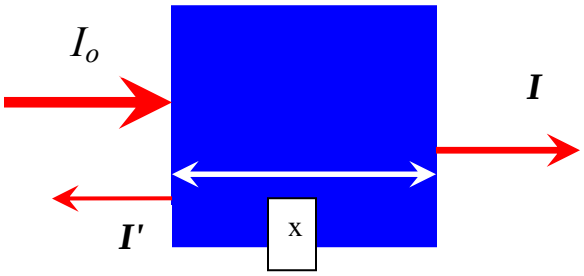

Fig. 1.6 Absorption, transmission and reflection in a planar sample

where, x is the width of media, I_o, I and I' stand for incident, transmitted and reflected light intensities, respectively. Thus the interaction only happens in the surface layer $L = 1/\alpha$ for a non-transparent material. For graphite, this depth is about 30 nm for 620 nm light (Seibert et al. 1990). For aluminum, the penetration depth is about 15 nm at 308 nm (Palik 1985).

The primary laser-solid interaction process involves the excitation of electrons from their equilibrium states to higher energy levels by photoabsorption. For example, in semiconductors electrons can be excited from the valence band to the conduction band by single or multiphoton absorption, as shown schematically in Fig. 1.7.

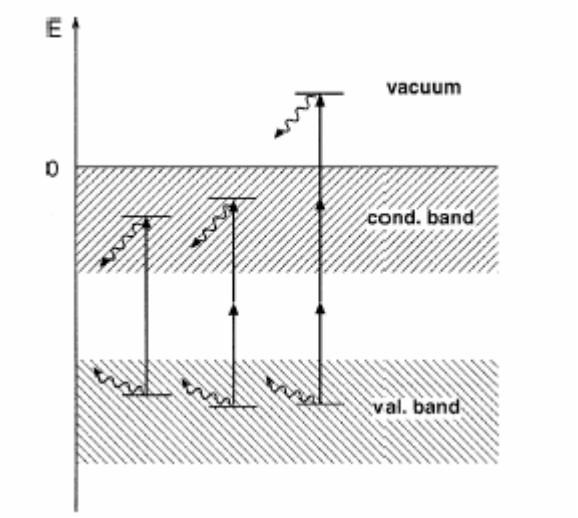

Fig. 1.7 Single-, double and three photon electronic excitations in a semiconductor

At a given laser fluence $F \propto I\tau$, a shorter pulse duration favors multiphoton excitation because the probability of nonlinear absorption increases strongly with laser intensity. Different interactions have been discussed by von der Linde et al. (1997) with increasing pulse widths.

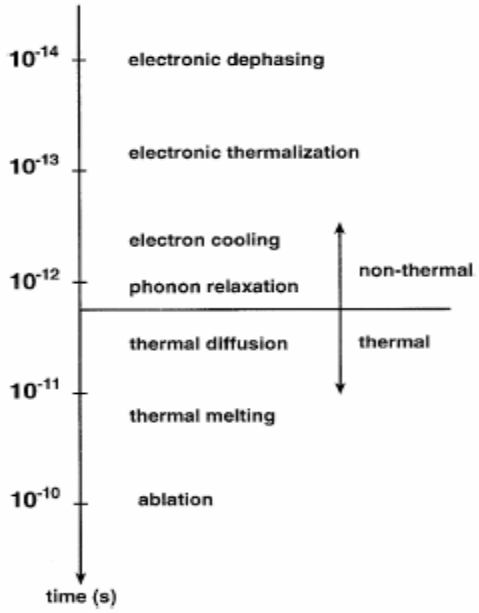

Fig. 1.8 Time scale for various secondary processes in laser-matter interactions

As shown in Fig. 1.8, a very short-lived transient coherent polarization is associated with a primary electronic excitation. This polarization is destroyed by a de-phasing process occurring at a time scale of 10 fs.

The initial distribution of excited electronic states corresponds to the coupling states of optical transitions. The occupation of these primary states is subsequently changed by nonthermal carrier-carrier Coulomb interaction on a time scale of about 100 fs. The hot electron state can be further cooled by emission of phonons. Electron cooling and phonon relaxation occurs in < 1 ps.

Thermal cooling occurs on time scales > 1 ps. Heat diffusion occurs by electron-lattice interactions and by phonon coupling. The lattice thermal melting is longer than 10 ps while ablation occurs during the laser pulse. Thus, the interaction between intense laser radiation and matter can be modeled by a two-temperature theory in which electrons and lattice remain at different temperatures.

1. 7 Two-temperature model

According to a one-dimensional, two temperature diffusion model (Kaganov et al. 1957, Anisimov et al. 1974), the energy of low intensity short laser pulses is absorbed by free electrons due to inverse Bremsstrahlung (Joule heat). The evolution of the absorbed energy involves thermalization within the electron gas (electron subsystem), energy transfer to the lattice and thermal diffusion in the lattice. These processes can be expressed as:

$$C_e \frac{\partial T_e}{\partial t} = -\frac{\partial Q(z)}{\partial z} - \gamma(T_e - T_i) + S \quad , \tag{1.2}$$

$$C_i \frac{\partial T_i}{\partial t} = \gamma(T_e - T_i), \tag{1.3}$$

$$Q(z) = -k_e \partial T_e / \partial z \quad , \qquad S = I(t) A \alpha \exp(-\alpha z) \tag{1.4}$$

Here z is the direction of energy propagation perpendicular to the target surface, Q(z) is the heat flux, S is the laser source function, I(t) the laser intensity, A=1-R is the surface transmissivity and α is the absorption coefficient. C_e and C_i are the specific heat of the electron and lattice subsystems with C_e

=aT_e where a is a constant, γ is the electron-lattice coupling parameter, and k_e is electron thermal conductivity.

In eq. (1.2-4) we should consider three characteristic time scales: τ_e, τ_i , and τ_L. $\tau_e = C_e/\gamma$ is the electron cooling time, $\tau_i = C_i/\gamma$ is the lattice heating time and τ_L the laser pulse width. Following previous studies (Chchkov et al. 1996, Momma et al. 1996, 1997, von der Linde et al. 1997), the pulses can be separated into three time regimes.

Femtosecond pulses

For a fs pulse, the laser width is much shorter than the electron cooling time, $\tau_L \ll \tau_e \sim$ 1ps. Then, $C_e T_e / t >> \gamma T_e$, and electron-lattice coupling can be neglected. If $D_e \tau_L < \alpha^{-2}$, where $D_e = k_e/C_e$ is the electron thermal diffusivity, the electron heat conduction term can be neglected in and eq. (1.2) reduces to

$$C_e' \partial T_e^{\,2} / \partial t = 2 I_a \alpha \exp(-\alpha z) \qquad (1.5)$$

and gives

$$T_e(t) = (T_o^{\,2} + \frac{2 I_a \alpha}{C_e'} t \exp(-\alpha z))^{1/2} \ . \qquad (1.6)$$

Here it is assumed that $I(t) = I_o$ and $I_a = I_o A$, while $T_o = T_e(0)$ is the initial temperature. $C_e' = C_e / T_e$ is a constant when T_e remains smaller than the Fermi energy (in temperature). At the end of the laser pulse the electron temperature is given by

$$T_e(\tau_L) \cong (\frac{2 F_a \alpha}{C_e'})^{1/2} \exp(-z/\delta) \ , \qquad (1.7)$$

where $T_e(\tau_L) >> T_o$, $F_a = I_a \tau_L$ is the absorbed laser fluence, and $\delta = 2/\alpha$ is the skin depth.

After the laser pulse the electrons are rapidly cooled due to energy transfer to the lattice and heat conduction into the bulk. Since the electron cooling time is very short, eq. (1.3) can be written as $T_i \sim$

$T_e(\tau_L)t/\tau_i$ (neglecting the initial lattice temperature). The maximum lattice temperature can be estimated from the average cooling time of the electrons, $\tau_e^a \sim \tau_e / 2 = C_e' T_e(\tau_L)/2\gamma$ and is given by

$$T_i \sim T_e^2(\tau_L)\frac{C_e'}{2C_i} \approx \frac{F_a \alpha}{C_i}\exp(-\alpha z) \ . \qquad (1.8)$$

Significant evaporation occurs when $C_i T_i > \rho L_v$, where ρ is the density and L_v is the specific heat of evaporation. Using (1.8), we can express the condition of strong evaporation as $F_a \geq F_{th}\exp(\alpha z)$, where $F_{th} \sim \rho L_v/\alpha$ is the threshold laser fluence with fs pulses. Then the ablation depth per pulse L is

$$L \approx \alpha^{-1}\ln(F_a / F_{th}) . \qquad (1.9)$$

Such a logarithmic dependence of the ablation depth per pulse has been confirmed by the ablation of copper in vacuum using 150 fs laser pulses (780 nm, Momma et al. 1997) and in the ablation of highly oriented pyrolytic graphite (HOPG) with 120 fs pulses (Shirk and Molian 2001).

Picosecond pulses

For a ps pulse, $\tau_e \sim 1\text{ps} < \tau_L < \tau_i \sim 10$ ps. At times $t >> \tau_e$, $C_e T_e / t << \gamma T_e$, eq. (1.2) becomes quasi-stationary, eqs. (1.2-4) reduce to

$$\partial/\partial z(k_e \partial T_e/\partial z) - \gamma(T_e - T_i) + I_a \alpha \exp(-\alpha z) = 0 \qquad (1.10)$$

$$T_i = \frac{1}{\tau_i}\int_0^t \exp(-\frac{t-\theta}{\tau_i})T_e(\theta)d\theta + T_o \qquad (1.11)$$

The integral corresponds to the temperature increase of the lattice. At $t << \tau_i$, (1.11) can be simplified due to the quasi-stationary character of the electron temperature. Neglecting T_o, we get

$$T_i \approx T_e(1-\exp(-t/\tau_i)) \approx (t/\tau_i)T_e \qquad (1.12)$$

It is obvious that in the ps regime the lattice temperature remains much less than the electron temperature. Thus the lattice temperature can be omitted in (1.10). When the condition $k_e T_e \alpha^2 << \gamma T_e$ is fulfilled (1.10) and (1.12) are very simple. The electron and lattice temperatures at the end of a ps pulse are given by

$$T_e \approx \frac{I_a \alpha}{\gamma} \exp(-\alpha z), \text{ and } T_i \approx \frac{F_a \alpha}{C_i} \exp(-\alpha z). \quad (1.13)$$

Note that the obtained lattice temperature is governed by the electron cooling time. Thus, in fs and ps regimes (1.8) and (1.13) give the same expression for the lattice temperature. This indicates that a logarithmic dependence of the ablation depth on laser fluence is also found in the ps regime. However, this conclusion is based on an assumption that the electron heat conduction is negligible. This is a very crude approximation since the electron heat conduction and the formation of melted zone must be related in ps ablation.

Nanosecond pulses

Ablation with ns pulses can be modeled with the condition $\tau_i \sim 10$ ps $<< \tau_L$. In this case, the electron and lattice temperatures are equal, $T_e = T_i = T$ and (1.2- 1.4) reduce to

$$C_i \partial T / \partial t = \partial / \partial z (k_o \partial T / \partial z) + I_a \alpha \exp(-\alpha z). \quad (1.14)$$

There are many experimental and theoretical studies on the processes involved in laser heating and irradiation with long pulses (Duley 1996). In this regime the target surface is first heated to the melting point and then to the vaporization temperature. During the interaction the dominant energy loss is heat conduction into the solid target. The heat penetration depth is given by $l \sim (Dt)^{1/2}$, where $D = k_o/C_i$ is the thermal diffusivity. Note that for a long pulse, $D\tau_L >> 1/\alpha^2$. The energy deposited inside the target per unit mass is given by $E_m \sim It / \rho l$. Evaporation occurs when $E_m \sim L_v$ at t_{th}, where L_v is the specific heat of evaporation. So, the condition for strong evaporation becomes, $E_m > L_v$ (or $\tau_L > t_{th}$) and

$$I \geq I_{th} \sim \frac{\rho L_v D^{1/2}}{\tau_L^{1/2}}, F > F_{th} \sim \rho L_v D^{1/2} \tau_L^{1/2} \quad (1.15)$$

for the laser intensity and the fluence, respectively. A striking characteristic is that the threshold laser fluence depends on the square root of the laser pulse width. A deviation of the damage threshold from the $\tau^{1/2}$ scaling with short pulses has been clearly evident by ablation of fused silica by infrared (1053 nm) and visible (526 nm) laser radiation (Perry et al. 1999).

In summary, fs pulses trigger a nonthermal ablation mechanism since both the electron-lattice thermal coupling and thermal diffusion to the lattice take longer time than the pulse width. ns pulses allow thermal equilibrium to occur between the electrons and the lattice.

1. 8 Plasma annealing theory

Work on high density electron-hole plasmas has been initiated by the investigation of laser annealing (Khaibulli et al. 1979) and nanosecond/picosecond laser-induced phase transitions in solid materials (Van Vechten 1979). The so-called plasma model describes processes occurring in laser excited e-h plasmas and plasma-induced softening of the crystal lattice (Van Vechten 1979; Heine et al. 1976; Biswas and Amebegaokar 1982; Kopaev et al. 1985; Stampfli and Bennemann 1990; Das Sarma and Senna 1994; Silvestrelli et al. 1996, Perry et al. 1999; Gamaly et al. 2002).

We suppose that the target fills half-space at x > 0, overlapped by the skin depth (optical penetration depth) $l_s = \frac{c}{\varpi k}$, where k is the imaginary part of the refractive index and ω the laser frequency. The dielectric function in the Drude approximation describes the initial solid state just before ablation:

$$\varepsilon = 1 - n_e \frac{\langle \sigma \rangle}{\omega}(i + \omega\tau_m) = 1 - \frac{\omega_{pe}^2}{\omega(\omega + i\nu_m)},$$

$$\varepsilon^{1/2} = n + ik \quad (1.16)$$

Here n_e is the electron density, $\omega_{pe} = (4\pi e^2 n_e / m)^{1/2}$ is the electron plasma frequency, v_{eff} is an effective collision frequency of electrons with the lattice (ions). For normal incidence, the absorption, reflection, and transmission coefficients, A, R, and T, are given by

$$R = \left| \frac{1-\sqrt{\varepsilon}}{1+\sqrt{\varepsilon}} \right| = \frac{4\,\mathrm{Re}\sqrt{\varepsilon}}{\left|1+\sqrt{\varepsilon}\right|^2} ,$$

$$T = \left| \frac{2\,\mathrm{Re}\sqrt{\omega}}{1+\sqrt{\omega}} \right| ,$$

and $$A = 1 - R \approx 4\,\mathrm{Re}\left(\frac{\sqrt{\varepsilon}}{|\varepsilon|} \right) \approx 2\frac{\nu}{\omega}\left(\frac{n_c}{n_e} \right)^{1/2} . \qquad (1.17)$$

Here $n_c = (\pi mc^2 / e^2\lambda^2)$ is the critical density.

Laser-matter interaction can be separated into excitation and transition stages. In the former, the photoionization process is sensitive to the Keldysh parameter (Keldysh 1965),

$$\gamma = \frac{\omega_e (2mU_I)^{1/2}}{eE} \qquad (1.18)$$

where U_I is the zero field ionization potential, ω_e is the electron quiver frequency in the light field, E is the peak electrical field, e and m are the charge and mass of the electron, respectively. At $\gamma << 1$, the ionization process is charactized as a tunneling procedure (Keldysh 1965). At $\gamma >> 1$, ionization is better modeled as a multiphoton process. Recently, the appropriate boundary of multiphoton regime is found closely to $\gamma > 0.5$ (Illov et al. 1992). The non-resonant n^{th} order multiphoton ionization rate (Gontier and Trahin 1984) is

$$P_i = \sigma_n \left(\frac{I}{\hbar\omega_e} \right)^n \qquad (1.19)$$

where σ_N is the generalized n^{th} order cross section and I is the peak laser intensity. With increasing electron density, the second ionization mechanism, impact ionization can not be avoided. Thus, the

time dependence of free electron density is defined by the rate equation (Perry et al. 1999; Raizer et al. 1977; All'insky and Keldysh 1994):

$$\frac{dn_e}{dt} = n_e P_{imp} + n_a P_i \tag{1.20}$$

Here n_a is the density of neutral atoms, P_{imp} is the probability for ionization by electron impact. For single ionization (Luther-Davies et al. 1992; All'insky and Keldysh 1994) these two probabilities can be expressed as

$$P_{imp} \approx \frac{\hbar\omega_e}{U_I}\left(\frac{2\omega^2 \nu_{eff}}{\omega^2 + \nu_{eff}^2}\right) ,$$

$$P_i \approx \omega n^{3/2}\left(\frac{\hbar\omega_e}{2U_I}\right)^n . \tag{1.21}$$

It is evident that the relative role of the impact and multiphoton ionization depends on the relation between the electron quiver energy and the ionization potential. For a 100 fs pulse, multiphoton ionization creates a substantial amount of free electrons. When the electron density approaches 10^{17} cm^{-3}, the collisional ionization rate begins to exceed the multiphoton ionization rate (Stuart et al. 1996). When this density approaches 10^{22} cm^{-3}, the reflectivity dramatically increases (Sokolowski-Tinten and von der Linder 2000). The maximum density was found to be in excess of 10^{22} cm^{-3}, which corresponds to approximately 10% of the total valence-band population (Sokolowski-Tinten and von der Linder 2000).

A lattice softening has been theoretically expected when 10% of the valence electrons are excited into the conduction band (Stampfli and Bennemann 1990 &1992). Lattice softening leads to melting, as predicted by ab initio molecular-dynamic calculation (Silvestrelli et al. 1996, 1997) and observed experimentally by time-resolved reflectivity (Reitze et al. 1992). Such melting is a ultrafast phenomenon and is not a consequence of conventional thermal heat transfer.

1. 9 Present work

In order to understand the interaction between femtosecond laser pulses and carbon a program of experimental and theoretical (ab initio chemical calculation) investigations have been undertaken:

1. Investigation of the carbon species in the fs ablation plume using time-of-flight (TOF) mass spectroscopy.
2. Investigation of microstructure evolution and phase transition by surface spectroscopic and microstructure characterization.
3. Investigation of the deposition of diamond-like carbon films by fs pulsed laser ablation together with a comparison study using ns pulsed laser ablation.
4. Investigation of the direct disassociation of small organic molecules in liquid.
5. *ab initio* density-function theory using Gaussian '03 for related small hydrocarbon molecules.

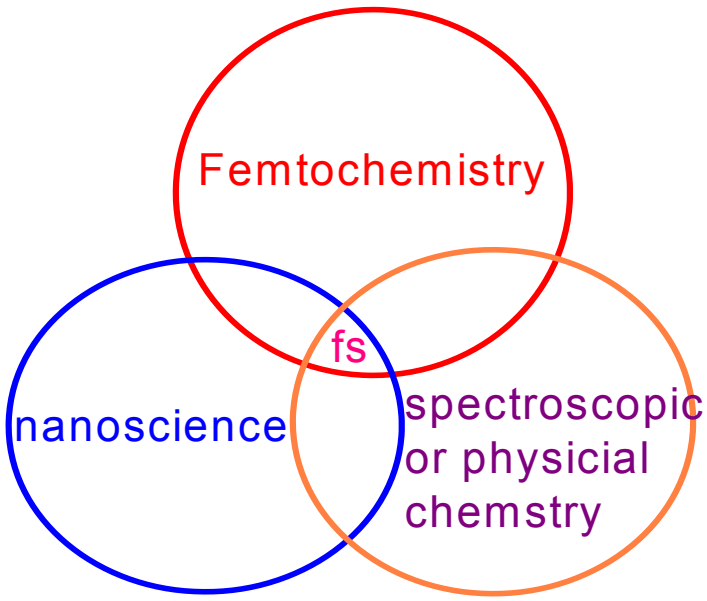

Fig. 1.9 Cutting-edge study with femtosecond laser sources

I thus will carry out a cutting-edge study, which covers femtochemistry, spectroscopic and physical chemistry and nanoscience. A femtosecond laser plays the core role in these investigations. We will show that the high-temperature high-pressure interaction between fs pulses and carbon occurs on the nanoscale. The intense laser-induced evolution of physicial structure and chemical states allows us to probe the nature of carbon in a novel scope under extreme conditions.

This thesis is organized as follows: Chapter II discusses the ablation mechanism, surface nano-engineering and surface carbon phase transitions in highly oriented pyrolytic graphite induced by fs laser irradiation. Chapter III shows the nanostructure and chemical binding states of diamond-like carbon films deposited by ns pulsed laser ablation. Chapter IV presents sub-micron cryogenic graphitization and buckling of tetrahedral amorphous carbon films deposited by ns pulsed laser ablation. Chapter V presents nanostructure and sp/sp^2 clustering of tetrahedral amorphous carbon films grown by femtosecond laser deposition. Chapter VI shows the molecular structure, SERS spectra and nanobuckling of diamond-like carbon films deposited by fs laser ablation. Chapter VII explores the synthesis of polyynes in organic solvents by directly disassociation of various hydrocarbon molecules and the direct deposition of hexagonal diamond films via a liquid method. Chapter VIII presents the results of *ab initio* calculations on the Raman spectra of carbynes, poly-acetylenic chains and poly-graphyne and the characterization of carbon species and the growth of carbon clusters in the fs ablation plume using TOF-MS.. In Chapter IX I will give some suggestions for the future work.

Although these materials are organized in each chapter by a relatively subjects along my practical research order, one can still found intrinsic relationships among these chapters: I. We first study the interaction of laser and carbon solid. Chapters 2, 3, 4, 5, 6 present the results on ablated carbon surface, deposited films and a comparative study to nanosecond laser ablation. II. We focus the laser-liquid interaction in Chapter 7. III. Chapter 8 gives the theoretical study compared to experiments given in these two fields (solid and liquid). TOF mass spectra, which characterize the carbon ion spicies in fs ablation plumes, are also demonstrated and discussed in this chapter in order to understand experimental results from both carbon condensed matters (solid and liquid).

Chapter II

Laser-induced nanopatterning and phase transition on graphite surfaces exposed to fs laser pulses

2.1 Introduction

Intense laser irradiation results in comprehensive microstructure, chemical phase transition and material ablation on solid surfaces (Duley 1996). Laser induced ordered structures are fundamental features to understand the light-matter interaction and possess the potential for surface engineering. A large variety of ordered structures have been observed at different laser wavelengths, intensities and at pulse widths ranging from cw to fss (Emmony et al. 1973; Preston et al. 1989; Ozkan et al. 1999; Vorobyev et al. 2007). The development of chirped pulse amplification has allowed the construction of table-top amplifiers which can generate pulses with millijoule energies and femtosecond durations, leading to peak powers of several terawatts (Strickland and Mourou 1985). In recent experiments using such fs laser pulses, several groups have reported a new type of periodic structure having nanoscale modulation (Ozkan et al. 1999; Vorobyev et al. 2007; Reif et al. 2002; Borowiec et al. 2003; Singh et al. 2002; Wu et al. 2003; Miyaji et al. 2006), which is much smaller than the incident wavelength. In most cases, these subwavelength structures (or nanostrctures) are observed at the edge of the irradiation area, where the laser fluence is relatively low. It is worth noting that the irradiation with fs laser pulses at fluences less than the single-pulse ablation threshold have produced nanostructures with spacings as small as ~ λ /10 on hard thin films such as diamondlike carbon (DLC) and TiN (Yasumaru et al. 2003 & 2005). An understanding of the origin of these very fine nanostructures can provide important information on the nature of fs laser-matter interactions.

Numerous theories have been developed for explaining the formation mechanism of surface patterning. The first is based on the interference between incident laser radiation and the wave scattered by the surface (Zhou et al. 1982, Sipe et al. 1983, Young et al. 1983). The second mechanism considers the instability of capillary waves created by thermal-capillary effects which can result in surface fluctuation and cellular structure in the melted film (Bugaev et al. 1986, Akmanov et al. 1985). A third case incorporates the formation of structure from the self assembly of nanoparticles. In this mechanism, nanostripes are formed by linear arrays of nanoparticles (Rudolph et al. 2004,

Varlamova et al. 2006). There are some novel explanations, such as, boson condensation, which can also lead to a surface ripple structure (Singh et al. 2002, Vechten 1981). Although it is possible that different mechanisms are important under specific experimental configurations, understanding the formation of nanostripes by fs laser irradiation requires further experimental studies and consideration of processes such as non-equilibrium freezing of a melt phase, the role of phase transitions and the evolution of chemical binding states.

The availability of unique carbon materials such as sp-bonded linear carbon chains (carbynes) nanodiamond, graphene, and carbon nanotubes is paving the way for carbon electronics (Amaratunga 2002, Berger et al. 2006, Ravagnan et al. 2002). Conversion between one carbon phase and another usually involves high-temperature and high pressure processes (Bundy et al. 1994). Obviously, a concise all-on-chip processing is desired. Here, I report the evidence of a phase transformation between graphite to carbyne and nanodiamond induced by fs laser pulses. Since carbynes are prototypes for 1D nanowires and precursor molecules in the formation of carbon nanotubes and fullerenes (Casari et al. 2007), the present work represents an initial step in the development of new technology based on processing with fs pulses.

The bombardment of graphite with intense nanosecond laser pulses has been demonstrated to be effective in synthesizing nanodiamond, fullerenes, and diamond-like amorphous carbon (Boneli et al. 1999; Luo et al. 2005, Shirk and Molian 2001). However, a significant lateral melting of target material up to ≈ 0.5 mm cannot be avoided due to thermal effect (Luo et al. 2005, Shirk and Molian 2001). In contrast, fs laser pulsed ablation displays a non-thermal mechanism since the characteristic time of electron-lattice interaction is a few picoseconds, at least one order of magnitude longer than the pulse width. Fs-ablation hence allows precise surface processing while minimizing lateral damage (Shirk and Molian 2001, Momma et al. 1997, Lenner et al. 2007). Recently, tetrahedral carbon films embedded with sp-bonded carbon chains have been fabricated by fs-ablation of graphite (Hu et al. 2007b). This stimulates us to study the phase transition of irradiated graphite.

This chapter reports the effect of irradiation with fs laser pulses on highly oriented pyrolytic graphite with different polarizations and wavelengths. The results show that the orientation of nanostripes is strongly correlated to the incident polarization and the spacing can be related to higher harmonic generation. Based on these results, an optical orientation model is proposed. It is also found that in the vicinity (tens of microns) of the irradiation crater fs pulses can induce direct phase transformations from sp^2-bonded carbon to carbynes or sp^3-bonded nanodiamond, dependent on laser intensity.

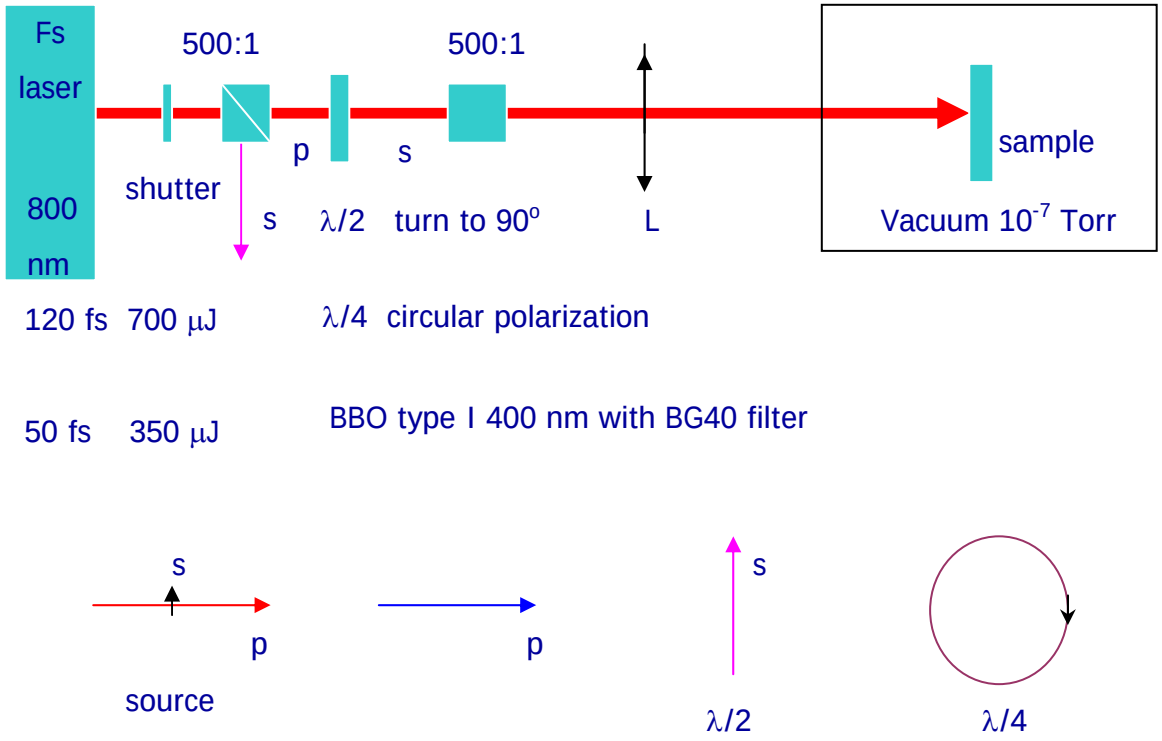

Fig. 2.1 Diagram of experimental set-up for surface patterning and phase transition

2.2 Experimental setup

Two 800 nm Ti:sapphire laser system were employed to irradiate a high oriented pyrolytic graphite (HOPG, Alfa Aesar, grade 2) target at 300K in a high vacuum chamber with a typical pressure of 3 x10^{-6} Torr (1 Torr =133.3 Pa). The first system (Spectra Physics: Tsunami pumped by Millennia and then further amplified by Spitfire) yields 120 fs 700 μJ pulses with a repetition rate of 500 Hz. The second laser system provides 50 fs 350 μJ laser pulse trains with a repetition rate of 1KHz. The pulse energy was measured just before the optical window of the vaccum chamber. For the latter, a seed laser (Femto laser production GmbH, pumped by Millennia, Spectra Physics) was amplified with a stretch-less compressor regenerative amplifier (home-made) pumped by a Q-switch green Nd: YLF laser (Quantronix). The laser beam was subsequently focused by a lens with a focal length of 9 cm.

The incident angle is 90^{o} to HOPG surface. A shutter was used to control the number of laser pulses. Incident polarization direction was varied using a *λ/2* plate and two broadband beam splitters. The circular polarization was achieved by a *λ/4* plate. The 400 nm light was obtained with a type-I BBO crystal. The input 800 nm laser is removed by BG40 filter (ThorLabs FGB37S). Microstructures of samples irradiated by overlapping pulses at energy of 30 μJ-700 μJ /pulse were characterized by scanning electron microscopy. The experiment displayed that the waist size of the focused beam was about 50 μm. Based on these beam parameters, a laser intensity more than 10^{14} W/cm^2 was achieved.

To study the surface phase transition, HOPG was irradiated with 120 fs pulses. The laser beam was focused on the surface of HOPG with 15 cm focal length lens at 300 K in a vacuum chamber at a typical pressure of $5x10^{-7}$ Torr, a lower vacuum pressure in order to avoid the oxidization of surface species.

The local chemical binding state was measured by UV-Ramam with 325 nm excitation wavelength, SERS (Surface enhanced Raman spectroscopy) and X-ray photoelectron spectra (XPS) (Hu 2007d). Prior to the recording of SERS spectra, the HOPG surface was coated in-situ with a silver nanoparticle film (Hu et al. 2007b). The SERS spectra were recorded with x50 objective using an excitation wavelength of 632 nm at a power of 0.3 mW. The magnetic properties of pristine and surface irradiated samples were determined from a DC magnetization with a superconducting quantum interference device (SQUID).

2.3 Optical orientation and linear arrays of surface carbon nanoparticles

2.3.1 Patterns with horizontally polarized wave (p wave)

Fig. 2.2 shows the morphology of HOPG in the vicinity of the laser focus after vertical irradiation by p-wave with (a) a 25 pulse train at energy of 500 μJ/pulse and pulse width of 120 fs and (b) a 50 pulse train at energy of 270 μJ/pulse and pulse width of 50 fs. It is worth noting that the less symmetric distribution of the latter is probably due to slight off-axis of focusing lens relative to the central maxium intensity of 50 fs beam. The beam size of 50 fs pulses from the regeneration amplifier is about 8 mm. It is difficult to determine the central maximum before checking the irradiated microstructure image (a beam profile meter is currently being built). It is also important to point out that a slight deviation of input focal lens will result in a big shift in the central crater in the SEM

images. However, the central crater in 50 fs irradiation is not clearly determined. This is probably due to an improper focusing of 50 fs which results in a low irradiation intensity. For 120 fs irradiation the central crater of 30 μm in diameter is surrounded by an outer region with less ablation. According to local microstructures, in both cases the irradiation can be clearly separated into 4 regimes. Regime I is the most outer belt which gradually transfers to nonirradiated surface. Regime II is a relatively smooth regime with a titled surface toward center. Regime III is a very steep ring-shape wall of crater. Regime IV is the crater bottom where laser has a highest intensity. In the following sections we will display that these 4 regimes have different microstructures and phase transitions.

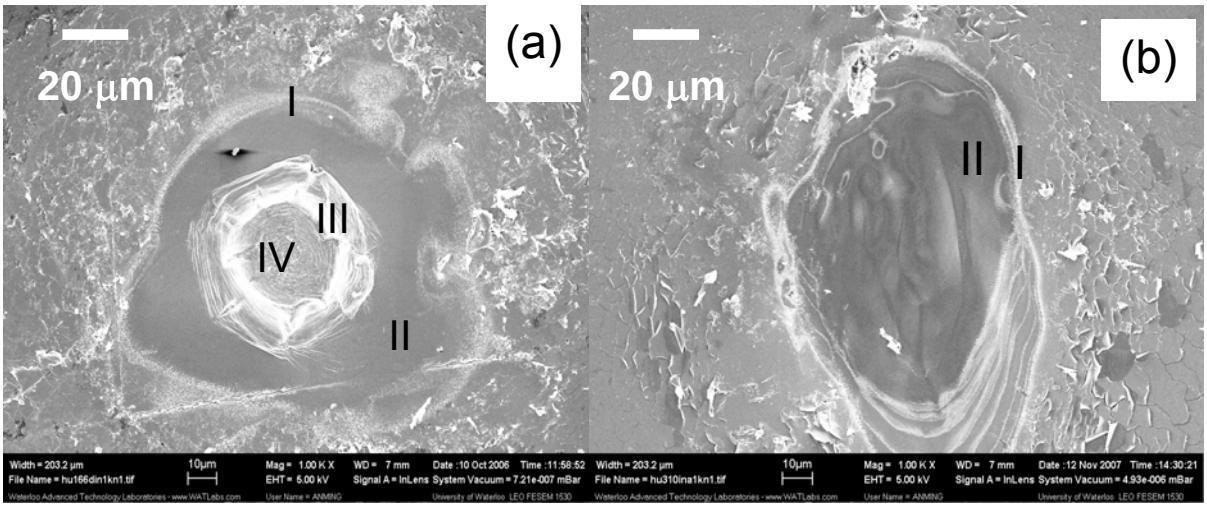

Fig. 2.2. Scanning electron microscopy micrograph of a highly oriented pyrolytic graphite after irradiation with (a) 25 overlapping 120 fs 300 μJ p-polarized laser pulses and (b) 50 overlapping 50 fs 270 μJ p-polarized laser pulses at a wavelength of 800 nm. I-IV stand for four different characterized regimes.

The individual characteristics of each region are shown in Fig. 2.3 for 120 fs and 2.4 for 50 fs pules. The oriented features (nanostripes and microstripes) are observed and stably repeated in both kinds of lasers. This is clearly evident that the surface patterns are not sensitive to the variation of pulse width. However, we do observe some subtle differences in strong ablation areas, which is worth further invesitgation. Anyway, with decreasing pulse energy to 100 μJ/pulse the regime I will gradually extend inside while Regimes II to IV get small and the modulation intensity gets weak. At

the pulse energy of 100 μJ/pulse regimes II-IV become almost invisible. This can be generally understood by the two-temperature model of fs ablation (Chchkov et al. 1996, Momma et al. 1996, 1997, and von der Linder et al. 1997), in which the central area (IV) corresponds to the strong ablation area where the laser density is extremely intense while the surrounding area (I and II) corresponds to the gentle ablation due to the relative weak laser intensity. Regime III is the boundary between two kinds of ablations.

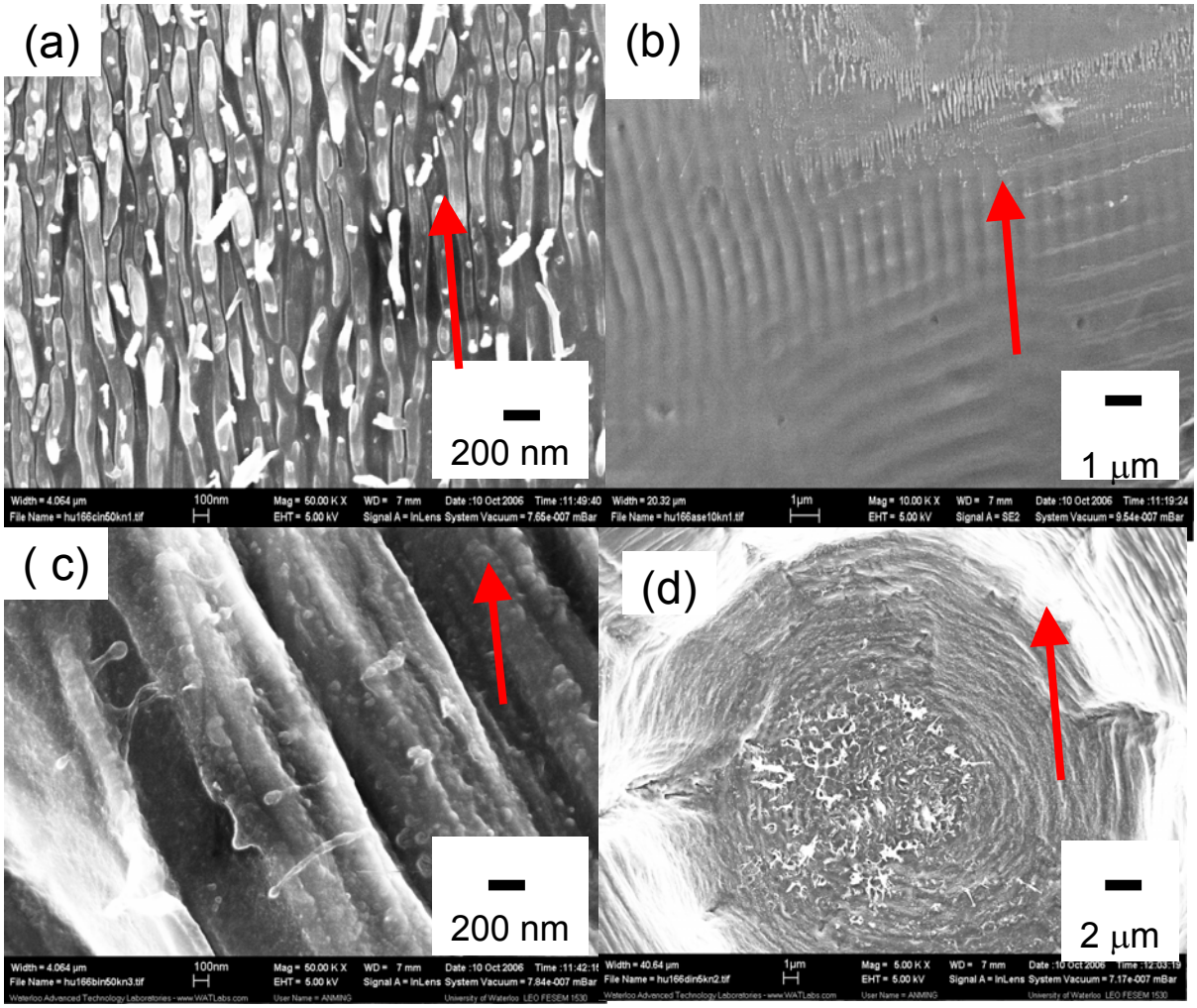

Fig. 2.3. SEM images of 4 regimes (a-d)from outer to center of vertical irradiation areas with a horizontally polarized light of 120 fs pulses (p-wave). The arrow indicates the magnetic field direction (vertical to the polarizon).

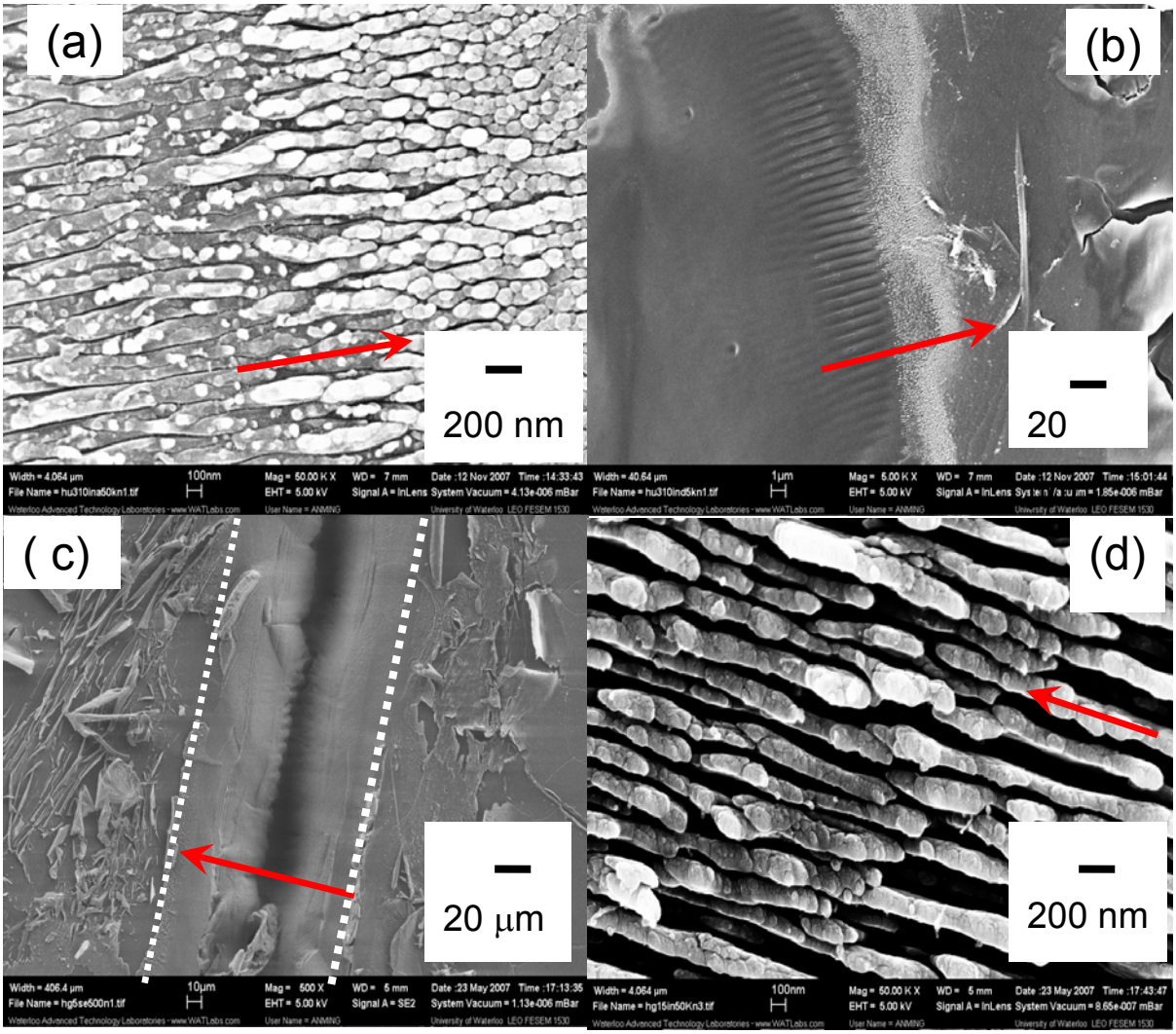

Fig. 2.4. SEM images of HOPG surfaces irradiated by a horizontally polarized light of 50 fs pulses. (a, b) 50 pulses of 270 μJ/pulse, (c, d) continuing shifting of the laser beam at 300 μJ/pulse with a scanning speed of about 0.2 mm/s. (d) is observed at the area indicating by the dash line in (c), which corresponds to Regime I marked in Fig. 2.2. The arrow indicates the magnetic field direction.

It is obvious that in the center region (Fig. 2.3 d) the cellular structure can be attributed to instability in the capillary wave of a melting liquid (Varlamova et al. 2006, Vechten 1981). These cellular structures are surrounded by an array of nano-filaments. In Fig. 2.3 c and Fig. 2.4 d one can easily see the nano-filamentary structure forms ridges in the crater wall. These arrays are curved on a scale of microns. The curved filamentary structure has a spacing *d* of 300 nm-400 nm, which can be explained

by capillary instability with $\lambda/m < d < \lambda$, where λ is the incident wavelength and m ≈ 6-7 is the optical extinction coefficient of liquid carbon (Varlamova et al. 2006, Vechten 1981, Talapatra et al. 2005). The liquid droplets on the surface of nanofilements in Fig. 2.3 c clearly indicate the melt of carbon. Fig. 2.4 (c) shows the hollow created by the accumulated ablation. However, there are no clear nanofilaments on the hollow wall. At the moment, it is unclear if this can be simply attributed to a lower irradiation energy than that of 120 fs pulses or the decreasing thermal effect by shortening the pulse width. A point-type irradiation with tightening focal beams is necessary to elucidate this issue.

Fig. 2.3 b and Fig. 2.4 (b) show microstripes having a spacing of about 800 nm or about one laser wavelength. This ripple structure can be explained by interference theory (Zhou et al. 1982, Sipe et al. 1983, Young et al. 1983). For an absorbing medium with a dielectric constant $\varepsilon = \varepsilon' + i\varepsilon''$, the incident wave with wave vector k can excite a surface wave of wave vector q under the condition

$$\left| q \pm k_p \right| \approx k = \frac{\omega}{c} \tag{2.1}$$

where k_p is the projection of incident wave vector on the surface. The incident angle θ one obtains

$$q \pm \frac{\omega}{c}\sin\theta = \frac{2\pi}{d} \pm \frac{\omega}{c}\sin\theta \approx \frac{\omega}{c}, \tag{2.2}$$

$$d = \frac{2\pi c}{\omega(1 \pm \sin\theta)} = \frac{\lambda}{1 \pm \sin\theta}. \tag{2.3}$$

One can easily find that such a mechanism indicates that the spacing of micropatterns due to the intereference is largely dependent on the incident angle. If the local surface has different incident angles, the spacing of microstripes may vary. This is clearly verified by observing the stripes approaching to the central crater: more near the central crater the larger the spacing. Besides, the surface roughness and defects will also induce different microstripes. In Fig. 2.3 b one can view two kinds of micropatterns with different orientations. This can related to the wavy surface. No matter how, this mechanism can not explain a spacing less than λ/2. A much narrower pattern with a spacing less than λ/2 is hard to be explained in this theoretical context.

In Fig. 2.3a and Fig. 2.4 (a, d), nanostripes are observed with a spacing of 60 nm to 100 nm. There are no remarkable spacing differences of nanostripes induced by two kinds of laser pulses. Moreover, both are parallel to the magnetic field direction. Obviously, this spacing cannot be generated by interference since the minimum value of d is 400 nm at an incident wavelength of 800 nm. Although this value is slightly smaller than *d/m* according to surface capillary instability, it is evident that this nanoscopic pattern in region I is linearly oriented, quite different from those in Region III and IV, which are curved in the micrometer scale. Indeed, the present nanostripes are always perpendicular to the polarization direction (parallel to the magnetic direction) at any points of the ring-shape Region I around the strongly ablated crater. It is important to note that there are no remarkable differences between microstructure in regions II to IV at different polarizations although these features are dependent on the laser intensity. Decreasing pulse energy to 100 μJ/pulse these modulations in regions II to IV become weaker. At pulse energies less than 100 μJ/pulse these features become almost disappear. In contrast, the spacing of nanostripes is not a function of laser intensity. We fail to observe the remarkable differences by attenuating pulse energy from 700 μJ/pulse to 100 μJ/pulse for 120 pulses and 350 μJ/pulse to 70 μJ/pulse for 50 fs pulses.

2.3.2 Patterns with s wave polarization

Fig. 2.5 shows the surface morphology of HOPG irradiated by a vertically polarized wave with a

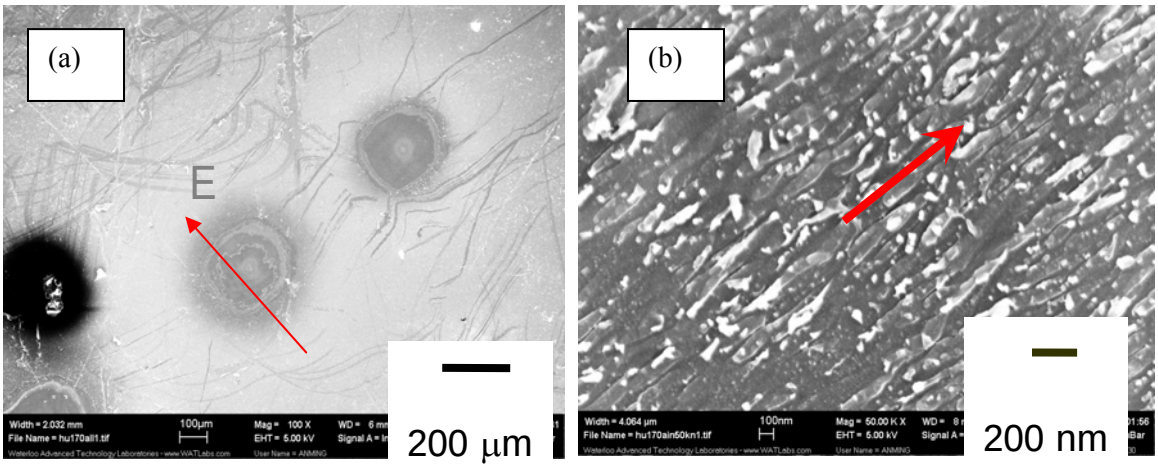

Fig. 2.5. SEM micrographs for HOPG surface irradiated by the vertically polarized wave (s wave). (a) shows serially irradiated areas with variable energys. The arrow indicates the direction of the electric field. (b) nanopatterns obted in Regime I. The Arrow indicates the magnetic field direction.

wavelength of 800 nm and 120 fs pulses. Regions I-IV can be easily distinguished in the pulse energy range of 150-300 μJ/pulse. In region I nanostripes are evident with a spacing of 60 -100 nm. One can find that nanostripes lie in the magnetic field direction, i.e., perpendicular to the direction of polarization. Indeed, when the polarization is rotated to a certain angle, these nanostripes rotate by the same angle. For all linear polarizations, these stripes are oriented in the direction of the magnetic field.

2.3.3 Absence of patterns with circularly polarized waves

To further elucidate the relationship between the orientation of stripes and polarization, we check the irradiation effect of circularly polarized light. Fig. 2.6 presents the morphology of HOPG irradiated with 25 consecutive circularly polarized pulses at 150 μJ/pulse and the pulse width of 120 fs. The pulse energy is reduced due to beam splitting. It is evident that in the edge area, where linearly polarized lights induce nanostripes there are no ordered structures but only a collection of nanoparticles. In regions II-IV, the characteristic microstructures are also weak due to low laser intensity. There are a few nanofilaments in region III where the laser intensity is higher. However, the remarkable difference between the effects of linearly and circularly polarized light is that the latter does not induce any nanostripes. This suggests that nanostripes can be correlated to optical orientation.

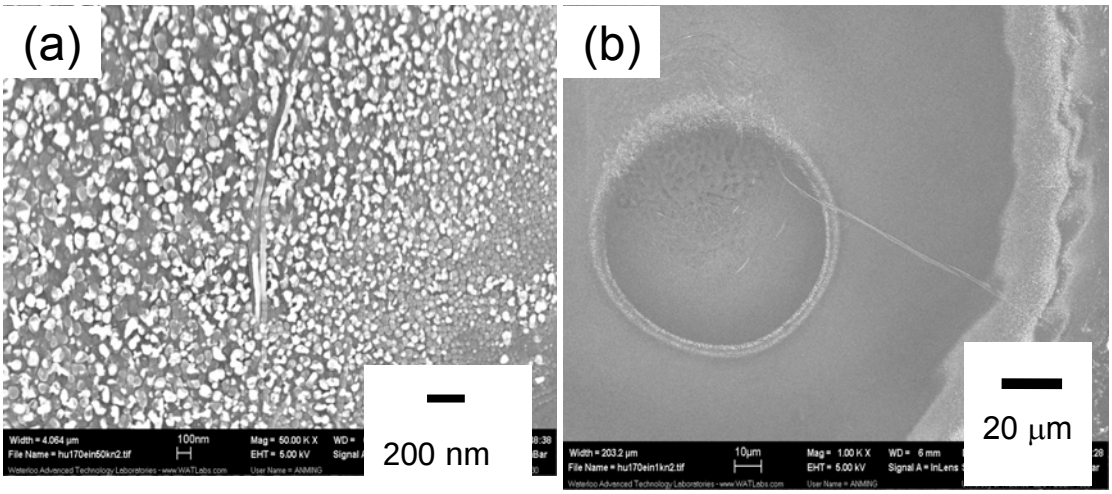

Fig. 2.6. SEM images of irradiation areas with a circularly polarized light at 150 μJ/pulse and pulse width of 120 fs. (a) Nanoparticles in the outer belt. (b) Central crater with a higher laser fluence.

2.3.4 Nanopatterns induced by linearly polarized waves with a wavelength of 400 nm

Fig. 2.7 shows the morphology of nanostripes induced by linearly polarized light at a wavelength of 400 nm of 50 fs pulses. The double frequency is generated by a type I BBO crystal. The remaining 800 nm light in the 400 nm output light was removed by a BG40 bandpass colored glass filter (THORLABS INC, FGB37S). For this filter the transmission is over 40% for the band of 330 nm - 600 nm. The transmission at 400 nm is over 92%. Wavelengths over 700 nm are cut off. Due to about 10% transferring coefficient of a BBO type I crystal, the incident energy was reduced to 30 μJ/pulse. It is obvious that the nanostripes move into the central area due to the decrease of laser intensity and regions II-VI disappear. It is evident that these nanostripes are oriented parallel to the magnetic field direction.

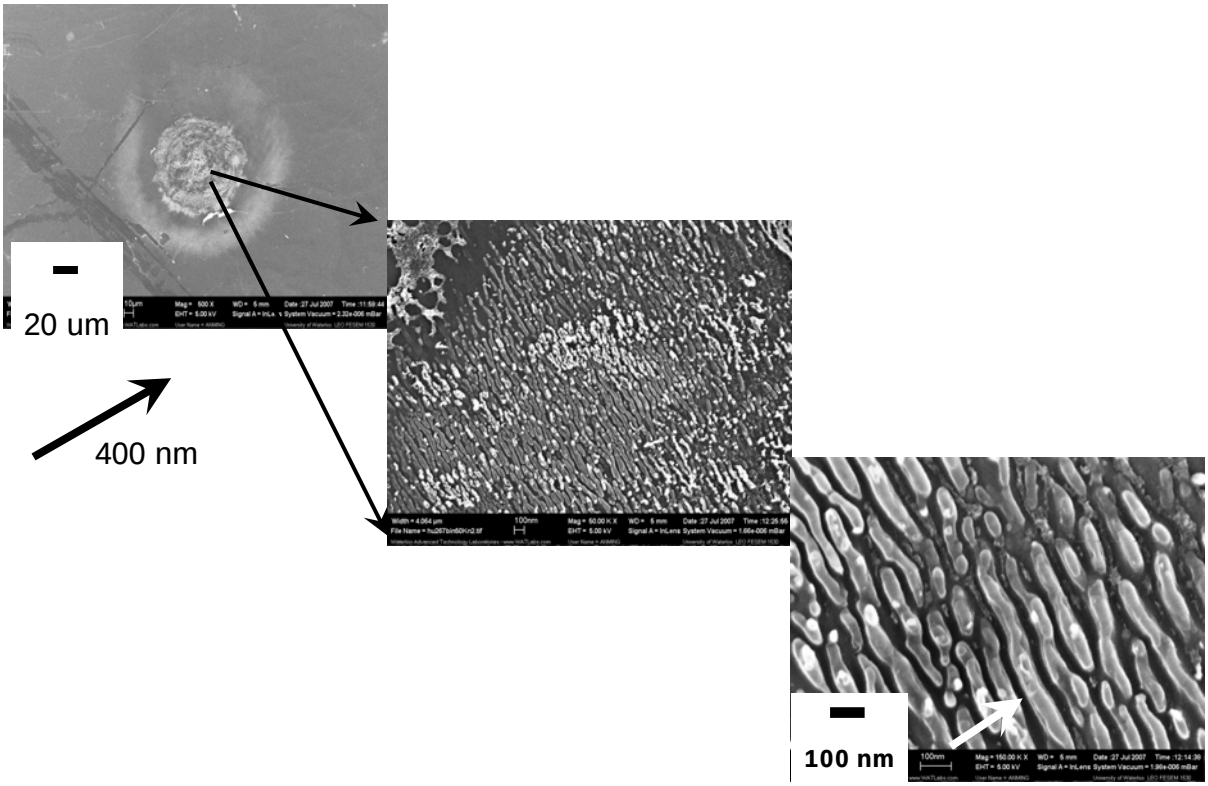

Fig. 2.7. SEM morphology of HOPG irradiated by linearly polarized fs laser at 400 nm and 50 fs of pulse width. The arrow indicates the polarization direction.

Furthermore, the spacing is only 30-50 nm, 1/13-1/8 of the incident laser wavelength, λ. This ratio clearly coincides with that obtained at the incident wavelength of 800 nm. Hence, one can conclude that the direction of the nanostripes is determined by the polarization while the spacing is correlated with incident wavelength. However, the present nanostripes cannot be explained by the interference model (Zhou et al. 1982, Sipe et al. 1983, Young et al. 1983), in which the minimum spacing is only half of incident wavelength. The thermal surface capillary wave cannot explain our results, either, since the orientation direction must be taken into account in such a mechanism (Bugaev et al. 1986, Akmanov et al. 1985). In addition, self-organization can also be ruled out since experiments show that the orientation and spacing as a function of incident laser is well established and repeatable. Such a relationship is not determined by the size, shape and other morphological features of carbon nanoparticles and nanoribbons. It is certainly difficult to relate nanostripe orientation to polarization in self-assembly model and Boson condensation. This allows us to rule out the possibility of nanostripes originating from these processes.

Comparing experiments to the theoretical culcalation according to the capillary instability, it is evident that the calculated spacing value of nanofilaments, $d = \lambda/m$ with m=6-7 for liquid carbon (Downer et al. 1993) is significantly larger than the observed stripes with a spacing $d = \lambda/13$ to $\lambda/8$. This indicates that the capillary instability can not account for the present nanostripes.

2.3.5 Optical orientation mechanisms

Previous studies have shown that fs laser irradiation can result in ulstrafast phase transitions in the HOPG surface (Hu et al. 2007b). In the edge area of irradiation where the laser intensity is relatively weak the dominant binding component is sp^3-bonded carbon as a consequence of sp^2-sp^3 high temperature and high pressure phase transition (Hu et al. 2007d). It is reasonable for us to identify the nanoribbons in Fig. 2.3a, Fig. 2.4a and nanoparticles in Fig. 2.6a are nanocrystalline diamond. According to recent studies, vacancy defects in nanodiamond can attribute a ferromagnetic moment (Talapatra 2005) and the high concentration of dangling sp^3-bond in the nanodiamond surface can induce a giant Pauli-like paramagnetic moment by forming alternative chains –C=C-C=C- due to surface reconstruction (Osipov et al. 2006). Fe impurities which are present in HOPG can also be incorporated into the surface of nanodiamonds giving rise to a ferromagnetic moment. For a 50 fs laser pulse at an energy of 200 μJ/pulse (for a 120 fs pulse at an energy of 400 μJ/pulse), an

instantaneous magnetic peak field of 50 T can be generated in a focus size of 50 μm. Such a strong field should easily line up magnetic nanocarbon particles.

Since the ionization is involved in the ablation procedure, it is reasonable to assume the surface species are charged. Thus an electronic orientation effect of fs pulses should be taken into account. Because graphite is a semi-metal and its surface is exposed to vaccum (or a dielectric medium), a surface plasmon can be induced by the incident laser (shown in Fig. 2.8). The displacement of charged carbon spicies can be directly driven by such a surface plasmon mode.

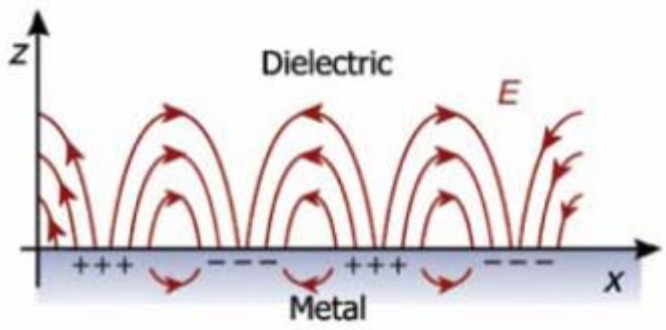

Fig. 2.8. Surface plasmon modes induced in the vicinity of metal-dielectric interfaces.

To understand the origin of nanospacing we consider the propagation of surface plasmon in liquid carbon/vaccum interface. The velocity of surface plasmon can be written

$$v = \frac{c}{n} = f_p d$$

where f_p and d are the frequency and wavelength of surface plasmon, c is the velocity of light, and n is the index of refraction. Because the surface plasmon is the resonant excitation of the incident light, one can express the plasmon frequency, f_p as

$$f_p = m f_{in}$$

with the frequency of the incident light, f_{in} and the integer m = 1, 2, 3,… For m =1, the theory gives a similar result as the capillary instability (Bugaev et al. 1986, Akmanov et al. 1985). For m = 2, one can easily find

$$d = \frac{\lambda}{mn} = \frac{\lambda}{2n}.$$

With n = 5-7 of liquid carbon at the concerning incident wavelength (Taft and Philipp 1965), one can find d = λ /10 to λ /14, well coinciding with present experiments. It is important to mention that the present model indicates that these nanostripes are not pulse width-dependent rather a incident wavelength. This explains why we obtain the similar nanopatterns in two kinds of laser. Besides, the strong second-harmonic generation has been observed in the rough metallic nanoparticle surface (Chen et al. 1983). Hence, further experiments to observe the second harmonic radiation can help to clarify the proposal mechanism. Finally, optical orientation due to both magnetic and electronic effect of fs pulses is illustrated in Fig. 2. 9.

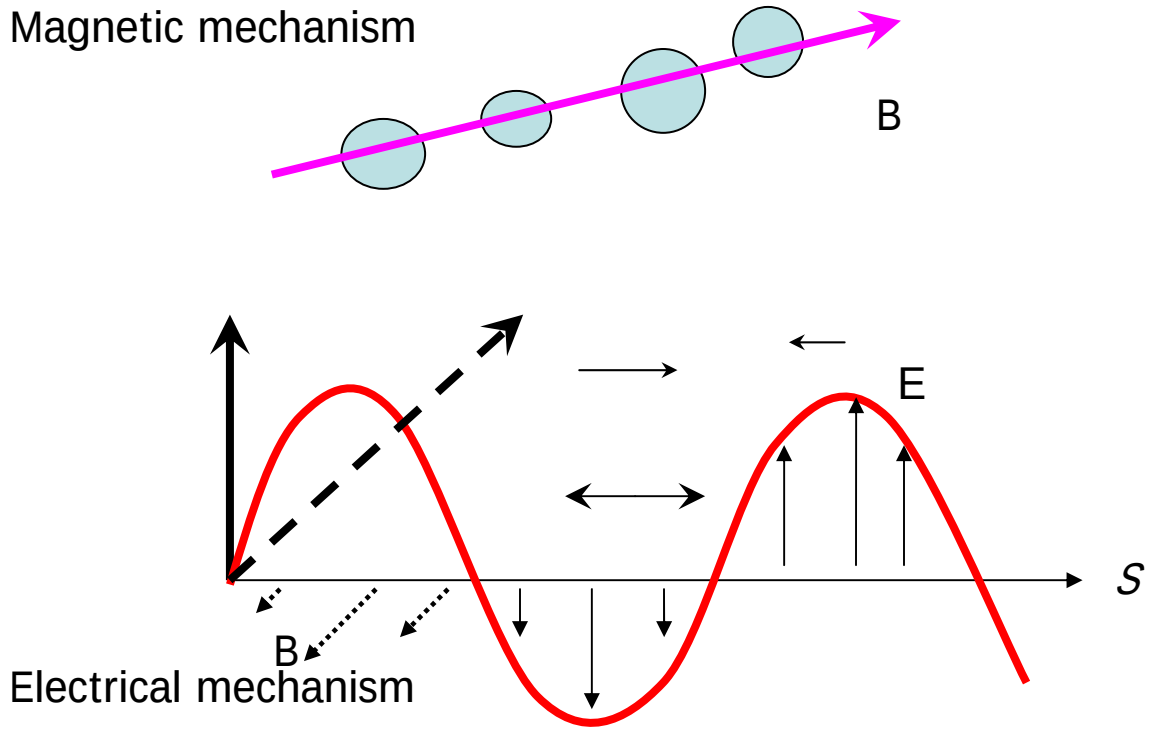

Fig. 2.9. Possible mechanisms involved in optical orientation to produce nanostripes. Upper panel: magnetic carbon nanoparticles are directly oriented by the pulsed magnetic field. Lower panel: charged carbon nanoparticles become oriented by excitation of a surface plasmon. The horizontal arrows indicate the direction of displacement of charged carbon nanoparticles. Particles are concentrated at the zero field value of electrical field intensity (also see Fig. 2.8) .

2.4. Surface phase transition and synthesis of sp-bonded carbon chains

Fig. 2.10 shows the morphology of HOPG in the vicinity of the laser focus after irradiation with 25 overlapping 120fs pulses at energy of 700 μJ /pulse. The central crater of 50 μm in diameter is surrounded by an outer region with less ablation. Such two-area irradiation features are found in the energy range of 700 μJ/pulse-150 μJ/pulse. These two areas as a function of pulse energy are shown in the inset in Fig. 2.10. At a given pulse energy we find that these two diameters are unchanged after 3-60 pulses, indicating that incubation effects are not important in determining the size of fs ablation (Lee et al. 1988). The inset in Fig. 2.10 shows condensed liquid droplets on the crater wall, indicating that melting of carbon occurs during ablation.

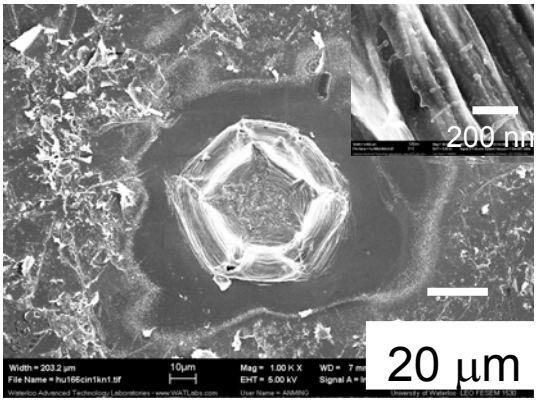

Fig.2.10. SEM micrographs of highly oriented pyrolytic graphite after irradiation with 25 overlapping 120 fs 700μJ laser pulses at a wavelength of 800 nm. Inset: SEM image of the wall of the central crater.

Fig. 2.11 shows the ablation depth (L) per pulse verse incident fluence. It is apparent that L can be described using a two-temperature model, $L = \alpha^{-1} \ln(F / F_{th})$, with α^{-1} is the electronic thermal penetration depth and F_{th} the damage threshold (Nolte et al. 1997). The best fit yields α^{-1} = 139 nm and F_{th} = 0.41 J/cm^2. These data are significantly larger than the measured optical penetration depth of 33 nm at a wavelength of 620 nm (Reitz et al. 2001) and the ablation threshold of 0.18-0.25 for HOPG (Shirk and Molian 2001). This is primarily due to the present ablation occurring at higher incident fluence.

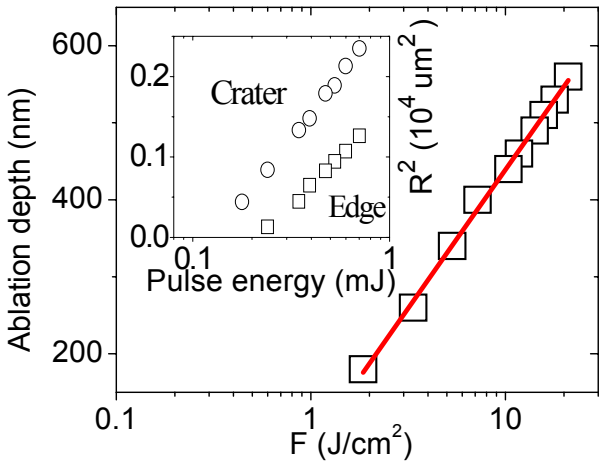

Fig. 2.11. Ablation depth per pulse as a function of incident fluence. The solid line corresponds to a two-temperature model. Inset: Measured area vs. pulse energy for the central crater (squares) and the weakly ablated surrounding region (circles).

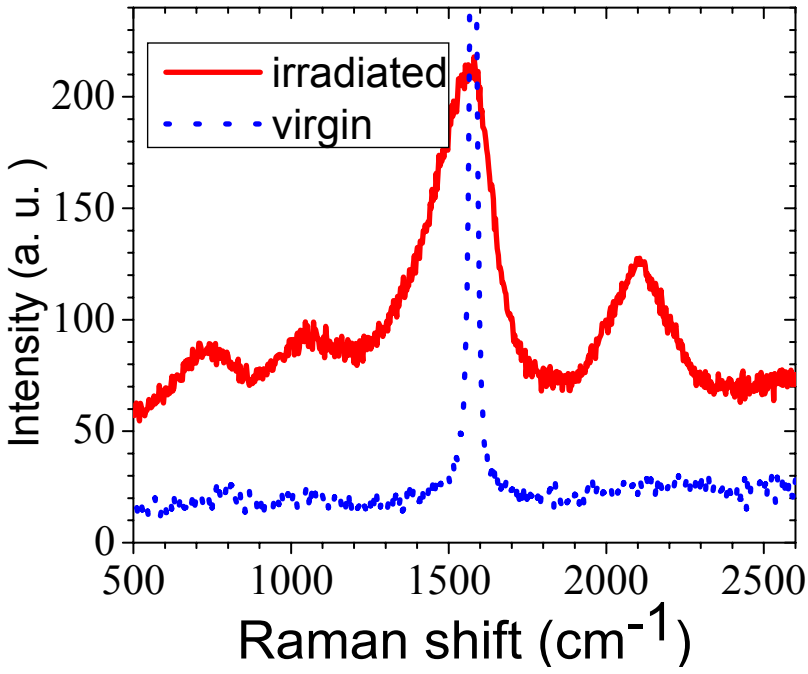

Fig. 2.12. UV Raman spectra of material within the central crater and far away from this region after fs irradiation.

Fig. 2.12 presents Raman spectra recorded at 325 nm of irradiated HOPG within the area of the crater. It is long known that the feature centered at 1570 cm^{-1} originates from the stretching mode of graphite (G band). The enhanced band at 1900-2300 cm^{-1} can be identified with *sp*-bonded carbon chains (Ravagnan 2002, Casari 2007). The presence of sp^3- bonded species is also indicated by the appearance of a T-band centered at 1050 cm^{-1} (Ferrari and Robertson 2001). Although roughly 10% of sp^3-bonded components can be estimated from the ratio of T/G bands there are no models available that permit the deduction of the remaining *sp* and sp^2 concentrations from Raman spectra of a material containing three types of carbon bond (Hu et al. 2007b, Ferrari and Robertson 2001), since *sp* and sp^2 cross sections are structure dependent and are governed by the sp chain length distribution and clustering of sp^2 network.

Although *sp*-bonded chains are more stable when they are formed in high vacuum (10^{-7} Torr), little change in UV spectra is observed after a one-month exposure to air. This enhanced stability of sp-bonded chains may arise because chains are pinned by bonding to sp^3 components (Hu et al. 2007b). Meanwhile, irradiation at 10^{-6}-10^{-5} Torr displays a dramatic decrease of the sp bonded carbon concentration. This is in accord with previous experiments, where, it is reveiled that the *sp*-bonded carbon chains oxidized or graphitized by cross-linking as exposing to dry air (Casari et al. 2004).

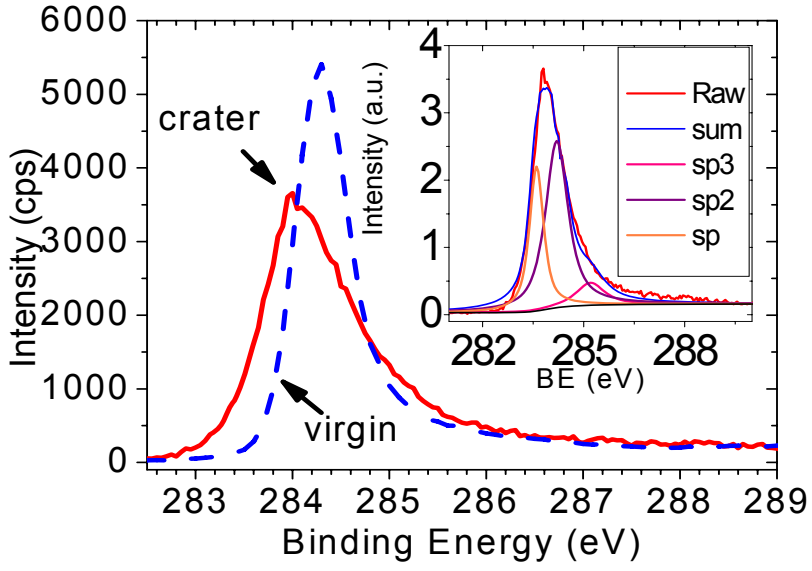

Fig. 2.13. X-ray photoelectron spectra of C1s lines measured within the irradiated crater and an unirradiated region. Inset: deconvolution of C1s line of irradiated crater with *sp*, sp^2 and sp^3 binding energy at 283.5 , 284.4 and 285.2 eV, respectively.

As shown in Fig. 2.13 local binding state transformations are also apparent in XPS spectra of C1s line for material in and outside the irradiated areas. An extended C1s lineshape with a tail shifting to lower binding energy in the central irradiated region is a fingerprint of the presence of carbynes (Hu 2007c). The deconvolution of the C1s line (Fig 2.13) in the irradiated region shows that the *sp*, sp^2 and sp^3 fractions in the central area are 0.3, 0.6 and 0.1, respectively (Haerle et al. 2001).

Fig. 2.14 shows SERS features associated with specific molecular groups. These features do not arise from contamination since they are absent in the SERS spectra of unirradiated areas (Virgin curve) (Otto 2002). SERS spectra of the central irradiated area show that peaks at 1960 and 2095 cm^{-1} can be identified with cumulenes, $(C{=}C)_n$.and polyynes, $(-C{\equiv}C-)_n$, respectively (Ravagnan et al. 2002, Lee et al. 1988). The presence of a diamond component can be seen in the lightly ablated area, which displays a band at 1260 cm^{-1} due to tetrahedral carbon (Beeman et al. 1984) and another at 1280 cm^{-1} corresponding to

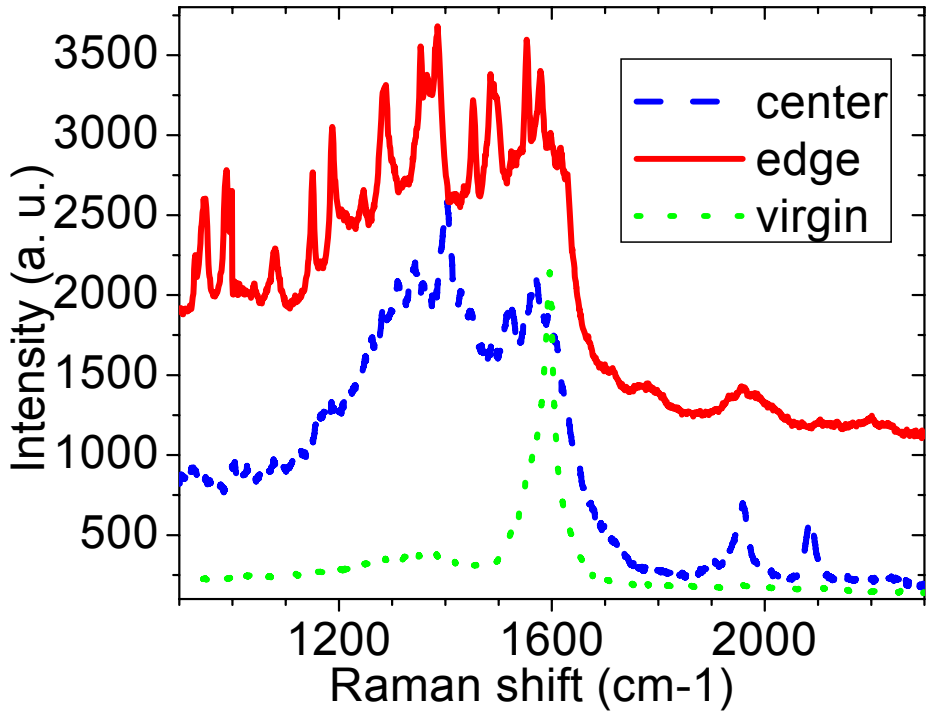

Fig. 2.14. Surface enhanced Raman spectra of a crater, in the weakly ablated region and for pristine HOPG surface recorded at 632 nm.

scattering by nano-diamond at the L point (Roy et al. 2002). Trans-polyacetylene chains having different lengths are identified by the presence of several modes at 1150, 1190 and 1450 cm^{-1} (Hu et al. 2007b, Lopez-Rios et al. 1996). Different SERS modes dependent on laser intensity agree with theoretical calculation and experiments showing that bonding in liquid carbon progresses from *sp* to sp^3 with increasing liquid density (Wang and Ho 1993, Johnson et al. 2005).

Further evidence for a phase transition can be found in Fig. 2.15, in which the microhardness is measured by a nanoindenter. Unirradiated HOPG surface yields a value of 2.6-2.8 GPa, while a higher value (4-6 GPa) is found in the edge (region I) where nanodiamonds are synthesized. In contrast, in the central valley of the crater, the hardness is only 240 MPa, indicating the presence of amorphous carbon. It is worth noting that the hardness of pyrolytic carbon can be as low as 75-80 MPa (Oberlin 2002). This suggests that the melted carbon in the central irradiated area involves a mix of

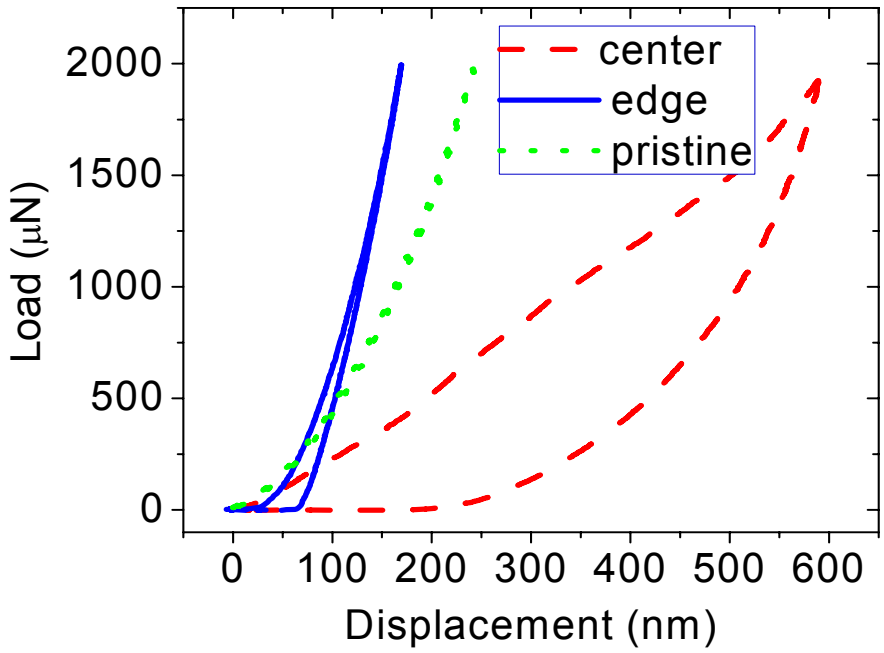

Fig. 2.15 Load-displacement curves measured by a nanoindenter at different positions on irradiated HOPG. “Pristine” stands for unirradiated HOPG surface. Edge: irradiated areas where nanodiamonds are synthesized. Center: central crater.

different types of carbon bonds. A low concentration of sp^3-bonded carbon can still dramatically enhance the local hardness.

In the crater, the incident fluence is so strong that the thermal effect significantly results in much liquid (evident in Figs. 2.3c and Fig. 2.4d). As a result, an abundance of *sp*-bonded chains is readily generated. Meanwhile in the lightly-ablated area outside the central crater the thermal effect is almost absent at lower fluence. Material removal is due to coulomb explosion and photodissociation favoring the formation of nanodiamond in a shock wave. Some trans-polyacetylene phase may also be created during this process. The two-temperature model can further explain the electronic thermal penetration depth α^{-1} obtained from the fit in Fig. 2.11 (Nolte et al. 1997). According to the thermal diffusion length $l = (D\tau_a)^{1/2}$, where $D \approx (1/3)v_F{}^2\tau$ is the thermal diffusivity, τ is electron relaxation time, $\tau_a = \tau \frac{M_{ion}}{M_e}$ electron-lattice interaction time, $\upsilon_F = 8 \times 10^5$ m/s, the Fermi velocity, assuming τ =2 fs (Johnson et al. 2005), one can deduce l =134 nm, which agrees with the experimental value of 139 nm.

2.5. Conclusions

fs laser pulses have been used to generate very fine nanostripes having a spacing of 1/13 to 1/8 of an incident wavelength. Experimetns unveiled that the spacing of nanostripes are not a function of pulse energy. It is not sensitive to the laser pulse widths by comparing 120 fs and 50 fs pulses. Such narrow stripes cannot be explained by presently available theories. By varying polarization and incident wavelength, it has been found that the presence of nano-stripes can be correlated with the extremely high magnetic fields generated by fs pulses. As a consequence of surface plasmon excitation, narrow nanostripes may be also attributed to the electronic orientation effect of the second harmonic resonance generated in the interaction.

It has been shown that local phase transformations on the surface of graphite are strongly dependent on the incident fs pulse fluence. A variety of carbon species including carbyne and trans-polyacetylene chains have been detected in addition to regions containing nano-diamond structure. This work reveals the potential of fs surface engineering for future applications.

Chapter III

Optical and micro-structural properties of diamond-like carbon films grown by nanosecond pulsed laser deposition

3.1. Introduction

Diamond-like carbon (DLC) films, deposited by nanosecond laser ablation (ns-PLD) of graphite, usually contain a high proportion of sp^3 – hybridized C bonds together with a relatively low concentration of sp^2 – hybridized bonds. These materials exhibit a wide range of mechanical, electronic, and electrochemical properties and are thus promising for applications involving the formation of protective coatings for magnetic recording disks and optical devices as well as in the development of field emission components for vacuum microelectronic devices (Robertson 1991; Voevodin 1996; Lifshitz 1996). DLC films having high sp^3 content deposited in the absence of hydrogen are also known as tetrahedral amorphous carbon (ta-C) (Wang 1993, Donadio 1999). The hydrogenated analog of tetrahedral amorphous carbon is ta-C:H and often has a low C-C sp^3 bond content and very low hardness (Roberston 1991, 2002). In this chapter we discuss some properties of ta-C prepared by nanosecond laser ablation in the absence of hydrogen. It has been shown that the mechanical properties of ta-C are mainly determined by the concentration of sp^3 – bonded C-C species, while sp^2 sites govern optical and electrical properties (Pappas et al. 1992; Chhowalla et al. 2000; Ferrari and Robertson 2001). It is likely that, in a sp^3 – dominated material such as ta-C, clustering of the sp^2 phase and the orientation of this phase in the sp^3 matrix, are the most important parameters in determining the overall properties of DLC films. Hence, a microscopic picture of the structure of ta-C and its relation to optical and mechanical properties is of interest.

It has been found that the energy of C ions during PLD of DLC films, together with the substrate temperature, are two major parameters that determine the relative concentration of sp^2 and sp^3 bonded C species in these materials (Pappas et al. 1992; Chhowalla et al. 2000, Prawer et al. 1996, Cuomo et al. 1991, Fallon et al. 1993). While there have been numerous investigations into the properties of films deposited at temperatures up to 1300^{o}C (Chhowalla et al. 1997, Sattel et al. 1997, Kalish et al. 1999, Ferrari et al. 1999), there are only a few studies on the properties of films deposited at cryogenic temperatures (Pappas et al. 1992, Cuomo et al. 1991). Since the energy of C ions in excimer laser ablation is typically 10-40 eV (Duley 1996, Pappas et al. 1992), PLD can be considered

to be an energetic process compared to plasma deposition. The temperature of the substrate is then expected to be especially important in determining the overall structure of these deposits. To date there appears to be no systematic characterization of microstructure in ta-C films deposited via PLD at cryogenic temperatures. In this chapter, the structure of ta-C films deposited at 77K and at higher temperatures up to 573K is discussed. We report the appearance of a novel nano-sized grain-assembled structure in ta-C films deposited at 77K. The relaxation of stress in these films and the morphology of the structures that result from this effect has been examined.

This work also provide a comparative study for understanding the deposition of diamond-like carbon films deposited by femtosecond pulsed laser ablation.

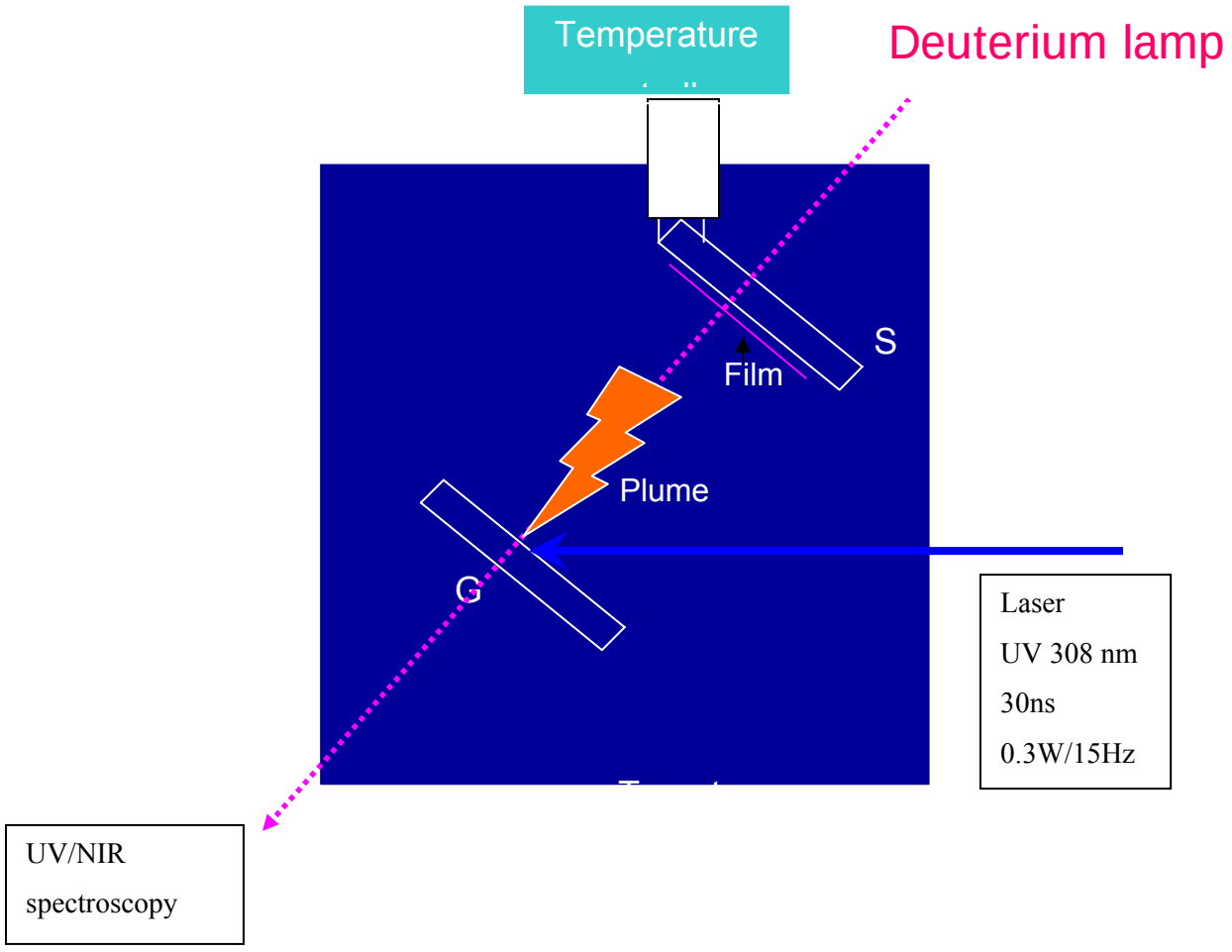

Fig. 3.1 Schematic of high vacuum deposition chamber with in-situ UV/NIR spectroscopy

3.2 Experimental

All depositions were carried out in a vacuum chamber at pressures between 5 x 10^{-7} and 6 x 10^{-6} Torr. Fig. 3.1 shows the experimental setup with a high vacuum chamber for film deposition. A high purity pyrolytic graphite rod was used as the ablation source and this was rotated during deposition to ensure a constant ablation rate. Deposition occurred on a fused quartz substrate oriented almost parallel to the target at a distance of 4.5 cm. This could be heated by conduction or cooled to liquid nitrogen temperature. The substrate temperature was measured by a Cu-constantan thermocouple in contact with the substrate holder. DLC films were deposited at 573 K (300^{o}C), 298 K (room temperature 25^{o}C) and 77K (LN_2) and the ablation source was a XeCl excimer laser (308 nm, 30 ns) operating at a repetition rate of 15 Hz. The incident laser intensity was 3 x 10^8 W/cm^2 corresponding to a fluence of 9 J/pulse.cm^2 at the target surface. The area of the focal spot was ≈ 0.03 mm^2. To avoid the formation the moisture on 77K films after the deposition we keep the high vacuum till the temperature reaches room temperature. The UV/VIS spectrum was monitored during deposition using an Ocean Optics spectrometer (HR4000 CG) and a deuterium lamp.

Raman spectra were recorded by a Renishaw micro-Raman spectrometer with a 50x objective and using an excitation wavelength of 633 nm and a power of up to 3mW. The spectral resolution was 2 cm^{-1} and the laser beam spot size on the target was 5 μm at full laser power. The Raman spectrometer was calibrated by the 520 cm^{-1} line of Si. single crystal. XPS measurements were carried out using a Kratos Ultra photoelectron spectrometer with a monochromatic *Al* K_α 1486.6 eV X-ray source. The spectrometer was calibrated by *Au* $4f_{1/2}$ (BE of 84 eV) with respect to the Fermi level. Microstructure characterization was performed with optical microscopy, scanning electron microscopy (Leo SEM) operating at 15 KV and a commercial atomic force microscope (AFM).

3.3. Experimental results

3.3.1 UV-NIR spectroscopy

The characteristic optical band gap, E_g, in amorphous semiconducting films can be obtained from the absorption coefficient α from a Tauc plot (Tauc et al. 1966). The absorption coefficient α can be evaluated using the expression of $T = (1-R)^2 e^{-\alpha d}$, where R is the reflectance and T = I/I_o is the

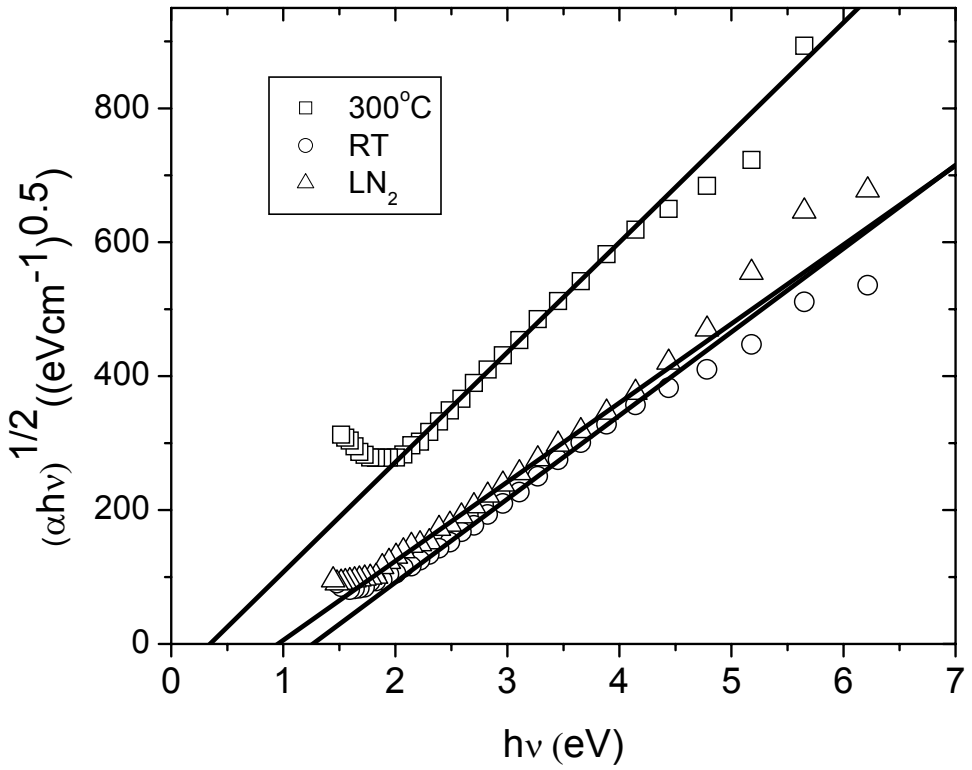

Fig. 3.2 Tauc plot of $(\alpha h\nu)^{1/2}$ versus photo energy hν for three typical films deposited at 77K, 298K and 573K respectively. The solid line is a linear fit over the energy range from 2 - 4 eV.

transmittance, which can be measured by UV/VIS/NIR spectroscopy, d is the film thickness (in this study about 150 nm for 20000 pulses measured with AFM). We measure the transmittance in-situ with varying thickness in order to neglect the reflectance. Fig. 3.2 shows Tauc plots at different substrate temperatures. The optical band gap E_g can be deduced from the extrapolation of the linear part of the curve at $\alpha = 0$,

$$(\alpha h\nu)^{1/2} = B(E_g - h\nu)$$

where B is the density of localized states and hν is photon energy. The film deposited at 573K displays the lowest gap energy (0.35 eV), while the gap energy is 1.27 eV and 0.95 eV for films deposited at 298K and 77K, respectively.

It is well known that the optical band gap of DLC films is controlled by the sp^2/sp^3 ratio, the level of impurity/doping and microstructural properties (Scheibe et al. 1994, Fonlani et al. 2003, Adhikary

et al. 2005). The effect of these terms can be characterized using Raman/XPS spectrometry and by observation of the film microstructure.

3.3.2 Raman/XPS spectra

Fig. 3.3 shows Raman spectra for three films deposited at different substrate temperatures. The Raman spectrum of the quartz substrate is also shown for comparison and indicates that features between 200 and 500 cm^{-1}, arise from quartz. The well-known broad Raman band near 1500 cm^{-1} can be attributed to a combination of the G and D peaks associated with scattering from sp^2 sites. The weak feature near 2900^{-1} cm^{-1} can be attributed to second-order scattering (Nemanich 1979).

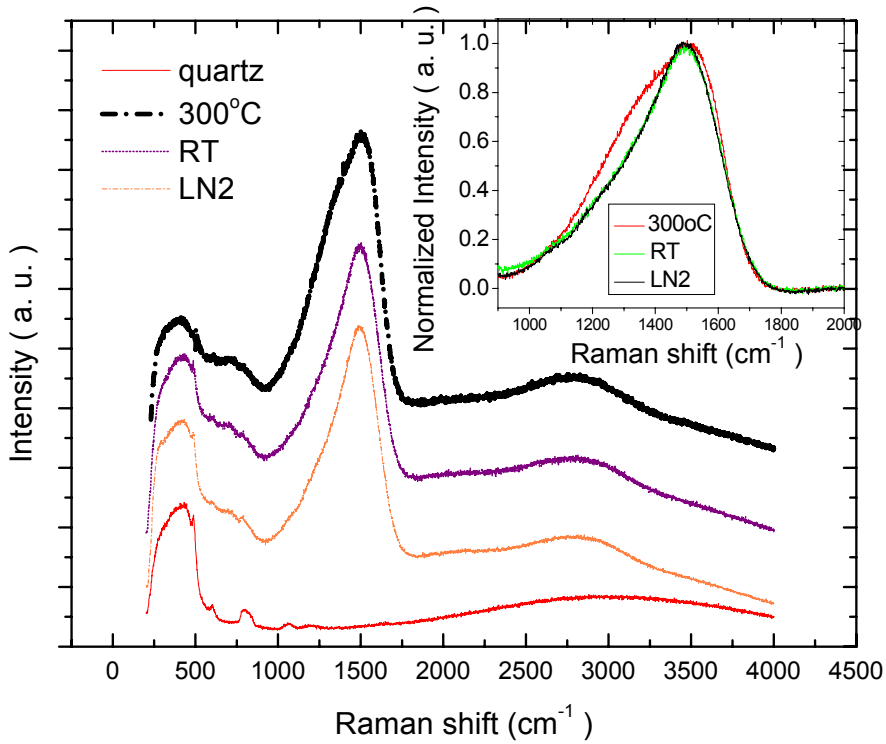

Fig. 3.3 Raman spectra of amorphous carbon films deposited at different temperatures. Inset: normalized D/G band

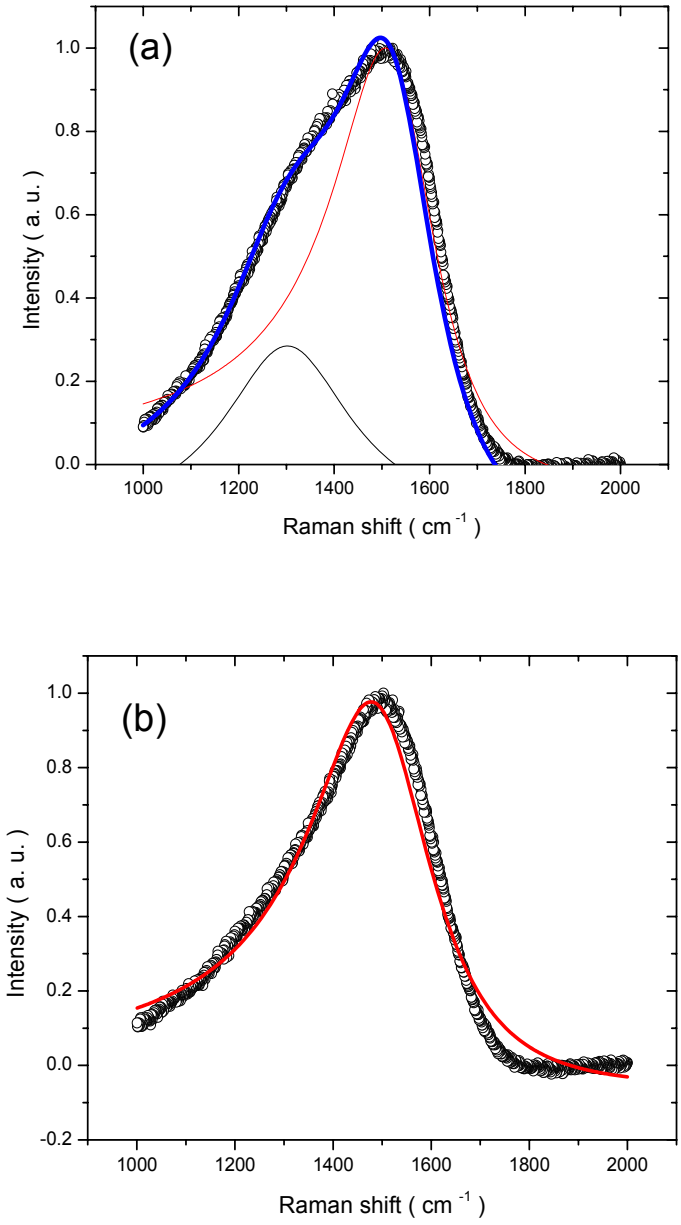

Fig. 3.4 Analysis of Raman spectra for (a) 598K films (b) 298 K films. The solid line corresponds to a theoretical fit. The G peak is fitted with a BWF function. In (a) the D peak is fitted with a Lorentzian line.

The inset in Fig. 3.3 shows the normalized D/G band for three different films. Clearly the FWHM (full width at half maximum) of the D/G peak is smaller in spectra of films deposited at 77K and 298K than in films deposited at 573K. Obviously a narrower Raman feature corresponds to a more transparent film. The D/G band width is known to be a function of laser ablation energy (Siegal et al. 2000) and deposition energy (Prawer et al. 1996) so the width of these features can be correlated to the sp^2/sp^3 bond ratio.

Spectral fits to the D/G peak are shown in Fig. 3.4 with a Breit-Wigner-Fano (BWF) profile for the G peak and a Lorentzian function to fit the D peak (Ferrari and Robertson 2001, Prawer et al. 1996). We find that a BWF fit to the data in Fig. 3.4 (b) gives Q = - 6.1, ω_o = 1503 cm^{-1} Γ = 310 cm^{-1}, where Q ,ω_o and Γ are respectively a coupling coefficient, the peak position and the full width at the half maximum (FWHM). A combined BWF/Lorentzian fit to the Raman profile of the film deposited at 598K (Fig. 3.4 a) yields Q = - 5, ω_o = 1533 cm^{-1} and Γ = 260 cm^{-1}, with a Lorentzian centered at 1302 cm^{-1} representing the D line. The I(D)/I(G) ratio in this film is 0.28. These data indicate that both 77 and 298K films contain more than 70% sp^3 bonded carbon while the 598K film has less than 20% sp^3 bonded carbon (Ferrari and Robertson 2001, Prawer et al. 1996). This is compatible with the existence of a phase transition from ta-C to a-C near 520K (Pappas et al. 1992, Chhowalla et al. 2000) above which a-C becomes the dominant structure.

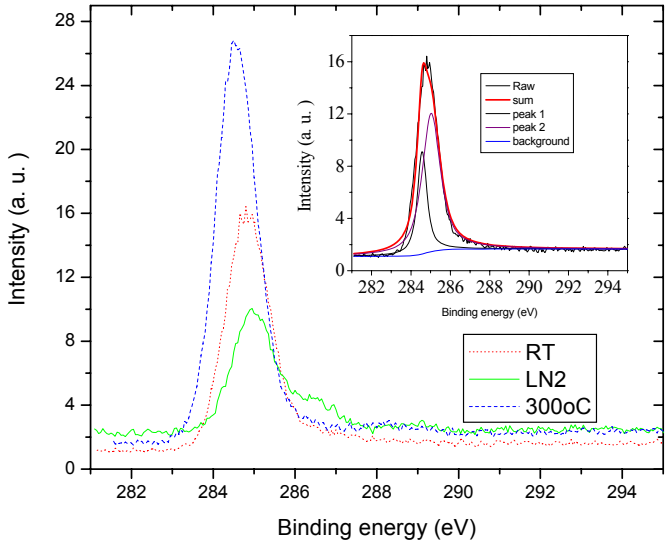

Fig. 3.5 XPS spectra of the C1s line for amorphous carbon films deposited at different temperature. The inset shows the deconvolution of the C1s peak in a 298K film.

At the Raman excitation wavelength of 632 nm the G peak in 77 K and 298K films shifts to 1503 cm^{-1}, about 50 cm^{-1} lower in energy than when excitation occurs at 514.5 nm (Ferrarri and Robertson 2001). This result agrees with previous studies on ta-C films (Ferrari and Robertson 2001, Wagner et al. 1989). The dispersion of the G peak arises from the presence of disordered carbon and is smaller in a-C than in ta-C (Ferrari and Robertson 2001). We observe the G peak at 1533 cm^{-1} in films deposited at 598K. This is consistent with an a-C structure in this material. It is worth noting that electron-energy-loss spectroscopy (EELS) is the direct tool to evaluate the sp^3/sp^2 ration. However, considering EELS as a destructive and time-consuming method we choose XPS as a complementary analysis to estimate the sp^3 content.

Fig. 3.5 shows C 1s spectra of amorphous carbon films deposited at three different temperatures. The inset shows the deconvoluted XPS spectrum of the film deposited at 298 K film. Each individual peak is comprised of a combined Gaussian and Lorentzian profile. These are centered at 284.4 and 285.2 eV corresponding to sp^2 C-C and sp^3 C-C bonds, respectively. The sp^2/sp^3 ratio can be obtained from ratio of the strength of the two components (Merel et al. 1998, Diaz et al. 1996). This calculation yields 72, 68 and 20% sp^3 in 298, 77 and 573 K films, in agreement with the estimate of this ratio from Raman spectra. Note that a band attributable to C-O appears at 286.5 eV in films deposited at 77K. This oxygen is certainly due to exposure to air because it can be removed by Ar-ion surface treatment. However, it may indicate a surface activation of 77K films since this band does not appear in spectra of the other two films.

3.3.3 Microstructure

Fig. 3.6 shows typical SEM images of films deposited at 77 and at 298K. It is apparent that temperature has a profound effect on structure as the film deposited at 77K consists of nanometer clusters embedded in a granular matrix, while films deposited at 298K are basically free from granular structure even at high resolution although C clusters are occasionally found on the surface of films deposited at 298K. Chemical compsotion analysis by the local energy dispersive X-ray spectra (EDAX) shows that these are C particles due to a “splashing” mechanism occurring during PLD (Singh et al. 1990). Films deposited at 598K have a similar morphology to those deposited at 298K. Images of 77K films show that the largest clusters, typically having a size of ≈ 0.5 μm, are assembled

from a collection of many nm particles. The matrix in these films consists of a range of additional clusters having sizes ≤ 100 nm.

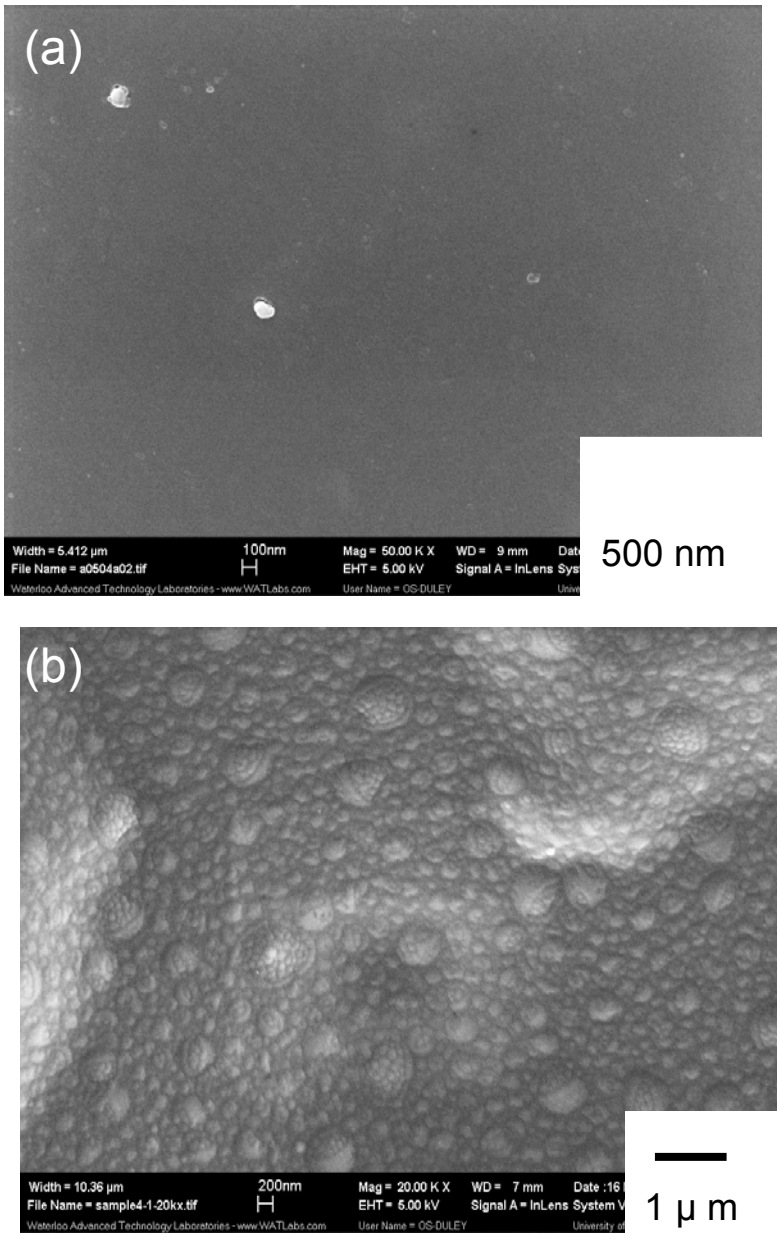

Fig. 3.6 SEM micrographs for (a) 298K films and (b) 77K films.

Fig. 3.7 shows AFM images recorded in tapping mode. It is found that no substructure exists in 298K films at a resolution > 10 nm. Films deposited at 77K appear to have been assembled from grains with sizes ≤ 40 nm. Furthermore, these grains preferentially aggregate into large clusters with sizes of ≈ 0.5 μm. Fig. 3.7 (c) and (d) show sample roughness along the straight lines in Figs. 3.7 (a, b), respectively. It is evident that 298K films are atomically flat except for a few particles attached to the surface. These particles are the same as those observed in SEM images (Fig. 3.6 (a)). The large clusters observed in 77K films are about 35 nm in height.

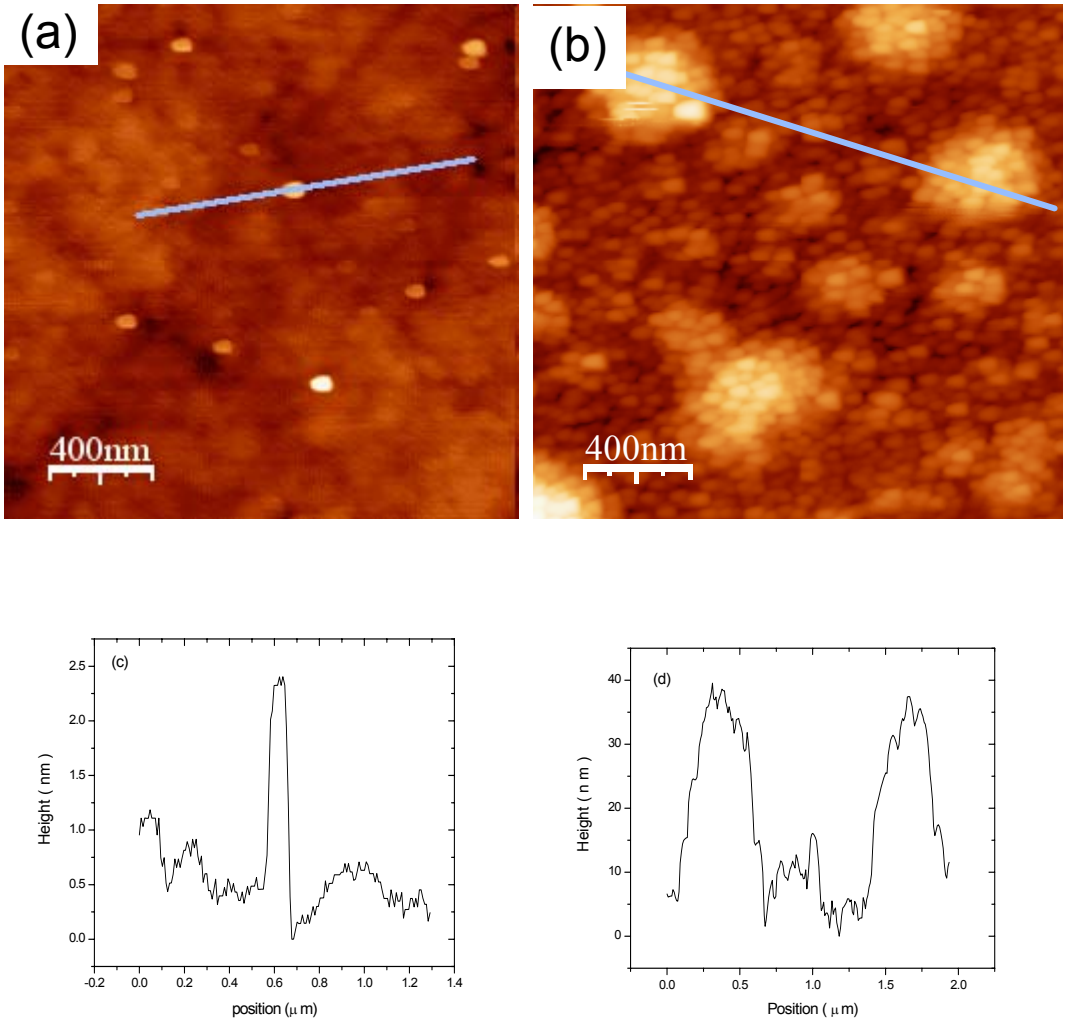

Fig. 3.7 Surface characterization of ta-C films by AFM. (a) 298K film. (b) 77K film.The solid line displays a roughness analysis depicted in Fig. 3.7 (c). The solid line displays a roughness analysis depicted in Fig. 3.7 (d).

Apparently, microstructure of this kind has not previously been observed in cryogenic films (Pappas et al. 1992, Cuomo et al. 1991).

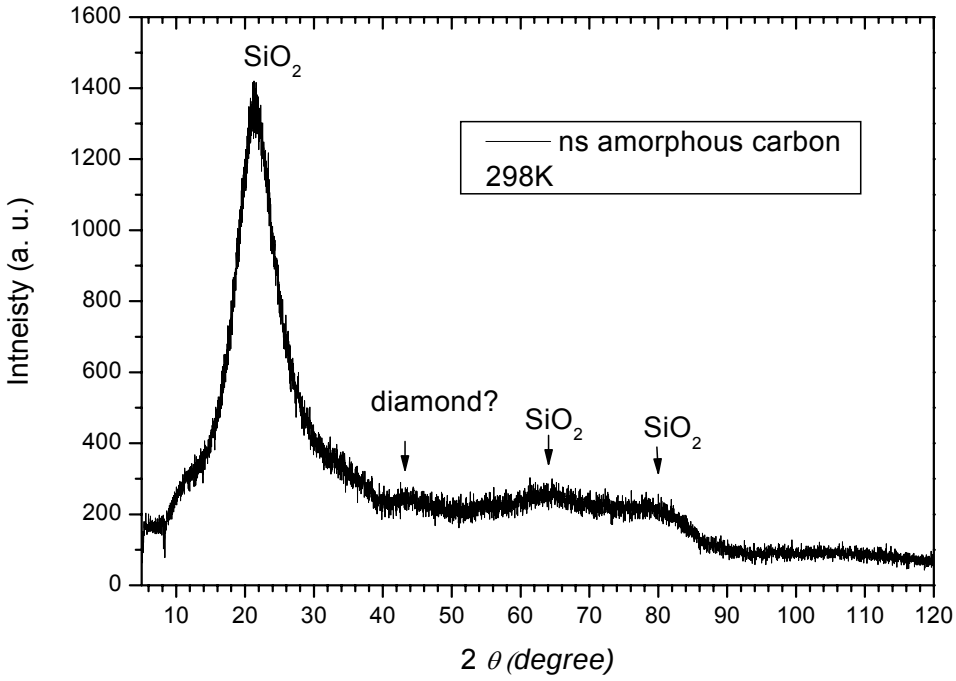

Fig. 3.8 X-ray diffraction patterns measured with Cu-K_α radiation.

Fig. 3.8 shows XRD patterns of carbon films deposited on silica at room temperature (298K). The dominantly extended peaks correspond to SiO_2 from the substrate. A very weak peak near 44^o can be assigned to cubic diamond (111) plane with a space group of Fd3m and lattice parameter of 3.56 Å. Similar XRD patterns are obtained for cryogenic and 573K films. It is long kown that the loss of long-range crystalline orders and the light carbon atomic mass may result in the weak XRD patterns of carbon films depositied by ns PLD. This confirms that the present film is amorphous. To characterize nanostructured carbon films, a high resolution XRD with the glazing angle can be an effective method.

3.4. Discussion

The clusters that appear in the images of Figs. 3.6 (b) and 3.7 (b) appear to constitute the building blocks of the resulting films. They are, in turn, aggregates of smaller (<40 nm) grains. These clusters are of mixed sp^2 / sp^3 composition as evidenced by the similarity between Raman spectra of 77 and 298K deposits. This indicates that the Raman spectrum is determined primarily by the composition of the smaller grains, rather than by that of the larger clusters. Further Raman study with UV laser excitation may clarify this point, since shorter wavelength excitation will probe closer to the surface.

The deposition of ta-C can be understood in the context of a sub-plantation model (Robertson 1993). In the present study, the average C ion energy, as inferred from Raman spectra, is about 20-30 eV (Duley 1996). A large compressive stress thus occurs due to a plastic deformation of the surface by ion bombardment. This internal stress can be released by post-annealing (Ferrari and Robertson 1999b), Cu/Ti doping (Siegal et al. 2000) or local structure clustering (Angus et al. 1988, Cary et al. 2004). Mercer *et al* (1998) have reported that nano-particles of about 100 nm can successfully be created by local electric stress induced by a scanning tunneling microscopy tip. Siegal *et al.* (2000) also showed that annealing to 600^{o}C results in the creation of a-C nano-composites in DLC films. Apparently, deposition at low temperature produces additional thermal stress compared to deposition at room temperature. It is possible that this thermal stress may encourage the ordering of nano-sized clusters during deposition.

From an analysis of the optical band gap energy, it can be concluded that the sp^2/sp^3 ratio governs the optical band gap of the DLC films produced in this set of experiments. The lower band gap energy in films deposited at 77K compared to those deposited at 298K, indicates that there is enhanced coupling between sp^2 clusters through the sp^3 bonded matrix. This property is further studied using transport measurements.

Finally, it is important to point out that cryogenic grain-assembled *ta-C* films are of interest in tribological applications (Voevodin 1995). Currently a nanoscale roughness modulation of *ta*-C films can be created by deposition on Ni-nano-dots (Lee et al. 2003, Park et al. 2005). Our results show that such a surface is naturally present in the present cryogenic films.

3.5. Conclusions

Optical and microstructure properties of diamond-like carbon films have been investigated at deposition temperatures between 77 and 598K. Raman/XPS analysis shows that tetrahedral amorphous C films were obtained at 77 and 300K while amorphous C films with predominant sp^2 bonding are obtained on deposition at 598K. Nano-structured cryogenic films with embedded submicrometer clusters have been produced, likely induced by the enhanced internal stress on deposition at cryogenic temperatures.

Chapter IV

Sub-micron cryogenic graphitization and buckling of tetrahedral amorphous carbon films

4.1 Introduction

Tetrahedral amorphous carbon (*ta-C*) films having relatively low concentrations of sp^2 bonds in an sp^3 bonded matrix are regarded as promising materials for ultrahard coatings and microelectronic applications. These applications are possible because the physical and chemical properties of these materials can be controlled by changing the sp^2/sp^3 bond ratio (Robertson 2002, Grill 1999). It is found that the sp^3 phase governs the optical band gap and yields a high hardness and transparency similar to diamond while the presence of sp^2 nanoclusters acts to modify the electrical conductivity and local electron affinity. For cold cathode applications and planar displays, sp^2 bonded species in ta-C have been shown to play a critical role in facilitating low field emission (Talin et al. 1996, Ilie et al. 2000). With regard to tribological properties, the presence of nanoscale undulation due to sp^2 bonded species on the surface of *ta-C* has been shown to dramatically suppress tribochemical reactions resulting in stable friction behavior (Park et al. 2005). These studies suggest that further work on clustering and segregation of the sp^2 phase in sp^3 bonded matrix is of fundamental importance.

Theoretical calculations predict that clustering of sp^2 bonds diluted in a sp^3 bonded matrix is favored energetically (Wang and Ho 1993, Marks et al. 1996, Schultz et al. 1999). However, this does not imply that there is any preference for the growth of large graphite-like grains. The Tuinstra-Koenig (TK) relationship shows that the average size L_a of graphite clusters can be obtained from $(1/L_a) \propto (I_{1355}/I_{1575}) = (I_D/I_G)$, the intensity ratio of the Raman D and G bands (Tuinstra et al. 1970). This analysis shows that the typical size of sp^2 clusters is ≈ 1-2 nanometers in *ta-C* (Ilie et al. 2000, Ferrari and Robertson 2000). Although there is some uncertainty whether or not the TK relationship can be applied to describe the properties of *ta-C* (Schwan et al. 1996), the direct observation of these sp^2 clusters by scanning tunneling microscopy yields a similar size (Carey et al. 2004). It is well-known that high temperature annealing can induce the coarsening of sp^2 clusters, however, only 3-5 nm sp^2 clusters have been identified by transmission electron microscopy in 600°C *ta-C* films (Siegal

et al. 2000). However, the formation of 100 nm sp^2 clusters in *ta-C* films with large stress gradients induced by a scanning electron microscopy tip has been reported (Mercer et al. 1998). In addition, Bolgiaghi et al. (2005) have reported the growth of micrometer scale glass-like clusters in carbon films at high helium pressure. There is, however, no clear evidence that these large clusters are sp^2 bonded. It is then of interest to see if micrometer-sized graphite-like grains can be fabricated in ta-C films using conventional techniques.

In this chapter, I show that nanostructured ta-C films containing embedded submicron graphitic grains can be produced on quartz substrates at 20 – 100K using pulsed laser deposition (PLD). Our study finds that these materials have a number of unique properties including enhanced surface chemical activation.

4.2 Experimental details

The films were deposited at temperatures between 20 and 573 K on cleaned fused quartz (silica) substrates. The vacuum chamber was evacuated using a turbo pump to pressures in the 2 x 10^{-6} Torr (2.66 x 10^{-4} Pa) range. High purity pyrolytic graphite (99.99%) was ablated with XeCl excimer laser radiation (λ=308 nm, pulse duration τ = 30 ns, repetition frequency 15 Hz, incidence angle 45^o). The incident laser intensity was 3 x 10^9 W/cm^2 corresponding to a fluence of 90 J/pulse.cm^2 at the target surface. The area of the focal spot was ≈ 0.03 mm^2. Further details on the deposition system have been reported elsewhere (Hu et al. 2007a). The substrate was heated to 300^{o}C by conduction from a resistive element. Low temperatures were obtained by cooling with liquid nitrogen and by using a refrigerator (CTI-Cryogenics). The temperature was measured by a thermocouple attached to the substrate. Film growth was monitored in-situ with a UV-NIR spectrometer enabling control of absorbance. Film thickness as measured by the AFM was typically 250-300 nm (Hu et al. 2007a).

Microstructure characterization and nanohardness measurements were carried out with a commercial atomic force microscope (AFM) with a Si_3N_4 tip. Resonant Raman spectra were examined by a Renishaw micro-Raman spectrometer with 10 mW He-Ne laser at an excitation wavelength of 633 nm (red) and with a Kimmon 5161R-GS Raman spectrometer using He/Cd laser radiation at 442 nm (blue) and 325 nm (UV). To avoid excessive heating of the carbon sample, 10% power was used at 325 nm and 50% power was used at 442 nm. XPS measurements were carried out using a Kratos Ultra photoelectron spectrometer with a monochromatic *Al* K_α 1486.6 eV X-ray source. The spectrometer was calibrated by *Au* $4f_{1/2}$ (BE of 84 eV) with respect to the Fermi level.

4.3 Results and Discussion

4.3.1 Microstructure characterization

Fig. 4.1 (a) shows the surface of a silica disc after ultrasonic cleaning in acetone and then in reagent alcohol (both HLPC grade) for 10 minutes. Surface roughness of the clean silica substrate is shown in Fig. 4.1(d). Apart from a few depressions, the substrate is smooth to less than 1 nm. Fig. 4.1 (b) shows the morphology of a ta-C film deposited at room temperature (RT). These deposits are

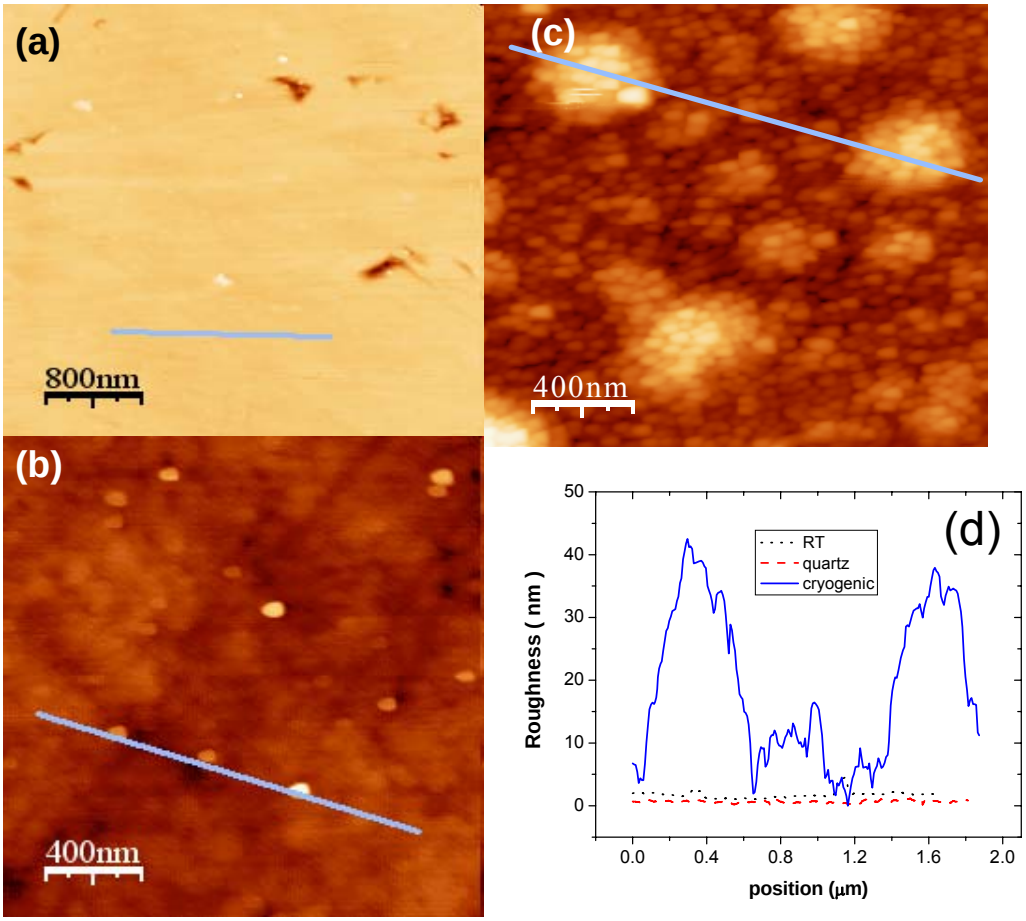

Fig. 4.1. AFM images of (a) clean quartz, (b) ta-C films deposited at room temperature (RT=25^{o}C, 298K) and (c) ta-C films deposited at 20-100K (cryogenic films). The surface roughness along a straight line is shown in Fig. 4.1 (d).

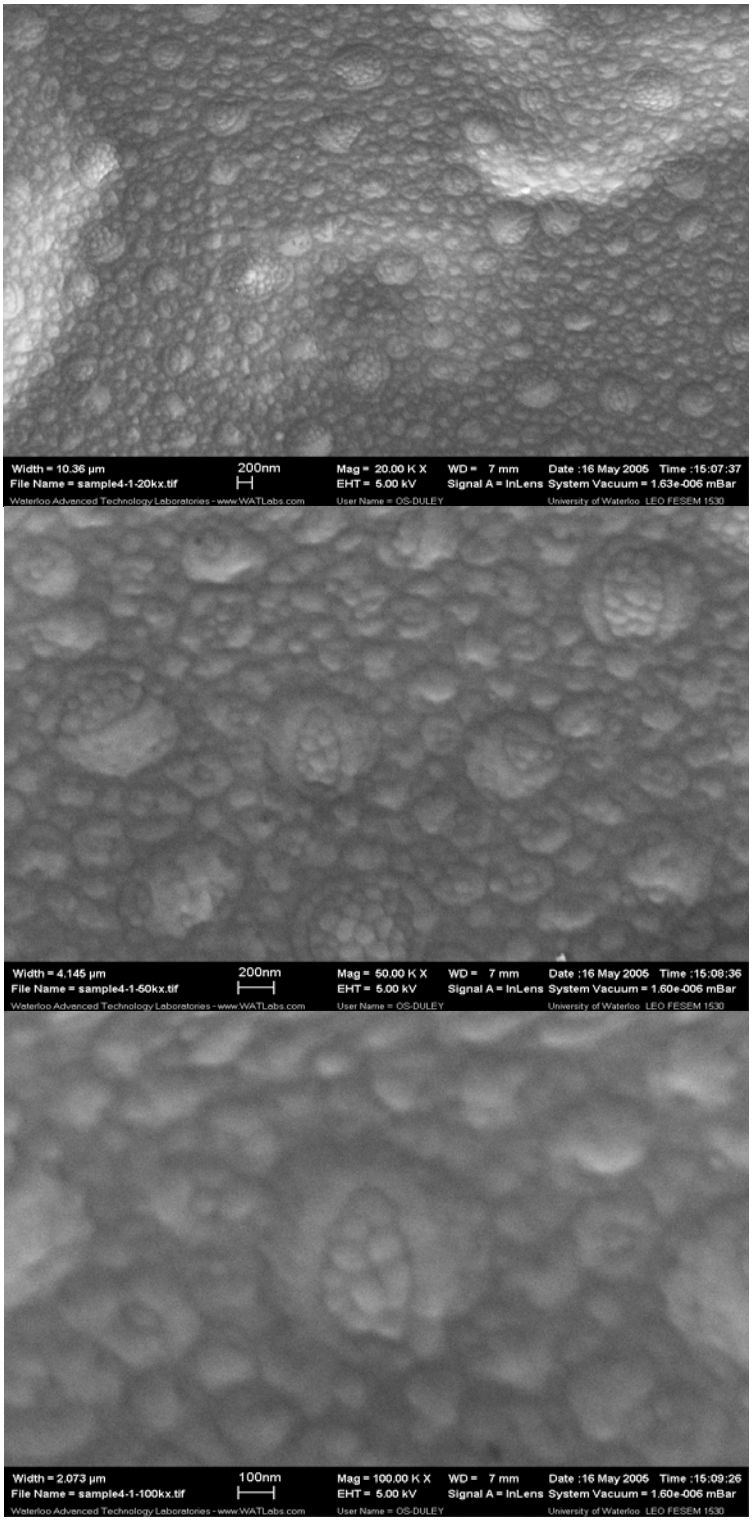

Fig. 4.2 SEM Micrographs of embedded submicron grains in nanostructure diamond-like carbon films. These images are taken at the same position with elevated magnifications.

amorphous and except for a few particles on the surface, the roughness measurement indicates that room-temperature films are atomically flat. This is a typical feature of *ta-C* films.

Compositional analysis, measured by energy dispersive spectroscopy, shows that the nanoparticles on the ta-C surface are carbon, and probably originate from a laser "splashing" mechanism during deposition (chapter 3). It was found that films deposited at 573K have a similar surface structure as that of the room temperature films (Hu et al. 2007a). Furthermore, films grown at 20-100 K possess similar morphologies. Fig. 4.1 (c) shows an AFM micrograph of a cryogenic film. It is assembled from nanoparticles having an average size of 40-50 nm. These nanoparticles further aggregate to form submicron grains with typical sizes of 0.4-0.5 μm. Fig. 4.1(d) shows that these grains are about 30-40 nm in height, and introduce surface modulation into cryogenic films. Although nanostructured ta-C films have been seen before (Carey et al. 2004, Siegal et al. 2000, Mercer et al. 1998), there are few reports of nanoparticle-assembled micrometer grains embedded in the ta-C matrix (Bolgiaghi et al. 2005). It is important to point out that the average size of nanoparticles inside the matrix and in grains are very similar in our cryogenic films. This is different from the morphology of *ta-C* films grown with various He gas pressures (Bolgiaghi et al. 2005). With He atmosphere, the particles which assemble micrometer grains either are quite big, about 1 micrometer in 60 Pa gas pressure, or are quite small, less than 10 nm in 250 Pa.

Fig. 4.2 shows the detailed SEM images of embedded submicron grains in cryogenic tetrahedral amorphous carbon films. It is evident that at a low magnification the distribution of these submicron grains is quite uniform with a spacing of ≈ 1 μm. The average size of these grains is 200-500 nm, which is in agreement with the AFM observation. With a high resolution SEM images show these grains are assembly by nanograins with a size of 20-50 nm. The size variation of these submicron grains indicates that they are formed by the segregation of nanoparticles.

4.3.2 Nanohardness

To help understand the composition of cryogenic ta-C films, we have measured the nanohardness both inside and outside of grains. Fig. 4.3 (a) shows the measurement configuration. The white points in this figure correspond to the measuring positions. Nanohardness is obtained by monitoring the deformation (corresponding to a current measured by the deflecting laser) of the AFM cantilever as the tip approaches the film, pierces to some depth, and then moves away from the film. This path

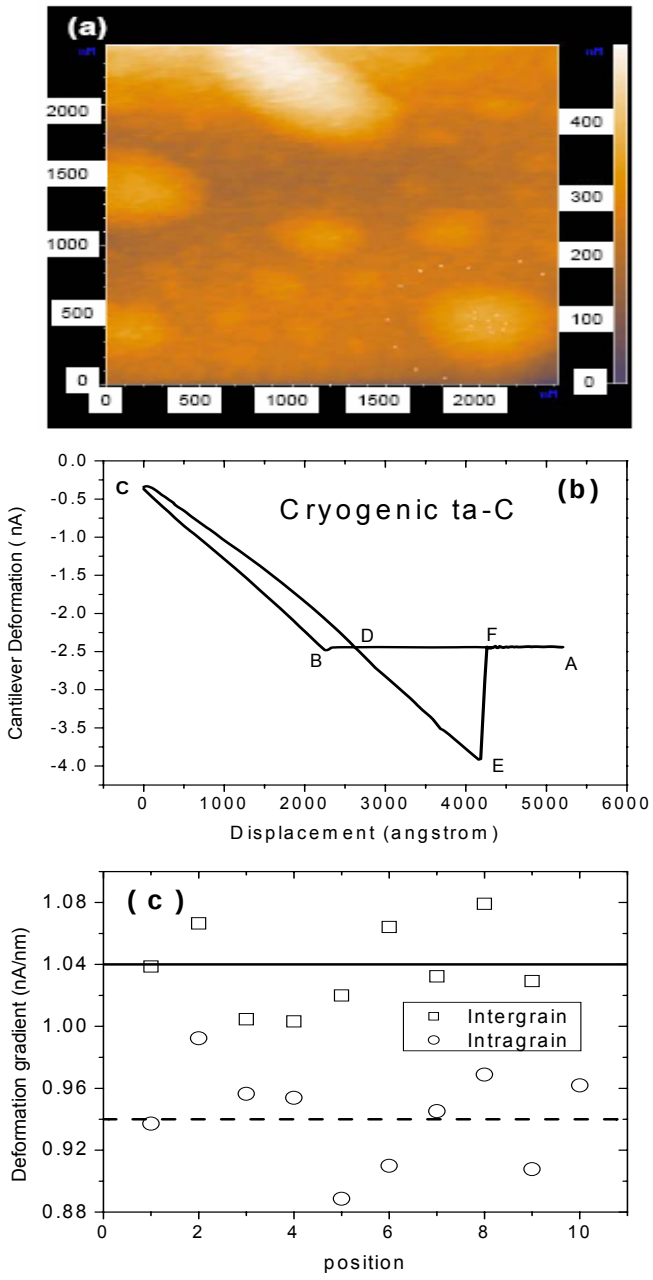

Fig. 4.3 Nanohardness characterization by AFM. (a) AFM image shows the grains selected. The white points indicate measured points. Unit: nm. (b) Cantilever deformation of the measured loop along AFM tips approaching, then piercing into the film and finally moving away from the surface. (c) Deformation gradient of AFM cantilever at individual measured point. Solid and dash lines correspond to the average deformation estimated using a linear least square fit.

corresponds to the cantilever deformation along the loop ABCDEF shown in Fig. 4.3 (b). In this measurement, the slope of BC is proportional to hardness. An analysis of these results is shown in Fig. 4.3 (c). It is evident that the intergranular hardness is remarkably higher than that inside a grain. This shows that graphitic bonding is localized within grains. To further confirm the present results, five grains and over 100 points have been measured, all with similar results. Thus it can be concluded that submicron grains must possess a higher concentration of sp^2 bonded carbon than exists in the matrix. Although the absolute value of nanohardness can in principle be obtained by imaging the tip shape and calibrating the cantilever deformation, it is expected that both granular and intergranular hardness will be less than the bulk value since the present interaction between ta-C and the AFM tip is mainly an elastic deformation. It is apparent that there is almost no indentation in Fig. 4.3 (a).

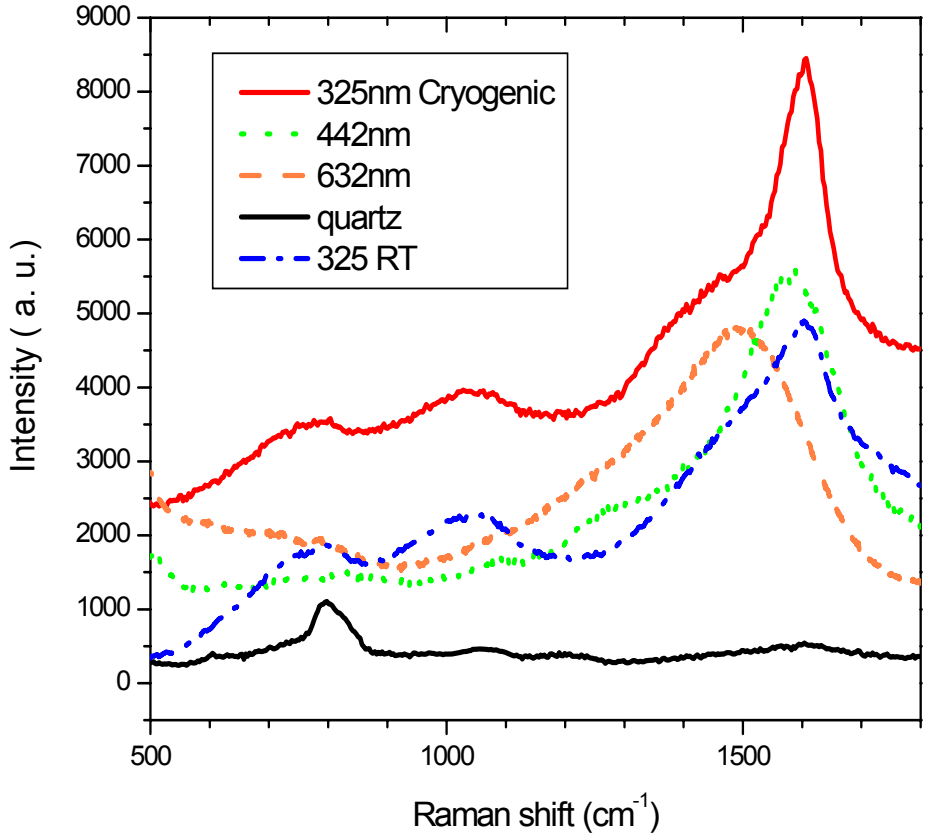

Fig. 4.4 Resonant Raman spectra of RT (298K) and cryogenic films.

4.3.3. Raman spectra

To understand bonding in these ta-C films, Raman spectra have been measured at 632, 442 and 325 nm. Fig. 4.4 shows Raman spectra for cryogenic films. For comparison, spectra from a RT film and a clean quartz substrate at 325 nm (3.8 eV) excitation wavelength are also plotted. In these spectra, the band near 800 cm^{-1} arises from the substrate. The broad band near 1500 cm^{-1} excited at 632 nm can be deconvolved into the G-band at 1570 cm^{-1} and D-band near 1355 cm^{-1}, corresponding to the stretching and breathing modes of sp^2 bonded carbon, respectively (Tuistra et al. 1970 and Hu et al. 2007a). The T-band centered at 1060 cm^{-1} can be assigned to sp^3 bonded species and only appears at an excitation wavelength of 325 nm (Gilkes 1997). In ta-C the $\pi \rightarrow \pi^*$ gap of sp^2 bonded species is about 2 eV while the $\sigma \rightarrow \sigma^*$ gap of sp^3 atoms is ≈ 5.5 eV, so that excitation at 442 nm (3.56 eV) and 632 nm (0.5 eV) couples primarily to the $\pi \rightarrow \pi^*$ excitation. It is apparent that there is a blue-shift of the D and G bands with decreasing excitation wavelength. This can be explained in term of the $\pi \rightarrow \pi^*$ resonant Raman scattering of sp^2 carbon clusters (Yoshikawa et al. 1988). If we assume there is a cluster size distribution of sp^2 bonded carbon atoms in the films, it is expected that Raman scattering from variable sp^2 bonded clusters will show a wavelength dependent resonant enhancement.

With excitation at 632 nm, the relative concentration of sp^3-bonded species can be evaluated by deconvolving the D/G band. We find that this concentration is ≈ 70% and 68% for RT and cryogenic films, respectively (Hu et al. 2007a). With UV excitation, the concentration can also be estimated from either the dispersion of G band or the Raman intensity ratio, I_T/I_G (Shi et al. 2001). However, it is important to point out that the D and G bands produced with 325 nm excitation are unusual. This anomaly can be clearly seen in Fig. 4.4. It is evident that the D and G bands of cryogenic films consist of two overlapping features: one broad weak band is similar to that seen in RT films while a second peak appears with significantly enhanced intensity. There is then some uncertainty in determining the center positions of the D and G bands as well as their widths. The narrow peak at 1600 cm^{-1} in cryogenic films corresponds to the well-known E_{2g} stretching mode in sp^2 sites (sixfold rings or aromatic and olefinic molecules). The enhancement of this peak indicates that there is a significant aggregation of sp^2 bonded atoms in cryogenic films. This result differs from that reported for glass-like grain assembled ta-C films grown in He gas (Bolgaghi et al. 2005) since those films displayed a Raman feature similar to that of microcrystalline graphite with the D band at 1375 cm^{-1} and the G band at 1575 cm^{-1}. The separation of D and G bands is consistent with a low concentration of sp^3 bonded atoms (Ferrari and Robertson 2001). Thus resonant Raman spectra of cryogenic films

are indicative of compositions in which graphitic grains assembled in a sp^3 bonded matrix generate two overlapping spectral features, one from atoms in the matrix and the other from those inside grains. This agrees with the conclusions reached from the results of AFM characterization. Hence, we conclude that sp^2 bonded atoms significantly segregate and accumulate in the submicron-sized grains. This directly contributes to different intragrain and intergranule nanohardnesses. Obviously, the origin of graphitization and clustering is worth further investigation. Since the PLD is an energetic process with C species of 20-40 eV (Duley 1996, Cuomo et al. 1991, Robertson 1993), this graphitization may occur on heating metastable C clusters in DLC films deposited at 20-100K. Meanwhile, at room temperature or higher temperatures, energetic C species are more mobile and can thus induce the relaxation of internal stress. Apparently, deposition at 20K-100K produces additional thermal energy compared to that at room temperature. It is possible that this energy transfer promotes the conversion of sp^3 to sp^2 bonds. Further dynamic stress relief may encourage the ordering of nano-sized clusters during deposition.

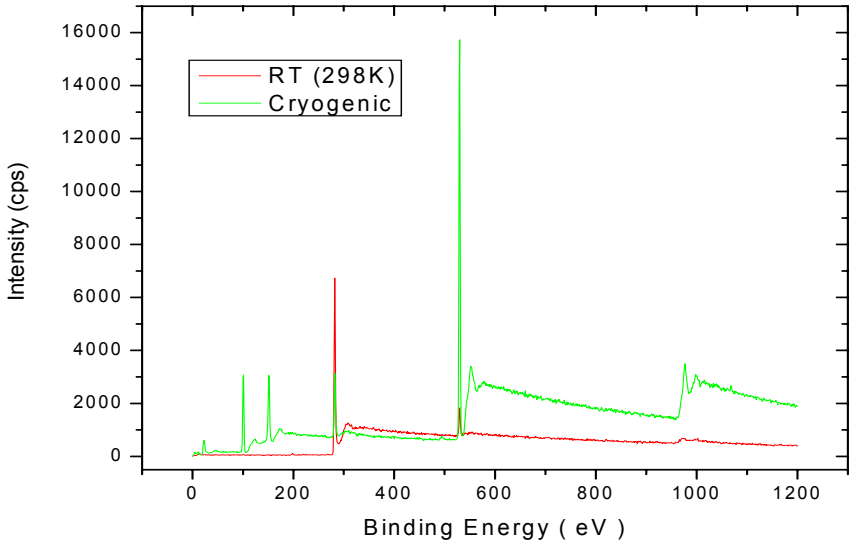

Fig. 4.5 XPS spectra for RT and Cryogenic (20K-100K) films.

4.3.4. X-ray photoelectron spectra (XPS)

Novel features in the present assembled nanostructure can be further elucidated by XPS characterization. It is found that cryogenic (20K-100K) films display very similar XPS spectra. A

comparison of the C1s binding energy range of 281-294 eV for RT (298K) and cryogenic (20-100K) films has been displayed in Fig. 3.5. The sp^3/sp^2 ratio can be obtained from a deconvolution of the C1s band (Merel et al. 1998, Diaz et al. 1996). In the RT film, this peak can be deconvolved into two Gaussian/Lorentzian profiles centered at 284.4 eV and 285.2 eV as shown in the inset. These peaks correspond to sp^2 C-C and sp^3 C-C bonds, respectively. We find that the concentration of sp^3 bonded atoms is 72 and 68% in RT and cryogenic films, respectively, coinciding with deconvolved Raman analysis (Hu et al. 2007a). This suggests that the sp^3 content is little affected by structure. We also find a band attributable to C-O at 286.5 eV in cryogenic films. To investigate this origin of this peak we have studied XPS spectra in a wider energy range (Fig. 4.5). These show a *Si2p* line at 100 eV in cryogenic films, together with a very strong O1s at 532.6 eV. From a fit to the peak area we find that the oxygen content in cryogenic films is about 17 times higher than that in RT films. The oxygen content is little affected by Ar-ion surface treatment, showing that cryogenic films react with oxygen to form C-O bonds. Since the sp^3/sp^2 ratio is nearly constant in these two types of films, this reactivity can be attributed to the submicron grain-assembled nanostructure of cryogenic films. Evidently, there are many dangling sp^2 bands on the surface of submicron grains, which enhances their affinity for oxygen. This property of cryogenic films suggests they may be potentially useful in gas sensor or biosensor applications.

4.3.5 Microbuckling and stress relaxation

Stress relief by film buckling is a common phenomenon in DLC films (Enke 1981, Nir 184, Matuda 1981, Iyer 1995) and has been observed in 77K films with thicknesses of ≈ 150 nm (Fig. 4. 6). Buckling and separation of films from the substrate initially occurs near the film edge after exposure to air and subsequently spreads into the center. This phenomenon is not observed in 298 and 573K films having similar thickness. In general, three types of buckling can be detected. Fig. 4. 6 (a) shows typical zigzag ridge lines with a turning angle of about 120^o while a sinusoidal pattern is seen in Fig. 4.6 (b). Fig. 4.6 (c) shows type of pattern in which sinusoidal structures originate from and/or end in some curved crack lines.

These structures can be attributed to the existence of a high intrinsic compressive stress, similar to that observed in hydrogenated amorphous carbon films (Enke 1981). The morphology of these stress relief patterns has been analyzed in terms of a linear theory of plate buckling (Nir 1984).

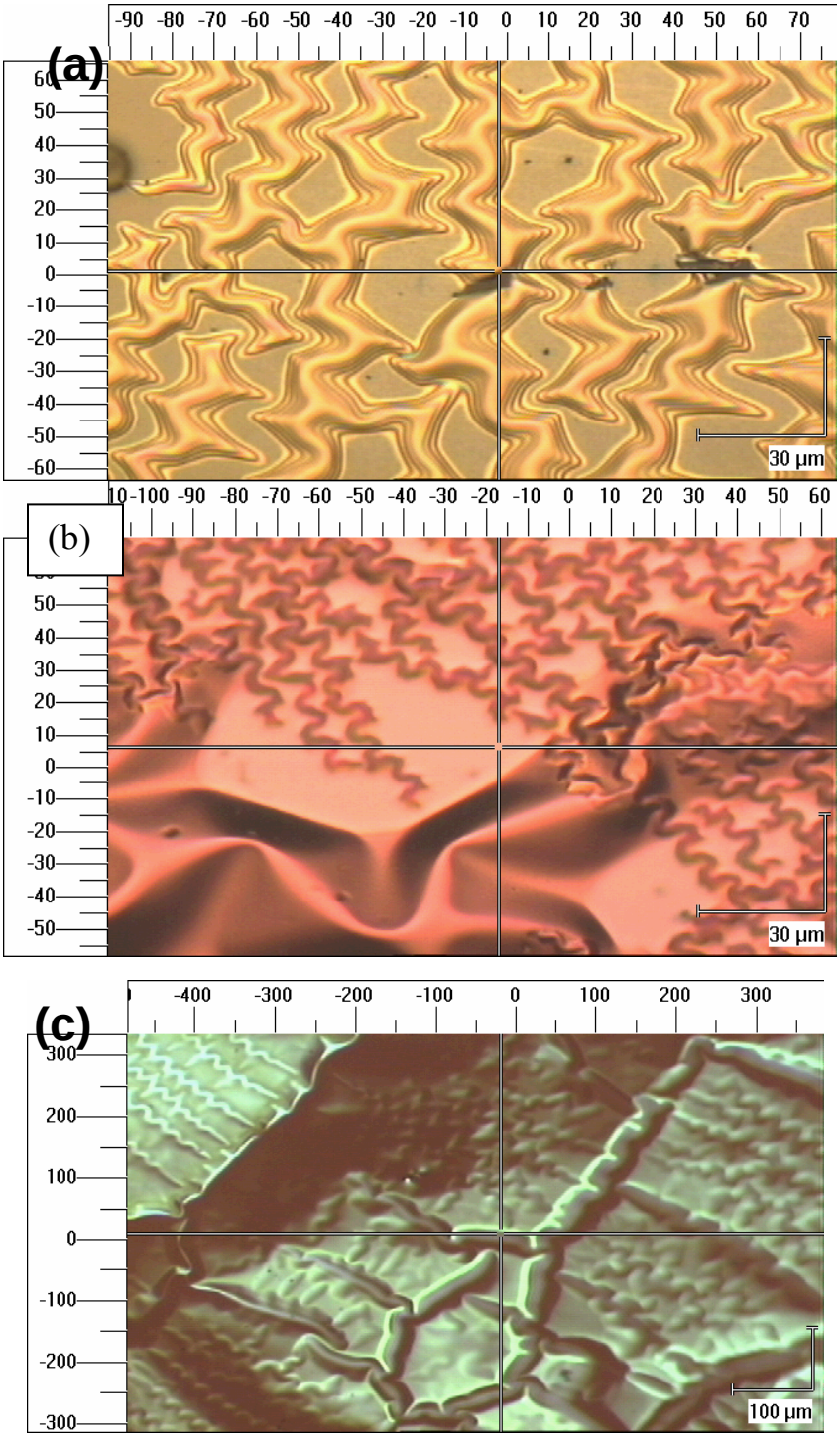

Fig. 4.6 Surface stress relief morphology of 77K films observed by optical microscopy. The focal point indicated by the cross lines.

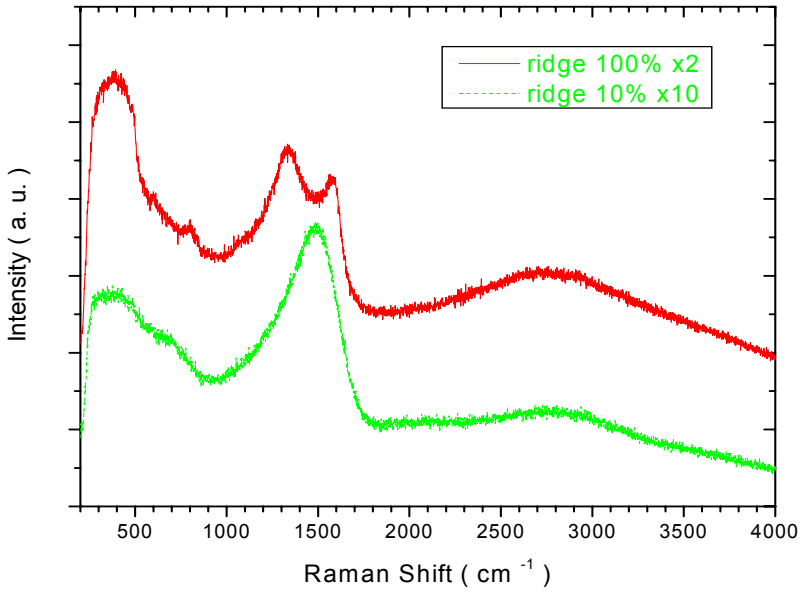

Fig. 4.7 Raman spectra focusing on the ridge of a 77K film at 100 and 10% laser power. The location of focus spot is shown in Fig. 4.6 (a).

Matuda *et al.* (1981) have calculated the residual internal stress in these structures as a function of film thickness. The elastic energy per area of wrinkles has been estimated by Iyer et al. (1995). These calculations suggest that stress relief patterns are correlated to film thickness and the adhesion energy of the film to the substrate (Iyer et al. 1995, Wei et al. 1999). In the present study, film buckling is found only in 77K films and is not seen in films of similar thickness, deposited on the same substrate at 298 and 598K. Fig. 4.7 shows Raman spectra at a point on the ridge shown in Fig. 4.6 (a). The top spectrum, obtained at full laser power (3 mW), shows the two characteristic peaks of microcrystalline graphite: a D peak at 1350 cm^{-1} and a G peak at 1550 cm^{-1}. This transformation is due to heating by the incident laser beam. By decreasing the laser power to 0.3 mW, the film is unaffected and the spectrum (lower curve in Fig. 4. 7) is the same as that obtained for points on the film that are in contact with the substrate. This indicates that the film in the ridge is completely peeled away from the substrate and that irradiation results a transformation from primarily sp^3 to sp^2 bonding at this location (Friedmann et al. 1996, Kalish et al. 1999, Ferrari and Robertson 1999).

The origin of microbuckling is further investigated by the deposition of DLC films on HOPG substrate at 77K. The SEM micrographs of these films are demonstrated in Fig. 4.8. The coexistance of microbuckling (in x500 image) and nanoscaled defects (in x50K image) is clearly observed. These nanodefects locate in the valley areas between microbucking ridges (black lines in x500 image). These nanodefects are similar to nanograins which are embedded in the matrix. This indicates the relationship between the graphitization of submicron grains and microbuckling: both of them are originated from the relaxation of internal stress.

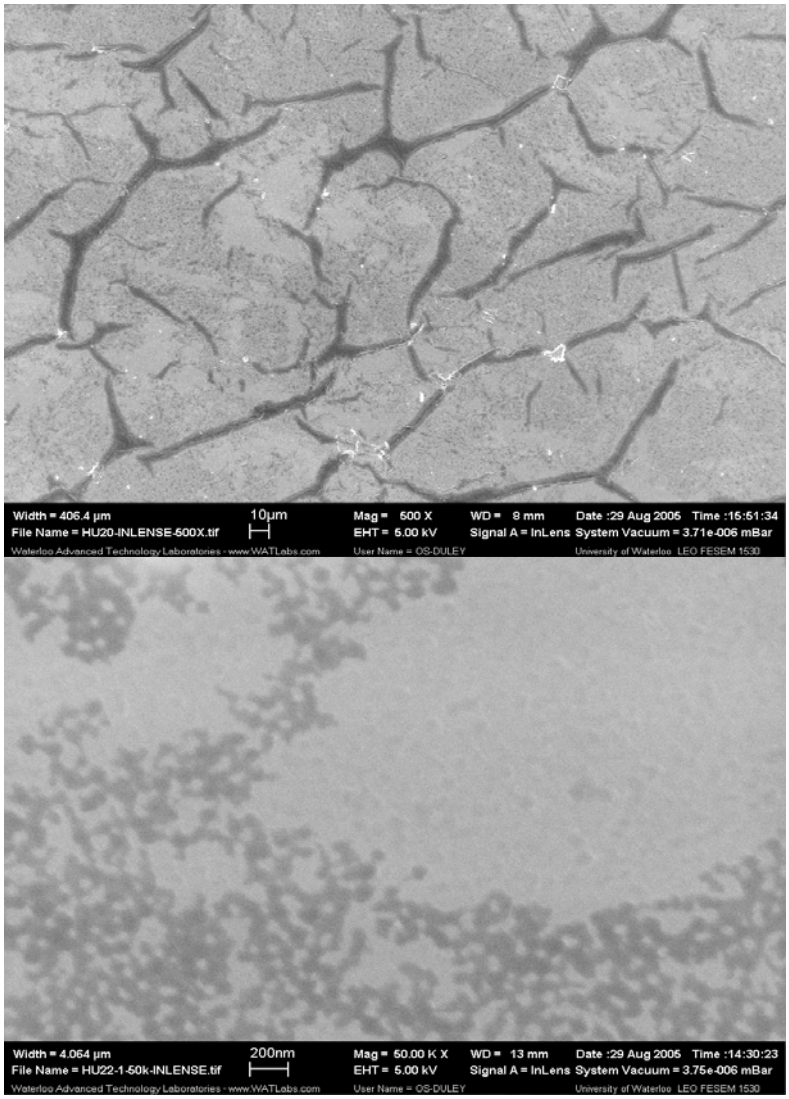

Fig. 4.8 SEM images of DLC films deposited on HOPG at 77K.

4.4. Conclusions

Although we mention partial characterization of nanostructured *ta-C* films deposited in 77K in Chapter 3, the detailed re;lationship between embedded submicrometer grains and the relaxation of internal stress is not unveiled there. In this chapter we focus this issue and investigate in a wide deposition temperature range. Furthermore, we have combined nanostructure characterization with AFM and several spectroscopic methods, which allow us to unveil the origin of submicrometer grains embedded in *ta-C* films.

In summary, the nanostructure of *ta-C* films grown at various croygenic temperatures has been investigated. It is found that a submicron-sized grain embedded matrix structure occurs in cryogenic films deposited between 20 and 100K. These submicron grains have lower hardness than that of the surrounding matrix. Resonant Raman spectra show that sp^2 bonded C atoms are concentrated within these grains. However, the overall fraction of sp^3 bonded atoms is as high as 68%. XPS spectra show that these films display an enhanced affinity for oxygen. Some possible applications of grain-assembled nanostructured *ta-C* cryogenic films are suggested. Microbuckling has also been discussed. Similarities in nanostructures indicates that both the graphitization of submicron grains and microbuckling arise from the relaxation of internal stress.

Chapter V

Nanostructure and sp/sp^2 clustering of tetrahedral amorphous carbon films grown by femtosecond laser deposition

5.1 Introduction

Pulsed laser vaporization/ablation has been successfully used to deposit advanced carbon materials including diamond-like amorphous carbon (DLC) films, carbon nanotubes and fullerenes (Voevodin and Donley 1996, Scott et al. 2001, Guo et al. 1991). Diamond-like carbon films with a dominant fraction of sp^3-bonded carbon containing embedded sp^2-bonded clusters are referred to as tetrahedral amorphous carbon (ta-C). The growth mechanism for these materials involves substrate-induced quenching of energetic ions generated during laser ablation followed by sub-implantation. The formation of sp^3-bonded carbon is attributed to the compressive internal stress induced by the plastic deformation of the surface as a result of ion bombardment (McKenzie et al. 1991, Robertson 1993, Cuomo et al. 1991). It has been found that kinetic ion energies in this process range from 20 to 100 eV (McKenzie et al. 1991, Robertson 1993, Cuomo et al. 1991). High ion energy induces annealing and appears to convert sp^3-bonded carbon to sp^2 bonded species.

With the availability of solid state femtosecond laser sources having pulse energy in the mJ range, the deposition of diamond-like carbon films (fs-DLC) has been extensively studied (Qian et al. 1999, Okoshi et al. 1999, Yao et al. 2000, Loir et al. 2003). Because the laser pulse width is so short, excited electrons cannot transfer their energy to the lattice. Thus ablation is enhanced relative to that produced by nanosecond laser pulses (Gamaly et al. 2002). In addition, carbon ion energies can be as high as 0.5-2 keV during fs ablation (Qian et al. 1999, Okoshi et al. 1999, Yao et al. 2000, Loir et al. 2003), almost one order of larger than the 30 eV energies obtained during ablation with nanosecond (ns) pulses (Duley 1996). The sp^3-bonded carbon content is then typically 20-60% in ta-C films deposited with fs pulses (Cuomo et al. 1991, Banks et al. 1999, Qian et al. 1999, Okoshi et al. 1999, Yao et al. 2000, Loir et al. 2003). Despite this change in composition, higher microhardness is found in fs-DLC in comparison with ns-DLC (Yao et al. 2000). In addition, C1s K-edge X-ray absorption fine structure (NEXAFS) spectra of fs-DLC films display several unidentified peaks (Ravagnan et al. 2006). These observations show that there are many unresolved questions concerning the nature of electronic bonding states and molecular structure in fs-DLC materials.

Linear carbon structures containing *sp* bonds, either as alternating triple and single bonds (polyynes) or with conjugated double bonds (polycumulenes), are important molecular components because they represent the building block and precursors that can be used to form

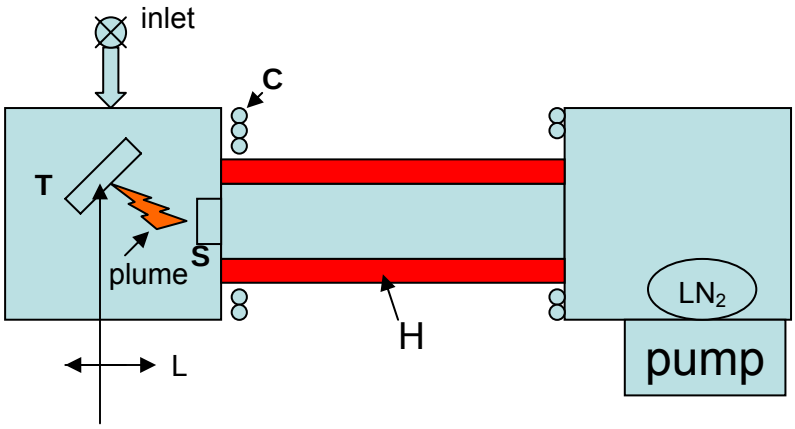

Fig. 5.1 Schematic of the vacuum furnace used for deposition at high temperatures. Symbols: (L) lens, (H) heater, (T) graphite target, (S) substrate, (C) cooling water pipe, (LN2) liquid nitrogen trap

fullerenes (Shvartsburg et al. 2000) and carbon nanotubes (Kiang and Goddard III 1996). These components are also promising as linear molecular conductors. Although natural *sp*-bonded carbon chains have been identified in carbon vapor at a temperature higher than 2600K (Pitzer 1959), in interstellar materials (Duley 1996) and in some biological species (Heimann et al. 1999), the synthesis of sp-coordinated all-carbon skeletons (carbynes) remains a challenging topic in carbon science. Theoretical calculations suggest that polyynes are more stable than polycumulenes (Rice et al. 1986). Both species are, however, highly reactive to oxygen and exhibit a strong tendency to form interchain cross-links leading to graphitization (Kavan 1997). Recently, Ravagnan et al. have fabricated carbyne-rich carbon films by deposition of larger carbon clusters containing up to ≈ 600 atoms in ultra-high vacuum (UHV) (Ravagnan et al. 2002). Such carbon films have been in-situ characterized as sp^2-dominated amorphous carbon with a sp/sp^2 ratio of 10-25% (Ravagnan et al. 2002&2006, D'Urso et al. 2006). Unfortunately, the concentration of *sp*-bonded species strongly decreases when an sp^2-dominated carbyne-like film is exposed to gases like H_2, He, N_2 and dry air or after annealing at temperatures up to 200°C (Casari et al. 2004). Hence, a method of creating stable carbon films having a high concentration of *sp*-chains for ex-situ studies is highly desired.

This paper discusses the microstructure and optical properties of fs-DLC films in more detail and the presence of both *sp* and sp^2 bonded carbon in an sp^3 bonded matrix has been confirmed. Nanocrystalline diamond is also evident in fs-DLC deposited at room temperature. The present experiments and analysis yield additional insight into the structure and composition of novel carbon systems fabricated by fs laser deposition.

5.2 Experimental setup

Diamond-like amorphous carbon films were deposited on silicon and quartz substrates by ablation of graphite using 120 fs pulses from an amplified Ti:sapphire laser operating at 800 nm. A base pressure of 2.67×10^{-5} Pa was obtained in a high vacuum chamber evacuated by a turbo-molecular pump with a liquid nitrogen trap. During deposition the pressure typically increased to 5×10^{-7} Torr (1Torr = 133.33Pa). A Ti:sapphire laser system (λ=800 nm, pulse duration τ=120 fs, repetition frequency 500Hz, pulse energy 1mJ, incidence angle 45^{o}) was employed to ablate high purity pyrolytic graphite (99.99%). The laser beam was focused into a 50 μm diameter spot using a quartz lens with a focal length of 90 mm. The peak laser intensity at the focus was 4.5×10^{14} W/cm^2. The design of the low temperature (77 – 273K) deposition chamber has been reported elsewhere (Hu 2006). Deposition at 293 – 873K was carried out in a separate high vacuum system attached to a furnace (Fig. 5. 1). The pressure and composition of a buffer gas was adjusted to generate different deposition conditions.

Film thickness was controlled by measuring the UV absorption of the sample during deposition. The final thickness was measured by a profilometer (AMBios XP-2) after deposition. Microstructure was characterized with scanning electron microscope equipped with a LaB_6 field emission gun. UV Raman spectra were obtained with a Kimmon 5161R-GS Raman spectrometer using He-Cd laser radiation at 325 nm (UV). To avoid excessive heating of the carbon sample, the laser power was reduced to 4.5 mW. Surface enhanced Raman spectra (SERS) were measured with a Renishaw micro-Raman spectrometer. Spectra were excited with 0.3- 3 mW of He-Ne laser radiation at a wavelength of 632 nm. The resolution was 1 cm^{-1} in both spectrometers. X-ray photoelectron spectrum (XPS) measurements were carried out using a multi-technique ultra-high vacuum imaging XPS microprobe spectrometer (Thermo VG Scientific ESCALab 250) with a monochromatic *Al* K_α 1486.6 eV X-ray source. The spectrometer was calibrated by Au $4f_{7/2}$ (binding energy of 84.0 eV with respect to the Fermi level). The chamber vacuum pressure was maintained below 2×10^{-10} Torr (1Torr = 133.33Pa). The spot size for the XPS analysis was approximately 0.5 x 1.0 mm.

5.3 Results and Discussion

5.3.1 Nanostructure and optical energy gap

Fig.5.2 shows the morphologies of fs-DLC films of various thicknesses deposited at temperatures between 77 and 573K in vacuum and in the presence of He. We find that nanobuckling often occurs in films deposited at 77K (Fig 5.2a, b). In 100 nm thick films, this takes the form of quasi-periodic, discrete point-like excursions extending over widths of 50-200 nm. (Fig.5.2a). This changes to a regular structure of ripples having a modulation period of 30-50 nm as the film thickness increases to 600 nm (Fig. 5.2b). The origin of this nanobuckling which can be attributed to the combined effect of reduced internal stress and enhanced Si-C binding between film and the substrate is discussed in the next chapter. It is worth noting that the tendency for nanobuckling does not depend on the presence of He gas. This demonstrates that He has little effect on the growth characteristics of these cryogenic films.

SEM micrographs of fs-DLC films deposited at room temperature are shown in Figs 5.2c (100 nm) and 5.2d (400 nm). It is apparent that very thin films prepared under these conditions are atomically smooth and have little structure, while thicker films are assembled from clusters having diameters between 20 and 100 nm. These results are consistent with other studies (Banks et al. 1999), in which nanostructure appears as the film thickness increases over 300 nm. It is important to point out that ns-DLC films deposited at room temperature are not nano-assembled even at thicknesses in excess of 400 nm (Hu et al. 2007a). This indicates that nanostructure seems to be a special character of fs-DLC.

Figs.5.2e and 5.2f show the morphologies of 400 nm thick films deposited at 573K in vacuum and in the presence of 100 millitorr of He, respectively. These films exhibit no nano-structure when deposited in vacuum but a nano-texture is found after deposition in He. This indicates that a higher substrate temperature enhances the mobility of deposited species suppressing the formation of structure (Wei et al. 2003). The role of a buffer gas such as He during ablation has been shown to promote the formation of carbon clusters (Hu et al. 2006). These clusters collide with the substrate during condensation and become incorporated in the resulting film (Fig 5.2f).

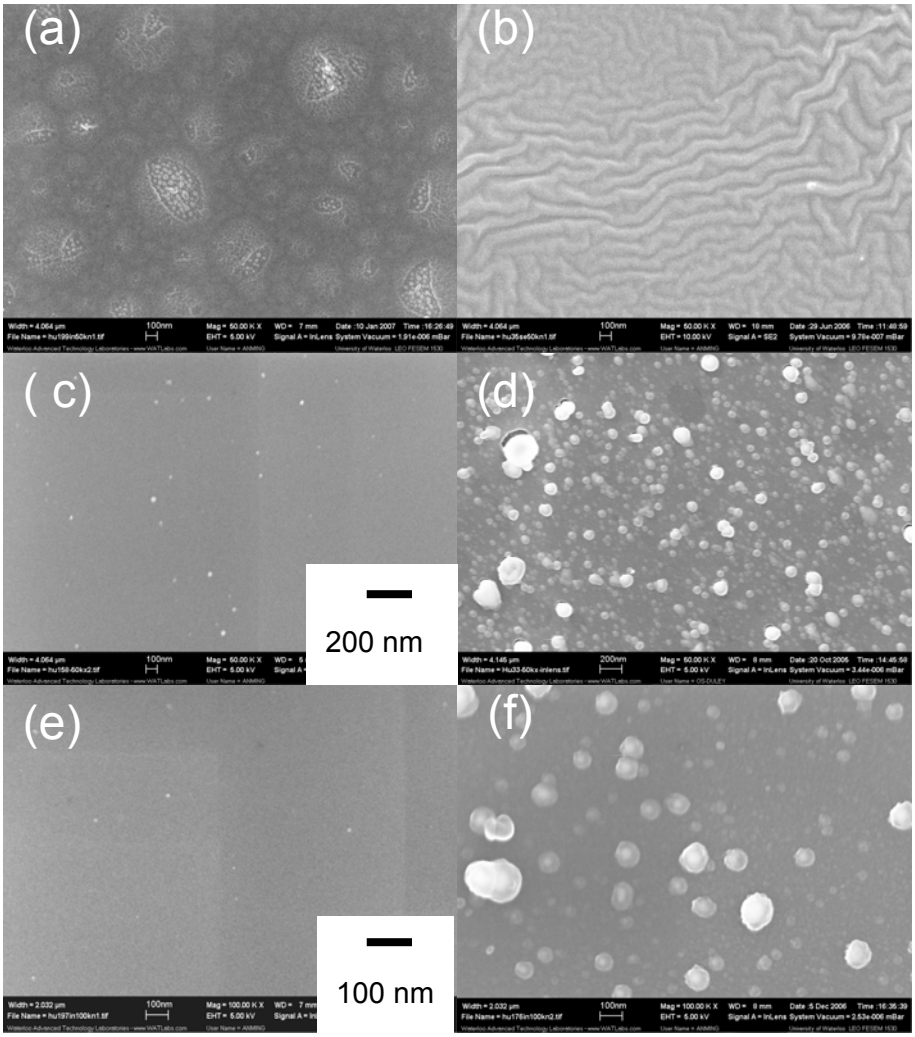

Fig. 5.2 Typical SEM images for fs-DLC films of various thicknesses deposited at representative temperatures: (a) a 200 nm thick film deposited at 77K; (b) a 600 nm thick film deposited at 77K; (c) a 100 nm thick film deposited at room temperature (RT=298K), (d) a 400nm thick film at 298K; (e) a 100 nm thick film deposited at 573K in He; (f) a 400 nm film deposited at 573K in He. Note that (a-d) have the same magnification as do (e) and (f).

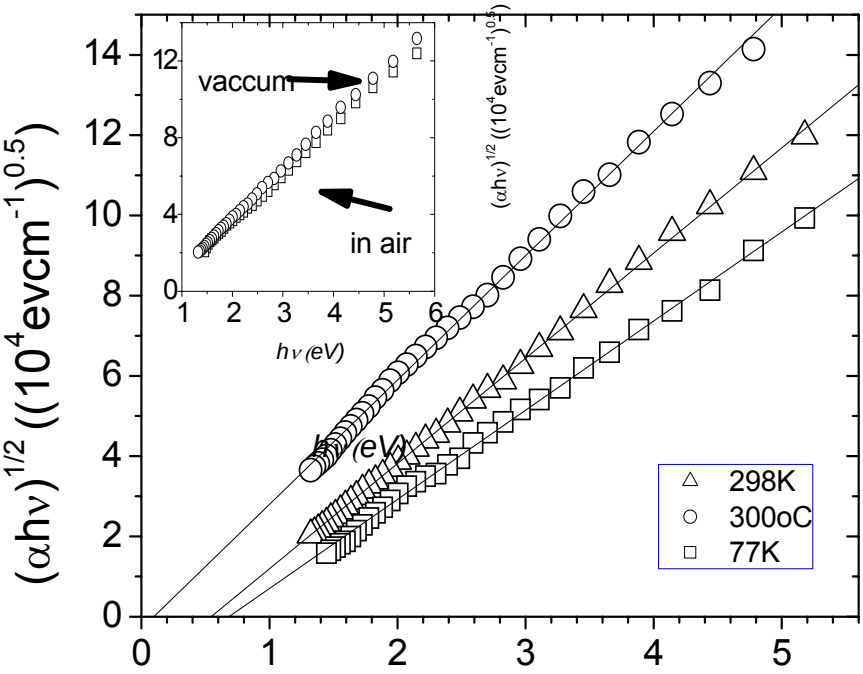

Fig. 5.3 Tauc plot of $(\alpha h\nu)^{1/2}$ as a function of photon energy hν for fs-DLC deposited at different temperatures. Solid line is a linear fit to data. Inset: a room-temperature (RT) sample measured in-situ (vaccum) and immediately after exposure to air.

Fig.5.3 shows a Tauc plot calculated from in-situ UV/VIS spectra for fs-DLC at three typical temperatures and a film thickness of ≈ 500 nm. The linear fit yields an optical energy gap, E_g, of 0.5 eV for RT films, 0.7 eV for 77K films and ≈ 0 eV for films deposited at 573K. Since E_g is not only dependent on the concentration of sp^3 bonded species, but is also governed by sp^2 clustering, localized chemical states and the presence of defects (Robertson 2002), these low values of E_g do not necessarily indicate a low sp^3 concentration. The inset in Fig. 5.3 shows that E_g increases slightly after exposure to air. This can be attributed to a reduction in the concentration of carbynoid species in the film after exposure to air (Casari et al. 2004). A reduction in the concentration of defects can be ruled out since there is no difference in E_g of samples in vacuum after 2 hours. A similar increase in E_g on exposure to air is also observed in films deposited at 77 and 573K.

5.3.2 VIS/UV Raman characterization

Fig. 5.4&5 show VIS-Raman spectra for fs-DLC deposited on quartz excited at 632 nm. Three major bands can be identified in this spectrum. A broad band, at 1100 -1800 cm^{-1}, corresponds to a combination of the breathing (D) and stretching (G) modes associated with Raman scattering from sp^2 sites (Ferrari 2000). Shown in the inset of Fig. 5.4 a small shoulder at 2100 cm^{-1} in RT and 77K films, which can be attributed to linear *sp*-bonded chains (Kavan 1997, Ravagnan et al. 2002 & 2004). The shoulder at 1300 cm^{-1} indicates an increase in the concentration of sp^2 bonded carbon in 573K films. As noted previously, the sp^2/sp^3 ratio in tetrahedral carbon can be evaluated by deconvolution of the D/G band using a Breit-Wigner-Fano (BWF) lineshape (Ferrari and Robertson 2000, Prawer et al. 1996). This analysis is shown in the inset in Fig.5.5. At 632 nm (1.97 eV) excitation, the G peak occurs at 1530 cm^{-1} and has a width of 225 cm^{-1} (Shi et al. 2001, Hu et al. 2006). The best fit to our Raman spectra yields a coupling factor of 3.53 indicating a sp^3 fraction of 55% and a deposition energy of 2 KeV, approximately in agreement with the results of Qian et al. (1999). Raman spectra of films produced at 77 and 573K have not deconvolved in this way because the related scale is likely not valid for films

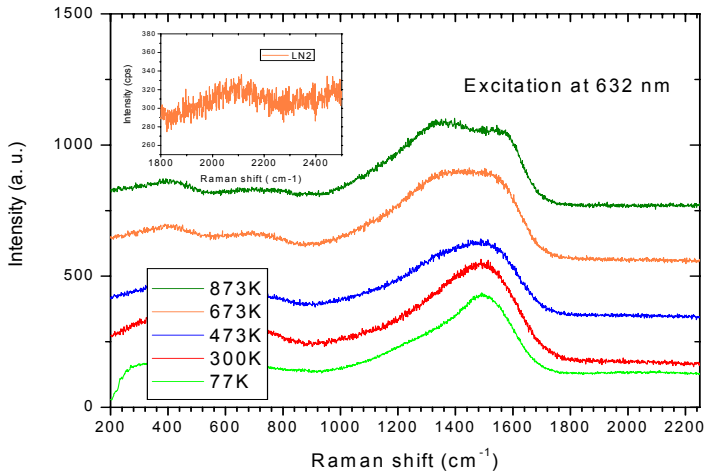

Fig. 5.4 Raman spectra of fs-DLC films deposited at various temperatures (elevated temperatures for curves from bottom to top) on Si wafers. The Raman excitation wavelength is 632 nm. Inset: the detailed Raman feature around 2100 cm^{-1} for T=77K.

deposited at these temperatures. However, Fig. 5.4 shows that sp^2-bonded amorphous carbon increasing with elevated substrate temperatures.

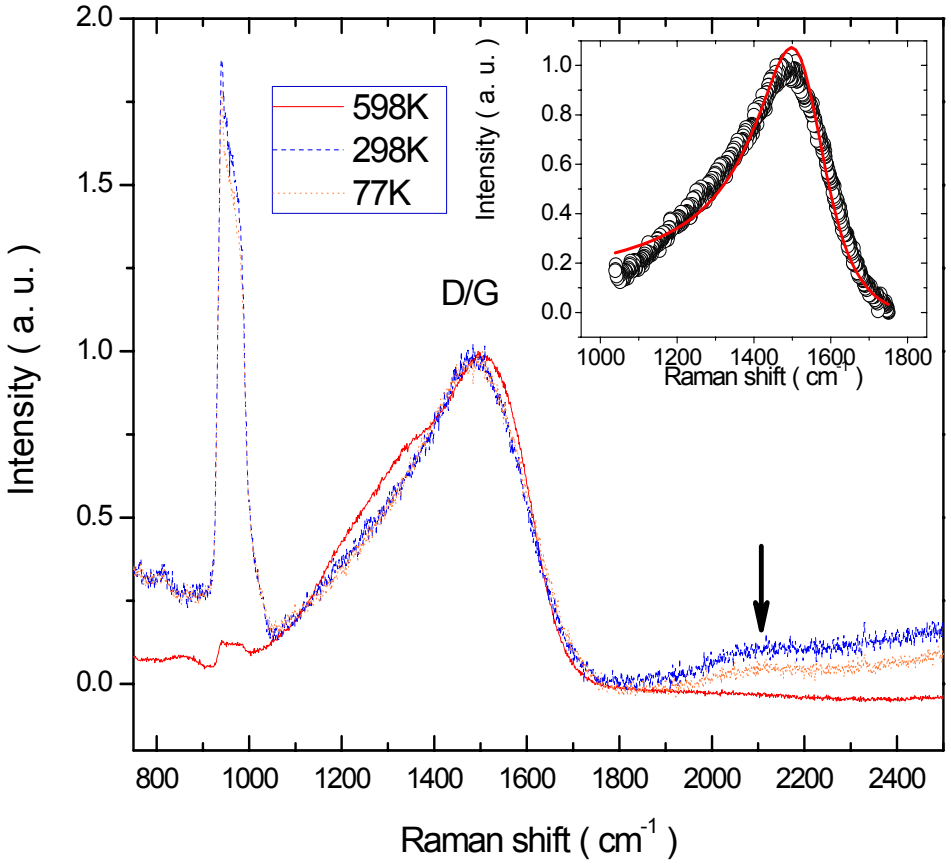

Fig. 5.5 Visual Raman spectra for fs-DLC samples deposited on SiO_2 at three deposition temperatures with an excitation at 632 nm (He-Ne laser). The arrow points to an additional band indicating Raman scattering from *sp* linearly bonded carbon chains. Inset: quantitative analysis of the Raman spectrum of a RT=298K sample. The solid line corresponds to a fit using a BWF lineshape.

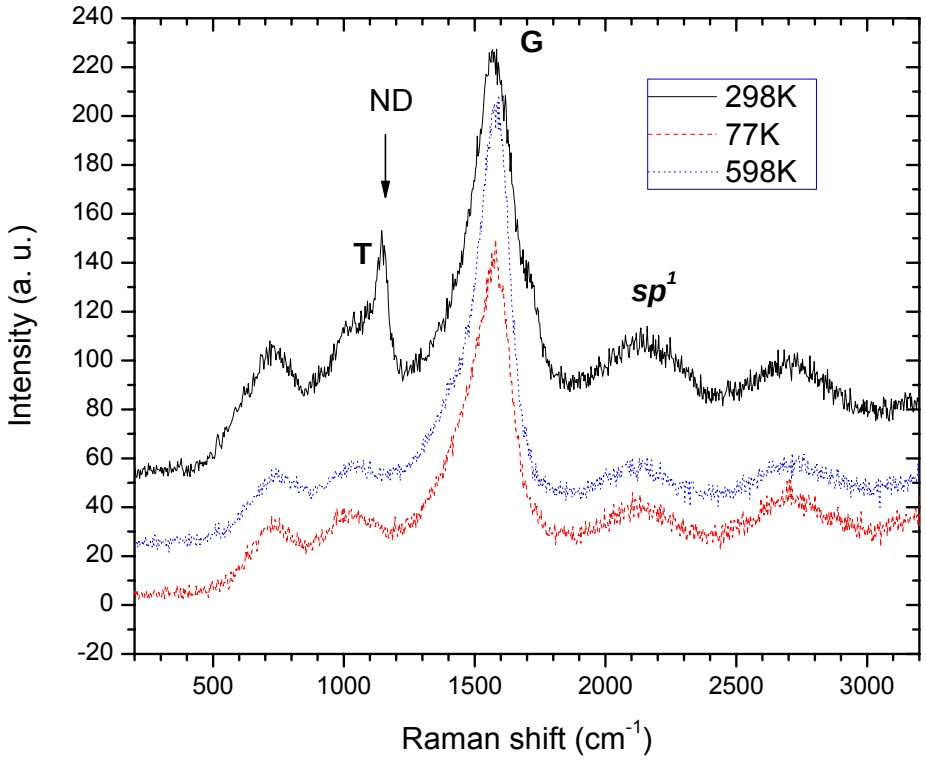

Fig. 5.6 UV Raman spectra for fs-DLC samples deposited at three temperatures with an excitation at 325 nm (Cd-He laser). G and *sp* stand for the vibration of graphitic G mode (sp^2) and the peak from *sp*-bonded carbon chains (carbyne). The broad band "T" is attributed to sp^3 bonds. The arrow points to a narrow peak from nanodiamond.

Fig. 5.6 illustrates UV-Raman spectra for three representative samples with an excitation at 325 nm (3.8 eV). In these spectra, the band near 800 cm^{-1} arises from the substrate (Hu et al. 2006) and the band centered at 2700 cm^{-1} is the second order of the G mode. The T-band centered at 1060 cm^{-1} can be assigned to sp^3 bonded species and does not appear with visual excitation (Ferrari and Robertson 2001). It is well-known that in ta-C there are mainly two kinds of bonds after the hybridization of the outer shell $2s^2$ and $2p^2$ electrons: a σ bond is formed by the head-to-head overlap of two *sp* orbits while a π bond comes from the shoulder-to-shoulder overlap of two *sp* orbits. It costs different energy to excite these two bonds: the $\pi \rightarrow \pi^*$ gap of sp^2 bonded species is about 2 eV while the $\sigma \rightarrow \sigma^*$ gap of sp^3 atoms is ≈ 5.5 eV, so that UV excitation primarily couples to the $\sigma \rightarrow \sigma^*$

transition. It should be noted that all three samples indicate the presence of sp^3 coordinated carbon. In addition, the Raman scattering cross-section of *sp* bonds increases at shorter excitation wavelengths (D'Urso et al. 2006), accounting for the enhancement of the 2100 cm^{-1} peak of *sp* chains in UV-Raman spectra. All samples show this feature. The RT spectrum of fs-DLC exhibits a narrow peak at 1140 cm^{-1} that can be identified with nanocrystalline diamond (Loir et al. 2003, Sharda et al. 2001). It is also apparent that the D band is almost absent with UV excitation and the G band is much narrower than that in VIS-Raman spectra. From the intensity ratio I_T/I_G of the T and G bands we can deduce the concentration of sp^3-bonded carbon (Shi et al. 2001). This analysis is summarized in Table 5.1. It is evident that the sp^3 concentration in RT fs-DLC films is consistent with that obtained from deconvolution of the VIS-Raman spectra. However, in both 573 and 77K films the concentration of sp^3-bonded carbon is quite small. This may account for the low value of E_g in films deposited at 573K films. It is important to mention that the concentration of *sp*-bonded carbon chains is highest in films deposited at 77K films, and slightly decreases at higher deposition temperatures.

Table 5.1. Summary of characteristic parameters for diamond-like carbon films deposited by fs pulsed laser deposition

Substrate Temperature	Optical energy gap (eV)	I_T/I_G	sp^3	I_{sp1}/I_G	C1s core-level energy (eV)
RT	0.5	0.31	55%	0.23	283.5
77K	0.7	0.23	27%	0.255	283.8
573K	0	0.20	20%	0.19	283.7

5.3.3 XPS spectra

Fig. 5.7 shows C1s core-level energy XPS spectra for three fs-DLC films deposited on Si at different temperatures. Measured values of the C1s binding energy are 284.4 eV in graphite, 285.2 eV in diamond and 284.6-285 eV in ns-DLC (Diaz 1996, Haerle 2001). These values are much higher than those measured in fs-DLC films. It is well known that the surface charging can seriously influence

peak position, especially in dielectric or non-conducting samples, but this is not important here because the *Si2p* core-level line in all our samples occurs at the standard value of 100.4 eV. Thus the chemical shift of the C1s core-level shown in Fig.5.6 is a true effect. It is also notable that the C1s line in the least conducting 77K films appears at 283.8 eV, the highest energy among the three samples. Moreover, the full width at half maximum (FWHM) of the peak in fs-DLC is about 1.6 -1.8 eV, which is much larger than that of graphite (FWHM 1.1 eV) or diamond (FWHM 1.25 eV) (Diaz et al. 1996, Haerle et al. 2001). This suggests that the C1s peak in fs-DLC

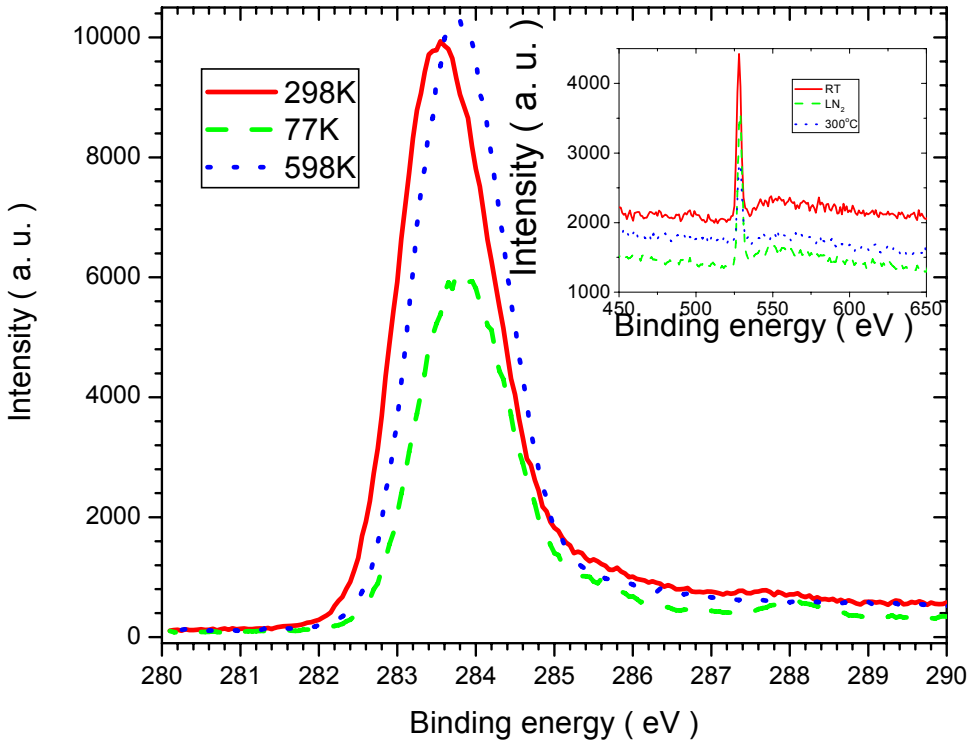

Fig. 5.7 XPS C1s core-level spectra for three fs-DLC films deposited at various temperatures. Inset is the survey for the binding energy for the identical three samples ranged from 450-650 eV.

arises from the hybridization of different carbon bonds. It has been found that the transfer of 0.1 electron per C atom to iodine in iodine-doped polyacetylene shifts the C1s energy to 283.8 eV (Salaneck 1980). However, in the present composition there is no similar oxidant that could result in

electron transfer, although it is possible that aromatic sp^2 clusters could have significant electron affinity.

An additional peak in 77K films is found at 288.4 eV, and can be attributed to C-O bonds. The survey XPS spectra shown in the inset display the O1s line at 530.8 eV. Surface cleaning by Ar ion bombardment effectively weakens both C-O bond and O1s peaks, which indicates these species are the consequence of surface oxidization. However, surface Ar ion etching does not influence the chemical shift of C1s core-level of fs-DLC films. Recently, Danno et al. have also reported that the C1s core level appears at 282.6 eV in carbyne-like carbon films (Danno et al. 2004). As a result, it can be concluded that the low energy of C1s peaks in fs-DLC (283.5 eV for RT and 283.7 eV for 573K films) arise from the presence of *sp*-bonded carbon chains.

5.4 Disccusion

Films deposited at 77K exhibit distinguishable microstructure and optical properties from those deposited at higher temperatures. These properties can be understood on the basis of growth by sub-implantation (Robertson 1993). The observation of surface buckling in these materials originates from the relaxation of internal stress. Low internal compressive stress in fs-DLC films has been reported by other groups (Banks et al. 1999, Loir et al. 2003). This stress relaxation arises when films are annealed by keV carbon ions, in a process similar to the stress reduction that occurs in high temperature annealing of ns-DLC films (Ferrari and Robertson 1999). It is significant that nano-buckling is not found in ns-DLC films. Because of this property, involving a growth mechanism associated with stress relaxation, much thicker films can be fabricated. In our current study, we have grown films having thicknesses of several micrometers that do not exhibit surface buckling at room temperature. In contract, ns-PLD can typically deposit DLC films with thicknesses of only a few hundred nanometers (Hu et al. 2007a). We find, however, that stress relaxation may result in a low concentration of sp^3-bonded species. In films deposited at 77K, the high kinetic energy of incident C ions also generates a higher concentration of amorphous carbon than in films deposited at RT. Meanwhile, defects in 77K films can be reduced due to localized heating activated by high energy ions. As a result, 77K films display a higher optical energy gap than RT films. In films deposited at 573K films, the phase transition from sp^3 to sp^2 at a deposition temperature higher than 523K should also be considered (Robertson 2002, Voevodin et al. 1996).

Nanocrystalline diamond found in RT films may account for a higher microhardness of fs-DLC than ns-DLC even with a mediate sp^3-bonded carbon concentration in fs-DLC (Loir et al. 2003). These spherical nanodiamonds are also evident in the laser irradiated induced graphite-diamond phase transition on graphite target (Bonelli et al. 1999). We expect these diamond particles in fs-DLC are directly removed by surface plasmas repulsion of Coulomb explosion. Further investigation of fs laser-graphite interaction is worth to elucidating this point.

sp-bonded carbon is evident in all fs-DLC films. It is important to note that the UV-Raman and XPS experiments were carried out after exposing films to air for over one month. This indicates that the stability of *sp*-bonded species in tetrahedral carbon films is significantly improved in comparison with amorphous sp^2-bonded carbon films (Ravagnan et al. 2002 & 2006, D'Urso et al. 2006, Casari et al. 2004). In those experiments, *sp* chains had to be studied in-situ in high vacuum due to the high reactivity of these groups to oxygen. After exposure to dry air for 0.6 hours, I_T/I_G ratio of Raman intensity with 532 nm excitation reduces from 40% to 3.6 % in amorphous sp^2-bonded carbon films (Casari et al. 2004). However, for one-month exposure to air, this ratio with 325 nm excitation for the present composition is still as high as 19%-26% for different deposition temperatures. Followed the model of D'Urso et al. (2006), one can compare these two Raman ratios at different excitation wavelengths from the *sp* fraction (relative to sp^2 bonded carbon), X_T/X_G, according to $X_T/X_G=1/R$ I_T/I_G, where R is the sp/sp^2 cross section ratio. With R=0.5 at 532 nm and R=2.5 at 325 nm, I_T/I_G of 18% is obtained for sp^2-bonded carbon films after exposing to air for only half hour. This may indicate that the oxidization and/or interchain cross-linking of *sp* chains in ta-C is much more slower than that in a sp^2 coordinated carbon film.

The reason for the appearance of enhanced stability of *sp*-chains in the present tetrahedral carbon samples is unclear, but one possibility is that these chains are intercalated by sp^2 aromatic clusters, similar to stabilizing by alkali metal inclusions (Heimann et al. 1999). However, the structure of *sp*-bonded carbon chains in ta-C and the length of these chains are still to be determined.

5.5 Conclusions

Microstructure and electronic bonding of fs-DLC have been investigated by combining SEM observation, UV/NIR spectroscopy, UV/VIS Raman and XPS spectra. The presence of nanocrystalline diamond and *sp*-bonded carbon chains in these materials is significant. It is found that

the stability of *sp*-bonded chains is greatly enhanced in tetrahedral carbon films. This may lead to the fabrication of stable carbyne-rich carbon films.

By comparison to ns-PLD, fs-PLD generates much energentic carbon ions, which allows us to deposite carbon films with novel species, such as, nanodiamonds, sp-bonded carbon. These novel species are interesting for material science and promising for applications, through surface bindings.

Chapter VI

Molecular structure, SERS spectra and nanobuckling in fs-DLC

6.1 Introduction

In Chapter V it has been shown that the concentration of *sp* chains in tetrahedral (sp^3) carbon is remarkably enhanced by replacing nanosecond pulse laser deposition with fs pulse deposition. However, a comparative study of these two types of material has not yet been carried out. Furthermore, the concentration of individual carbon binding states, i.e. *sp*, sp^2 and sp^3 bonded carbon in fs-DLC, are not quantitatively characterized. Hence, a thorough study combining various spectroscopic methods is necessary. This study will reveal the co-existence of sp^2 clusters and *sp* chains in the sp^3-bonded matrix. To elucidate this structure, high resolution spectroscopic observations are required.

Surface enhanced Raman spectroscopy (SERS) is a highly sensitive tool that can be used to investigate molecule structure, particularly in interfacial systems (Kneipp et al. 1997, Nie et al. 1997). The enhancement of Raman cross-sections in SERS is can be attributed to the excitation of a surface plasmon resonance in metal nanoparticles as well as to local mixing of molecular and metal energy levels leading to a phenomenon similar to that occurring in the resonance Raman effect (Creighton et al. 1978, Lombardi et al. 1984). SERS spectra have been previously used to identify vibrational modes and bond structures in CVD diamond and amorphous carbon films, but this technique has not yet been utilized in a detailed characterization of carbon films prepared by fs ablation (Roy et al. 2000, Kudelski and Pettinger 2000).

There have been several studies of diamond-like carbon films deposited using fs laser deposition (Banks et al. 1999, Qian et al. 1999). Higher deposition rates are obtained with fs laser sources (fs-DLC) than with nanosecond pulsed lasers (ns-DLC). In addition, carbon ion energies can be as high as 0.5-2 keV in fs ablation, some 1-2 orders of magnitude larger than the 10-100 eV energy found during ablation with ns pulses (Merkulov et al. 1998, Cuomo et al. 1991, Duley 1996). High ion energy can give rise to a conversion of sp^3-bonded species into graphitic components in fs-DLC with a resultant decrease in the concentration of the diamond phase in these materials. Electron energy loss spectroscopy (EELS) (Banks et al. 1999, Qian et al. 1999) has shown that the sp^3 concentration in these materials may be as low as 40%-55%. This does not imply that the remaining component can

be exclusively associated with sp^2 bonded carbon as a variety of *sp* bonded species are also possible. Analysis of this phase in fs-DLC is the subject of this chapter. It is found that both *sp* and sp^2 bonded carbon chains are present in addition to sp^3 bonded species in fs-DLC, but the same bonding environment is not present in ns-DLC films. The relative concentration of these components has been obtained from Raman spectra of fs-DLC.

The role of internal stress on buckling and delamination of thin films deposited on substrates has been the subject of much interest because of the importance of thin films in industrial products. For example, buckling without delamination of thin metallic films deposited on compliant elastomer substrates can be used to create optical sensors on deformable devices (Bowden et al. 1998, Lacour et al. 2003). In another application, enhanced field emission has been observed in partially detached diamond-like carbon (DLC) films (Thaigen et al. 2001). It is well-known that DLC is an amorphous material in which nano-scale sp^2-bonded carbon clusters are embedded in a sp^3-coordinated carbon matrix (Hu et al. 2007a, Hu et al. 2006a). High internal compressive stresses have been found to be generated in DLC by the surface implantation of energetic carbon ions during deposition (Mckenzie et al. 1991). Relief of this internal stress involves buckling and the localized separation of the film from the substrate (Nir and Emory 1984, Iyer et al. 1995).

On the other hand, DLC films deposited using femtosecond pulsed laser ablation (fs-DLC) exhibit low stress despite the fact that carbon ion energies are often in the keV range (Banks et al. 1999, Qian et al. 1999). Low compressive stress in these materials is evidently due to the annealing during high energy ion impact (Garrelie et al. 2003). This effect is not observed in DLC films deposited using nanosecond laser ablation (ns-DLC), where the ion energy is ≤ 10 eV. This difference may be due, in part, to the relatively low fraction of sp^3-bonded carbon in fs-DLC deposited at room temperature (0.4 - 0.6) compared to that in ns-DLC (≈ 0.7) (Hu et al. 2007 c). It has been shown that a fs-DLC film deposited at room temperature possesses a mixture of *sp*, sp^2 and sp^3 coordinated carbon (Hu et al. 2007 c). Since *sp* bonded carbon chains are linear molecular conductors and have been shown to be the precursors of nanotubes (Ravagnan et al. 2002), it is of interest to study the microstructure and electron bonding states in fs-DLC films deposited at cryogenic temperatures.

In this chapter, I report the observation of a nano-buckling structure in fs-DLC deposited on Si. The occurrence and evolution of this structure has been investigated using AFM analysis as well as by Raman and XPS spectroscopy. The mechanical properties of these materials have also been characterized using nano-indentation techniques. These measurements are shown to reveal insight

into the origin of nano-buckling in DLC materials as well as the role played by the presence of sp/sp^2 clusters.

6.2 Experimental setup

Amorphous carbon thin films were deposited on polished p-type Si wafers with (100) orientation. Before deposition, the Si wafer was first degreased in an ultrasonic bath of acetone (high-performance liquid chromatography grade), and then further cleaned by immersion in a 1% HCl solution. The wafer was then rinsed in nanopure water (18MΩ). The Si wafer was cooled to 77K by liquid nitrogen in a high-vacuum deposition chamber at a base pressure of 2.67×10^{-5} Pa evacuated with a turbo-molecular pump. During deposition the pressure typically increased to 6.65×10^{-5} Pa. A regenerative Ti:sapphire laser system (λ=800 nm, pulse duration τ=120 fs, repetition frequency 500Hz, incidence angle 45^o) was employed to ablate high purity pyrolytic graphite (99.99%). Either a Ti:sapphire laser system (λ=800 nm, pulse duration τ=120 fs, repetition frequency 500Hz, incidence angle 45^o) or a XeCl excimer laser (λ=308 nm, pulse duration τ=30 ns, repetition frequency 15 Hz, incidence angle 45^o) was employed to ablate high purity pyrolytic graphite (99.99%). The pulse energy was 1mJ for the fs laser source and 20 mJ for the excimer laser. The laser beam was focused into a spot with a typical size of 100 μm by a quartz lens with a focal length of 160 mm. The peak laser intensity was 1.1×10^{14} W/cm^2 corresponding to a fluence of 12.7 J/cm^2 at the target surface. Details on the deposition system with the ns laser source have been discussed in Chapter 4 & 5 (Hu 2006b, 2007a).

Film thickness was monitored in-situ by measuring the UV absorption of the sample during deposition. The final thickness was measured with a profilometer (AMBios XP-2) after deposition. Microstructure was characterized via scanning electron microscope (SEM) equipped with a field emission gun and atomic force microscopy (AFM). The microhardness and reduced elastic modulus were determined from load-displacement curves obtained using a Nano Indenter (Hysitron) apparatus. A three-sided pyramid Berkovich indenter was used in the experiment.

UV Raman spectra were obtained with a Kimmon 5161R-GS Raman spectrometer using He-Cd laser radiation at 325 nm (UV, 3.8 eV). To avoid excessive heating of the carbon sample, the laser power was reduced to 4.5 mW. Visual Raman spectra were measured using a Renishaw micro-Raman spectrometer with 0.3- 3 mW He-Ne laser at an excitation wavelength of 632 nm (1.97 eV). For both spectrometers the resolution was 1 cm^{-1}. X-ray photoelectron spectrum (XPS) measurements were carried out using a multi-technique ultra-high vacuum imaging XPS microprobe spectrometer

(Thermo VG Scientific ESCALab 250) with a monochromatic *Al* K_α 1486.6 eV X-ray source. The spectrometer was calibrated by *Au* $4f_{7/2}$ (Binding energy of 84.0 eV) with respect to the Fermi level. The chamber vacuum level was maintained below 2.67 x 10^{-8} Torr. The constant pass energy was set at 160 eV for survey scans at 1 eV step and 100 millisection per scan. Only one scan was used to collect the spectra. The pass energy of 20 eV was used for C1s/O1s/Si2p scans, with an energy resolution of 0.05 eV. The dwell time was 250 millisection and 3 sweeps were used. Films with 300 nm were used for the survey scanning and the C1s line study while a 40 nm thin film was employed for the *Si2p* and *O1s* line scanning in order to focus on binding properties of film-Si substrate interfaces. To obtain optimum conditions for SERS, a silver film was deposited on the surface of the DLC films using femtosecond laser ablation of a pure Ag target. For both fs-DLC and ns-DLC the same processing parameters were used for surface Ag deposition.

6.3 Results

6.3.1 Comparative spectroscopic studies of ns-DLC and fs-DLC

Fig. 6.1 shows conventional (non-SERS) Raman spectra of fs- and ns-DLC films obtained at for excitation at 632 nm. It can be seen that the FWHH (full width at half height) of the 1500 cm^{-1} feature in fs-DLC is much larger than that occurring in the spectrum of ns-DLC. Since the broad peak at 1000-1700 cm^{-1} can be attributed to the overlap of the D (1350cm^{-1}) and G (1570cm^{-1}) breathing and stretching modes of sp^2 hybridized rings, respectively, the sp^2/sp^3 ratio is conventionally obtained by fitting Raman spectra in this region with a Breit-Wigner-Fano (BWF) lineshape (Ferrari and Robertson 2000, Hu et al. 2007a). This approach suggests that fs-DLC contains ≈ 51 % of sp^3 bonded carbon atoms while the sp^3 content in ns-DLC is ≈ 72% (Hu et al. 2007a). In ta-C, the $\pi \rightarrow \pi^*$ gap of sp^2 bonded species is about 2 eV while the $\sigma \rightarrow \sigma^*$ gap of the sp^3 component is ≈ 5.5 eV. Thus the excitation at 632 nm (1.98 eV) primarily couples to the $\pi \rightarrow \pi^*$ transition of sp^2 groups (Ferrari and Robertson 2001). On the other hand, UV excitation couples to *sp* and sp^3 groups so that UV Raman spectra provide extra insight into the presence of these species in DLC films.

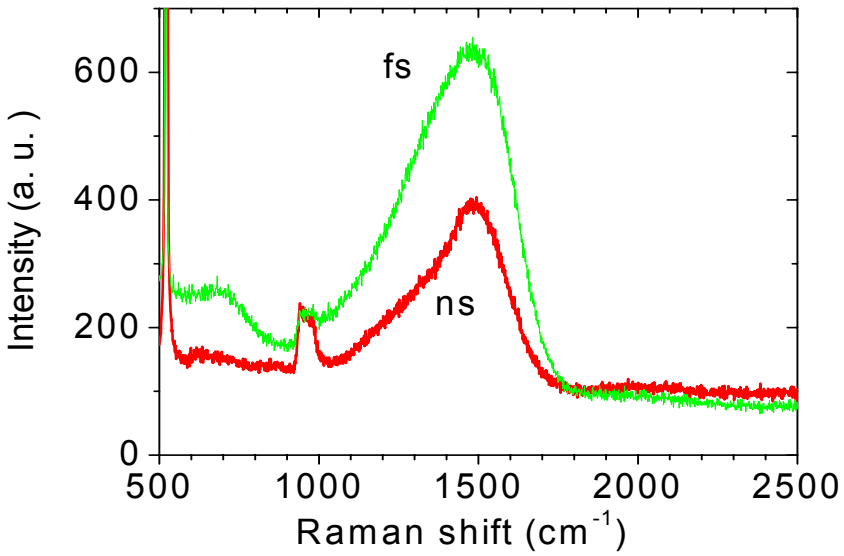

Fig. 6.1 Visual Raman spectra for fs- and ns- DLC samples, both deposited at room temperature (293K).

UV-Raman spectra of fs- and ns-samples are shown in Fig. 6.2 and differ from Raman spectra obtained at lower photon energy (Fig. 6.1). A peak appearing at 750 cm^{-1} in Fig. 6.2 can be assigned to the bending mode of sp^2 bonded components while the band centered at 2700 cm^{-1} is the second order of the G mode (Merkulov et al. 1997). The T-band centered at 1050 cm^{-1} only appears with 325 nm (3.8 eV) excitation and can be attributed to a C-C stretching mode of sp^3 bonded species. From the intensity ratio I_T/T_G, it can be concluded that the concentration of the sp^3 component is greater in ns-DLC than in fs-DLC films. The shift of the D and G bands to higher energy with UV excitation arises from the well-known dispersion of these features (Ferrari and Robertson 2000).

A notable feature of UV-Raman spectra of fs-DLC is the presence of a band in the 2000-2200 cm^{-1} range. This is unlikely to arise from adsorbed CO (Haslett 1995) as it is absent in ns-DLC films. We assign this feature to *sp* carbon chains since previous studies (Ravagnan et al. 2002) have shown that cumulenes $(C=C)_n$ and polyynes $(C\equiv C)_n$ give rise to Raman bands in this spectral range. Because the sp/sp^2 cross section ratio, R, is enhanced by over one order of magnitude on changing the excitation wavelength from 632 nm ($R\approx0.25$) to 325 nm ($R\approx2.5$) (D'Urso 2006), the *sp* band at 2000-2200 cm^{-1} in UV Raman spectra is virtually absent in Raman spectra recorded with 632 nm excitation (Fig. 6.1).

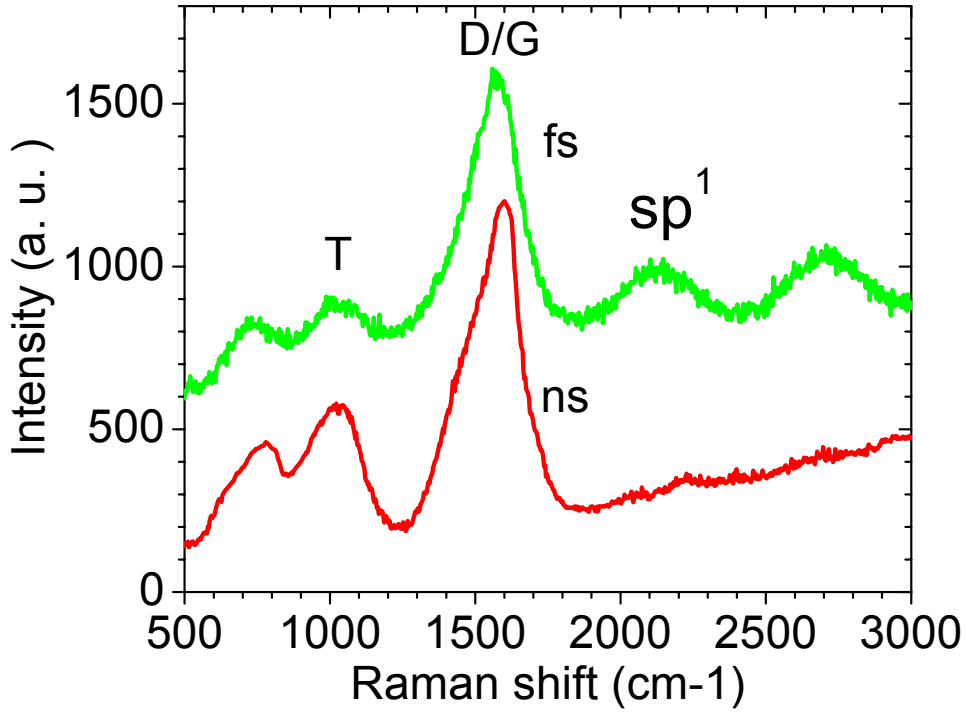

Fig. 6.2 UV Raman spectra for fs-DLC and ns-DLC samples with excitation at 325 nm (Cd-He laser). D/G and *sp* stand for the vibration of graphitic D/G modes (sp^2) and the peak from *sp*-bonded carbon chains (carbyne). The broad band "T" is attributed to sp^3 bonds.

Following the model proposed by D'Urso et al. (2006), the *sp* fraction relative to that of sp^2 bonded carbon is $X_{sp}/X_{sp2}=(1/R)\ (I_{sp}/I_{sp2})$ where $I_{sp}/I_{sp2}=0.38$ is the Raman intensity ratio at 325 nm. Then, $X_{sp}/X_{sp2} \approx 0.15$ in fs-DLC. As the previous estimate of the sp^3 carbon fraction in fs-DLC is ≈ 0.51, the *sp*, sp^2 and sp^3 fractions in fs-DLC are 0.06, 0.43 and 0.51, respectively (Table 6.1). These fractions are those existing in samples that have been exposed to air for over one month. This may indicate that oxidation and/or cross-linking of *sp* chains in fs-DLC is much slower than that in other carbon films, where the I_{sp}/I_{sp2} ratio has been found to decrease to ≈ 0.036 after exposure to dry air for 0.6 hour at 532 nm excitation (R=0.5), which corresponds to an I_{sp}/I_{sp2} ratio of 0.18 at 325 nm (Casari et al. 2004).

Table 6.1. Summary of characteristic parameters for diamond-like carbon films deposited by fs and ns pulsed laser deposition.

samples	sp^3	I_T/I_G	I_{sp1}/I_G	X_{sp}/X_{sp2}
fs-DLC	51%	0.28	0.38	15.2%
ns-DLC	73%	0.41	0	0

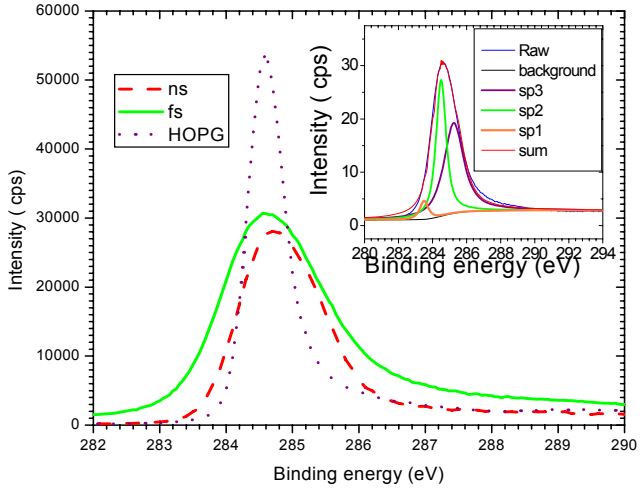

Fig. 6.3 XPS spectra for the C1s core-level binding energy for fs-DLC (300 nm in thickness), ns-DLC (300 nm in thickness) (both deposited at room temperature, 298K) and HOPG samples. Inset: deconvolution of C1s peak.

XPS spectra of fs-DLC, ns-DLC and a highly oriented pyrolytic graphite (HOPG) sample in the C1s region are shown in figure 6.3. The fs-DLC and ns-DLC films were both deposited at 77K with a thickness of 300 nm. In these spectra, the C1s peak in fs-DLC has a full-width-at-half-height (FWHH) of 1.9 eV while the FWHH in ns-DLC is 1.5 eV. The C1s peak in HOPG has a FWHH of 0.7 eV. Deconvolution of the broad C1s core-level peak into sp^2 bonded carbon (at 284.4 eV) and sp^3 bonded carbon (at 285.2 eV) components in ns-DLC can be used to show that the sp^2 content in these films is 0.68 (Hu et al. 2007a, Haerle et al. 2001, Jernigan et al. 2000). The C1s peak of carbyne (sp-bonded carbon chains) is found at 283.5 eV, a lower level (Zhang et al. 2007, Sergushin et al. 1978).

Hence, the broad C1s peak in fs-DLC which includes an additional component near 284 eV indicates that these films contain *sp* as well as sp^2 and sp^3 bonded species. Based on a mixture of *sp* (283.5 eV), sp^2 (284.4eV) and sp^3 (285.2 eV) bonded components a deconvolution of C1s line of fs-DLC is shown in the inset to Fig. 6.3. The concentrations of three bonded carbons in cryogenic fs-DLC are obtained as 0.05 (*sp*), 0.4 (sp^2) and 0.55 (sp^3), in consistent with the quantitative analysis of UV-vis Raman spectra while a slightly higher sp^3 content (0.51 in fs-DLC deposited in room temperature) (Hu 2007b).

6.3.2 Surface enhanced Raman spectroscopy (SERS)

Fig. 6.4 shows the morphology of fs-Ag particles deposited on the surface of carbon films by laser ablation of Ag. The deposit consists of 10-30 nm Ag nanoparticles and 100 nm - 1 μm grain aggregates embedded in a matrix of finer material. The Ag film on the ns-DLC has a similar structure. Optimized SERS spectra can be obtained after a 5 min deposition. Under these conditions, the silver totally masks the DLC film and Raman spectra are enhanced through the entire DLC deposit. Since the Ag nanoparticle film are in-situ deposited the surface contamination can be minimized.

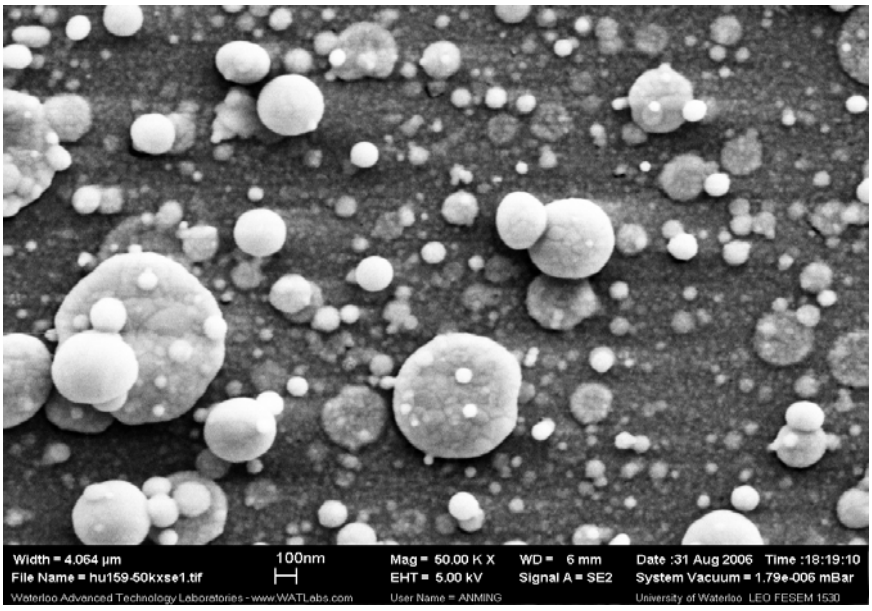

Fig. 6.4 Typical SEM image of a SERS sample.

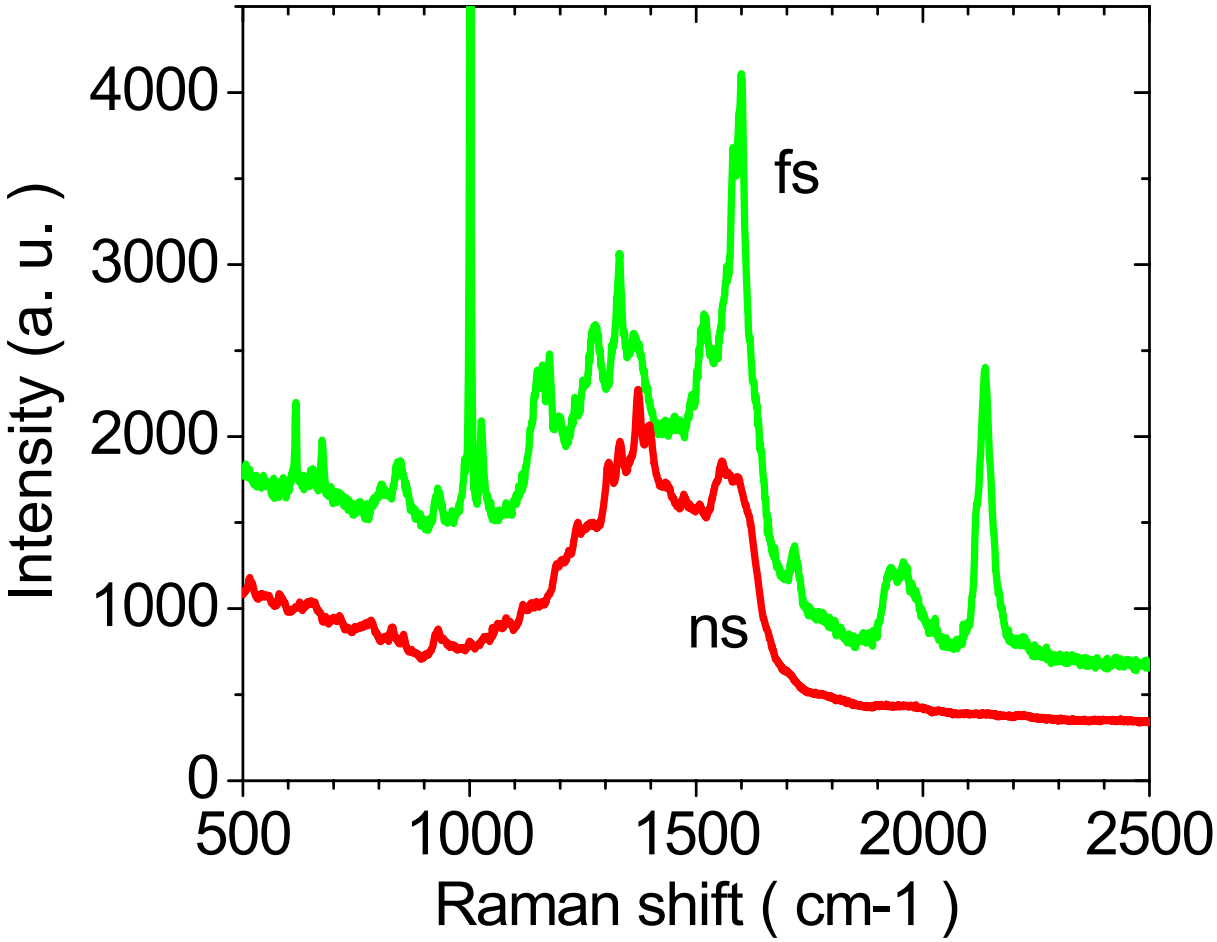

Fig. 6.5 Surface enhanced Raman spectra of a fs-DLC and a ns-DLC film.

A comparison between SERS spectra of fs- and ns-DLC films is given in Fig. 6.5, and a list of major spectral features together with possible assignments is shown in Table 6.2. Both spectra show structures that are not present in conventional Raman spectra. The appearance of discreet features in the region of the D and G bands can be understood as arising from the enhancement of scattering from specific molecular structures within a nominally amorphous material. This indicates that the D and G bands are inhomogeneously broadened, and that the presence of Ag particles selects out specific components of this inhomogeneously broadened profile. The spectral width of individual

SERS components (5-30 cm^{-1}) is consistent with a model in which the primary source of broadening is vibrational relaxation, rather than as the result of variations in chemical bonding. This indicates that the SERS features that do appear out of the broad D and G bands, likely correspond to chemical groups associated with well-defined, reproducible, structures within these films. This is expected as these films are nano-assembled, and specific molecular structures will dominate under these conditions. The occurrence of a larger number of lines in fs-DLC compared to ns-DLC, then reflects the fact that smaller molecular components are generated in the fs ablation of graphite than in ns interactions. These small molecular components become embedded in the overall deposit, resulting in the appearance of characteristic frequencies in SERS spectra.

Evidence for this can be seen in Fig. 6.5 where strong features corresponding to vibrational modes of aromatic hydrocarbon ring structures are observed at 674, 848, and 1002 cm^{-1} in the SERS spectrum of fs-DLC. These features are not seen in SERS spectra of ns-DLC, although other weaker bands are observed in the same spectral region. The Raman band at 1002 cm^{-1} is characteristic of the breathing vibration of substituted benzene rings (Liu et al. 2006), suggesting that small rings are present in this material. The mode of 1307 cm^{-1} can be attributed to hexagonal diamond (Schwan et al. 1996). fs-DLC and ns-DLC films also have features at 1600 and 1559 cm^{-1} corresponding to the stretching mode in larger aromatic rings (Ferrari and Robertson 2000) together with bands near 1360-1370 cm^{-1} arising from the breathing mode of these molecular groups (Roy et al. 2002, Mapelli et al. 1999). Additional spectral lines are observed in the region 1500-1620 cm^{-1} indicating that a range of ring structures are to be found in these materials. A feature appears at 1332 cm^{-1} in some spectra that can be identified with crystalline diamond (Roy et al. 2000) while fs-DLC shows several bands in the 1100-1200 cm^{-1} region that can be associated with the presence of trans-polyacetylene (t-PA) chains of different length (Ferrari and Robertson 2001, Lopez-Rios et al. 1996). Other features in the 1450-1480 cm^{-1} range may also arise from t-PA (Ferrari and Robertson 2001). This indicates that the overall structure of fs-DLC films consists of sp^2 bonded rings and sp^3 bonded diamond-like structures linked by chains of various length and composition.

Table 6.2. Assignment of the peaks of DLC films reported in the literature and as shown in SERS characterization.

Peak position (cm^{-1})	fs	ns	Possible origin	References
~2138	x		polyyne	Ravagnan 2000
~1957	x		cumulene	Ravagnan 2000
~1929	x		cumulene	..
~1717	x		HOPG mode, aldehyde	Kasashima 79
~1600	x	x	”G”	Ferrari 99
~1559	x	x	“G”	Ferrari 99
~1520	x		hexabenzocoronene	Mapelli 99
~1472	x	x	trans-polyacetylene	Ferrari 99
~1397		x	E_{2g} coronene	Mapelli 99
~1372		x	“D” microcystalline graphite	Ferrari 99
~1362	x		“D”	Roy 02
~1332	x	x	diamond, Γ point	Roy 02
~1307		x	hexagonal diamond?	Schwan 96
~1280	x		scattering at L point from diamond	Roy 02
~1176	x		*trans*-polyacetylene	Lopez-Rios 96
~1160	x		*trans*-polyacetylene	Ferrari 99
~1149	x		*trans*-polyacetylene	Lopez-Rios 96
~1036	x			
~1002	x		subst. benzene, coronene	Liu 06
~ 863	x		A_{2u} crystal graphite?	Nemanich 79
~ 848	x		out-of-plane (oop) ring	Mapelli 99
~ 674	x		oop ring	Mapelli 99
~ 617	x			

Further insight into the nature of these chains is obtained by the observation of Raman features in the energy range 1800-2500 cm^{-1}. In keeping with previous studies (Ravagan et al. 2002 &2006, D'Urso et al. 2006, Lucotti et al. 2006, Szepanski et al. 1997), these bands can be assigned to CC stretching modes in polyyne and cumulene chains. Two major Raman bands, each containing substructure, are seen in the spectrum of fs-DLC. That centered at 2140 cm^{-1} can be assigned to polyyne chains $(-C\equiv C-)_n$ with n = 3 -4, while the band centered at 1950 cm^{-1} would appear to be due to cumulenic chains $(C=C)_n$ having a similar number of carbon atoms. It should be noted that a Raman peak near 2140 cm^{-1} can also be produced by adsorbed CO (Haslett et al. 1995). As we do not detect a peak at 2140 cm^{-1} in our ns-DLC films, it is unlikely that adsorbed CO is present in our samples.

These results are consistent with SERS spectra of carbon chains prepared by electric arc discharge in methanol (Lucotti et al. 2006) that show strong bands at 1975 and 2110 cm^{-1}. The 25-30 cm^{-1} energy shifts of these bands in the present spectra compared to spectra in methanol likely derive from the fact that there is no direct Ag-chain bond in our samples, since Ag is deposited after the fs-DLC sample has been created. Analysis of Raman scattering by carbon chains in carbonized fluoropolymers (Kastner et al. 1995) has shown that energy, $\nu(N)$, of the CC stretching mode in polyynic chains is approximately $\nu(N) = 1750 + (3980/N)$ cm^{-1}, where N is the number of C atoms. If this correlation also holds for fs-DLC, then $N \approx 10$ in our samples. This is somewhat larger than the value of N derived from DFT calculations for isolated polyyne chains, reflecting the fact that the bonding environment is quite different in fs-DLC deposits and the average chain length may be smaller. On the basis of this model, the observation of structure in the bands at 1950 and 2140 cm^{-1} can be attributed to the presence of chains of different length.

The appearance of extensive structure in the SERS spectrum of fs-DLC compared to that observed in ns-DLC, shows that the ablation mechanism has a profound effect on the properties of the resulting deposit. In particular, the high energy and high charge of carbon ions produced during fs ablation seem to favor the formation of carbon chains. As a result, t-PA, polyynic and cumulenic chains are observed in fs-DLC but not ns-DLC films. The occurrence of chains in fs-DLC then acts to stabilize novel (*sp, sp^2, sp^3*) - bonded carbon compositions that incorporate a range of small carbon molecules including C_6 rings. This is not possible in ns-DLC deposits since the *sp* phase seems to be absent. Thus, without the stabilizing effect of the *sp* phase, the composition of ns-DLC is a mixed sp^2/sp^3 structure consisting primarily of nanocrystalline diamond and nanocrystalline graphite embedded in a tetrahedral carbon matrix.

6.3.3 Nanobuckling in cryogenic fs-DLC

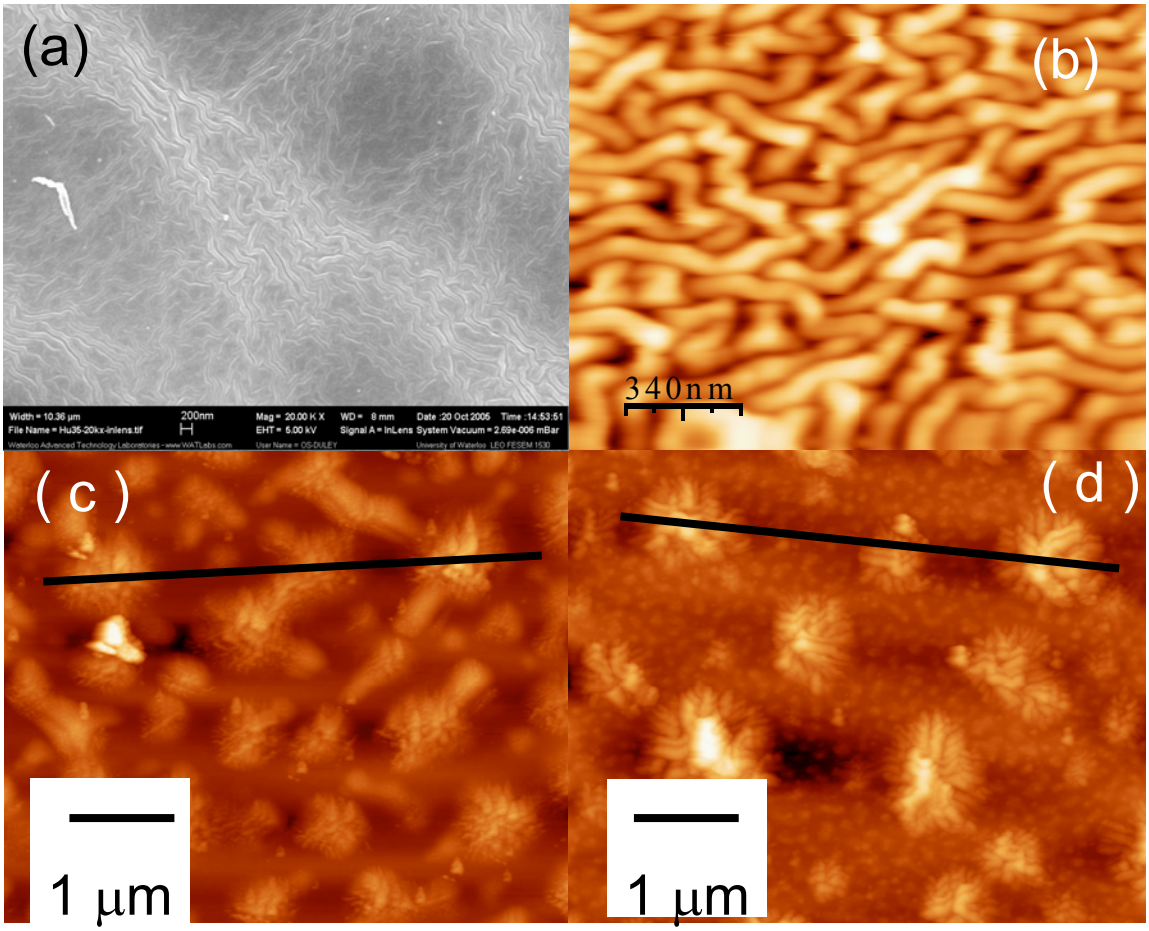

Fig. 6.6 Morphology of diamond-like carbon films deposited by fs laser deposition at 77K. (a) SEM image of a film with 600 nm thickness (sample A) (b) AFM micrograph of sample A, (c) SEM image of a film with 450 nm thickness (sample B), (d) SEM image of a film with 300 nm thickness (sample C).

Figure 6.6 shows the nanostructure observed in fs-DLC films deposited on Si at 77K as a function of deposition time. The morphology of films after a 7 min deposition (sample A) is shown in figures 6.6 (a) and 6.6 (b). Figures 6.6 (c) and (d) (samples B and C respectively) were deposited for 5 and 3 min, respectively. The film thickness for samples A and C as measured with a profilometer is shown in figure 6.7 (a). The sharp step in figure 2(a) occurs along the line where the substrate was masked prior to deposition. Surface roughness along the straight lines appearing in figures 6.6 (c) and 6.6 (d)

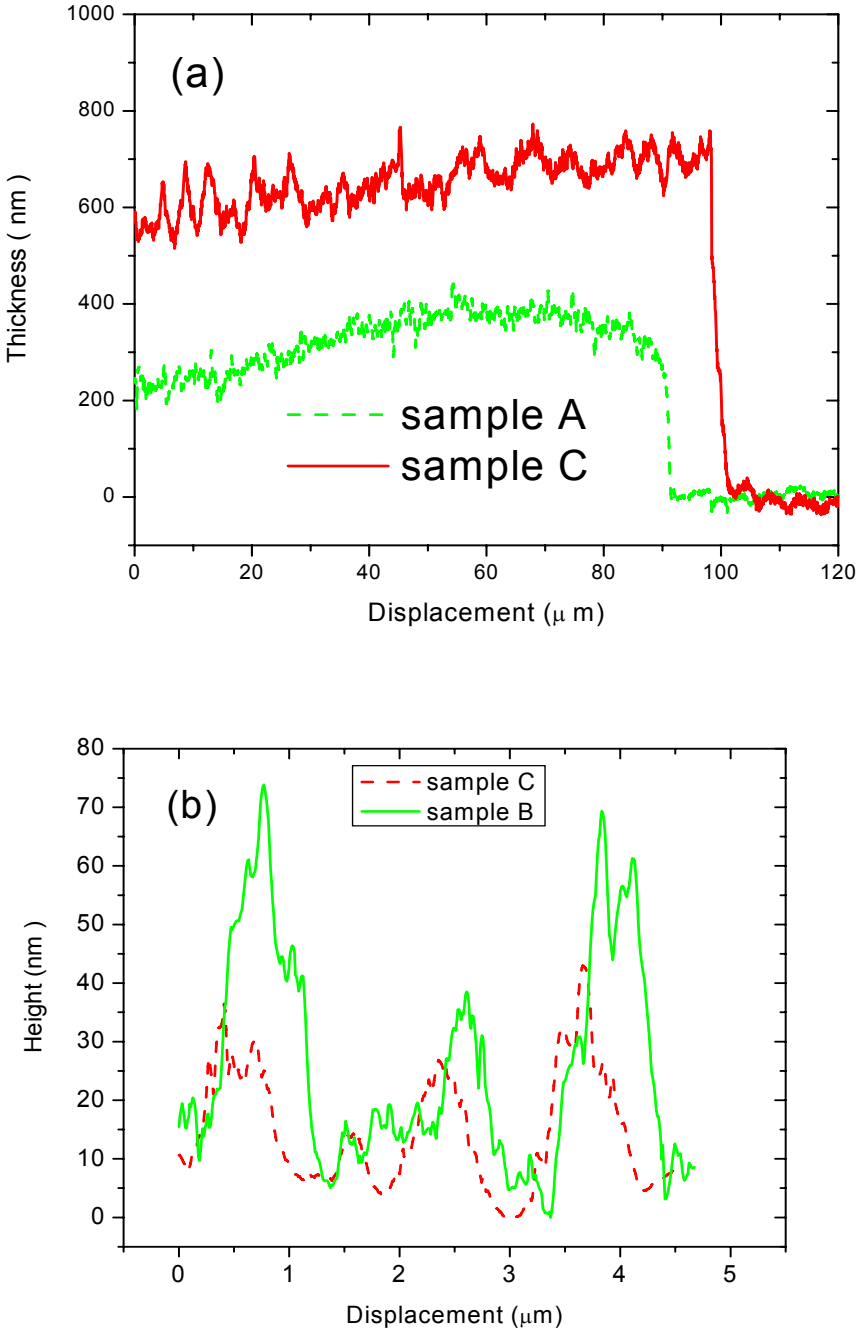

Fig. 6.7. (a) film thickness as measured using a profilometer. (b) Surface roughness analysis along the straight lines shown in Figs. 6.6 c and 6.6 d. The thicknesses for sample A, B and C are 600 nm, 450 nm and 300 nm.

is recorded in 6.7 (b). These measurements show that surface buckling develops as the film thickness increases. At a thickness of 300 nm (sample C), peeling occurs at intervals of ≈ 1.5 micrometer in the form of point-like buckling sites having dimensions of ≈ 1 micrometer. The amplitude of height modulation in these regions is ≈ 20 nm. The regions of the film between the sites of point-like buckling appear granular i.e. consist of a matrix-assembled from nanoclusters.

As the thickness increases to 450 nm (sample B) the buckling amplitude increases to ≈ 60 nm (figure 6.7 (b)) and surface peeling develops a linear structure with segments oriented approximately perpendicular to each other. The resulting ripples can be clearly seen in figure 6.1(c). With a further increase in film thickness to 600 nm (figures 6.6 (a), (b)), these ripples increase in amplitude and are separated by ≈ 100nm. Each ripple extends over a length of ≈ 500-3000 nm and the pattern, as a whole, is found to cover the entire surface of the sample. The morphology observed in fs-DLC samples is quite different from that seen in DLC films, where partially detachment of films occurs on a scale of micrometers and there is no substructure in the detached regions (Tharigen et al. 2001, Nir 1984, Iyer et al. 1984).

To explore the origin of nanobuckling in fs-DLC, we further investigate films with smaller thickness and examine the effect of thermal processing on these samples. Figures 6.8 (a) and 3(b) shows the microstructure of a 50 nm thick film (sample D) after deposition for 1 min. Figures 6.8 (c) and 6.8 (d) are micrographs of thick sample B (as initially shown in figure 6.6 (c)) after temperature cycling between 77 and 300K. This cycle involved taking a sample deposited at 77K to 300K in half hour and keeping there for 30 min., and then recooling it to 77K before final observation at 300K. The same rate is employed for warming up and cooling down. This cycle was carried out in vacuum in order to avoid the influence of moisture. Figures 6.8 (a, b) display the buckling that appears in the 50 nm film, which is representative of the initial growth stage.

Figure 6.8 (a) shows that the buckling takes the form of a grouping of discrete dots in a low magnification SEM image. The details of individual points taking a form of the nanostripes that are evident in figure 6.8 (b). The line profile shows the height of such a nanobuckling is about 40 -50 nm. Figure 6.8 (c) shows the micron-scale buckling formed by thermal cycling in a 300 nm thick fs-DLC film (sample E). The local morphology at one buckling site is shown at higher magnification in figure 6.8 (d). This type of buckling also appears thick ns-DLC films, and likely originates from thermally induced stress relief (Tharigen et al. 2001, Nir 1984, Iyer et al. 1984). It is necessary to mention that the present temperature increasing/decreasing rate is the biggest value we can employ. With a slower

rate, such as a thermal cycling in 2 hours, the microbuckling almost disappears. Hence, the present results show that nano-scale buckling created during deposition and micron-scale buckling generated by thermal stress, can coexist in fs-DLC films deposited at cryogenic temperatures.

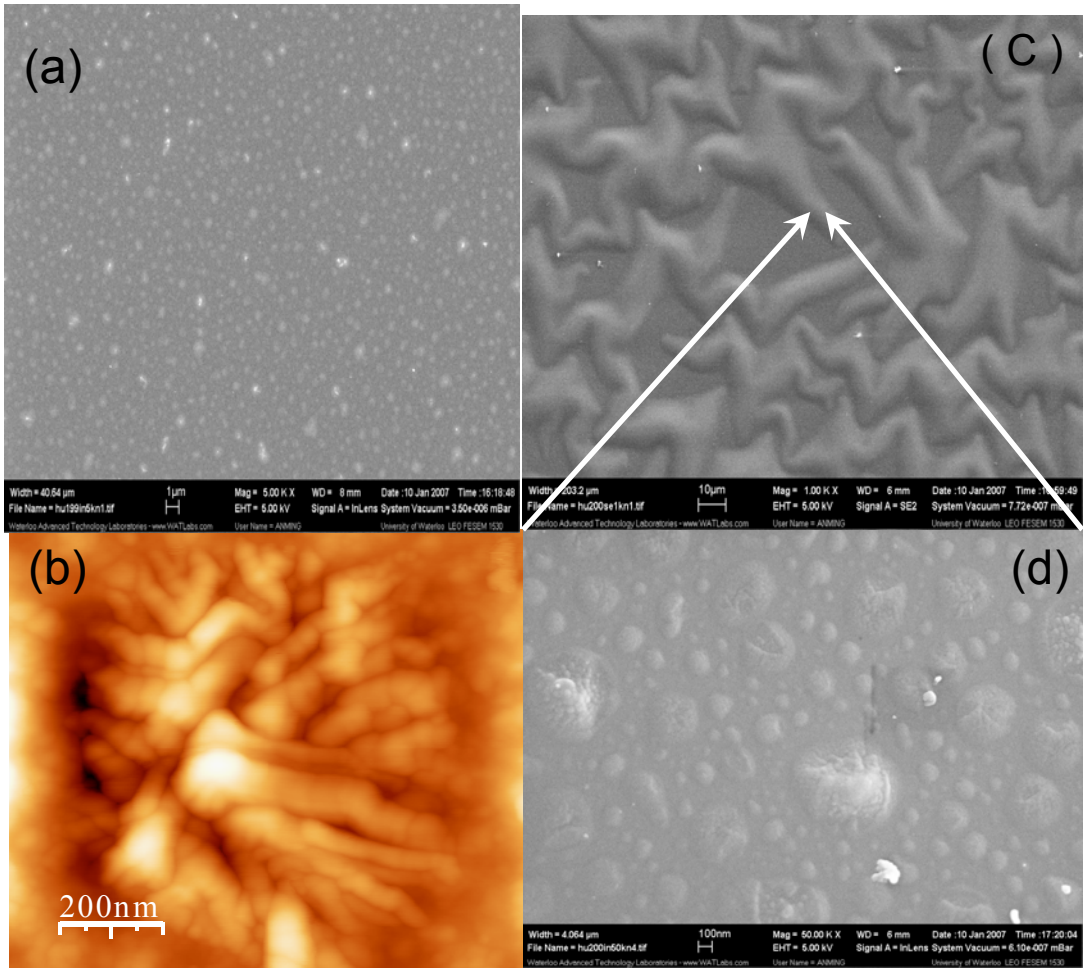

Fig. 6.8. (a) SEM image and (b) AFM micrograph of fs DLC films deposited for 1 min with a thickness of 50 nm (sample D). (c) SEM image of fs-DLC films with a thickness of 300 nm after thermal processing (sample E). (d) A magnified SEM image corresponding to a point located on a buckling branch as indicated in (c). The white arrow points to the position observed at a high resolution.

6.3.4 Internal stress and Nano-hardness

Figure 6.9 shows Raman spectra of two fs-DLC films with different bucklings deposited at 77K recorded with 623 nm excitation. The broad asymmetric band at 1100-1700 cm^{-1} corresponds to the overlapped D and G bands of tetrahedral carbon. The D and G bands, centered at 1355 cm^{-1} and 1570 cm^{-1}, respectively, arise from the stretching and breathing modes of sp^2 bonded carbon (Hu et al. 2006b). As a result, the relative concentration of sp^3-bonded species can be estimated by deconvolving the D/G band into the two components (Hu et al. 2007a, Hu et al. 2006a, Ferrari and Robertson 2000). Such an analysis shows that the fraction of sp^3-bonded carbon in these materials is ≈ 0.51 (Hu et al. 2007b). As the D/G band is sensitive to internal stress and shifts to higher frequency with increasing stress, the Raman spectrum can be used to map this effect (Ager et al. 1995, Ferrari and Robertson 2000). Spectra in figure 6.9 then show that the D/G band of fs-DLC is independent of thickness, indicating that both internal stress and the concentration of sp^3 –bonded carbon are not functions of film thickness.

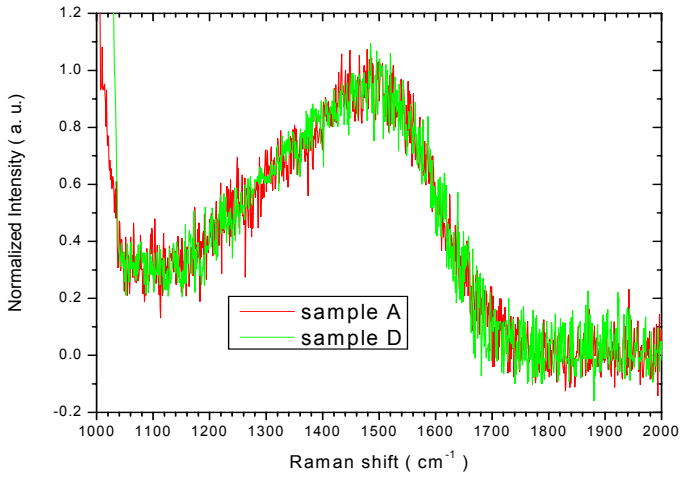

Fig. 6.9 Raman spectra recorded at 632 nm for fs-DLC films. Note that the Sample A is a 600 nm sample coverd by nanobuckling, sample D is a 50 nm sample only with separated point-like buckling.

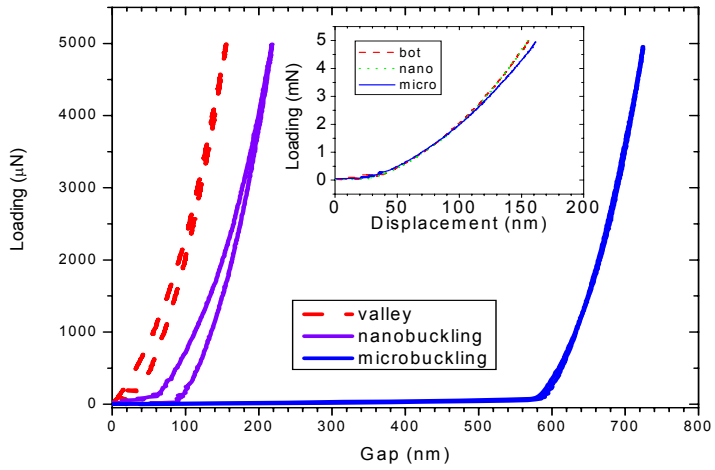

Fig. 6.10 Load-displacement curves measured by nano-indenter at different positions of sample E. Inset: scaling of loading curves. Sample E is a sample mixing micro- and nanobuckling.

Figure 6.10 demonstrates three loading-displacement curves measured at different positions of sample E by a nano-indenter with a 5 micro-Newton force. The plot designated as "microbuckling" is obtained at a peak of the microbuckling pattern. The "nanobuckling" plot was measured in the valley of the microbuckling pattern, but on top of a nanobuckling feature. The "valley" line corresponds to a measured point at a point on the surface without any buckling. Values of the nanohardness, reduced elastic modulus and contact stiffness can be obtained by fits to free-load drawback curves (Robertson 2002). By fitting to the valley curve, a hardness of 16.7 GPa, and a reduced modulus of 177 GPa are found in non-buckling areas. These values are slightly lower than those measured for fs-DLC deposited at room temperature, where the sp^3 bonded carbon fraction is 0.7 (Garrelie et al. 2003).

The curves measured on the top of both microbuckling and nanobuckling features show unsupported displacements of 580 and 60 nm, respectively. From the roughness analysis shown in figure 6.10 it is reasonable to conclude that this initial free-loading displacement is a consequence of partial detachment of the films from the substrate. The load-displacement curves have been re-plotted in the inset in figure 6.10 after removal of the displacement at a force of 2μN and it evident that valley and nanobuckling curves then coincide. This indicates that the mechanical properties are unchanged in both micro- and nano-buckling regions. However, microbuckling shows a slightly

larger displacement at a given loading than is seen in the other two locations. This may signal a higher concentration of defects in this region, leading to reduced hardness.

6.3.5 Interfacial binding states and origin of nanobuckling

To examine the influence of interfaces between carbon film and Si substrate on nanostructure, XPS spectra of fs-DLC and ns-DLC films deposited at 77K, both with a thickness of about 40 nm, are compared in figure 6.11. Figure 6.11 (a) shows spectra of fs-DLC and ns-DLC films in the region of the *Si2p* core energy level. Three distinct valence states of Si are detected, one located at 99.6 eV, the second at 100.2 eV and the third at 103.6 eV. The peak at 99.6 eV can be attributed to Si substrate and 100.2 eV is identified with the charge neutral covalent state in SiC while that at 103.6 eV arises from the +4 oxidation state in SiO_2 (Didziulis and Fleischauer 1990, Hartney et al. 1989, Smith and Black 1984). To obtain a detailed deconvolution of *Si2p* one has to consider the split of Si2p and low-shifting of *Si2p* by the screening of a covalent state. However, it is evident that the Si2p peak of fs-DLC films at an intensity approximately twice that of the peak seen in ns-DLC films. As a result, it is apparent that SiC is preferentially formed at the C-Si interface in fs-DLC. The passivating SiO_2 layer present on Si is absent in fs-DLC, but is found in ns-DLC films. This effect can be also seen in figure 6.11 (b) which shows spectra of the O1s core energy level in fs- and ns-DLC films. The intensity of the O1s level in ns-DLC is roughly 3 times that in fs-DLC indicating that a SiO_2 layer is attached to the substrate surface in ns-DLC but has been partially removed in fs-DLC films.

The origin of this SiO_2 layer is uncertain since cleaning in dilute HCl will remove the majority of the original SiO layer on the Si wafer and inhibits further oxidation by dangling Si bonds with H atoms. However, after deposition at cryogenic temperatures, ns-DLC graphitizes on a sub-micron scale and exhibits an enhanced affinity for oxygen (Hu et al. 2006a). Diffusion of oxygen may then further oxidize the Si surface. As a similar graphitization does not occur in fs-DLC, this may account for the presence of SiO_2 in ns-DLC and not in fs-DLC, which only shows a preferential SiC layer. It is also possible that the high energy ions in fs ablation can remove any residual SiO_2 at the Si surface. This model would be consistent with the observed low abundance of SiO_2 in ns-DLC deposited at room temperature (Hu et al. 2006a). The thickness of SiC layer is worth further investigation.

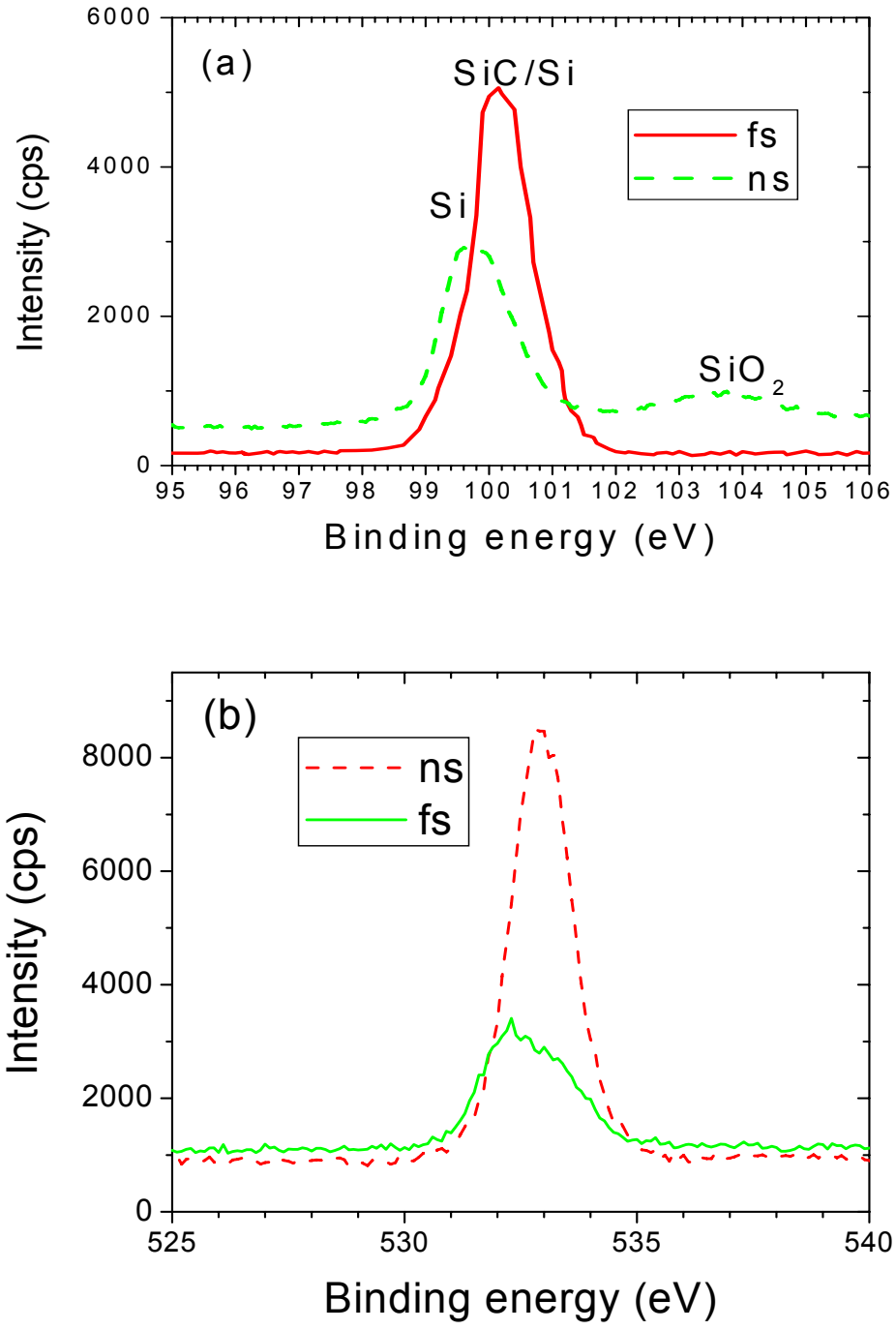

Fig. 6.11 (a). Si2p core-level XPS spectra for fs-DLC and ns-DLC samples (both 40 nm in thickness) deposited at 77K. (b) O1s core-level binding energy for fs-DLC and ns-DLC samples (both 40 nm in thickness) deposited at 77K.

6.4. Discussion

It is well established that buckling originates in response to stress relief and that the resulting profile of the surface is governed by the distribution of internal stress. These quantities reflect the value of Young's modulus as well as the adhesion energy at the film-substrate interface (Nir 1984, Iyer et al. 1995, Matuda et al. 1981). Furthermore, enhanced bonding between film and substrate in fs-DLC is evident from XPS spectra which show the formation of Si-C covalent bonds at the interface. These bonds are less apparent in spectra of ns-DLC. As a result, one expects higher adhesion energy in fs-DLC than in ns-DLC films. From Matuda et al. (1981), the adhesion energy, U_a, as a function of buckling width is $U_a = \frac{c^2\pi^2 E d^3}{12(1-\nu^2)}\frac{L}{l^2(L-l)}$, where E is Young's modulus, ν is the Poisson ratio, d is the film thickness, L the width of the whole film, c is a constant, and l is the buckling wavelength. Then, as U_a increases, l will generally decrease. This connection between buckling width and adhesion energy explains why nanobuckling is observed in fs-DLC and not in ns-DSLC films. One can also see that as d increases, l will also increase if U_a is constant. This correlation is also evident in Fig. 6. 1. Since the energy of C ions in fs ablation is 1-2 keV, compared to ≤ 10 eV in ns-DLC (Banks et al. 1999, Qian et al. 1999, Duley 1996), C ions can directly implant into the substrate surface forming covalent Si-C bonds. This may explain why nanobuckling is absent in ns-DLC films deposited at cryogenic temperatures (Hu et al. 2006a). Other solutions of the buckling equation based on a thin shell model predict point-like, flower-shaped, and wavy relief patterns (Nir 1984, Iyer et al. 1995). This may account for point-like and stripe-like patterns observed in fs-DLC although further analysis of these effects is required for nano-scale buckled structures.

Surface charging in XPS samples result in shifting of peaks to higher energy. Hence, the red-shift of the C1s peak in fs-DLC (Figure 6.3) cannot be attributed to surface charging. The presence of *sp*-bonded carbon chains in fs-DLC would be in keeping with the shift of the C1s level to lower energy as seen in Figure 6. 3. Then it can be concluded that fs-DLC films can be regarded as constituting a novel carbonaceous material with mixed $sp/sp^2/sp^3$ bonding. The data discussed here show that the inclusion of sp-bonded carbon does not dramatically modify the mechanical properties of DLC. However, unlike semiconducting/insulating ns-DLC (~GΩ) the present fs-DLC films are conducting (~MΩ). Due to the enhanced stability of sp-bonded carbon chains in the present composition we assume they are terminated by graphite clusters (Hu et al. 2006b). Because sp-bonded carbon chains are molecular conductors, the conductivity of fs-DLC films can be enhanced by a percolation

network, i.e., bridging sp^2 clusters by sp-bonded carbon chains although the *sp*-concentration is still low. The microstructure and mechanical properties of nanobuckled fs-DLC films then make this material a promising candidate for field emission sources or as an element in electromechanical devices since the buckling significantly change transporting properties (Bowden et al. 1998, Lacour et al. 2003, Tharigen et al. 2001). A special application is a pressure sensor sampling a nanoscopic displacement. Due to the high hardness of nanobuckling of fs-DLC such a sensor is expected to work on a high pressure range than that of microbuckling metallic films on elastomer substrates.

6.5. Conclusions

We find that carbon contained in trans-polyacetylenic, polyynic and cumulenic chains containing 6-8 carbon atoms represents a significant fraction of the composition of fs-DLC films. These chains act to stabilize a composition in which relatively small aromatic rings, together with diamond-like material are present in an amorphous structure. The relative fraction of *sp,* sp^2*,* and sp^3 – hybridized bonded material in these films has been found to be 0.06, 0.43 and 0.51, respectively. The corresponding fractions in ns-DLC are ≈ 0, 0.27 and 0.73, respectively. SERS spectra of fs-DLC films exhibit a wide range of features that can be identified with molecular species, including substituted benzene, coronene and larger polycyclic aromatic hydrocarbon rings.

The presence of microstructure and nanobuckling in fs-DLC films deposited at 77K has been investigated. A nanobuckling structure has been found to be a function of film thickness and is shown to arise from enhanced film-substrate adhesion energy. This occurs as the result of the formation of C-Si covalent bonds as high energy C ions impact on the Si surface during the initial stages of deposition. Our analysis indicates that these materials have mixed $sp/sp^2/sp^3$ bonding. This may make these materials of interest in applications.

Chapter VII

Dissociation of hydrocarbon compounds by femtosecond laser irradiation: synthesis of *sp*-bonded carbon chains and nanodiamonds in organic solvents

7.1 Introduction

In Chapter V we have shown that linear carbon structures with *sp* hybridization represent novel systems for fundamental aspects related to the science of fullerenes and nanotubes. Recent studies have shown that *sp*-bonded carbon species can directly work as functional elements in molecular devices such as conducting nanocables formed by inserting *sp*-bonded molecules into carbon nanotubes (Nishide et al. 2006 & 2007). A nonlinear optical response has also been observed in polyynes (Eisler et al. 2005). This further highlights the potential scientific importance of *sp*-bonded carbon chains for nano-optoelectronic applications.

The formation of *sp* carbon chains is expected in the initial stage of formation of small carbon clusters leading to fullerenes when the sp^2 phase is energetically less favorable (Lagow et al. 1995, Shvartsburg et al. 2000, Kent et al. 2000). *sp* hybridization is also thought to be present in large metastable carbon clusters (Bogana et al. 2005) and in interstellar dust (Duley 2000). Wakabayashi et al. (Wakabayashi et al. 2004) deposited small isolated *sp* clusters in a solid Ar matrix to investigate the reactivity of these species when interacting with each other. The amorphous sp/sp^2 carbon films are synthesized by supersonic cluster beam deposition (Ravagnan et al. 2002 & Casari et al. 2004). Recently we have reported the presence of *sp* carbon chains embedded in tetrahedral amorphous carbon films (Hu et al. 2007 a-d). In solvents, isolated *sp* chains have been synthesized by pulsed laser irradiation (nsec pulse width) of carbon-based particles suspended in various solvents (Tsuji et al. 2002& 2003, Tabata et al. 2004&2006a &b, Compagnini et al. 2007) or by arcing graphite electrodes under organic solvents (Cataldo 2003). It is worth pointing out that a source of solid carbon has to be presented in these studies. To obtain a solution of sp-bonded chains the solid carbon source has to be filtered. Direct irradiation with nanosecond laser pulses (second harmonic 532 nm, Nd:YAG laser) of organic solvents does not produce linear carbon chains (Tsuji et al. 2002). This suggests that

is worthwhile investigating the direct dissociation of organic molecules in solution by fs laser irradiation.

Nanocrystalline diamonds (NDs) are promising carriers for drug delivery due to a lack of cytotoxicity (Huang et al. 2007). The surface of NDs is also readily functionalized while strong fluorescence from nitrogen-vacancies in NDs ensures that these particles are well suited for cellular labeling applications (Fu et al. 2007). The key to the use of NDs in biomedical applications is the preparation of dispersive nanodiamond solutions. Although nanodiamonds can be synthesized by detonation on a commercial scale (Greiner et al. 1988), purification to remove graphite soot and other contaminants as well as de-aggregation of NDs from larger grains is a significant challenge (Kruger et al. 2005, Baidakova et al. 2007). Alternative methods of preparation are therefore of interest, especially those involving the growth of NDs in solution.

Lonsdaleite is the name of the hexagonal diamond phase of the sp^3-bonded carbon structure. It can be synthesized by static compression of crystalline graphite at ≈ 13 GPa and at temperatures > 1000^{o}C (Bundy and Kasper 1967). Hexagonal diamond is energetically unfavored and is therefore observed much less frequently than the normal cubic phase of diamond. Trace amounts of hexagonal diamond are often found in the crystalline boundary of chemical vapor deposited (CVD) diamond films, where it accommodates large anisotropic stresses (Rossi 1998). Misra et al. successfully deposited 88% hexagonal diamond films on strained gallium nitride-coated quartz substrates at 800^{o}C by hot filament CVD (Misra et al. 2006). Another technique, involving the dissociation of methane molecules in water with nanosecond UV laser pulses (λ=193 nm), only results in the formation of diamond-like nanoparticles consisting of tetrahedral carbon with graphitic inclusions (Hidai and Tokura 2005). Recently, it has been found that a localized graphite-diamond phase transition can be induced by fs laser pulses due to the generation of high pressure and temperature in a laser-induced shock wave (Hu et al. 2007d).

In this chapter, I report that intense femtosecond laser irradiation of organic solvents can break all chemical bonds of hydrocarbon compounds. As a consequence, C and C_2 species are created as building blocks for the formation of sp-bond carbon chains in organic solvents. High-purity hexagonal nanodiamonds can be also fabricated in the presence of iron. These experiments are necessary to explore various novel applications of these materials.

7.2 Experimental setup

The output beam of a regenerative amplified Ti:sapphire laser operating at 800 nm, and producing 50fs pulses at a frequency of 1KHz was focused into a quartz cell containing 20 ml of organic hydrocarbon liquid by a 3 cm focal length lens. A simple device skeleton is shown in Fig. 7.1. *Sp*-bonded carbon chains were fabricated in various alkanes, including pentane, hexanes, heptanes, octane, decane, dodecane and hexadecane. Acetone, methanol, benzene and cyclohexane were also examined. As the diameter of the focused beam was ≈ 10 μm, the resulting laser intensity was ≥ 10^{15} W/cm^2 at a pulse energy of 350 μJ. The irradiated solution was first filtered through a PVDF Acrodisc® membrane having pore size of 0.45 μm to remove any possible suspended carbon particles

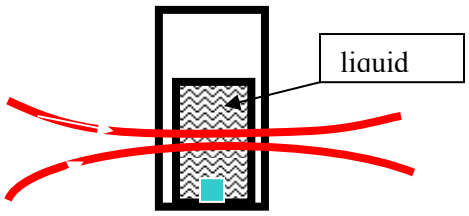

Fig. 7.1. Schematic diagrams of laser irradiation processing. A stir bar is located on the bottom of the quartz cell.

due to premature crosslinking reaction or to the aggregation of amorphous carbon. The chemical composition of irradiated solution was identified by high performance liquid chromatography (HPLC) combined with ion trap mass spectrometry (HP100/1100MSD). 10 μL per run of the filtered solution were injected into a 4.6 x 150 mm column (Zorbax Eclipse XDB-C_8 or C_{18}). A mobile phase of CH_3CN/H_2O of 80/20 (v/v) was used under isocratic conditions at a flow rate of 2 ml/min and 160 bar. The polyynes eluted from the column were measured by variable wavelength diode detectors and mass spectrometry. The wavelength was set at 225, 250, 274, 295 and 350 nm, respectively. All analyses were made by keeping the HPLC column at room temperature. The irradiation also resulted in lot of bubbles. These bubbles were collected in sealed vials and analyzed by gas chromatography combined with ion trap mass spectrometry (GC-MS).

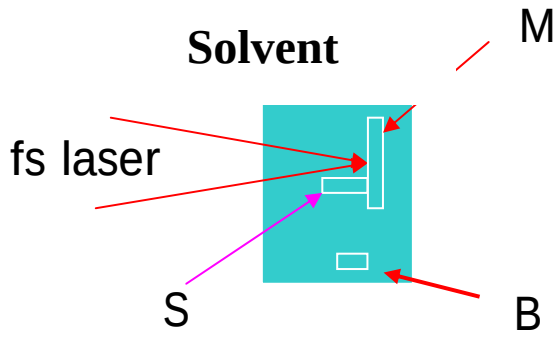

Fig. 7.2 Schematic diagram of nanodiamond deposition in solvents. M: metal, S: substrate, B: stirring bar.

For the deposition of nanodiamond films, as shown in Figure 7.2, a transition metal plate was immersed in the liquid and the laser was focused on its surface. The liquid was stirred during irradiation to ensure uniformity. The resulting diamond deposit was collected on a Si substrate placed in the vicinity of the laser focus. Before deposition, the Si wafer was first degreased in an ultrasonic bath of acetone (high-performance liquid chromatography HPLC grade), and then further cleaned by immersion in a 1% HCl solution. The wafer was then rinsed in nanopure water (18MΩ). This deposit took the form of a light grey film. The chemical composition and structure of the deposited films were characterized using visual Raman spectra and x-ray photoelectron spectra (XPS). Molecular species in the solution following irradiation were also investigated from surface enhanced Raman spectra (SERS) after mixing at a ratio of 5:1 with a 0.1 M silver nanoparticle solution. Silver nanoparticles suspended in nanopure water (18MΩ) were synthesized through a standard citrate reduction procedure (Lee and Meisei 1982, Kneipp et al. 1993). SERS spectra were recorded by focusing a 632 nm laser beam into the resulting solution with a x50 objective at an excitation power of 0.3 mW.

7.3 Chemical species in irradiated organic solvents

7.3.1 Surface enhanced Raman spectra (SERS) of irradiated solvents

Fig. 7.3 shows typical TEM mircograph of nanosilver particles used for surface enhanced Raman spectra. It is evident that the typical size of silver particles is about 20 nm. Fig. 7.4 shows the SERS spectra of acetone irradiated by 50 fs laser pulse trains at the pulse energy of 350 μJ and repetition rate of 1 KHz for 30 minutes. For comparison, the pristine acetone (HPLC grade) is also displayed. It is clearly evident that after irradiation strong vibration modes corresponding to sp-bonded carbon chains appears in the range of 1800 -2200 cm^{-1}. It is long known that the modes at high frequencies centered around 2100 cm^{-1} arising from polyynes with alternative single and triple C-C bonds and at lower modes centered of 1980 cm^{-1} originating from poly-cumulenes with double C-C bonds (Ravagnan et al. 2002, Casari et al. 2004, Hu et al. 2007b). The shifted vibration frequency is attributed to variable chain lengths of both polyynes and cumulenes (Lucotti et al. 2006, Kastner et al. 1995, Kurti et al. 1995, Akagi et al. 1987). A longer carbon chain yields a lower vibration frequency. Although the overlapped spectra do not allow us to identify individual chain lengths 4 peaks in the present spectra clearly display the mixing of various polyynes and cumulenes in the irradiated acetone (Tabata et al. 2006 a&b).

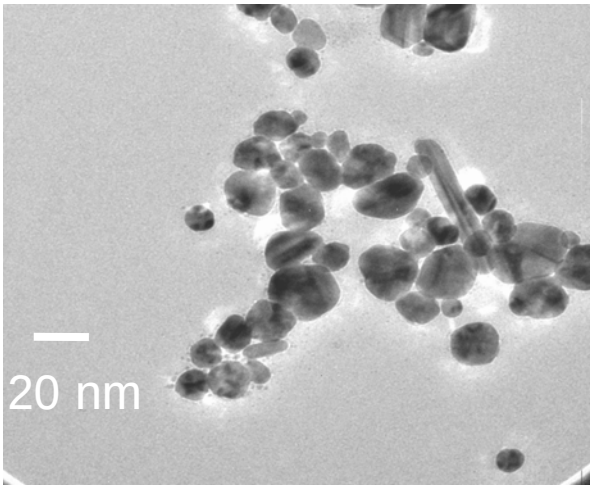

Fig. 7.3. Typical TEM images of nanosilver particles suspended in water fabricated by the reduction of citrate.

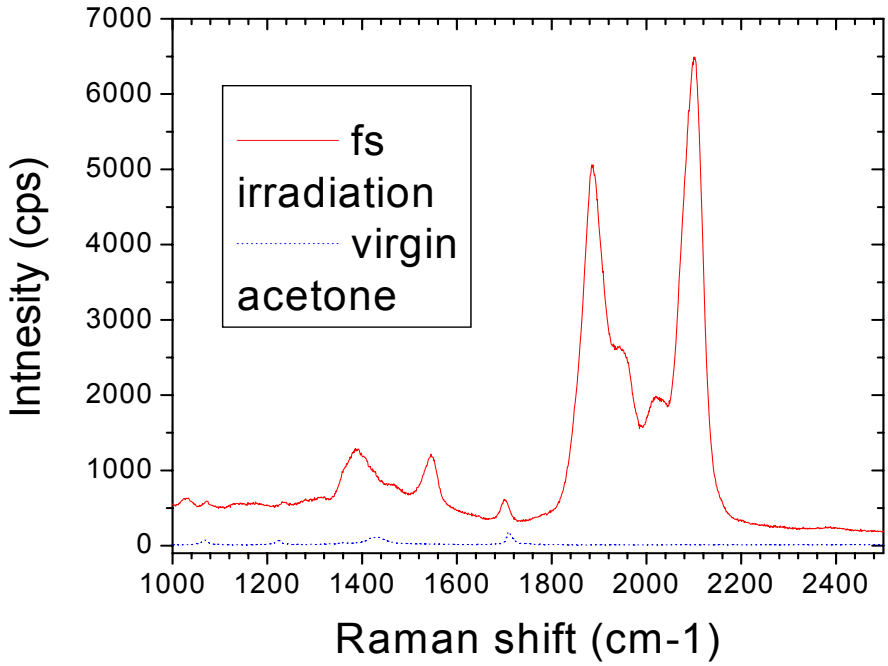

Fig. 7.4. Surface enhanced Raman spectra of acetone irradiated by 50 fs pulse trains at an energy of 350 μJ/pulse and incident wavelength of 800 nm.

It is important to point out that the present spectra show a lower band range than that in nanosecond laser irradiation, where the carbynes appear at 1900-2200 cm^{-1} (Lucotti et al. 2006, Tabata et al. 2006 b, Wakabayashi et al. 2007). This indicates that linear carbon chain molecules have a longer chain length in fs irradiation in comparison with ns irradiation. Besides, sp^2-bonded graphitic carbon is also observed after irradiation. The bands centered at 1350 cm^{-1} and 1570 cm^{-1} stand for the breathing and stretching modes of graphite (Hu et al. 2006). From the spectra one can easily conclude the concentration of sp^2-bonded graphite has a low value in comparison with that of carbynes.

In case of alkanes and benzene, which possess a low solubility in water, SERS measurements are carried out by focusing the excitation laser near the interface between organic solvent and nanoAg solution. To optimize the spectra, the solution is violently vibrated or stirred in order to well bond carbon chains to the surface of silver nanoparticles. Fig. 7. 5 shows the SERS spectra measured at different positions near interfaces. It is obvious that there are some nanoAg particles diffused into pentane and well diluted carbon chains in water solution. The spectra display strong carbyne species while enhanced sp^2-bonded compositions. The carbynes show a wide distribution of chain lengths and

even longer chains since there is a strong band centered at 1780 cm^{-1}. With the similar procedure SERS spectra are successfully obtained in benzene, hexanes, heptane, octane, dodacane and hexadecane with different focal positions.

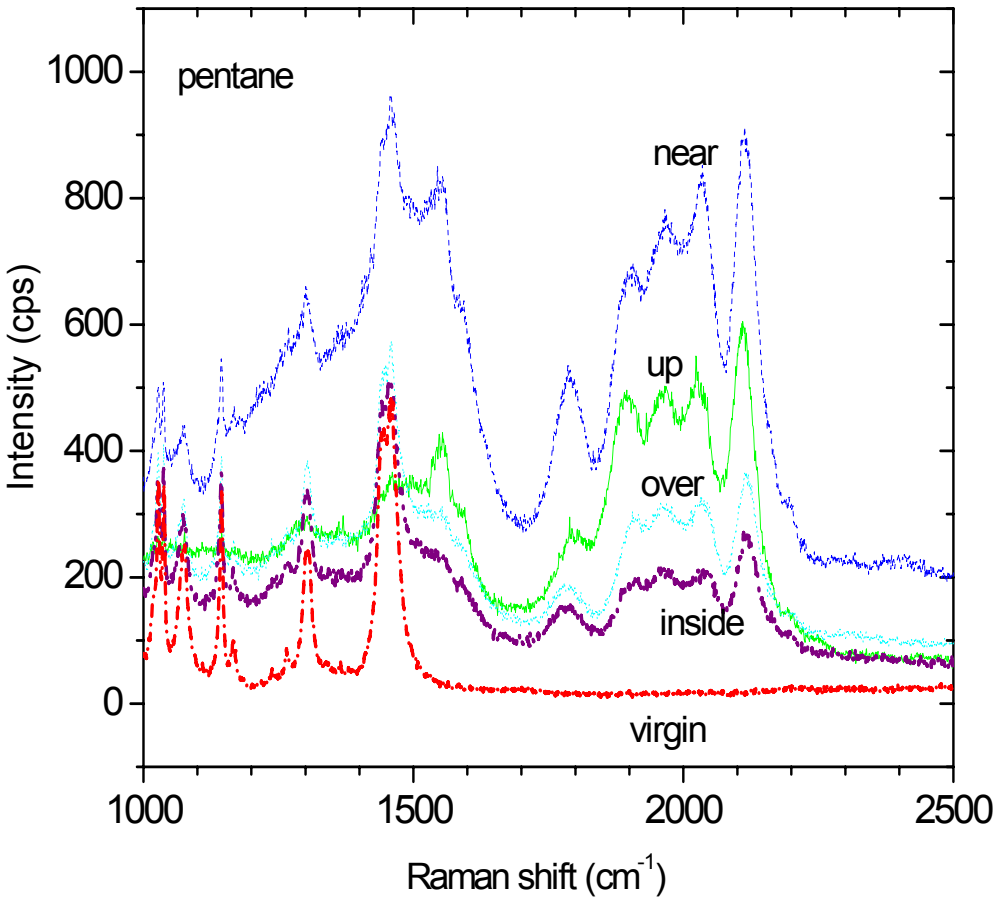

Fig. 7.5. SERS spectra of irradiated pentane (350 μJ, 1KHz, 30 min.) measured at variable positions in the vicinity of penate/water interface. Up: the focal point locates inside pentane at 1mm away from interface. Near: almost cross the interface. Over: inside nanoAg water solution at about 1 mm of depth away from interface. Inside: about 2 mm away from interface inside water. Virgin: nonirradiated pentane.

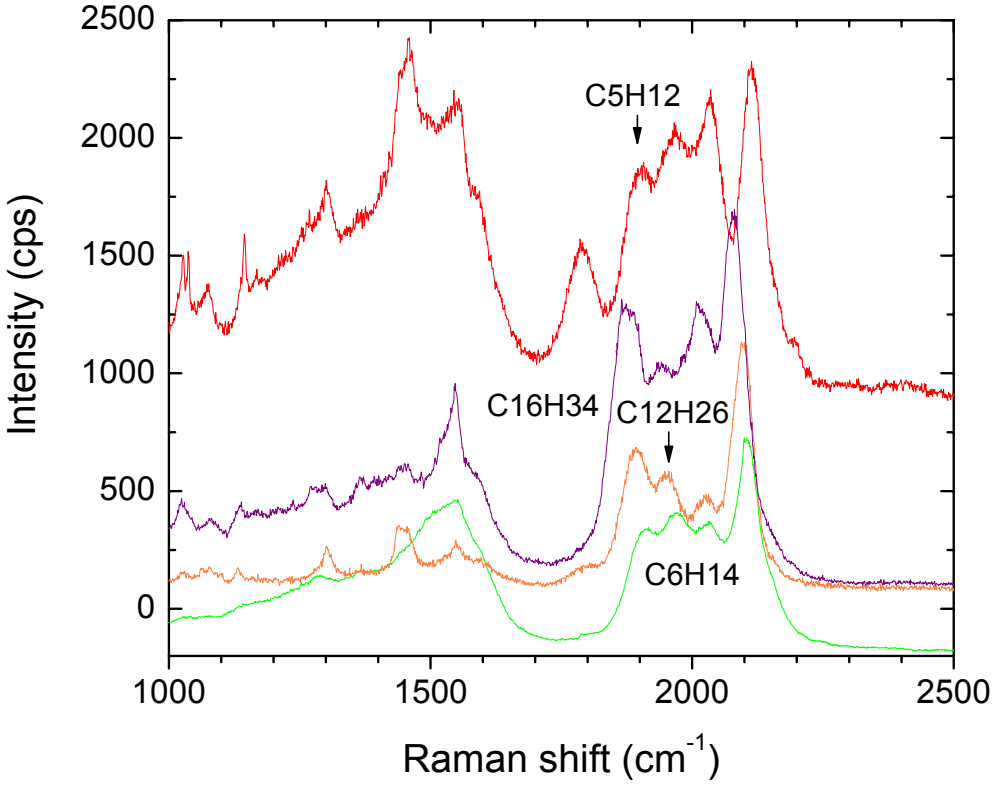

Fig. 7.6. Optimized SERS spectra of species produced from representative alkanes (350 μJ, 1KHz, 30 min.) as a function of C-C chain length.

Fig. 7.6 shows carbyne species dependent on different alkanes as carbon sources. Except for an extra band at 1780 cm^{-1} in irradiated pentane, the vibrational modes of carbynes shift to lower frequencies with increasing alkane chain length. This indicates that carbynes with longer chain lengths can be obtained by irradiating larger alkane molecules. The additional band at 1780 cm^{-1} in pentane may be attributed to different quenched conditions of alkanes since the stability of carbynes is a function of temperature (Heymann 2005, Casari et al. 2006). Longer carbynes are much more easily oxidized and can be graphitized by cross-linking at elevated temperatures. It is possible that dissociated species in pentane are quenched much faster than that in other alkanes.

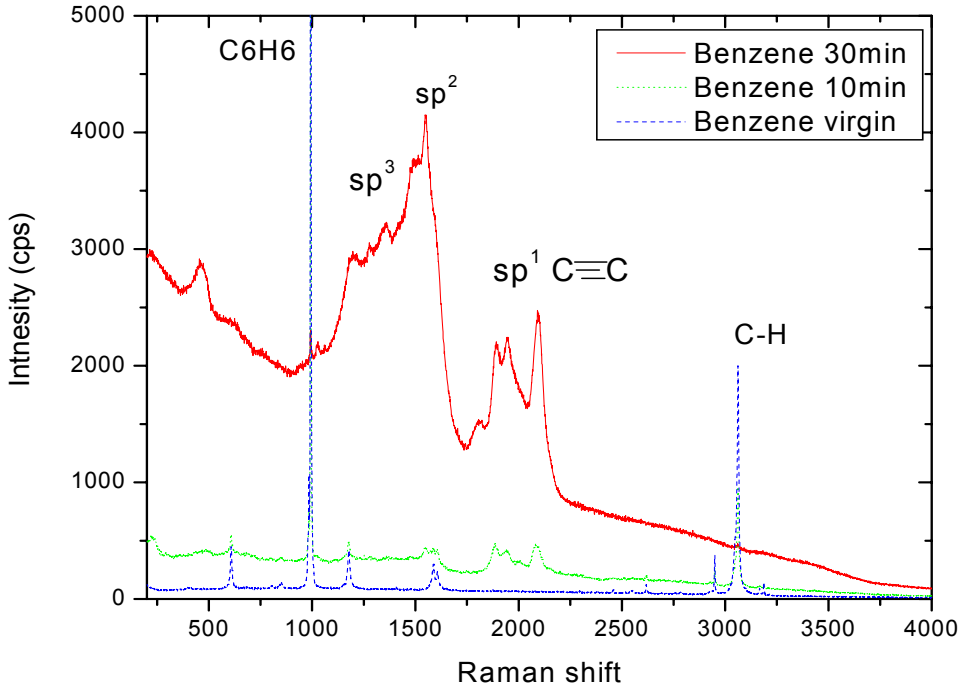

Fig. 7.7. SERS spectra of benzene irradiated at different times (350 μJ, 1KHz).

Fig. 7.7 show SERS spectra of benzene for different irradiation times. Extended irradiation leads to higher concentrations of the obtained species. It is easily found that sp-bonded carbon chains possess lower fractions than that of graphitic species. It is interesting that sp^3-bonded carbon (diamond) is also created by fs irradiation. These species display Raman modes at 1300 cm^{-1} and 1330 cm^{-1}, which indicate a mixture of conventional diamond and hexagonal diamond (lonsdalite) (Bundy and Kasper 1967, Knight and White 1989). This shows us an approach to synthesize a nanodiamond solution, which will be discussed later in this chapter. Diamond films with mixed cubic and hexagonal structure have been deposited with UV photolysis of nanosecond pulses of benzene (Singh et al. 1993) and cyclohexane (Sharma et al. 1993). These films are generally ultrathin (a few nanometers in thickness) due to a low yield of solid species. The dissociation mechanism with a nanosecond pulses is associated with thermal diffusion inside the liquid. Transferring of photo energy to thermal vibration of molecules may dramatically lower the dissociation effect. Even with these drawbacks, these ultrathin diamond films can work as seeds for CVD growth of diamond thick films (Singh et al. 1993).

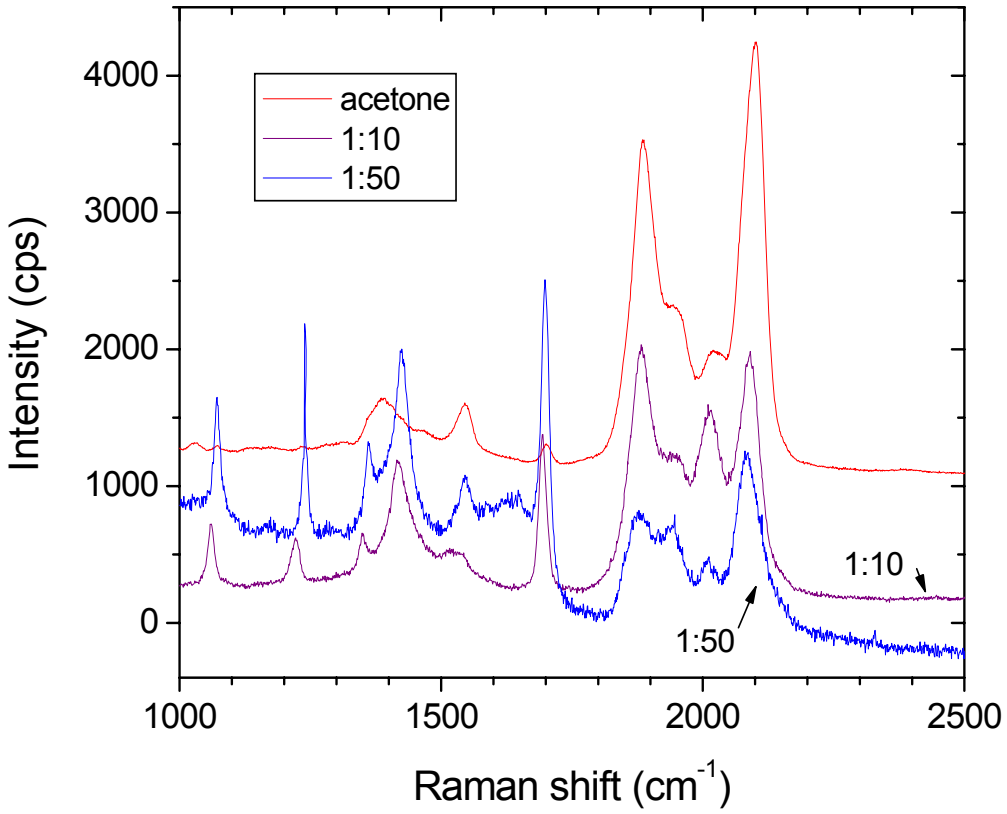

Fig. 7.8. SERS spectra of irradiated acetone diluted in pure acetone (HPLC grade).

Fig. 7.8 shows SERS spectra of diluted acetone after irradiation. Dilution leads to a reduction in the intensity of *sp*-bonded carbon chains. The vibration frequency shifts to lower energy is clearly evident. Such a red-shift can be explained by decreasing interchain crosslinking which increases the average chain length (Tanaba et al. 2006c).

Fig. 7.9 shows SERS spectra of pentane and octane irradiated with 50 fs pulsed trains with an attenuated intensity for 30 min. It is obvious that lower laser intensity results in longer carbon chains, which is evident by both the appearance and enhancement of a vibrational band at low frequencies. This can also be understood by decreasing thermal effects leading to enhanced stability of longer sp-bonded carbon species (Heymann 2005, Casari et al. 2006).

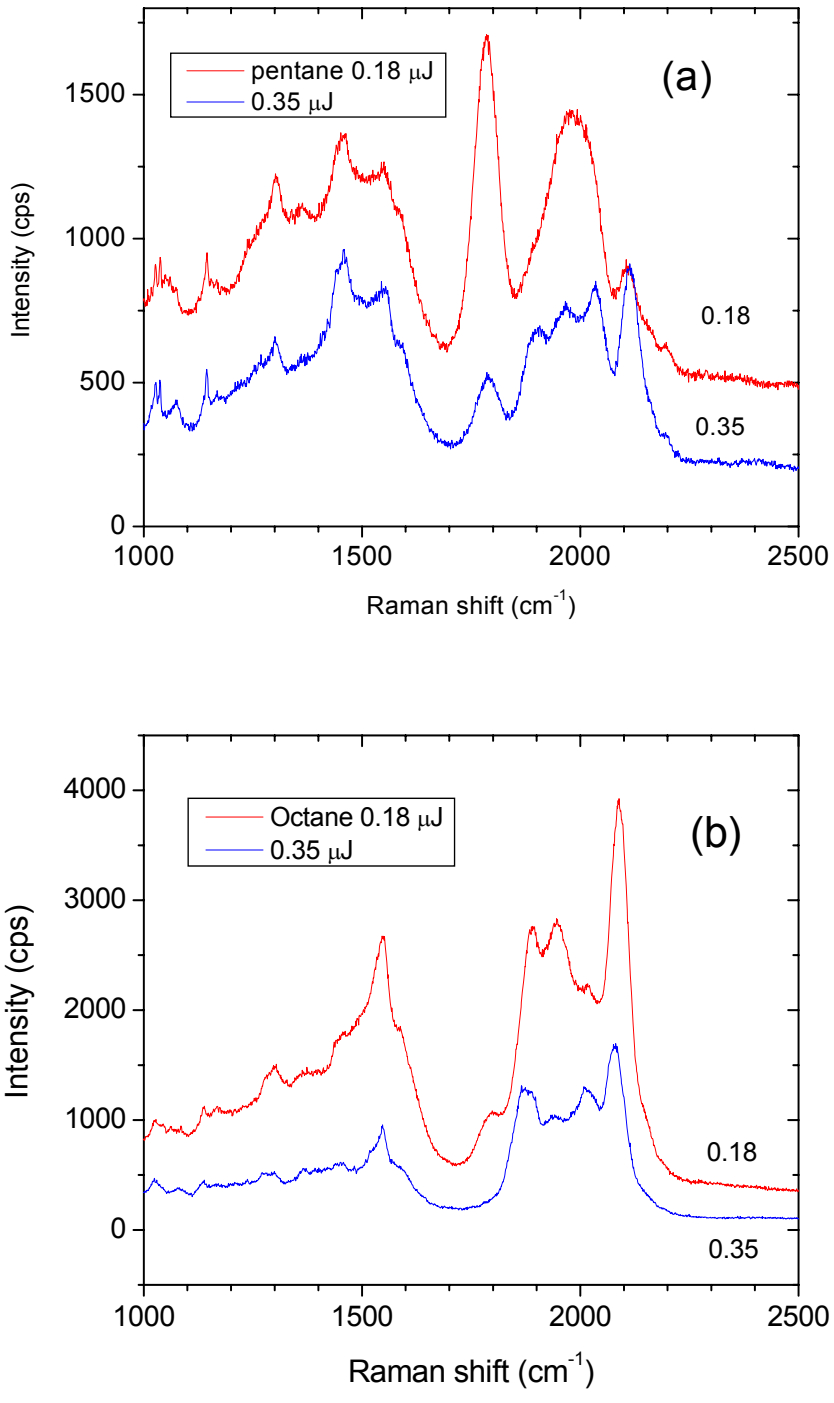

Fig. 7.9. SERS spectra of (a) pentane and (b) octane, two representative alkanes irradiated with 50 fs pulse trains at lower intensity.

7.3.2 High performance liquid chromatography and mass spectroscopy (HPLC-MS)

Fig. 7.10 shows HPLC spectra of irradiated hexanes measured at 198 nm. Similar characterizing conditions allow us to identify the species by comparison with previous studies (Eastmond et al. 1972, Tsuji et al. 2003, Cataldo 2004). The results show that 50 fs irradiation yields sp-bonded carbon chains of C_6H_2, C_8H_2, $C_{10}H_2$, $C_{12}H_2$, and $C_{18}H_2$. In addition, 120 fs irradiation results in C_6H_2, C_8H_2, $C_{10}H_2$, $C_{12}H_2$, $C_{14}H_2$ and $C_{16}H_2$. A peak at longer retention times after 50 fs irradiation may indicate the presence of longer carbon chains. These species have different concentrations but C_8H_2 is the dominant product. It is worth noting that the proportion of $C_{18}H_2$ and $C_{16}H_2$ are much high under 50 fs and 120 fs irradiation conditions, respectively. Both are dramatically different after nanosecond irradiation (Tsuji et al. 2003, Tanaba et al. 2006 a-c), where concentration decreases rapidly with increasing chain length and $C_{18}H_2$ and $C_{16}H_2$ are only found at a trace level (Cataldo 2004). The observation of longer carbon chains after 50 fs irradiation than after 120 fs irradiation can be attributed to a reduction of thermal effects at shorter pulse length.

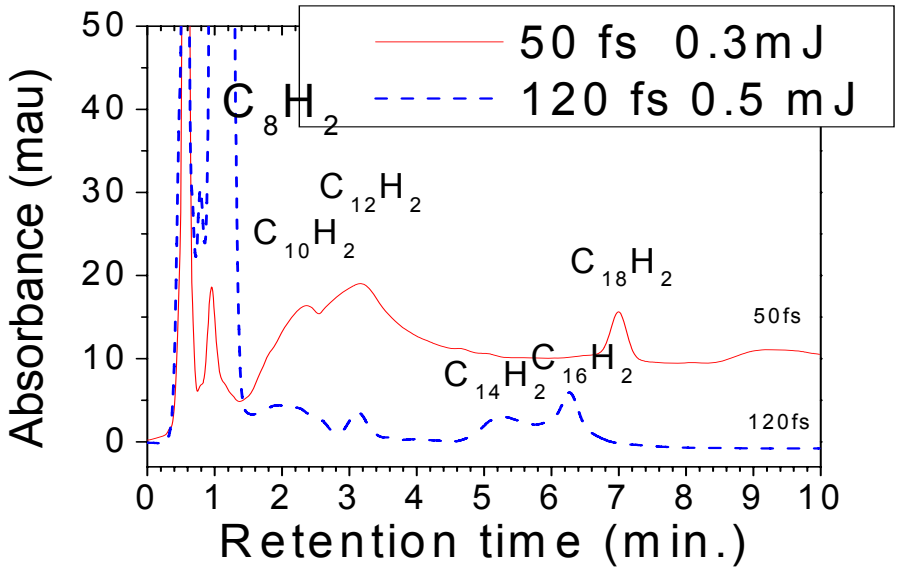

Fig. 7.10. HPLC spectra of products resulting from fs laser irradiation of hexanes at room temperature. The detection wavelength is 198 nm.

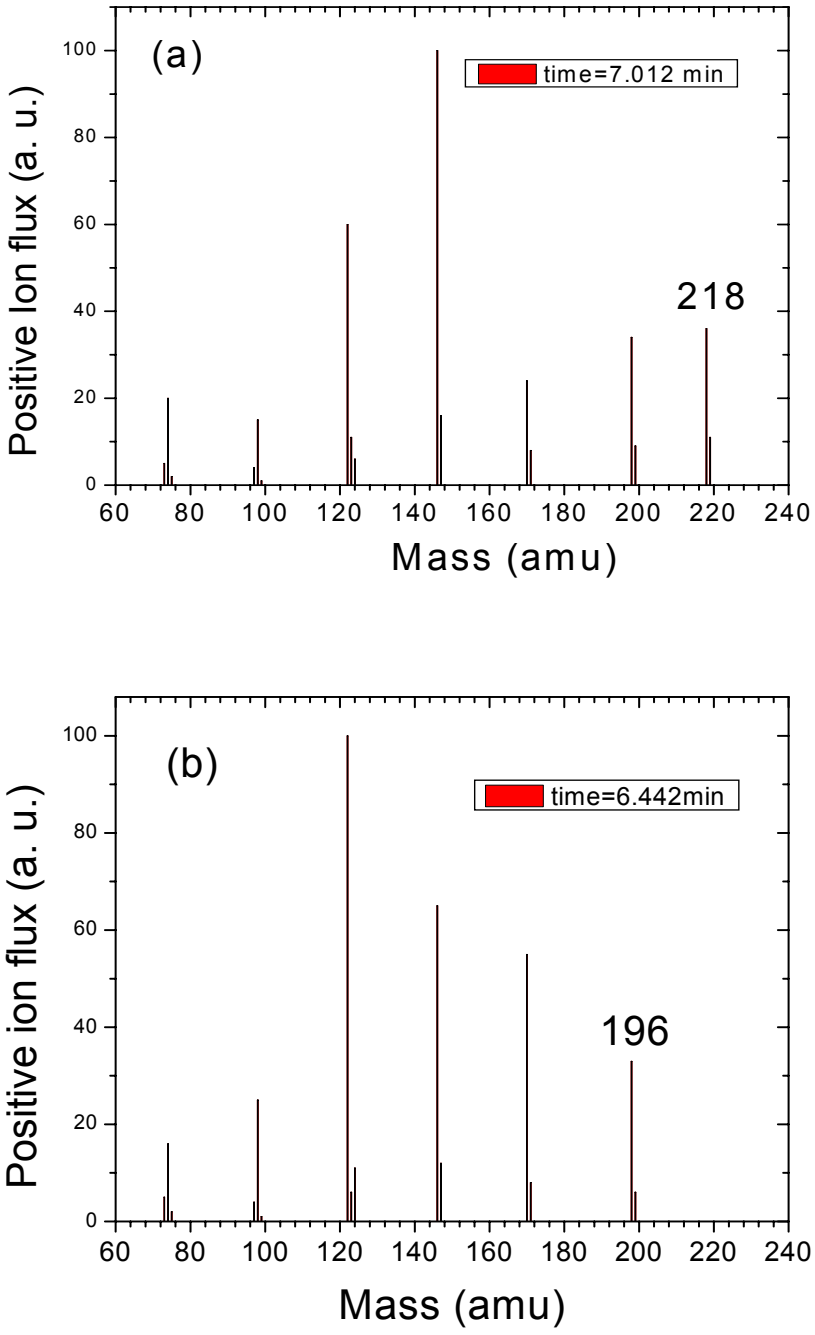

Fig. 7.11. Mass spectra of irradiated hexanes at certain retention times. (a) 7.012 min for 50 fs irradiation. (b) 6.442 min for 120 fs irradiation.

These assignments in the HPLC spectra are also consistent with mass spectra. Fig. 7.11 shows mass spectra of irradiated hexanes at 7.012 min for 50 fs irradiation and 6.442 min for 120 fs irradiation. It is evident that the maximum molecular mass is 218 and 196, respectively. This corresponds to $C_{18}H_2$ and $C_{16}H_2$, respectively. Other mass peaks correspond to isotope and the daughter species due to electrospray ionization.

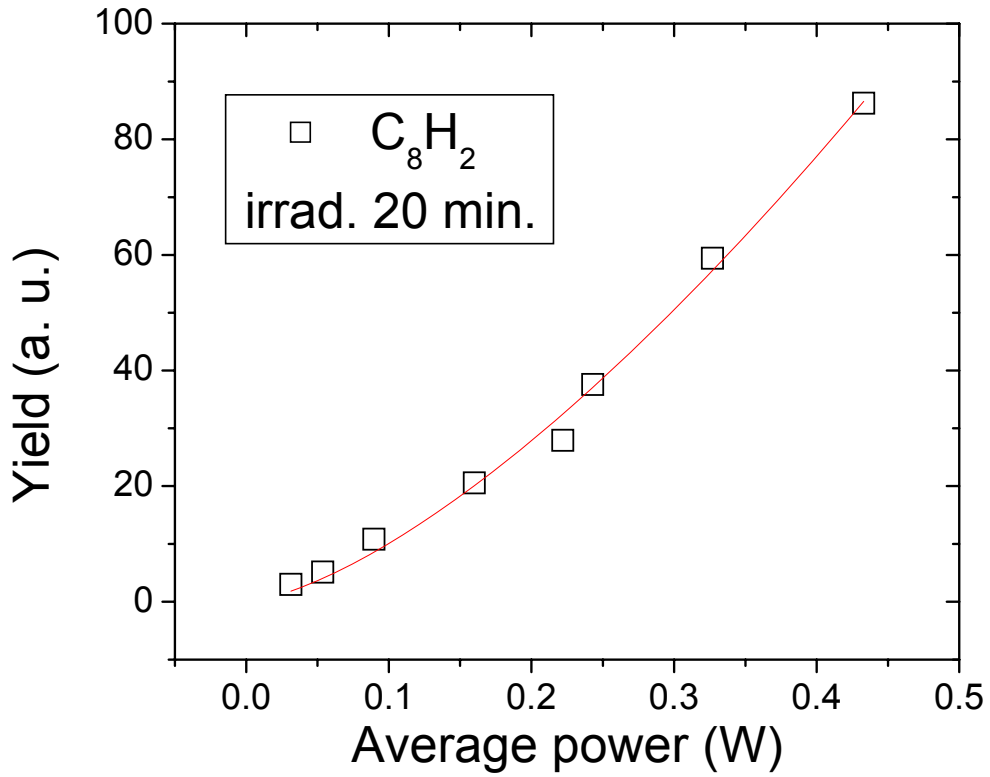

Fig. 7. 12. Yield of C_8H_2 as a function of average irradiation power in hexanes for 20 minute reaction time.

Fig. 7. 12 shows that C_8H_2 concentration in hexanes irradiated by 120 fs laser for 20 mins at a repetition rate of 500 Hz. The yield is estimated from the area of the HPLC peak at a retention time of 1.182 min. The best fit to these data gives $Y \propto I^{1.47}$, which corresponds to a nonlinear relationship. Since the irradiation products include series of carbynes, sp^2- and sp^3- bonded species, a multiphoton dissociation is expected.

7. 4. Synthesis of hexagonal nanodiamonds in organic solvents

Figure 7.13 shows Raman spectra of carbon films deposited using different transition metal targets in HPLC (high-performance liquid chromatography) grade hexane. Carbon films deposited using Cu show spectra that are typical of tetrahedral amorphous carbon in which the G band (the stretching band of graphite) at 1570 cm^{-1} overlaps with a D band (graphitic breathing mode) at 1350 cm^{-1} (Hu et al. 2006). A small bump near 1900 cm^{-1} can be attributed to Raman scattering from carbynes accompanying Cu nanoparticles (Hu et al. 2007b). Carbon films deposited from Co show two modes near 1320 and 1600 cm^{-1}, indicating the presence of a mixture of hexagonal diamond and microcrystalline graphite (Hu et al. 2007b, Knight et al. 1989, He et al. 2002). Carbon films deposited

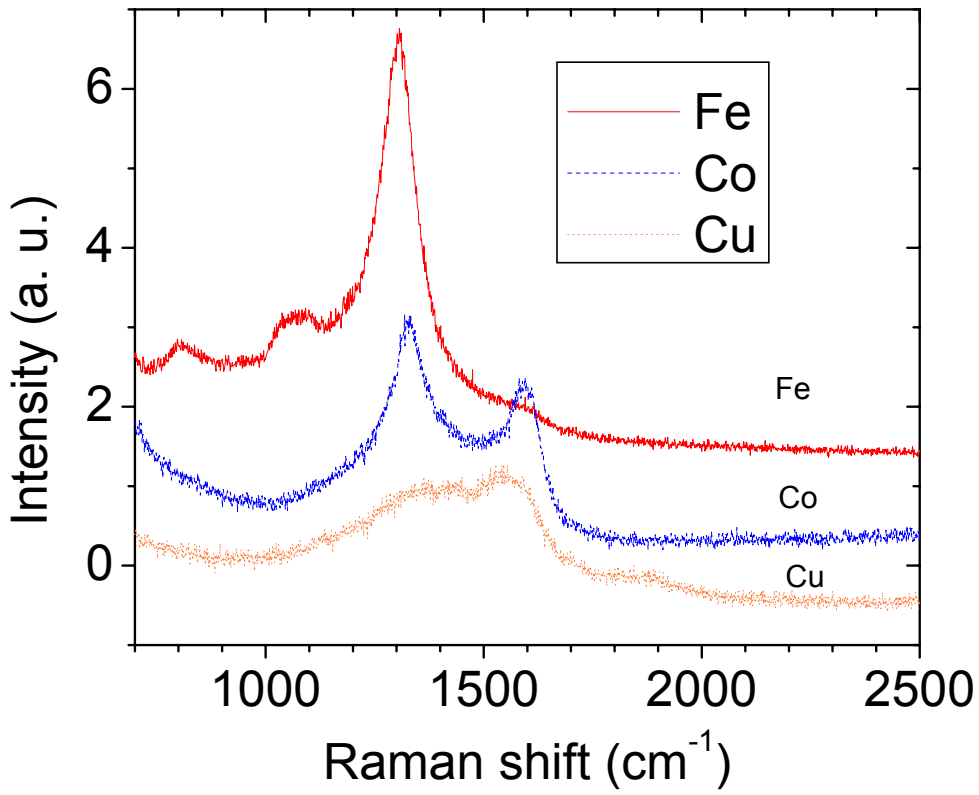

Fig. 7. 13. Raman spectra of diamond films deposited in liquid hexane after fs laser irradiation of Cu, Co and Fe.

from Fe show a strong Raman feature at 1308 cm^{-1} that can be attributed to hexagonal diamond (Hu et al. 2007b, He et al. 2002, Schwan et al. 1996). A weak band extending from 1050 to 1140 cm^{-1} can be assigned to trans-polyacetylene chains (Hu et al. 2007b, Ferrari and Robertson 2001). It is worth noting that pyrolytic amorphous carbon possesses two Raman modes centered at 1355 cm^{-1} and 1570 cm^{-1} (Darmstadt et al. 1997). It is thus evident that the presence of different metals can dramatically influence the final chemical binding states of carbon films. Fe is the proper choice for synthesizing hexagonal diamond in hexane.

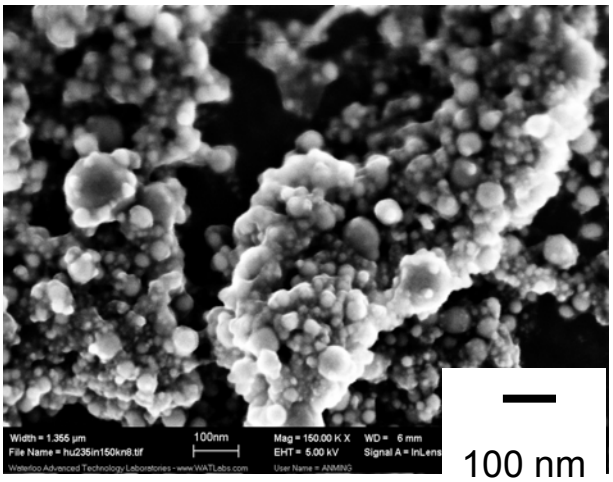

Fig. 7.14. Scanning electron microscopy (SEM) images of deposited nanodiamonds for Fe in hexane.

Fig. 7.14 shows a typical micrograph of hexagonal diamond films deposited in hexane after irradiation with a pulse energy of 350 μJ for 15 minutes. These films are assembled from individual NDs with an average size of 10 nm. Aggregated grains form larger structures with sizes up to several 100 nm. These films cover a substrate area of ≈ 1 cm^2 and have a thickness of ≈ 300 nm. Their thickness varies with distance and orientation relative to the focal point. Fig. 7.15 illustrates the evolution of chemical binding in these carbon films as characterized by the C1s core level XPS spectra with different alkanes as the parent organic compound. It is apparent that the C1s binding energy increases as the chain length in the alkane becomes longer. The small peak near 288.4 eV corresponds to C=O bonds. The fraction of different hybridized bonded carbon components can be

estimated by deconvolution of the C1s peak (Hu et al. 2007 c&d). Using this technique, deconvolution of the C1s core-level peak into sp^2-bonded carbon (284.4 eV) and sp^3-bonded carbon (285.2 eV) indicates that the fraction of sp^3- bonded carbon component is 72.6, 80.7 and 88.6% in pentane, hexane and hexadecane, respectively.

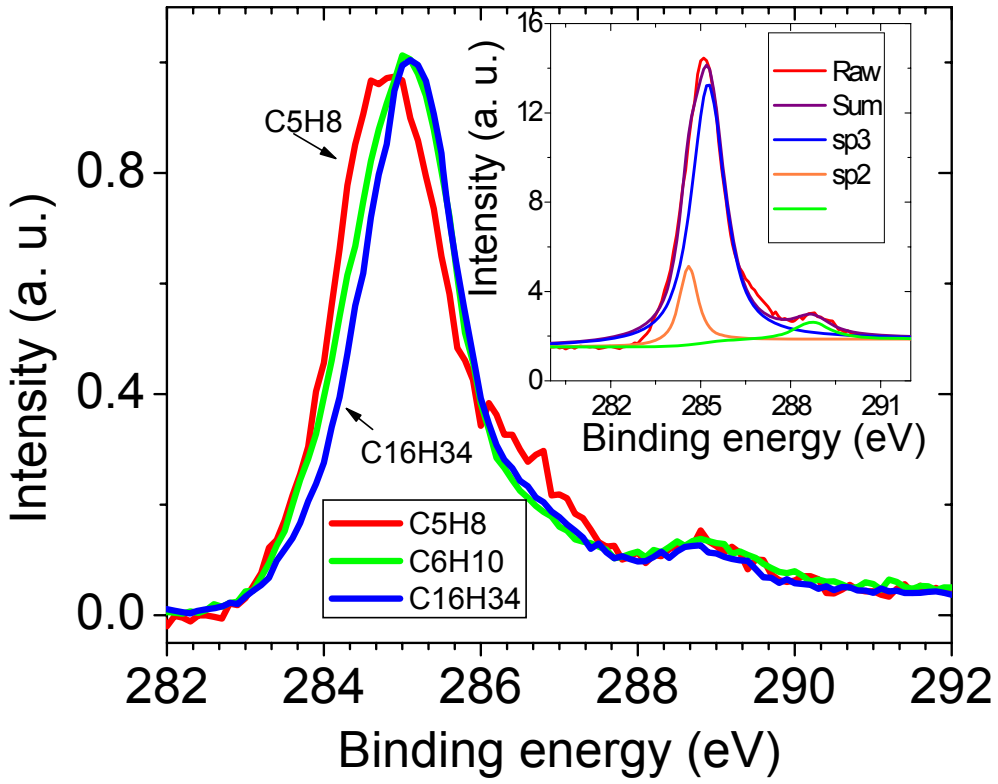

Fig. 7.15. XPS spectra for the C1s core-level binding energy for hexagonal nanodiamond synthesized in different alkanes. Inset: deconvolution of C1s peak with sp^2 and sp^3 binding energy at 284.4 eV, 285.2 eV, respectively. The peak at 288.4eV corresponds to a C=O bond.

7.5 Discussion

Additional experiments have shown that hexagonal diamond films can also be synthesized in a variety of other hydrocarbon liquids, including acetone, methanol, and benzene when Fe is used as the substrate at the laser focus. This suggests that the composition of the parent hydrocarbon is not

critical in the formation of hexagonal diamond as the liquid only acts as a source of carbon. It is well known that pyrolytic carbon can be synthesized by heating hydrocarbons to 700-1200^{o}C (Shi et al. 1997) but pyrolysis is unlikely in our experiments because the interaction between fs pulses and molecules is a non-thermal process (Hu et al. 2007d). Some additional insight into the photolysis of liquid hydrocarbons by fs radiation can be obtained from SERS spectra of the solution after irradiation. Figure 7.16 shows SERS spectra of pristine acetone and acetone after irradiation in the presence of Cu and Fe substrates. Spectra of irradiated solutions both show the

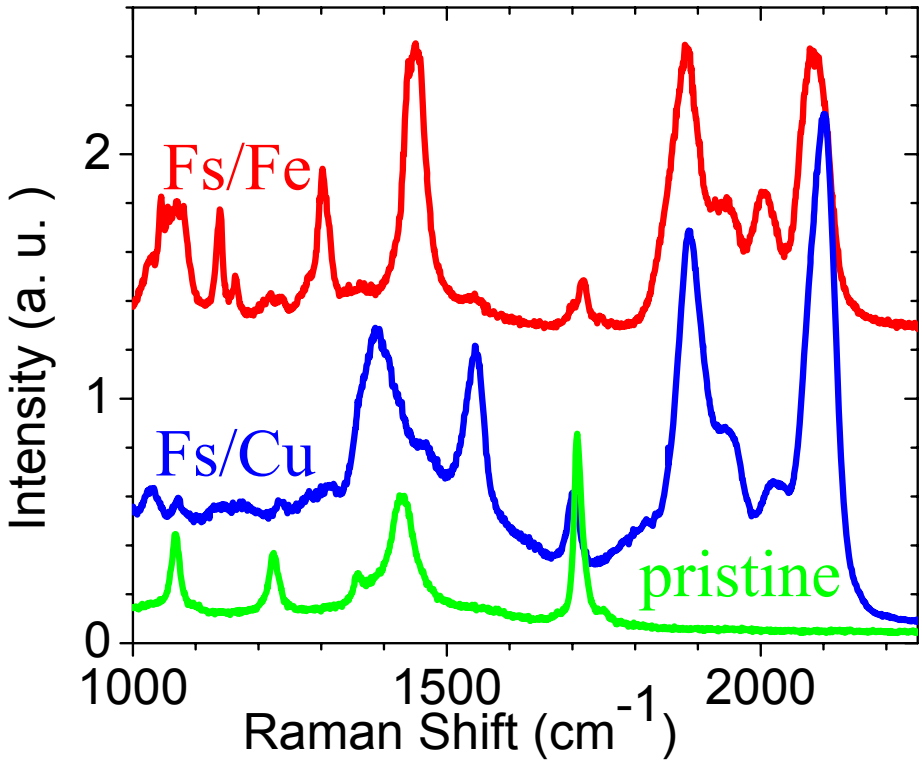

Fig. 7.16. Surface enhanced Raman scattering spectra for fs laser irradiated acetone with the presence of Fe or Cu. The SERS spectrum of pristine acetone is also given for comparison. Note that the spectra of irradiated acetone with and without the presence of Cu are the same.

characteristic Raman bands of carbynes at 1800-2200 cm^{-1} (Hu et al. 2007 c&d). This indicates that sp-bonded carbynes are one of the primary products of fs laser photolysis. It is important to point out that without a catalyst (directly focusing laser inside the liquid) and with the presence of Cu, the

spectra of irradiated solutions are identical and the amorphous carbon is evident in characteristics of 1370 and 1560 cm^{-1}. This suggests that Cu does not promote the formation of NDs. However, fs irradiation of hexanes with Fe results in hexagonal diamonds as evidenced by the Raman feature at 1308 $cm.^{-1}$, trans-polyacetylene chains with Raman modes at 1140, 1160 and 1450 cm^{-1} and carbynes. These results suggest that the dominant mechanism in fs irradiation may be multiphoton ionization which causes a step-wise dissociation of the precursor hydrocarbon molecules. This conclusion is in harmony with the gas product analyzed by gas-chromatography and mass spectrometry (GC-MS). In our experiments, the dissociation of hexanes yields C_2H_4 and CH_4. The dissociation of acetone yields CO and C_2H_4. We expect H_2 and H_2O should be included in the gas products, but it was difficult to be detected due to small molecule mass. This conclusion is further supported by the observation that C_2 dimers can act as fundamental building blocks in the growth of nanodiamond and carbynes (McCauley et al. 1998, Tsuji et al. 2002). In the dissociation process, chemical bonds will break in order of their binding energy. For example, the sequence of the primary dissociation of acetone involves the sequential breaking of C-C, C-O and C-H bonds as the laser intensity is gradually increased (Tang et al. 2003). To get elemental carbon and the carbon dimmer, all hydrocarbon bonds must be dissociated. It has been previously found that a laser intensity of $\approx 10^{15}$ W/cm^2 is required to dissociate C-H bonds (Buzza et al. 1996, Wang et al. 2003) and this condition is roughly satisfied in the current experiments. As this laser intensity is close to the threshold for Coulomb explosion of gas molecules, we attribute fs-induced dissociation in hydrocarbon solutions to this effect.

7.6 Conclusions

Isolated sp-bonded carbyne chains have been synthesized in various organic solvents by dissociation of hydrocarbon compounds and characterized by surface enhanced Raman spectroscopy, high performance liquid chromatography and mass spectrometry. Variable carbon chain lengths of alkanes lead different carbyne lengths. A long carbyne chain can be generated using large alkane molecules as the carbon source. The process is enhanced by the dissociation at lower pulse energy and with shorter pulse width. Diluted irradiated solvents also result in a increase in the concentration of longer carbyne chains.

Nanocrystalline hexagonal diamond films have been synthesized by fs laser dissociation of liquid hydrocarbons at room temperature. Spectroscopic studies show that the concentration of sp^3-bonded

carbon in these samples is ≥ 88.6%. This new synthetic route to hexagonal diamond solution may open up novel applications for this material in a variety of fields.

Chapter VIII

Theoretical vibrational spectra of nanocarbon species and time-of-flight mass spectra of fs pulsed laser ablation

8.1. Introduction

ab initio theoretical calculations based on density function theory (DFT) has been successfully applied to understand novel molecule structures, electronic binding states, vibrational spectra and optical and transportation properties, and even transient states. Recently, Raman spectra of polyynes (Lucotti et al. 2006, Tabata et al. 2006, Wakabayashi et al. 2007) and nanocrystalline, and electronic structure of one-dimensional and zero-dimensional graphene (Shemella et al. 2007) have been characterized. Such a study provides considerable insight into the nature of these nanocarbon species and further predicts novel applications, such as the properties required to form nanocables (Nishida 2006&2007) based on polyyne molecules encapsulated in single wall carbon nanotubes. There are also applications involving nanoscale field effect transitors (Ouyang et al. 2006, Obradovic et al. 2006), and nanobiosensors made of graphitic nanostrips (Gunlycke et al. 2007). Obviously, theoretical modeling is especially important when a pure polyyne compound is not available. In this Chapter we will investigate vibration modes and electronic structure of several carbon chain molecules. The discussion focuses on a comparison between theory and experimental results.

Although ex *situ* surface morphology and surface enhanced Raman spectroscopy yield many details on processes involved in laser-carbon interaction (Chapter II), time-of-flight mass spectroscopy (TOF-MS) is a direct tool to characterize ablated species and their relation to the evolution of carbon clusters. Previous studies used detectors with low mass resolution (Qian et al. 1995&1999, Banks et al. 1999, VanRompay et al. 1998, Lenner et al. 2007). A high resolution TOF spectrum of fs laser ablated carbon is not reported yet. In this study, a multi-channel plate (MCP) with a gain of over 10^6 is used as the positive ion detector. Narrow ion flight peaks allow us to identify highly charged ion species, small carbon clusters as well as carbon clusters with large molecular weight.

8.2 Computational procedure

Molecular species were modeled using the Gaussian 03 package. Calculations were performed using the three-parameter hybrid functionals of Becker and the correlation function of Lee, Yang, and Parr (B3LYP). The 6-31G(d) and 6-311G(d, p) bases were chosen for comparison, but major differences in calculated results were noted for most of the molecules that were investigated. Geometries were optimized using the Berny algorithm and vibrational frequencies were determined by computing the second derivatives of the energy with respect to the Cartesian nuclear coordinates.

To edit an input file for density function theory simulation using Gaussian package, Gauview03 is employing for an interface work station. The structure is first imaged and designed according to chemical basics and the single point energy is calucalted. Once a minimum of single point energy is found the structure is optimized. The vibration mode is further calculated according the optitimized structure. In most cases, the difficulties are that the single point energy calucation does not convege. This means that the structure can not be optimized. Several skills are employed to circumvent this issue: 1. The structure is first optimized with a low-level basis, like 3-21G and the advanced basis is calculated. 2. The structure is further distorted, such as, making the bond length a bit longer or shorter, and then caluculated. 3. An intermediated structure is achieved from the monitoring file of the broken calculation and then used as a new inout file after slight changes.

For the output file, the vibration frequency and intensity are given. Peak intensities correspond to the vibration strength according to quantum chemistry. Different mocules give different vibration intensities since these are their fingerprints. The frequency has to be scaled in order to compare to experimental spectra. The different bases have different scaling factors.

8.3 Vibrational spectra of sp-bond carbon chains

It is well known that linearly sp-bonded carbon chains (carbynes) can be formed either by alternating triple and single bonds (polyynes) or by conjugated double bonds (cumulenes). Fig. 8.1 shows two configurations of carbynes composed of 4 carbon molecules. Previous theoretical calculations proved that the first structure is energetically more favorable (Kertesz et al. 1978, Springborg and Kavan 1992).

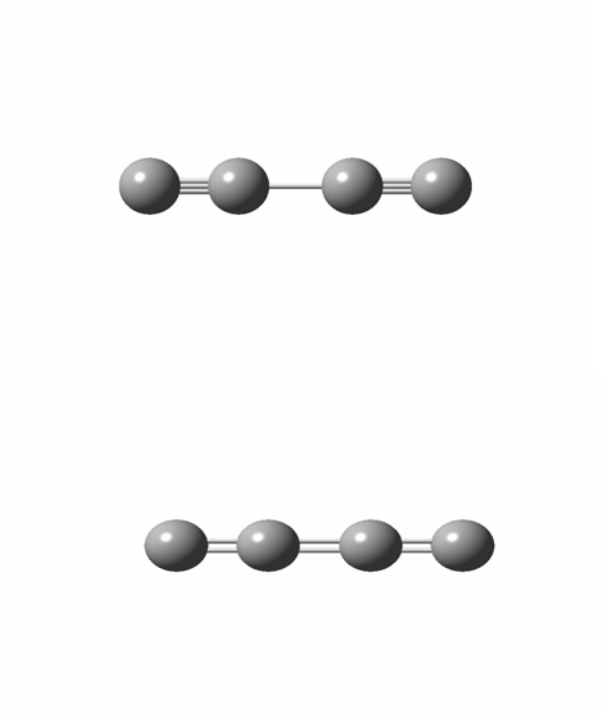

Fig. 8.1. Polyyne and cumulene structures of C_4 molecules.

Table 8.1 presents the optimized bond length in numerous C_n polyynes. The alternative chain structure is clearly evident. Meanwhile, the bond length for both trible bonds and single bonds in the middle is much shorter than that of the edge bonds, indicating a stronger interaction inside of molecule chains.

Table 8.1. Optimized bond lengths (Å) of polyynes C_n with n = 10-16 at the B3LYP level using the 6-31G(d) basis set

Bond	C10	C12	C14	C16
C1-C2	1.2963	1.2945	1.2933	1.2924
C2-C3	1.2953	1.2961	1.2967	1.2972
C3-C4	1.2764	1.2754	1.2745	1.2740
C4-C5	1.2856	1.2859	1.2864	1.2866
C5-C6	1.2781	1.2779	1.2774	1.2771
C6-C7	1.2856	1.2847	1.2847	1.2846
C7-C8	1.2764	1.2779	1.2783	1.2785
C8-C9	1.2953	1.2859	1.2847	1.2840
C9-C10	1.2963	1.2754	1.2774	1.2785
C10-C11		1.2961	1.2864	1.2846
C11-C12		1.2945	1.2745	1.2771
C12-C13			1.2967	1.2866
C13-C14			1.2933	1.2740
C14-C15				1.2972
C15-C16				1.2924

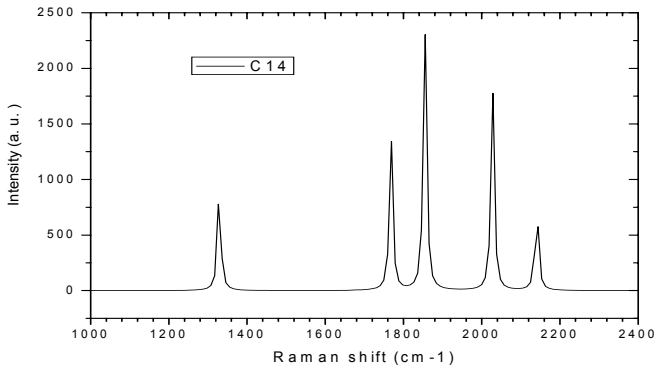

Fig. 8.2. Raman activities of calculated C_{14} molecules.

Fig. 8.2 shows calculated Raman spectra of C_{14} polyyne. Four strong stretching bands, centered at 1768, 1854, 2027 and 2140 cm^{-1} are apparent in the range of 1750-2200 cm^{-1} with a factor of 0.9614 (Scott et al. 1996). Fig. 8.3 shows the calculated vibration patterns in bond length from the equilibrium bond lengths of these 4 modes.

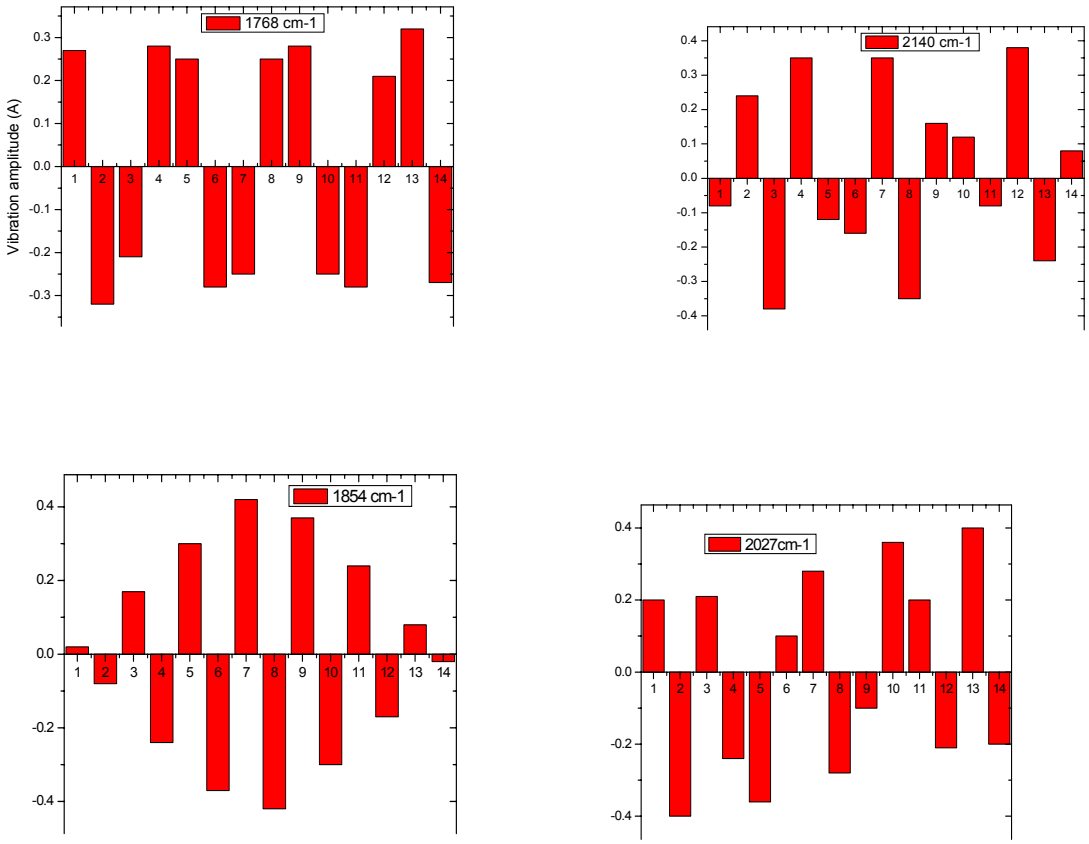

Fig. 8.3. Patterns of the CC stretching vibrational modes obtained by DFT simulation, with vibration at the indicated frequencies. The bars represent relative variations in bond length from the equilibrium bond lengths given in Table 8.1.

The patterns displaying at 1854 cm^{-1} turn out to be one kind of interesting modes for all polyyne chains: triple bonds expand and single bonds shrink. Such a mode appears at different frequencies depending on the total chain length of the molecule.

Fig. 8.4 shows a comparison between experimental spectra and calculated spectra. One can see that there is good agreement of frequencies between calculated and experimental SERS spectra of sp-bonded carbon chains.

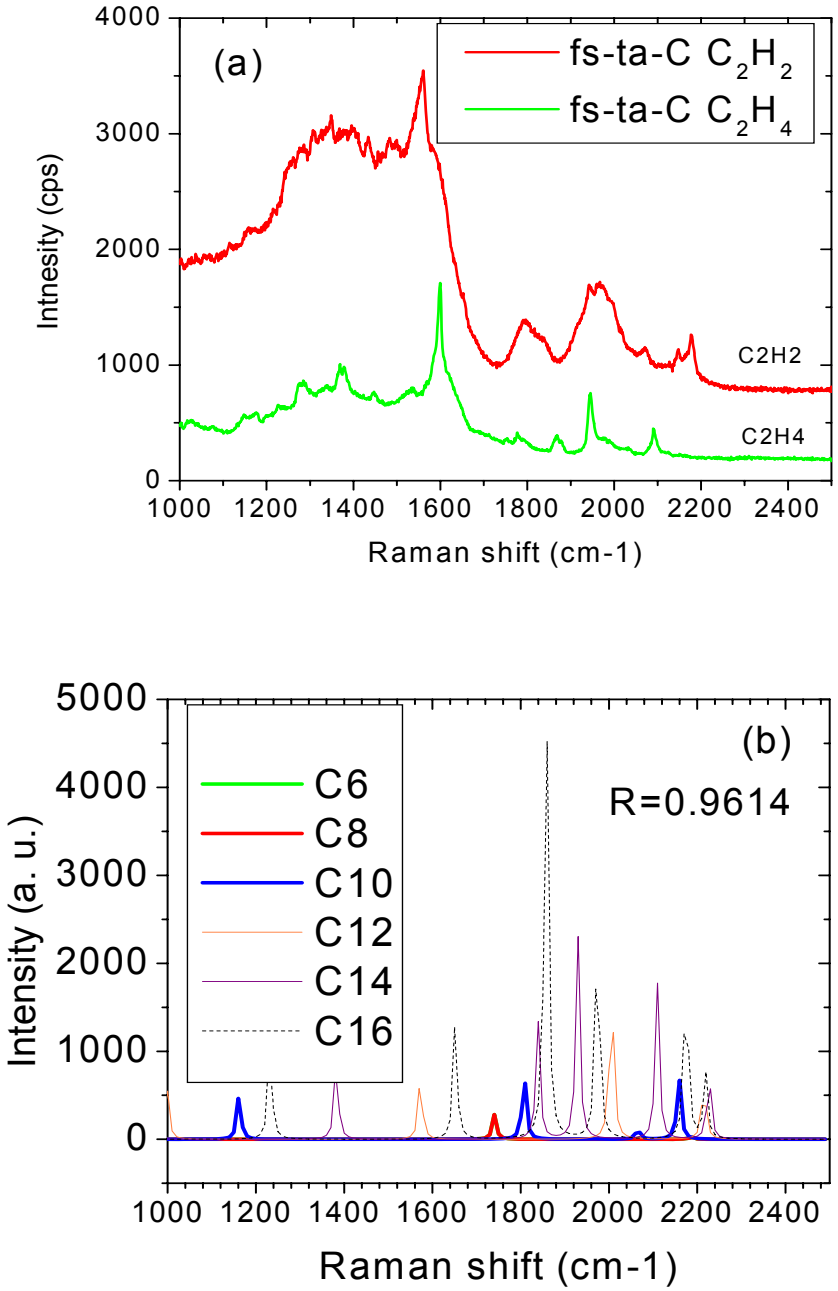

Fig. 8.4. (a) SERS spectra of fs-DLC films deposited in acetylene and ethylene and (b) calculated Raman spectra of linear carbon chains after application of a scaling factor of 0.9614.

This frequency agreement indicates that there is a distribution of different chain lengths for linear carbon molecules embedded in tetrahedral amorphous carbon films. Vibrational modes of C_8-C_{16} contribute to the Raman features found in the 1800-2200 cm^{-1} range. However, the spectrum intensities keep mismatching between theoretical and experimental spectra. This difference can be understood by considering different concentrations of individual polyynes. Since the SERS spectra of a film sample is still much broad, it is difficult to deconvolute experimental spectra based on theorectical calculation.

8.4 Polyynes terminated by either hydrogen or silver atoms

Table 8.2. Optimized bond lengths (Å) of H-terminated polyynes C_nH_2 with n = 10-16 at the B3LYP level using 6-31G(d) basis set

	$C_{10}H_2$	$C_{12}H_2$	$C_{14}H_2$	$C_{16}H_2$
H-C1	1.0666	1.0666	1.0648	1.0667
C1-C2	1.2161	1.2164	1.2220	1.2166
C2-C3	1.3558	1.3551	1.3556	1.3544
C3-C4	1.2285	1.2295	1.2338	1.2302
C4-C5	1.3445	1.3427	1.3428	1.3412
C5-C6	1.2314	1.2334	1.2379	1.2349
C6-C7	1.3445	1.3402	1.3391	1.3370
C7-C8	1.2285	1.2334	1.2390	1.2364
C8-C9	1.3558	1.3427	1.3391	1.3360
C9-C10	1.2161	1.2295	1.2379	1.2364
C10-C11		1.3551	1.3428	1.3370
C11-C12		1.2164	1.2338	1.2349
C12-C13			1.3556	1.3412
C13-C14			1.2220	1.2302
C14-C15				1.3544
C15-C16				1.2166

Table 8.2 presents optimized bond lengths (Å) of H-terminated polyynes C_nH_2 with n = 10-16 at the B3LYP level using 6-31G(d) basis set. These data are well corresponding to the bond lengths calculated with cc-pVDZ basis set (Tabata 2006) and 6-311G** basis set (Lucotti et al. 2006).

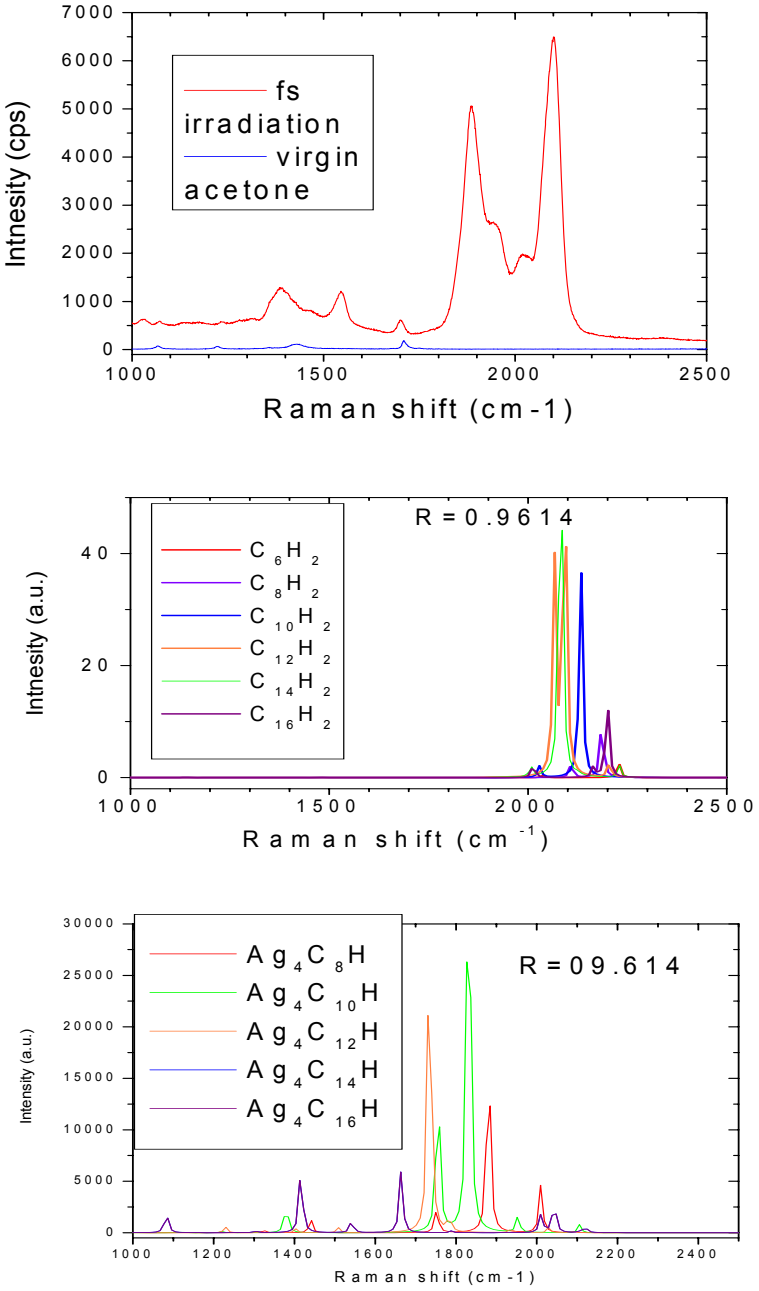

Fig. 8.5. SERS spectra of irradiated acetone (upper spectrum) compared to simulated C_nH_2 polyynes (middle) and simulated Ag_4C_nH molecules (lower spectrum).

To compare with experimental data, polyyne Raman vibrational spectra have also been calculated for molecules terminated with Ag atoms. DFT modeling for Ag uses a 3-21G* basis set. The SERS spectrum of acetone and calculated spectra for C_nH_2 and Ag_4C_nH molecules are shown in Fig. 8.5. Laboratory spectra can be partially reproduced by isolated C_nH_2 polyynes and by Ag terminated polyyne groups Ag_4C_nH. This confirms the presence of isolated polyynes directly synthesized by fs laser irradiation.

8.5 Trans-polyacetylene and cis-polyacetylene chains

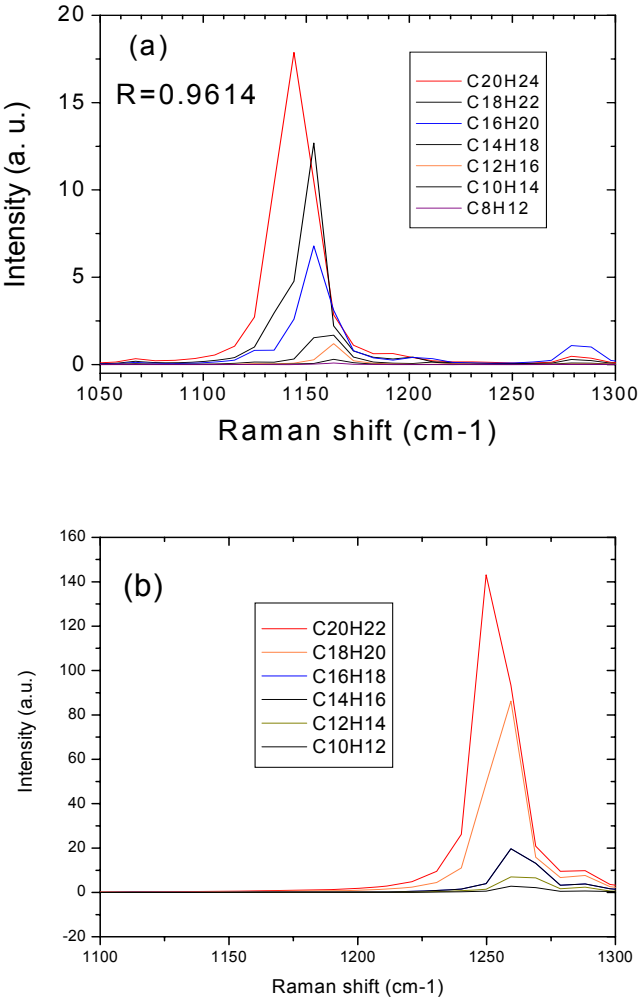

Fig. 8.6. Theoretical Raman spectra of (a) trans- and (b) cis-polyacetylene chains.

Fig. 8.6 shows Raman spectra of trans- and cis-polyacetylene chains in the 1000-1300 cm^{-1} frequency range. It is evident that the vibrational mode shifts to a lower energy with increasing chain length. Trans-polyacetylene chains possess Raman features in the 1100-1200 cm^{-1} region in agreement with the assignments of experimental SERS spectra of irradiated HOPG in chapter 2 and fs-DLC films in chapters 3-5. This indicates the presence of trans-polyacetylene chains in our samples.

8.6 Graphynes

Graphyne is a carbon allotrope, which consists of layered carbon sheets containing *sp* and sp^2 carbon atoms (Baughman et al. 1987). Recently graphyne and graphdiyne have been synthesized and consist of graphitic rings bridged by acetylenic (-C≡C-) and diacetylenic (-C≡C-C≡C-) linkages (Ferrara et al. 1987, Haley et al. 1997, Narita et al. 1998). Here we apply this structure to simulate sp/sp^2 dominant composition in fs-DLC films. Fig. 8.7 shows a graphyne molecule connected with acetylenic species. Fig. 8.8 presents theoretical Raman spectra of this graphyne molecule. In this spectrum, the vibrational mode of the acetylenic linkage is intense. The band at 1570 cm^{-1} corresponds to the stretching mode of graphitic ring and 3100 cm^{-1} corresponds to the stretching mode of C-H groups. These characteristics show features that are similar to the SERS spectra of fs-DLC films (chapters 3-5).

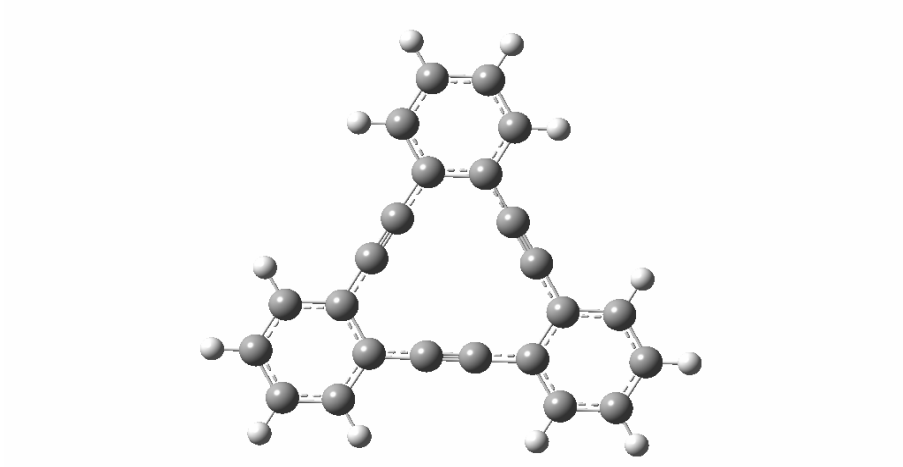

Fig. 8.7. Graphyne linked by acetylenic species and terminated with hydrogen.

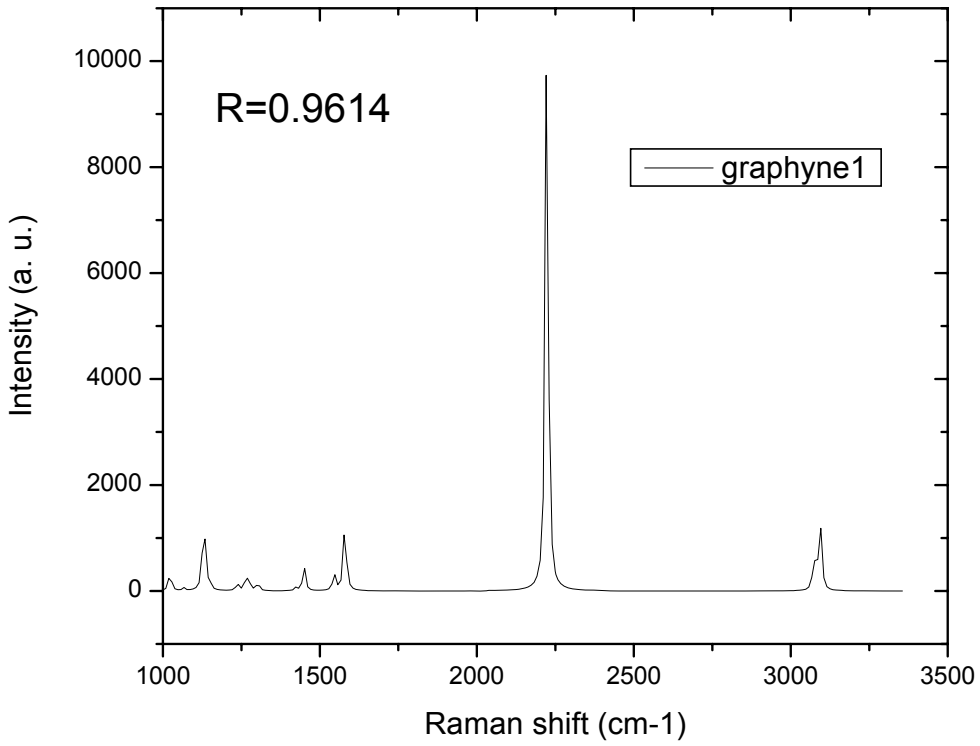

Fig. 8.8. Calculated Raman spectra of the graphyne molecule with acetylenic linkage.

8.7 Time-of-flight mass spectroscopy

Fig. 8.9 shows experimental configurations of time-of-flight mass spectrometry for fs laser ablation of graphite. The pulse number was controlled by a mechanical shutter with an exposure time of 7.5 ms. Within this period, 3 consecutive pulses can be chosen from a 500 Hz pulse train. The laser output was separated into two beams. The oscilloscope trigger signal was obtained from a diode and laser power was varied using an attenuator. The laser beam was tightly focused on the surface of graphite target with a 9 cm focal length lens. Ablation experiments were carried out at a pressure of 8×10^{-8} Torr. Ablated species are accelerated by a constant electric field with a voltage of 0 - 4 k V through 6.5 cm acceleration electrodes and then enter a free drift chamber with a size of 96.4 cm. A Chevron configured multichannel plate works as a positive ion

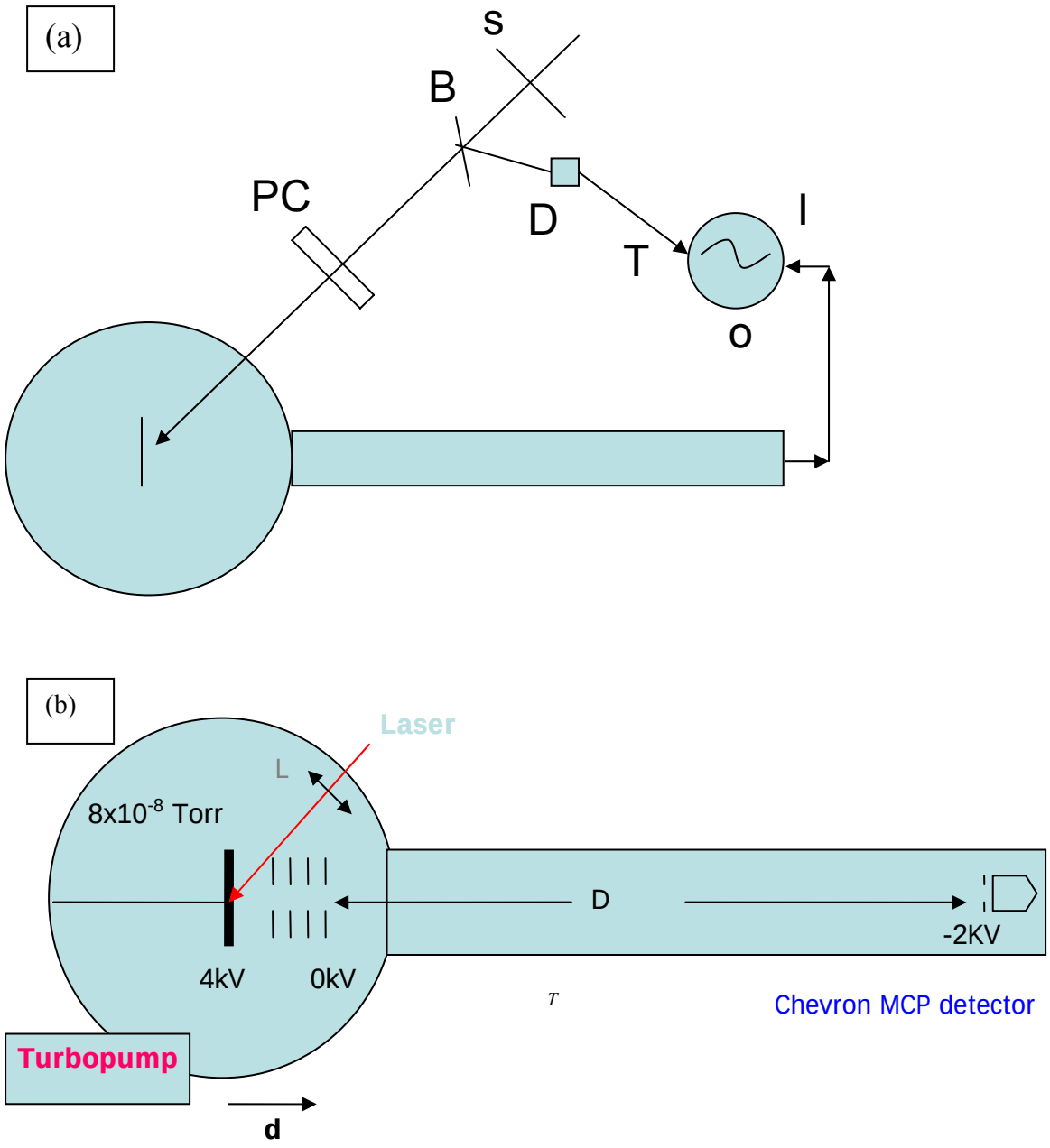

Fig. 8.9. Schematic diagram of the TOF-mass spectrometer. (a) light path: S: shutter, B: 95% beamsplitter, D: photodiode, PC: laser power attenuator, O: oscilloscope, T: trigger signal, I: input signal. (b) inside of ablation chamber, drift tube and MCP detector.

detector. The detector operates at ground potential with -2kV acceleration and the detector gain was ≥ 10^6. The light source is a 50 fs laser operating at 800 nm with a repetition rate of 1000 Hz. The average power is attenuated at a range of 0.019-0.255 W. According to the SEM images, the diameter of the irradiated crater at the surface of the HOPG was less than 100 μm. From this information, the incident laser intensity was found to range from 1.2 x 10^{14} - 1.63 x 10^{15} W/cm^2.

It is reasonable to assume that the length of the ion path can be obtained from the effect of a constant acceleration combined with a initial velocity. Then one can easily find that the time of flight can be expressed as

$$T_{ToF} = \frac{D}{\sqrt{v_o^2 + 2qU/m}} + d\frac{m}{qU}\left(\sqrt{v_o^2 + 2qU/m} - v_o\right) \qquad (8.1)$$

Where, V_o is the initial ion velocity, U is the acceleration voltage. d is the distance over which acceleration occurs, D is the drift length. In our case, d=6.5 cm and D=96.4 cm. By varying the acceleration voltage, one can easily determine the ratio of q/m and further identify the ions.

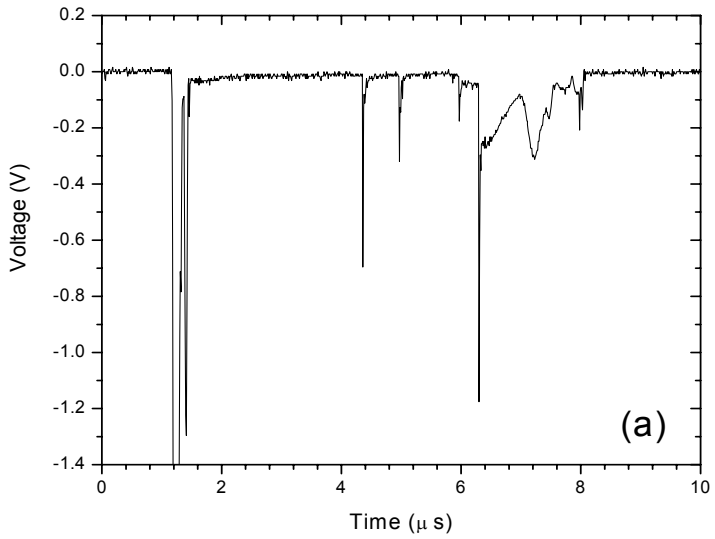

Fig. 8.10 Time-of-flight mass spectrum of carbon species ablated at an intensity of 1.96 x 10^{14} W/cm^2 with an acceleration voltage of 4 kV.

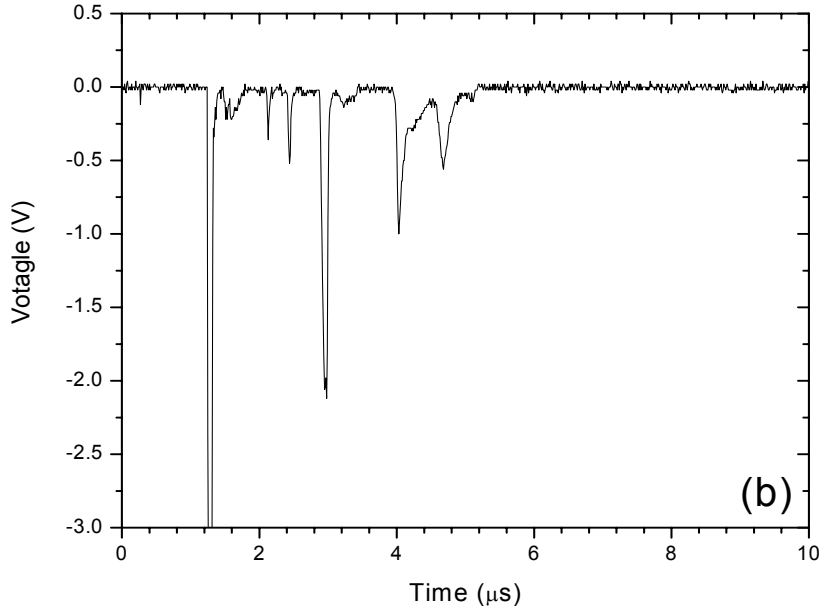

Fig. 8. 11 Time-of-flight mass spectrum of carbon species ablated at an intensity of 1.17 x 10^{15} W/cm^2 with an acceleration voltage of 4 kV.

Figs. 8.10-11 show TOF mass spectra of carbon species ablated at different laser intensities. It is apparent that several species appear at short times corresponding to high charged ions. These species are due to superheated ions (Qian et al. 1999, Ehler 1978). At lower incident laser intensity peaks associated with these ions become weaker. At intensities < 2 x10^{14} W/cm^2, these suprathermal species are undetectable. Instead, molecules are generated with lower drift velocity. It is notable that the present TOF spectra are quite different from those in previous reports (Qian et al. 1999, Banks et al. 1999), where only two suprathermal ion and plasma peaks were observed. This difference can be attributed to the higher resolution of the present detector. These species can be further identified by altering acceleration voltages. Using eq. (8.1) one can calculate the initial ion velocity at a certain charge/mass q/m ratio. It is reasonable to assume that initial velocity remains constant as the acceleration voltage changes since these initial velocities are produced in the laser-matter interaction. In addition highly oriented pyrolytic graphite is used as a target, and the incident laser beam is focused perpendicular to the HOPG surface. The use of a high purity target and the reproducibility of the irradiation conditions simplify the identification of mass peaks.

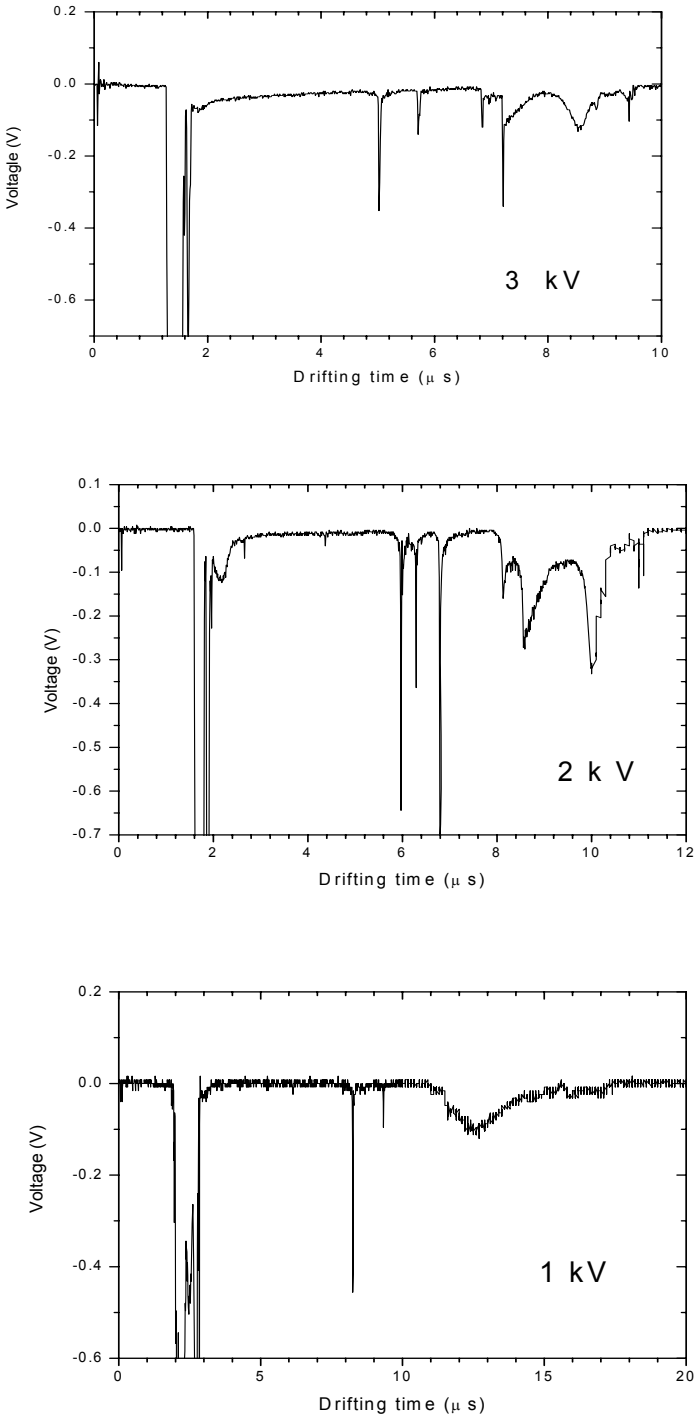

Fig. 8. 12 TOF mass spectra of carbon species ablated at 1.96 x 10^{14} W/cm^2 with an acceleration voltage 3kV (upper), 2kV (middle) and 1kV (lower).

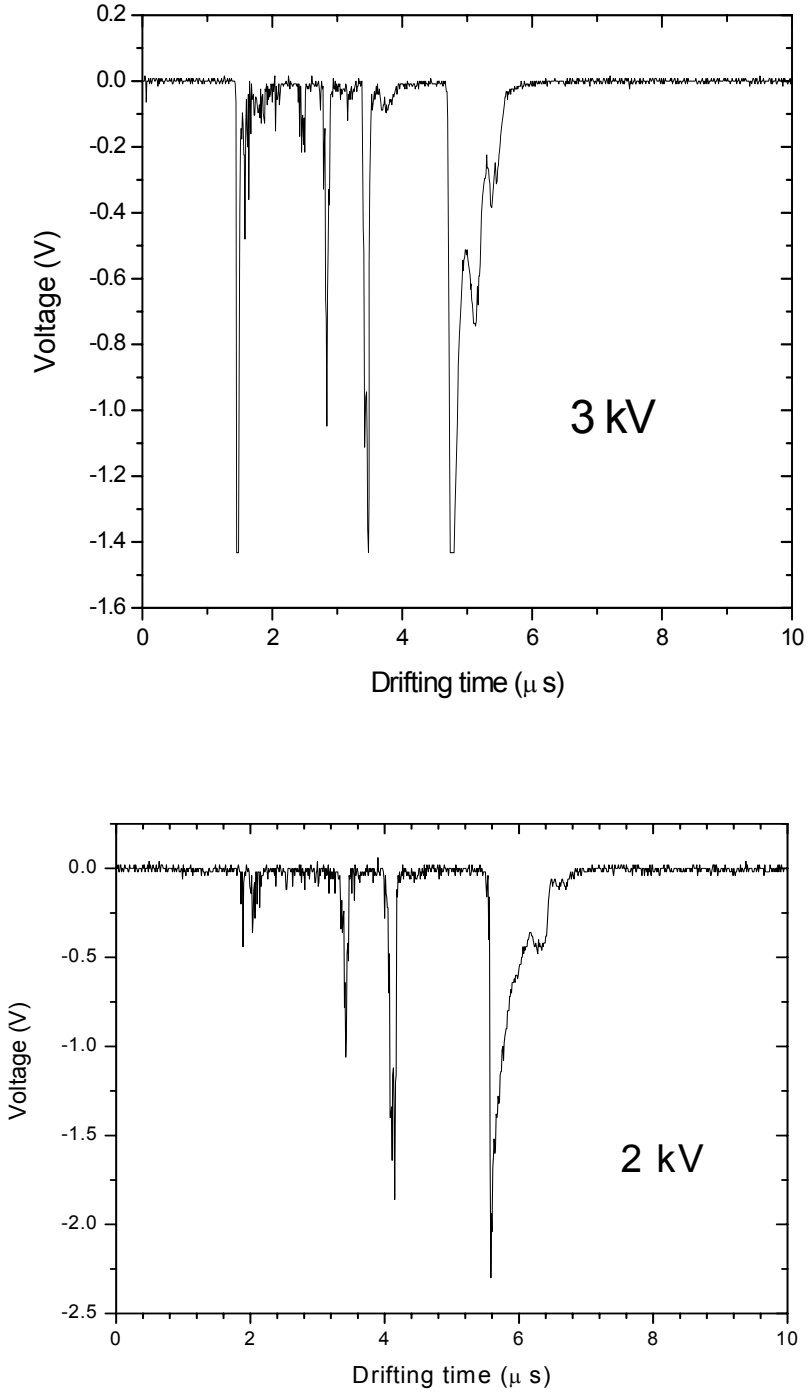

Fig. 8.13. TOF mass spectra of carbon species ablated at 1.17 x 10^{15} W/cm^2 with an acceleration voltage 3KV (upper), and 2KV (lower).

Figs. 8.12-13 show TOF mass spectra obtained at different acceleration voltages. Highly charged carbon species and small carbon clusters are assigned to individual peaks according to eq. (8.1). This analysis indicates that highly charged carbon species consist of C^{4+}, C^{3+}, and C^{2+}. Small carbon species correspond to C^+, C_2^+, C_3^+, C_4^+, and C_5^+. Table 8.3 gives the initial velocities as a function of incident laser intensity. Highly charged carbon ions have the higher velocities than that of the charged monomer (only one carbon atom), dimer (2C+), trimer (3C+), tetramer (4C+) and pentamer (5C+). This difference should be related to the ablation mechanism by fs pulses.

Table 8.3. Initial velocity (m/s) as a function of incident intensity (W/cm^2).

Intensity (w/cm^2)	C4+	C3+	C2+	C+	2C+	3C+	4C+	5C+
$1.63x10^{15}$	91300	83900	88200	42700				
$1.17x10^{15}$		70660	63000	32300				
$6.85x10^{14}$			56600	27600				
$3.32x10^{14}$			30098	14120	16100			
$1.96x10^{14}$				12790	15300	14500	13660	12160
$1.2x10^{14}$					14730	13900	12200	

It is notable that the velocity of C^{2+} monomer is almost double of that of C^+ monomer at a given incident intensity. This suggests that highly charged carbon particles are created by Coulomb explosion since the momentum scaling is common for multi-charged ions generated by such as mechanism (Lenner et al. 2007, Stoian et al. 2002). Under the Coulomb explosion picture, electrons which bond atoms forming the lattices are taken away by mutiphoton excitation. The positive ions are immediately (through a ultrafast procedure) expanded due to Coulomb repulsion. Injected ions will gain the initial kinetic energy through a similar accelerating potential. Obviously, if the momentum of multicharged ions can be scaled by their charged number this indeed means they are generated by the identical channel. It is hard for them to obey a momentum scaling law through a step-ionization because there are little possibilities for the further interaction between fs photons and ions once ions are generated. However, both C^{3+} and C^{4+} are not held a proper momentum scaling. This can probably be related to the pulse shape. The 50 fs pulse is not a well-established Gaussian pulse rather a narrow

pulse stands on an uncharacterized background pulse (under investigation). It is unclear if this background pulse can ionize species before the central peak comes. A detailed energy scanning can help elucidate this point. However, one can easily see the substructure of the fastest TOF peak in Fig. 10-13. To identify such a structure can be of benefits to understanding the Coulomb explosion. Further work is planning to focus on these issues.

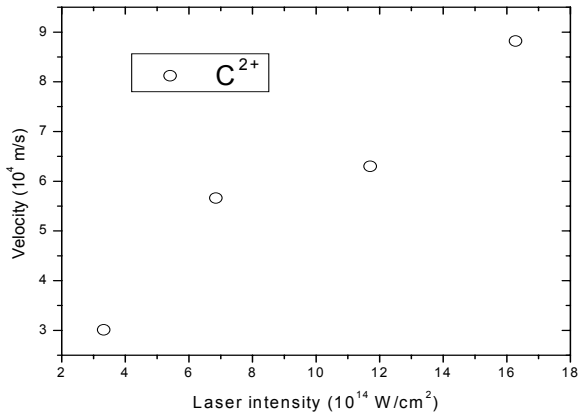

Fig. 8. 14. Initial velocity of C^{2+} as a function of incident laser intensity

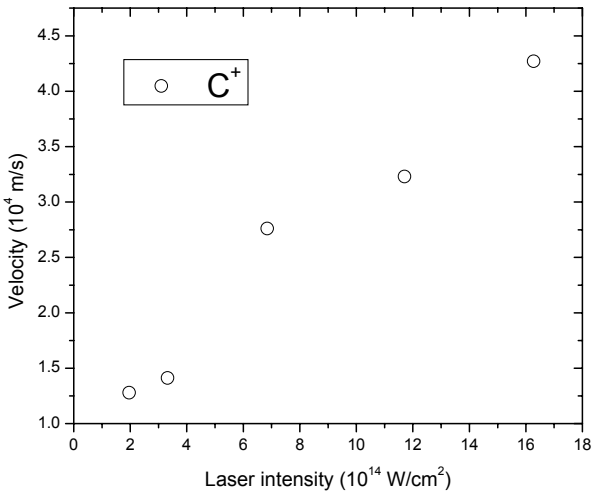

Fig. 8. 15. Initial velocity of C^{1+} as a function of incident laser intensity

Figs. 8. 14-15 show initial velocities verse incident laser intensity. It is evident that the initial velocities increase with incident laser intensity. This is consistent with previous reports of fs ablation (Qian et al. 1999, Banks et al. 1999).

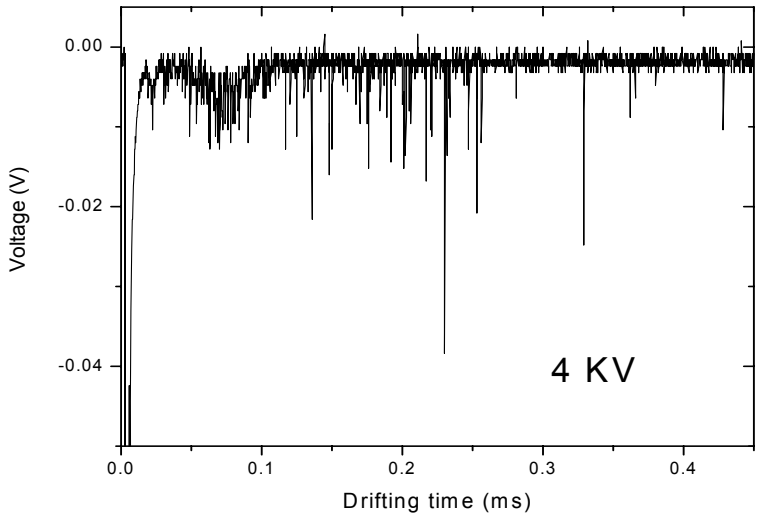

Fig. 8.16. TOF mass spectra of carbon species ablated at an intensity of 1.63 x 10^{15} W/cm^2.

Fig. 8.16 shows TOF mass spectra at long drift times. Large carbon clusters are clearly evident. The small ions, the most abundant products, are followed by some medium-size carbon clusters (N=10-40). Some heavy ions with N=300-500 are also detected.

8.8. Conclusions

Theoretical calculations confirm that there are abundant linearly *sp*-bonded polyyne molecules embedded in fs-DLC films. The simulations carried out indicate that these carbon chains occur as linkages to form large carbon molecules by linking graphitic rings and nanodiamonds. Isolated hydrogen-terminated polyyne chains are also evident in various irradiated organic liquids.

Time-of-flight mass spectra show the presence of highly charged carbon species. Momentum scaling confirms that ablation is due to Coulomb explosion. The initial kinetic energy of highly charged ions is up to several keV, while small carbon species possess energies of a few hundred eV.

Chapter IX

Suggestions for Future Work

Through my Ph. D research work the following conclusions have been obtained: 1. Interaction between fs pulses and HOPG is a nonthermal processing. We have successfully synthesized polyynes on HOPG surface by fs irradiation. 2. During interaction with carbon, nanopatterns of carbon particles are induced by optical orientation of fs pulses. 3. Coulomb explosion is evident by TOF mass spectra of fs ablation of carbon. 4. Molecular structure and chemical binding states are elucidated by combining UV/Vis/SERS Raman, XPS and UV/NIR optical spectroscopy. These results are further applied to simulate and identify astronomical spectra. 5. Isolated polyyne chains and hexagonal nanodiamonds are successfully synthesized by the direct disassociation of hydrocarbon solvents by fs pulses. 6. Calculation indicates the polyyne in both fs-ta-C and fs-a-solvent has a chain length between 2-8 C-C pairs. The major accomplishments are listed below:

1. We have elucidated the interaction between fs laser pulses and solid carbon.
2. We have developed two novel methods to synthesize polyynes and nanodiamonds in graphite surface and in organic solutions. Both have high scientific value and possible high commercial potiential.
3. We build our own surface enhanced Raman spectroscopic methods and materials, which can repeatably characterize solid thin films and solutions with very high resolutions.
4. Based on these works I have published 10 1st authored papers (excludes one under review) on professionally referenced journals. Half of them are the leading journals on Applied physics, Chemical Physics. and Astrophysics. Some of them are immediately cited by other researchers and virtual journals of Ultrafast Science and Applied Physics.

During these researches some new topics are founded and planning to be investigated in the future work. Some of them are presented below:

1. Identification of heavy species by time-of-flight mass spectroscopy in femtosecond laser ablation has been initiated in a following cooperation project.
2. Deposition and dissociation with a few fs short pulses (less than 10 fs) will be of interest to extend present studies.

3. Present works display that nanocarbon possesses novel magnetic properties. The nature of nanomagnetism is unclear. Theoretical calculation is possible to probe the spin distribution of graphitic nanoribbons with variable boundaries. However, further experimental and theoretical investigations are desired to elucidate femtosecond laser irradiation-induced magnetization.
4. Surface enhanced Raman spectroscopy has a capacity of the ultrahigh resolution to detect single molecule. The development of the periodic array of silver nanoparticle is very promising to develop practial molecular analystic methods and investigate cold surface plasmons.
5. Application of the nanodiamond solution and surface nano-engineering to biomedical projects is highly rewarding. This is being carried out in a postgraduate study.

Appendix A
List of Publications

PUBLICATIONS IN REFEREED JOURNALS

[11] **A. Hu**, and W. W. Duley, "16-20 Micron spectra of carbon nanoparticles", ***Astrophysical Journal Letters***, **672**, L81 (2008)

[10] **A. Hu**, and W. W. Duley, "Surface enhanced Raman spectroscopic characterization of molecular structures in diamond-like carbon Films", ***Chem. Phys. Lett***. **450**, 375 (2007)

[9] **A. Hu**, M. Rybachuk, Q. –B. Lu ,W. W. Duley, "Direct synthesis of *sp*-bonded carbon chains on graphite surface by femtosecond laser irradiation***", Appl.. Phys. Lett.*** **91**, 131906 (2007)

[8] **A. Hu**, S. Griesing, M. Rybachuk, Q. –B. Lu, W. W. Duley, "Nanobuckling and X-ray photoelectron spectra of carbyne-rich tetrahedral carbon films deposited by fs laser ablation at cryogenic temperatures", ***J. Appl. Phys.*** **102**, 074311 (2007)

[7] **A. Hu** , Q. –B. Lu ,W. W. Duley, M. Rybachuk, "Spectroscopic characterization of carbon chains in diamond-like carbon films synthesized by femtosecond pulsed laser deposition", ***J. Chem. Phys.*** **126**, 154705 (2007)

[6] **A. Hu** and W. W. Duley, "Laboratory simulation of 11-15 micron spectra associated with polycyclic aromatic hydrocarbon molecules", ***Astrophysical Journal Letters*** **660,** L137-L140 (2007)

[5] **A. Hu** , M. Rybachuk, I. Alkhesho, Q. –B. Lu ,W. W. Duley, "Nanostructure and sp/sp^2 clustering of tetrahedral amorphous carbon thin films grown by femtosecond laser deposition"
Journal of Laser Applications, (2008) in press

[4] **A. Hu**, I. Alkhesho, H. Zhou, W. W. Duley, "Optical and Microstructural Properties of Diamond-like Carbon Films Grown by Pulsed Laser Deposition", ***Diamond and Related Materials***, **16,** 149-154 (2007)

[3] **A. Hu**, I. Alkhesho & W. W. Duley, "High-resolution spectra of carbon nanoparticles: laboratory simulation of the infrared emission features associated with polycyclic aromatic hydrocarbons" ***Astrophysical Journal Letters*** **653**, L157-160 (2006).

[2] **A. Hu**, I. Alkhesho, H. Zhou and W. W. Duley, "Cryogenic graphitization of submicrometer grains embedded in nanostructured tetrahedral amorphous carbon films", ***J. Appl. Phys.*** **100**, 084319 (2006).

[1] **A. Hu**, J. Sanderson, C. Wang, and W. W. Duley, "Synthesis of nanocrystalline hexagonal diamond in organic solvents by fs laser irradiation", submitted

COLLABORATION

[5] C. Xu, **A. Hu**, N. Sakai, I. Hirabayashi, M. Izumi, "Enhanced superconducting properties of air-processed $GdBa_2Cu_3O_{7-\delta}$ single domains with $BaCO_3/BaCuO_{2-x}$ addition", ***J. of Supercond. and Novel Magnetism***, 20 (2007) 309

[4] **A. Hu**, C. Xu, M. Izumi, I. Hirabayashi, M. Ichihara, "Enhanced flux pinning of air-processed $GdBa_2Cu_3O_{7-\delta}$ superconductors with addition of ZrO_2 nanoparticles", ***Appl. Phys. Lett.*** 89 (2006) 192508

[3] M. R. Koblischka**,** M.Winter, **A. Hu**, M. Murakami and U. Hartmann, "Stripe and criss-cross patterns in high-Tc superconductors revealed by AFM and STM***", Jpn. J. Appl. Phys.*** 45 (2006) 2259

[2] **A. Hu**, I. Hirabayashi, M. Winter, M. R. Koblischka, H. Zhou, "Nanoscopic netted structure of compositional modulation in $(Sm_{0.33}Eu_{0.33}Gd_{0.33})Ba_2Cu_3O_{7-x}$ superconductors", ***Appl. Phys. Lett***. 86 (2005) 092505

[1] M. R. Koblischka, M. Winter, **A. Hu**, M. Muralidhar, U. Hartmann and M. Murakami, "Nanoscaled flux pinning sites in high-Tc superconductors", ***Phys. Status Solidi C*** 2 (2005) 1720

PUBLICATION IN REFEREED PROCEEDINGS

(bulk for presenter)

[5] **M. Rybachuk**, J. M. Bell, A. Hu, "sp-linear chains and photoexcited trans-polyacetylene in diamond-like carbon", oral presentation, Diamond 2008, Nagano, Japan. To be published on ***Carbon***.

[4] **A. Hu**, J. Sanderson, and W. W. Duley, "Optical orientation of amorphous carbon nanoparticles on the surface of graphite exposed to fs laser pulses**",** oral presentation on MRS-fall meeting, Boston, USA, Nov. 2007

[3] **A. Hu** and W. W. Duley **"**Synthesis of nanocrystalline hexagonal diamond films in organic solvents by femtosecond laser irradiation**",** poster presentation on MRS-fall meeting, Boston, USA. Nov. 2007, MRS conference proceeding, *in press*.

[2] A. Hu, M. Rybachuk, Q-B. Lu, **W. W. Duley**, "Femtosecond pulsed laser deposition and optical properties of diamond-like amorphous carbon films embedded with sp-bonded carbon chains", presentation on Diamond 2007, Berlin, Germany, Sept. 2007. Diamond Related Materials (2008) *in press*.

[1] **H. Zhou**, W. Martens, T. Tesfamichael, G. Will, A. Hu, J. M. Bell, "Microstructures and photocatalytic properties of Nitrogen-Implanted titania Nanostructured films", oral presention in the SPIE international symposium "Microelectronics, MEMS, and Nanotechnology", Brisbane, Australia, Dec. 11-14, 2005, SPIE proceedings 6037 (2005) 6037 0F

Bibliography

Adhikary S., Tian X. M., Adhikari S., Omer A. M. M.. Uchida H., and Umedo M., 2005. Diamond Red. Mater. **14**, 1832.

Ager III J. W., Anders S., Anders A., and Brown I. G., 1995. Appl. Phys. Lett. **66,** 3444.

A Il'insky Yu. And Keldysh L. V., 1994. "Electromagnetic Response of Material Media", Plenum, New York.

Akmanov S. A., Emel'yanov V. I., Kototeev N. I., and Seminogov V. N., 1985. Sov. Phys. Usp. **28,** 1084.

Akagi K., Nishgushi M., and Shirakawa H., 1987. Synth. Met. **17**, 557.

Amaratungnga G. A. J., 2002. Science **297**, 1657

Andrew P., and Barnes W. L., 2004. Science **306**, 1002

Angus J. C., Jansen F., 1988. J. Vac. Sci. Technol. **6**, 1778.

Anisimov S. I., Kapeliovich B. I., Perel'man T. L., 1974. *Sov. Phys. –JETP* **39**, 375.

Baidakova M. and Vul A., 2007. J. Phys. D: appl. Phys. **40**, 6300.

Banks P. S., Dinh L., Stuart B. C., Feit M. D., Komashko A. M., Rubenchik A. M., Perry M. D., McLean W., 1999. Appl. Phys. A **69**, S347.

Baughman R. H., Eckhardt H., and Kertesz M., 1987. J. Chem. Phys. **87**, 6687.

Beeman D., Silverman J., Lynds R., and Anderson M. R., 1984. Phys. Rev. B **30**, 870.

Benchikh N., Garrelie F., Donnet C., Wolski K., Fillit R. Y., Rogemond F., Subtil J. L., Rouzaud J. N., and Laval J. Y., 2006. Surf. Coat. Tech. **200**, 6272.

Berger C., Song Z., Li X., Wu X., Brown N. Naud C., Mayou D. Li T., Hass J. Marchenkov A. N., Conrad E. H., First P. N. and Heer W. A. 2006. Science **312**, 1191

Bernholc J., Phillips J. C., 1986. J. Chem. Phys. **85**, 3258.

Biswas R. and Amebegaokar V., 1982. Phys. Rev. B **26**, 1980

Bogana M., Ravagnan L., Casari C. S., Zivelonghi A., Baserga A., Li Bassi A., Bottani C. E., Vinati S., Salis E., Piseri P., Barborini E., Colombo L., and Milani P., 2005. New J. Phys. **7**, 81.

Bolgiaghi D., Miotello A., Mosaner P., Ossi P. M., Radnoczi G., 2005. Carbon **43**, 2122.

Bonelli M., Mitotello A., Ossi P. M., Pessi A., Gialanella S., 1999. Phys. Rev. B **59**, 13513

Borowiec A.and Haugen H. K., 2003. Appl. Phys. Lett. **82**, 4462.

Bowden N., Brittain S., Evans A. G., Hutchinson J. W., and Whitesides G. W., 1998. Nature **393,** 146.

Bugaev A. A., Zakharchenya B. P., Ivanov M. G., and Merkulov I. A., 1986. Sov. Tech. Phys. Lett. **12**, 91.

Bundy F. P. and Kasper J. S., 1963. Science **139**, 340.

Bundy F. P., Bassett W. A., Weathers M. S., Hemley R. J., Mao H. K., and Goncharov A. F., 1991. Carbon **34**, 141

Buzza S. A., Snyder E. M., and Castleman Jr. A. W., 1996. J. Chem. Phys. **104**, 5040.

Carey J. D. And Silva S. R. P., 2004. Phys. Rev. B **70**, 235417.

Casari C. S., Li Bassi A., Ravagnan L., Siviero F., Lenardi C., Piseri P., Bongiorno G., Bottani C. E., and Minani P., 2004. Phys. Rev. B **69**, 075422.

Casari C. S., Russo V., Li Bassi A., Bottani C. E., Cataldo F., Lucotti A., Tommasini M., Del Zoppo M., Castiglioni C., Zerbi G., 2007. Appl. Phys. Lett. **90**, 01311.

Cataldo F., 2003. Carbon **41**, 2653.

Cataldo F., 2004. Carbon **42**, 129.

Chhowalla M., Ferrari A. C., Robertson J., and Amaratunga G. A. J., 2000. Appl. Phys. Lett. **76**, 1419.

Chichknov B. N., Momma C., Nolte S., von Alvensleben F., and Tunnerman A, 1996. Appl. Phys. A **63**, 109.

Compagnini G., Mita V., Cataliotti R. S., D'Urso L., Puglisi O., 2007. Carbon **45**, 2445.

Creighton J. A., Albrecht M. G., Hester R. E., and Matthew J. A. D., 1978. Chem. Phys. Lett. **55**, 55.

Cuomo J. J., Pappas D. L., Bruley J., Doyle J. P., and Saenger K. L., 1991. J. Appl. Phys. **70**, 1706.

Danno T., Okada Y., and Kawaguchi J., 2004. American Institute of Physics conference proceedings **723**, 431.

Darmstadt H., Summchen L., Roland U., Roy C., Kaliaguine S., and Adnot A., 1997. Surf. Inter. Anal. **25**, 245.

Das Sarma S. and Senna J. R., 1994. Phys. Rev. B **49**, 2443

Davis C. A., Amaratunga G. A. J., and Knowles K. M., 1998. Phys. Rev. Lett. **80**, 3280.

Diaz J., Paolicelli G., Ferrer S., Comin F., 1996. Phys. Rev. B **54**, 8064.

Diederich F. and Rubin Y., 1992. Ang. Chem. Int. Ed. Engl. **31**, 1101.

Diziulis S. V. and Fleischauer P. D., 1990. Langmuir **6**, 621.

Donadio D., Colombo L., Milani P., and Benedek G., 1999. Phys. Rev. Lett. **83**, 776.

Downer M. C., Ahn H., Reitze D. H., and Wang X. Y., 1993. Int. J. Thermphys. **14**, 361.

Duley W. W., 1996. "UV Lasers: Effects and Applications in Materials Science", Cambridge University Press, Cambridge

Duley W. W., 2000. Astrophys. J. **528**, 841.

D'Urso L., Compagnini G., and Puglisi O., 2006. Carbon, **44**, 2093.

Eastmond R., Johnson T. R., and Walton D. R. M., 1972. Tetrahedral **28**, 4601.

Eisler S., Slepkov A. D., Elliott E., Luu T., McDonald R., Hegmann F. A., and Tykwinski R. R., 2005. J. Am. Chem. Soc., **127**, 2666.

Ehler A. W., 1975. J. Appl. Phys. **46**, 2464.

Emmony D. C., Howson R. P. and Willis L. J., 1973. Appl. Phys. Lett. **23**, 598.

Enke K, 1981. Thin Solid Films, **80**, 193.

Fallon P. J., Veerasamy V. S., Davis C. A., Robertson J., Amaratunga G. A., Milne W. I., Koshinen J., 1993. Phys. Rev. B **48**, 4777.

Ferrara J. D., Tessler-Youngs C., and Youngs W. J., 1987. Organometallics 6, 676.

Ferrari A. C., Kleinsorge B. Morrison N. A., Hart A., Stolojan V., and Robertson J., 1999. J. Appl. Phys. **85**, 7191.

Ferrari A. C. and Robertson J., 2000. Phys. Rev. B **61**, 14095.

Ferrari A. C. and Robertson J., 2001. Phys. Rev. B **64,** 075414. a

Ferrari A. C. and Robertson J., 2001. Phys. Rev. B **64**, 121405R. b

Ferrari A. C. Rodil S. E., Robertson J., Milne W. I., 2002. Dia. Relat. Mater. **11**, 994.

Fonlani A., 2003. J. Phys. D: Appl. Phys. **36**, 394.

Friedmann T. A., McCarty K. F., Barbour J. C., Siegal M. P., Dibble D. C., 1996. Appl. Phys. Lett. **68**, 1643.

Fu C. C., Lee H. Y., Chen K., Lim T. S., Wu H. Y., Lin P. K., Wei P. K., Tsao P. H., Chang H. C., and Fann W., 2007. Proc. Natl. Acad. Sci. USA 104, 727.

Fuge G. M., Ashfold N. R., Henley S. J., 2006. J. Appl. Phys. **99**, 014309.

Gamaly E. G., Rode A. V., Luther-davies B., and Tikhonchuk V. T., 2002. Phys. Plasmas, **9**, 949.

Garrelie F., Loir A. S., Donnet C., Rogemond F., Le Harzic R., Belin M., Audouard E., and Laporte P., 2003. Surf. Coat. Tech. **163-164**, 306.

Gaumet J. J., Wakisaka A., Shimizu Y., Tamori Y., 1993. J. Chem. Soc. Faraday Trans. **89**, 1667.

Geusic M. E., Mcllrath T. J., Jarrold M. F., Bloomfield L. A., Freeman R. R., and Brown W. L., 1986. J. Chem. Phys. **84**, 2421.

Gilkes K. W. R., Sands H. S., Batchelder D. N., Robertson J., Milne W. I., 1997. Appl. Phys. Lett. **70**, 1980.

Gogotsi Y. G., Kailer A., Nickel K. G., 1999. Nature **401**, 663

Gontier Y. and Trahin M., 1984. "Multiphoton ionization of Atoms", ed. Chin S. L. and Lambropoulos P. , Academic, New York.

Grill A, 1999. Diamond Relat. Mater. **8**, 428

Gunlycke D., Li J., Mintmire J. W., White C. T., 2007. Appl. Phys. Lett. 91, 112108.

Guo T., Jin C., and Smalley R. E., 1991. J Phys. Chem. **95**, 4948.

Haerle R., Riedo E., Pasquarello A., and Baldereschi A., 2001. Phys. Rev. B **65**, 045101.

Haley M. M., Brand S. C., and Pak J. J., 1997. Ang. Chem. Int. Ed. Engl. **36**, 836.

Hartney M. A., Chiang J. N., Hess D. W., and Soane D. S., 1989. Appl. Phys. Lett. **54**, 1510.

Haslett T. L., Fedrigo S., and Moskovits M., 1995. J. Chem. Phys. **103**, 7815.

Haerle R., Riedo E., Pasquarello A., and Baldereschi A., 2001. Phys. Rev. B **65,** 045101.

Hauert R. 2003. Diamond Relat. Mater. **12**, 583.

He H., Sekine T. and Kobayashi T., 2002. Appl. Phys. Lett. **81**, 610.

Heath J. R., Zhang Q., O'Brien S. C., Curl R. F., Kroto H. W., and Smalley R. E., 1987. J. Am. Chem. Soc. **109**, 359

Heimann R. B., Kleiman J., and Salansky N. M., 1983. Nature **306**, 164.

Heimann R. B. 1994. Diamond Relat. Mater. **3**, 1151.

Heimann R. B., Evsyukov S. E., and Kavan L. (ed.), 1999. "Carbyne and Carbynoid Structure", Kluwer Academic, Dordrecht.

Heymann D., 2005. Carbon **43**, 2235.

He H., Sekine T. and Kobayashi T, 2002. Appl. Phys. Lett. **81**, 610.

Heine V., and Van Vechten J. A., 1976. Phys. Rev. B **13**, 1622.

Hidai H., Tokura H., 2005. J. Appl. Phys. **98**, 094907.

Hlavaty J., Kavan L, Kasahara N., Oya A., 2000. Chem. Comm. 737.

Hu A., Alkhesho I., Duley W. W., and Zhou H., 2006. J. Appl. Phys. **100**, 084319. a

Hu A., Alkhesho I., and Duley W. W., 2006. Astrophys. J. Lett. **653**, 157. b

Hu A., Alkhensho I., Zhou H., Duley W. W., 2007. Diamond Rel. Mater. , **16**, 149. a

Hu A., Lu Q. B., Duley W. W., and Rybachuk M., 2007. J. Chem. Phys. **126**, 154705. b

Hu A., Griesing S., Rybachuk M., Lu Q. –B., Duley W. W., 2007. J. Appl. Phys. **102**, 074311. c

Hu A., Lu Q. -B, Duley W. W., and Rybachuk M., 2007. Appl. Phys. Lett. **91**, 131906. d

Hu A., and Duley W. W., 2007. Chem. Phys. Lett. **450**, 375. e

Huang H., Puerstoff E., Osawa E., and Ho D., 2007. Nanolett. 7, 11

Ilie A., Ferrari A. C., Yagi T., Robertson J., 2000. Appl. Phys. Lett **76**, 2627.

IIkov F. A., Decker J. E., and Chin S. L., 1992. J. Phys. B: Mol. Opt. Phys. **25**, 4005.

Iyer S. B., Harshvardhan K. S., Kumar V., 1995. Thin Solid films **256**, 94.

Jernigan G. G., Stahlbush R. E., and Saks N. S., 2000. Appl. Phys. Lett. **77,** 1437.

Johnson S. L., Heimann P. A., MacPhee A. G., Lindenberg A. M., Monteiro O. R., Chang Z., Lee R. W., and Falcone R. W., 2005. Phys. Rev. Lett. **94**, 057407.

Kaganov M. I., Lifshitz I. M., and Tanatarov L. V. , 1957. *Sov. Phys.-JETP* **4**, 173

Kalish R., Lifshitz Y., Nugent K. and Prawer S., 1999. Appl. Phys. Lett. **74**, 2936.

Kavan L., Dousek F. P., Micka K., Weber J., 1988. Carbon **26**, 235.

Kavan L., and Kastner J., 1994. Carbon **32**, 1533.

Kavan L, Hlavaty J., Kastner J., and Kuzmany H., 1995. Carbon **33**, 1321.

Kavan L., 1997. Chem. Rev. **97**, 3061.

Kastner J., Kuzmany H., Kavan L., Dousek F. P., and Kurti J., 1995. Marcomolecule **28**, 344.

Kawashima Y. and Katagiri G., 1995. Phys. Rev. B **52**, 10053.

Keldysh L., 1964. Zh. Eksp. Teor. Fiz. 47, 1945 [1965 Sov. Phys. JETP **20**, 1307].

Kent P. R. C., Towler M. D., Needs R. J., Rajagopal G., 2000. Phys. Rev. B **62**, 15394.

Kertesz M., Koller J., and Azman A., 1978. J. Chem. Phys. **68**, 2779.

Khaibulli I. B., Shtyrkov E. I. Zaripov M. M., Bayazitov R. M., and Galjantdinov M. F., 1979. Radiat. Eff. **36**, 225

Kiang C. –H., and Goddard III W. A., 1996. Phys. Rev. Lett. **76**, 2515

Kneipp K., Roth E., Engert C., and Kiefer W., 1993. chem.. Phys. Lett. **207**, 450.

Kneipp K., Wang Y., Kneipp H., Perlman L. T., Itzkan I., Dasari R. R., and Feld M. S., 1997. Phys. Rev. Lett.**78**, 1667.

Knight D. S., and White W. B., 1989. J. Mater. Res. **4**, 385.

Kodai F., Yamamoto K., Koga Y., 2000. Proc. SPIE **3885**, 193.

Koo Y., Choi Y., lee K. H., Jung K., 2002. Bull. Korean Chem.. Soc. **23**, 309.

Kopaev Yu. V., Menyailenko V. V., and Molotkov S. N., 1985. Fiz. Tverd. Tela (Leningrad) 27, 3288. [1985 Sov. Phys. Solid State **27**, 1979].

Kruger A., Kataoka F., Ozawa M., Fujino T., Suzuki Y., Aleksenskii A. E., Vul Y. A., Osawa E., 2005. Carbon **43**, 1722.

Kudelski A. and Pettinger B., 2000. Chem. Phys. Lett. **321**, 356.

Kurti J., Magyar C., Balazs A., and Rajczy P., 1995. Synth. Met. **71**, 1865.

Lagow R. J., Kampa J. J., Wei H. –C., Battle S. L., Genge J. W., Laude D. A., C. J. Harper, Bau R., Stevens R. C., Haw J. F., Munson E., 1995. Science **267**, 362.

Lacour S. P., Wagner S., Huang Z., and Suo Z., 2003. Appl. Phys. Lett. **82,** 2404.

Lee C. S., Kim T., Lee K., Ahn J., Yoon K., 2003. Chem. Phys. Lett. **380**, 774.

Lee P. C. and D. Meisei, 1982. J. Phys. Chem. **86**, 3391.

Lee Y., Becker M. F., and Walser R. M., 1988. J. Opt. Soc. Am. B **5**, 648.

Lenner M. Kaplan A., Palmer R. E., 2007. Appl. Phys. Lett. **90**, 153119.

Lifshitz Y., Lempert G. D., and Grossman E., 1994. Phys. Rev. Lett. **72**, 2753.

Lifshitz Y., 1996. Diamond Relat. Mater. **5**, 388

Liu G., Ren B., Wu D., Duan S., Li J., Yan J., Gu R. A., and Tian A. -Q, 2006. J. Phys. Chem. B **110,** 17498.

Loir A.-S., Garrelie F., Subtil J. –L., Gautaland F., Belin M., Le Harzic R., Donnet C., Ouerdane Y., Rogemond F., Laporte P., 2003. Appl. Surf. Sci. **208-209**, 553.

Lombardi R., Birke R. L., Sanches L. A., Bernard I., and Sun S. C., 1984. Chem. Phys. Lett. **104,** 240.

Lopez-Rios T., Sandre E., Leclercq S., and Sauvain E., 1996. Phys. Rev. Lett. **76**, 4935.

Lucotti A., Tommasini M., Del Zoppo M., Castiglioni C., Zerbi G., Cataldo F., Casari C. S., Li Bassi A., Russo V., Bogana M., and Bottani C. E., 2006. Chem. Phys. Lett. **417**, 78.

Luo S., Tschauner O., Tiemey T. E., Swift D. C., Chipera S. J. and Asimow P. D., 2005. J. Chem. Phys. **123**, 024703.

Luther-Davies B., Gamaly E. G., Wang Y., Rode A. V., and Tikhonchuk V. T., 1992. Sov. J. Quantum Electron, **22,** 289.

von der Linde D., Sokolowski-Tinten K., and Bialkowski J., 1997. *Appl. Surf. Sci*. **109/110**, 1.

Mapelli C., Castiglioni C., Zerbi G., and Mullen K., 1999. Phys. Rev. B **60**, 12710.

Marks N. A., Mckenzie D. R., Pailthorpe B. A., Bernasconi M. and Parrinello M., 1996. Phys. Rev. Lett. **76**, 768.

Matuda N., Baba S., and Kinbara A,, 1981. Thin Solid Films **81**, 30.

McCauley T. G., Gruen D. M., and Krauss A. R., 1998. Appl. Phys. Lett. **73,** 1646.

McKenzie D. R., Muller D., and Pailthorpe B. A., 1991. Phys. Rev. lett. **67**, 773.

Mercer T. W., DiNardo N. J., Rothman J. B., Siegal M. P., Friedmann T. A., 1998. Appl. Phys. Lett. **72**, 2244.

Merel P., Tabbal M., Chaker M., Moisa S., Margot J., 1998. Appl. Surf. Sci. **136**, 105.

Merkulov V. I., Lannin J. S., Munro C. H., Asher S. A., Veerasamy V. S., and Milne W. I., 1997. Phys. Rev. Lett. **79,** 4869.

Merkulov V. I., Lowndes D. H., G. E. Jellison, Puretzky A. A. Jr., and Gohegan D. B., 1998. Appl. Phys. Lett. **73**, 2591.

Misra A., Tyagi P. K., Yadav B. S., Rai P., and Misra D. S., Pancholi V., and Samajdar I. D., 2006. Appl. Phys. Lett. **89,** 071911.

Miyaji G., and Miyazaki K., 2006. Appl. Phys. Lett. **89**, 191902.

Momma C., Chichkov B. N., Nolte S., von alvensleben F., Tunnerman A., Welling H., and Wellegehausen B., 1996, Opt. Comm. **129**, 134.

Momma C., Nolte S., Chichkov B. N., von alvensleben F., Tunnerman A., 1997, Appl. Surf. Sci. **109/110**, 15.

Narita N., Nagai S., Suzuki S., and Nakao K., 1998. Phys. Rev. B **58**, 11009.

Nemanich R. J. and Solin S. A., 1979. Phys. Rev. B **20**, 392.

Nie S. and Emory S. R., 1997. Science **275**, 1102.

Nishide D., Dohi H., Wakabayashi T., Nishibori E., Aoyagi S., Ishida M., Kikuchi S., Kitaura R., Sugai T. Sakata M., Shiohara H., 2006. Chem. Phys. Lett. **428**, 356.

Nishide D., Wakabayashi T., Sugai T., Kitaura R., Kataura H., Achiba H., and Shinohar H., 2007. J. Phys. Chem. C **111**, 5178.

Nir D., 1984.Thin Solid Films, **112**, 41.

Nolte S., Momma C., Jacobsm H., Tünnermann A., Chikov B. N., Wellegehausen B., and Welling H., 1997. J. Opt. Soc. Am. B **14**, 2716.

Oberlin A., 2002. Carbon **40**, 7.

Obradovic B., Kotlyar R., Heinz F., Matagne P., Rakshit T., Giles M. D. and Stettler M. A., Nikonov D. E., 2006. Appl. Phys. Lett. 88, 142102.

O'keefe A., Ross M. M., and Baronavski A. P., 1986. Chem. Phys. Lett. **130**, 17.

Okoshi M., Higuchi S., and Hanabusa M., 1999. J. Appl. Phys. **86**, 1768.

Okoshi M., Higuchi S., Hanabusa M., 2000. Appl. Surf. Sci. **154-155**, 376.

Osipov V., Baidakova M., Takai K., Enoki T., and Vul' A., Full., 2006. Nano. and Cabon Nano. **14**, 565.

Otto A., 2002. J. Raman Spec. **33**, 593.

Ozkan A. M., Malshe A. P., Railkar T. A., and Brown W. D., Shirk M. D. and P. A. Molian P. A., 1999. Appl. Phys. Lett. **82**, 3716.

Ouyang Y., Yoon Y., Fodor J. K., and Guo J., 2006. Appl. Phys. Lett. 89, 203107.

Palik, E. D. (ed.), 1985. "Handbook of Optical Constants of Solids", Academic Press, New York.

Pappas D. L., Saenger K. L., Bruley J., Krakow W., Cuomo J. J., Gu T., and Collins R. W., 1992. J. Appl. Phys. **71**, 5675.

Park S. J. , Lee K., Ko D. 2005. Diamond Relat. Mater., **14**, 1291

Perry M. D., Stuart B. C., Banks P. S., Feit M. D., Yanovsky V., and Rubenchik A. M., 1999. J. Appl. Phys. **85**, 6803

Pitzer K. S., 1959. J. Am. Chem. Soc. **1**, 4477.

Prawer S., Nugent K. W., Lifshitz Y., Lempert G. D., Grossman E., Kulik J., Avigal I., and Kalish R., 1996. Diamond Relat. Mater. **5**, 433.

Preston J. S., van Driel H. M. and Sipe J. E., 1989. Phys. Rev. B **40**, 3942.

Qian F., Craciun V., Singh R. K., Dutta S. D., Pronko P. P., 1999. J. Appl. Phys. **86,** 2281.

Ravagnan L., Siviero F., Lenardi C., Piseri P., Barborini E., and Milani P., 2002. Phys. Rev. Lett. **89**, 285506.

Ravagnan L., Barborini E., Bandiera D., Salis E., Piseri P., Milani P., Lenardi C., Coreno M., De Simone M., and Prince K. C., 2006. Carbon **44**, 1518.

Raizer Yu. P., 1977. "Laser-Induced Discharge Phenomena", Consultant Bureau, New York.

Reif J., Costache F., Henyk M., and Pandelov S. V., 2002. Appl. Surf. Sci. **197-198**, 891.

Reitze D. H., Ahn H. and Downer M. C., 1992. Phys. Rev. B **45**, 2677.

Rice M. J., Phillpot S. R., Bishop A. R., and Campbell D. K., 1986. Phys. Rev. B **34**, 4139.

Robertson J., 1991. Prog. Solid State Chem. **21**, 199

Robertson J., 1993. Diam. Relat. Mater. **2**, 984.

Robertson J., 2002. Mater. Sci. Eng. R. **37**, 129

Rohlfing E. A., Cox D. M., Kaldor A., 1984. J. Chem. Phys. **81**, 3322.

Rossi M. C., 1998. Appl. Phys. Lett., **73**, 1203.

Roy D., Barber Z. H., and Clyne T. W., 2002. J. Appl. Phys. **91**, 6085.

Roy Greiner N., Philips D. S., Johnsonn J. D., Volk F., 1988. Nature 333, 440.

Rudolph P. and Kautek W., 2004. Thin Solid Films **453-454**, 537.

Saito S., 1997. Science **278**, 77

Salaneck W. R., Thomas H. R., Bigelow R. W., Duke C. B., Plummer E. W., Heeger A. J., and MacDiarmid A. G. , 1980. J. Chem. Phys. **72**, 3674.

Sattel S., Robertson J., Ehrhardt H., 1997. J. Appl. Phys. **82**, 4566.

Scandolo S., Bernasconi M., Chiarotti G. L., Focher P., and Tosatti E., 1995. Phys. Rev. lett. **74**, 4015.

Scott C. D., Arepalli S., Nikolaev P., and Smalley R. E., 2001. Appl. Phys. A **72**, 573-80.

Scheibe H. J., Drescher D., Jackel R., Kuenzelmann U., 1994. Diamond Red. Mater. **3,** 732.

Schultz P. A. , Leung K., and Stechel E. B., 1999. Phys. Rev. B **59**, 733.

Schwan J., Ulrich S., Batori V., Erhardt H., Silva S. R. P., 1996. J. Appl. Phys. **80,** 440.

Seibert K., Cho G. C., Kurt W., Kurz H., Reitze D. H., Dadap J. I., Ahn H., Downer M. C., Malvezzi A. M., 1990. Phys. Rev. B **42**, 2842

Sergushin I. P., Kudryavtsev Yu. P., Elizen V. M., Sadovskii A. P., Sladkov A. M., Nefedov V. I., and Korshak V. V., 1977. J. Struct. Chem. **18**, 553.

Sharda T., Soga T., Jimbo T., and Umeno M., 2001. Diamond Rel. Mater. **10**, 1592.

Sharma A. K., Vispute R. D., Joag D. S., Ogale S. B., Joag S. D., Ayyub P., Multani M., Dey G. K., and Banerjee S., 1993. Mater. Lett. **17**, 42.

Shemella P., Zhang Y., Mailman M., Ajayan P. M., Nayak S. K., 2007. Appl. Phys. Lett. **91,** 042101.

Shi J. R., Shi X., Sun Z., Lau S. P., Tay B. K., Tan H. S., 2001. Diamond Rel. Mater. **10**, 76.

Shi R., Li H. J., Yang Z., and Kang M. K., 1997. Carbon **35**, 1789.

Shibagaki K., Kawashiwa T., Sasaki K., Kadota K., 2000. Jpn. J. Appl. Phys. **39,** 4959.

Shibagaki K., Takada N., Sasaki K., Kadota K., 2002. J. Appl. Phys. **91**, 2449.

Shirk M. D., and Molian P. A., 2000. Phys. Rev. Lett. **85**, 4092

Shirk M. D., and Molian P. A., 2001. Carbon **39**, 1183.

Shvartsburg A. A., Hudgins R. R., Dugourd P., Gutierrez R., Frauenheim T., and Jarrold M. F., 2000. Phys. Rev. Lett. **64**, 2421

Siegal M. P., Tallant D. R., Provencio P. N., Overmyer D. L., Simpson R. L., Martinez-Miranda L. J., 2000. Appl. Phys. Lett. **76**, 3052.

Silvestrelli P. L., Alavi A., Parrinello M., and Frenkel D., 1996. Phys. Rev. Lett. 77, 3149; 1997. Phys. Rev. B **56**, 3806.

Singh A. P., Kapoor A., Tripathi K. N., Ravindra Kumar G., 2002. Opt. Laser Technol. **34**, 37.

Singh J., Vellaikal M., and Narayan J., 1993. J. Appl. Phys. **73**, 4351.

Singh R. K., Bhattacharya D., and Narayan J., 1990. Appl. Phys. Lett. **57**, 2022.

Sipe J. E., Young J. F., Preston J. S., and van Driel H. M., 1983. Phys. Rev. B **27**, 1141.

Smith K. L. and Black K. M., 1984. J. Vac. Sci. Technol. A **2**, 744.

Sokolowski-Tinten K., and von der Linder D., 2000. Phys. Rev. B **61**, 2643

Springborg M., and Kavan L., 1992. Chem. Phys. **168**, 249.

Stampfli P. and Bennemann K. H., 1990. Phys. Rev. B **42**, 7163; 1992. Phys. Rev. B **46**, 10686

Stioan R., Rosenfeld A., Ashkensari D., Hertel I. V., Bulgakova N. M., and Campbell E. E. B., 2002. Phys. Rev. Lett. **88**, 097603.

Strickland D., and Mourou G., 1985. Opt. Commun. 56, 219.

Stuart B. C., Feit M. D., Herman S., Rubenchik A. M., Shore B. W., and Perry M. D., 1996. Phys. Rev. B **53**, 1749

Szafert S. and Gladysz J. A., 2003. Chem. Rev. **103**, 4175

Szczepanski J., Ekern S., and Vala M., 1997. J. Phys. Chem. A **101**, 1841.

Tabata H., Fujii M., Hayashi S., 2004. Chem. Phys. Lett. **395**, 138.

Tabata H., Fujii M., Hayashi S., 2006. Carbon **41**, 522. a

Tabata H., Fujii M., Hayashi S., Doi T., Wakabayashi T., 2006. Carbon **44**, 3168. b

Tanaba H., Fujii M., Hayashi S., 2006. Chem. Phys. Lett. **420**, 166. c

Tang X., Wang S., Elshakre M. E., Gao L., Wang Y., Wang H., and Kong F., 2003. J. Phys. Chem.. **A 107**, 13.

Taft E. A. and Philipp H. R., 1965. Phys. Rev. A **138**, 197.

Talapatra S., Ganesan P. G., Kim T., Vajtai R., Huang M., Shima M., Ramanath G., Srivastava D., Deevi S. C., and Ajayan P. M., 2005. Phys. Rev. Lett. **95**, 09701.

Talin A. A., Pan L. S., McCarty K. F., Felter T. E., Doer H. J., Bunshan R. F., 1996. Appl. Phys. Lett. **69**, 3842.

Tauc J., Grigorovici R., and Vancu A., 1966, Phys. Status Solidi **15**, 627.

Tharigen T., Hartmann E., Lenk M., Mende A., Otte K., Lorenz M., and Hallmeier K. H., 2001. Appl. Surf. Sci. **182,** 142.

Tuinstra F. and Koenig J. L., 1970. J. Chem. Phys. **53**, 1126.

Tsuji M., Tsuji T., Kuboyama S., Yoon S. –H., Korai Y., Tsujimoto T., Kubo K., Mori A., Mochida I., 2002. Carbon **355**, 101.

Tsuji M., Kuboyama S., Matsuzaki T., Tsuji T., 2003. Carbon **41**, 2141.

Utsumi W., and Yagi T., 1991. Science **252**, 1542

Van Duyne R. P., 2004. Science **306**, 985.

Van Vechten J. A., Tsu R., and Saris F. W., 1979. Phys. Lett. **74A**, 422.

VanRompay P. A., Nantel M., Pronko P. P., 1998. Appl. Surf. Sci. **127-129**, 1023.

Varlamova O., Costache F., Reif J., Bestehorn M., 2006. Appl. Surf. Sci. **252**, 4702.

Vechten V., 1981. Solid State Comm. **39**, 1285.

Voevodin A. A,, Donley M. S., Zabinsky J. S., and Bultman J. E., 1995. Surf. Sci. Coat. Technol. **77**, 534.

Voevodin A. A., Donley M. S., 1996. Surf. Coat. Technol. **82**, 199.

Vorobyev A. Y., Markin V. S. and Guo C., 2007. J. Appl. Phys. **101**, 034903.

Wagner J., Ramsteiner M., Wild Ch., and Koidl P., 1989. Phys. Rev. B **40**, 1817

Wakabayashi T., Tabata H., Doi T., Nagayama H., Okuda K., Umeda R., Hisaki I., Sonada M., Tobe Y., Minematsu T., Hashimoto K., Hayashi S., 2007. Chem. Phys. Lett. **433**, 296.

Wakisaka A., Gaumet J. J., shimizu Y., Tamori Y., Sato H., Tokumaru K., 1993. J. Chem. Soc. Faraday Trans. **89**, 1001.

Wang C. Z., and Ho K. M., 1993. Phys. Rev. Lett. **71**, 1184.

Wang C. Z., and Ho K. M., 1994. Phys. Rev. Lett. **50**, 12429.

Wang S., Tang X., Gao L., Elshakre M. E., Kong F., 2003. J. Phys. Chem. **A107**, 6123.

Wei Q., Narayan R. J., Sharma A. K., Sankar J., and Narayan J., 1999. J. Vac. Sci. Technol. **17**, 3406.

Wu Q., Ma Y., Fang R., Liao T., Yu Q., Chen X.and Wang K., 2003. Appl. Phys. Lett. **82**, 1703.

Yagi T., Utsumi W., Yamakata M. Kikegawa T., Shimomura O., 1992. Phys. Rev. B **46**, 6031.

Yao D. S., Liu J. Wang L. Yu C. Zhan R., 2000. Chin. Phys. Lett. **17**, 540.

Yang G. W., and Wang J. B., 2000. Appl. Phys. A **72**, 475.

Yang S., Taylor K. j., Craycraft M. J., Conceicao J., Pettiette C. L., Cheshnovsky O., Smalley R. E., 1988. Chem. Phys. Lett. **144**, 431.

Yasuda A., Kawase N., Matsui T., Shimidzu T., Yamaguchi C., Matsui H., 1999. React. Func. Polym. **41**, 13.

Yasumaru N., Miyazaki K., and Kiuchi J., 2003. Appl. Phys. A: Mater. Sci. Process. **76**, 983.

Yasumaru N., Miyazaki K., and Kiuchi J., 2005. Appl. Phys. A: Mater. Sci. Process. **81**, 933.

Yoshikawa M., Katagiri G., Ishida H., Ishitani A., Akamatsu T., 1988. J. Appl. Phys.**64**, 6464.

Young J. F., Preston J. S., van Driel H. M., and Sipe J. E., 1983. Phys. Rev. B **27**, 1155.

Zhang L., Ma H., Yao N., Lu Z., and Zhang B., 2007. J. Vac. Sci. Technol. B **25**, 545.

Zhou G., Fauchet P. M., and Siegman A. E., 1982. Phys. Rev. B **26**, 5366.